Universidade Federal de Santa Catarina

Centro de Ciências Físicas e Matemáticas

Programa de Pós-Graduação em Física

Mateus Reinke Pelicer

Nuclear pasta in a relativistic mean field model: fluctuations and transport properties

Supervisor: Prof. Dr. Débora Peres Menezes

Co-supervisor: Prof. Dr. Francesca Gulminelli

Florianópolis - SC

2023

Mateus Reinke Pelicer

Nuclear pasta in a relativistic mean field model: fluctuations and transport properties

Tese submetida ao Programa de Pós-Graduação em Física da Universidade Federal de Santa Catarina como requisito para a obtenção do título de Doutor em física.
Orientadora: Profª. Drª. Débora Peres Menezes
Co-orientadora: Profª. Drª. Francesca Gulminelli

Florianópolis - SC

2023

Ficha de identificação da obra elaborada pelo autor,
através do Programa de Geração Automática da Biblioteca Universitária da UFSC.

Pelicer, Mateus Reinke
Nuclear pasta in a relativistic mean field model: fluctuations and transport properties / Mateus Reinke Pelicer ; orientador, Débora Peres Menezes, coorientador, Francesca Gulminelli, 2023.
182 p.

Tese (doutorado) - Universidade Federal de Santa Catarina, Centro de Ciências Físicas e Matemáticas, Programa de Pós-Graduação em Física, Florianópolis, 2023.

Inclui referências.

1. Física. 2. física-nuclear. 3. astrofísica. 4. fase pasta. 5. transporte. I. Menezes, Débora Peres. II. Gulminelli, Francesca. III. Universidade Federal de Santa Catarina. Programa de Pós-Graduação em Física. IV. Título.

Mateus Reinke Pelicer

Nuclear pasta in a relativistic mean field model:
fluctuations and transport properties

O presente trabalho em nível de doutorado foi avaliado e aprovado por banca examinadora composta pelos seguintes membros:

Prof. Dr. André da Silva Schneider
Universidade Federal de Santa Catarina

Prof. Dr. Emmanuel Gräve de Oliveira
Universidade Federal de Santa Catarina

Prof. Dr. Sidney dos Santos Avancini
Universidade Federal de Santa Catarina

Profª. Drª. Constança Providência
Universidade de Coimbra

Prof. Dr. Alexandre Magno Silva Santos
Universidade Federal de Santa Catarina

Certificamos que esta é a versão **original e final** do trabalho de conclusão que foi julgado adequado para obtenção do título de doutor em física.

Documento assinado digitalmente
Paulo Henrique Souto Ribeiro
Data: 03/04/2023 14:18:17-0300
CPF: ***.886.506-**
Verifique as assinaturas em https://v.ufsc.br

Coordenação do Programa de Pós-Graduação

Documento assinado digitalmente
Debora Peres Menezes
Data: 03/04/2023 15:50:37-0300
CPF: ***.032.478-**
Verifique as assinaturas em https://v.ufsc.br

Supervisor: Profª. Drª. Débora Peres Menezes

Florianópolis, 2023

Acknowledgements

This thesis could not have happened without these people. My tremendous gratitude to:

- My wife, Laura, for the companionship, love, and support during all these years.
- My parents, Márcia and Flavio, for all the love given to me since birth.
- My supervisors, Débora, Francesca, and Emmanuel, for the guidance, the enriching discussions, and for all the opportunities you have given me.
- All my friends and collaborators.
- CAPES, CNPq, LPC-CAEN, FAPESC, and INCT-FNA for the support.

Obrigado.

"*Sometimes I'll start a sentence, and I don't even know where it's going. I just hope I find it along the way.*"

Michael Scott (*The Office US, S05E12)*

Resumo

Matéria bariônica, quando próxima da densidade de saturação, assume formatos inomogêneos complexos coletivamente chamados de fase pasta. Em temperaturas finitas, as diferentes formas geométricas que compõem a pasta devem coexistir, com potenciais consequências na condutividade das crostas de estrelas de nêutrons e no transporte de neutrinos em supernovas. Utilizando um formalismo estatístico para considerar os múltiplos componentes, nós calculamos a composição de matéria na fase pasta permitindo flutuações nas geometrias e densidades dos núcleos. Nós mostramos que diferentes geometrias podem de fato coexistir em uma grande porção da fase pasta, mesmo em temperaturas da ordem da temperatura de cristalização da crosta de estrelas de nêutrons, e calculamos a variância do número efetivo de prótons a fim de quantificar impurezas relacionadas à carga e geometria. Em seguida, fornecemos expressões analíticas para as taxas de colisão em espalhamentos elétron–pasta elásticos e os usamos para calcular a condutividade elétrica de matéria magnetizada. Para estes cálculos, nós usamos um funcional de energia realista a partir de um modelo de campo médio relativístico, e uma tensão de superfície com dependência em temperatura e isospin, ajustada para reproduzir a aproximação de Thomas-Fermi.

Palavras-chaves: física-nuclear. astrofísica. fase-pasta. transporte.

Resumo expandido

Estrelas de nêutrons são objetos extremamente compactos, contendo fases da matéria hádronica que não podem ser encontradas em condições terestres. Portanto, provêem condições para o estudo da matéria nuclear em condições extremas. Na crosta destas estrelas, a densidade pode chegar próxima à densidade de saturação da matéria nuclear, fazendo com que os íons fiquem muito próximos, e a energia de Coulomb e a energia nuclear sejam da mesma magnitude. Esta competição de forças leva à deformação dos íons, que assumem formas geométricas anisotrópicas que são coletivamente chamados de fase pasta. O estudo da pasta é essencial para a descrição precisa de propriedades macroscópicas das estrelas de nêutrons, como a evolução térmica e magnética, a emissão de ondas gravitacionais e a frequência de modos de vibração radial, por exemplo. A opacidade de neutrinos em proto-estrelas de nêutrons também pode ser modificada pela pasta.

Atualmente, é impossível descrever estados hádrônicos pela teoria fundamental da força nuclear, a cromodinâmica quântica, e por isso diversos modelos efetivos são utilizados. As propriedades da fase pasta podem ser calculada em modelos como a dinâmica molecular, em que potenciais entre núcleons são utilizados, e geometrias complexas são obtidas, ou também em modelos como teoria de campos efetiva, que é um modelo relativístico onde os hádrons são descritos por espinores de Dirac e geometrias simplificadas são assumidas a priori. Modelos do primeiro tipo são robustos, porém requerem simulações extremamente custosas. Eles indicam que as diferentes geometrias que compõem a pasta podem coexistir em uma condição termodinâmica fixa, com potenciais consequências na condutividade das crostas de estrelas de nêutrons e no transporte de neutrinos em supernovas. O segundo tipo de modelo descreve uma ampla gama de fenômenos nucleares simultaneamente, porém permite o cálculo de uma única geometria em uma dada condição termodinâmica fixa.

O objetivo deste trabalho é estender cálculos da pasta com modelos relativísticos efetivos. Em primeiro lugar, a meta é calcular uma distribuição de estruturas da fase pasta, com diferentes números de próton e geometria. Com isto, é possível estimar o parâmetro de impureza da crosta interna da estrela, que é um possível mecanismo para limitar o período de pulsares de raio–X isolados. Em seguida, o objetivo é prover expressões analíticas para a frequência de colisões elásticas entre elétrons e pasta. Tais frequências são elementos essenciais no cálculo de propriedades de transporte de carga e calor, como a condutividade elétrica e térmica. O espalhamento entre elétrons e pasta é o mecânismo dominante na condutividade, e por isto é o

elemento de estudo deste trabalho. Tais propriedades são amplamente estudadas na literatura para a parte mais exterior da crosta, onde os núcleos são esféricos, porém no caso da pasta tais cálculos são inexistentes.

Com este fim, a metodologia utilizada consiste, na primeira parte, em um formalismo estatístico para considerar os múltiplos componentes da fase pasta. A composição de matéria na pasta é calculada permitindo flutuações na geometria e nas densidades dos prótons e nêutrons presentes nos núcleos. Um termo de rearranjo é adicionado à energia livre da pasta, e demonstramos que este é um elemento essencial para manter a equivalência entre o formalismo estatístico e o de núcleo único, feito pela minimização da energia livre. Na segunda parte, para calcular as propriedades de transporte, nós generalizamos a expansão da taxa de transição entre os estados iniciais e finais de elétrons que participam do espalhamento elétron-pasta em esféricos harmônicos para o caso em que o núcleo não é esférico. Nós mostramos que, neste caso, há um total de nove frequências de colisão para uma geometria arbitrária, mas estas são reduzidas a duas quando as simetrias da fase pasta são aplicadas, denominadas frequências de colisão axial e perpendicular. Para obter resultados numéricos quantitativos as propriedades da pasta são cálculadas utilizando um funcional de energia realista advindo de um modelo de campo médio relativístico. Este modelo é utilizado em todo o trabalho. A tensão de superfície utilizada possui dependência em temperatura e isospin, e foi ajustada para reproduzir a aproximação de Thomas-Fermi do modelo relativístico.

Os resultados obtidos mostram que, em modelos relativísticos, as estruturas da pasta com diferentes geometria e número de próton coexistem em grande quantidade em uma dada profundidade da estrela. Os valores da impureza são grandes, maiores que a unidade, e estão de acordo com valores propostos de maneira ad hoc na literatura com o intuito de descrever fenômenos macroscópicos. Estes resultados são válidos mesmo em temperaturas da ordem da temperatura de cristalização da crosta da estrelas de nêutrons, $T \approx 0.1$ MeV. Em seguida, nós mostramos que as taxas de colisão axial e perpendicular em espalhamentos elétron–pasta elásticos se tornam cada vez mais diferentes conforme o tamanho da pasta aumenta, porém em altas temperaturas, se as correlações na pasta são omitidas, esta diferença não é consideravelmente grande devido ao tamanho limitado da pasta. A condutividade elétrica é cálculada, e mostramos que a fase pasta reduz a condutividade na crosta da estrela também de acordo com discussões qualitativas presentes na literatura. Devido à pequena anisotropia da pasta, na presença de um campo magnético forte as condutividades perpendicular e paralela ao campo magnético são diferentes

somentes para campos maiores que 10^{18} G.

Palavras-chaves: física-nuclear. astrofísica. fase-pasta. transporte.

Abstract

Baryonic matter close to the saturation density presents complex inhomogeneous phases collectively known under the name of pasta phase. At finite temperatures, the different geometric structures that make up the pasta are expected to coexist, with potential consequences on the neutron star crust conductivity and neutrino transport in supernova matter. In the framework of a statistical multi-component approach, we calculate the composition of matter in the pasta phase by allowing fluctuations in the geometry and densities of nuclei. We show that different geometries can indeed coexist in a large fraction of the pasta phase, down to temperatures of the order of the crystallization temperature of the neutron star crust, and calculate effective proton number variances in order to quantify charge and geometric impurities. Next, we provide analytic expressions for the anisotropic collision rates of the elastic electron–pasta scattering and use them to calculate the electric conductivity of magnetized matter. For these calculations we use a realistic energy functional from relativistic mean field theory and a surface tension with temperature and isospin dependence fitted from Thomas-Fermi calculations.

Key-words: neutron-star. astrophysics. pasta-phase. transport.

Contents

1 Introduction **14**

2 Relativistic mean field theory and the pasta phase **20**

2.1 Non-linear Walecka model 20

2.2 RMF parametrizations and constraints 28

2.3 Nuclear pasta: one-component plasma 31

3 Fluctuations in the pasta phase **43**

3.1 Multi-component plasma 43

3.2 Ensemble equivalence: the rearrangement term 47

3.3 Impurities 52

4 Conductivity of nuclear pasta **56**

4.1 Transport coefficients and the Boltzmann equation 56

4.2 The collision integral 61

4.3 Isotropic case 74

4.4 Anisotropic collision rates 75

4.5 Pasta conductivity 85

5 Digression: related work **92**

5.1 Effect of short-range correlations in nuclear pasta 92

5.2 Delta baryons in magnetars 95

5.3 Deconfinement phase transition in magnetars 102

Conclusions and Perspectives **107**

Bibliography **109**

A Coulomb energy **129**

A.1 Sphere 130

A.2 Cylinder 131

A.3 Slab 132

B Publications **133**

1 Introduction

Neutron stars (NS) are compact objects with masses up to $\sim 2.5\, M_\odot$ and a radius around 10 km that are born either out of the supernovae explosions generated by stars from the zero age main sequence with masses (roughly) between 8 and 25 $M_\odot$, or from the merging of two existing neutron stars. Due to the conservation of angular momentum and magnetic flux, they rotate quickly ($1.4\,\mathrm{ms} \lesssim P \lesssim 30\,\mathrm{s}$), and have very strong magnetic fields ($10^{10}\,\mathrm{G} \lesssim B_{\mathrm{surf}} \lesssim 10^{15}\,\mathrm{G}$) [1]. The name neutron star stems from the high neutron content due to electron captures ($e + p \longrightarrow n + \nu_e$), but their composition is much richer. The baryon density inside the star ranges from a fraction to several times saturation density ($\rho_{\mathrm{sat}} \approx 0.16\ \mathrm{fm}^{-3}$), so the different NS layers contain various phases of cold β-equilibrated nuclear matter. We refer to a NS as a cold compact object because, even though it is hot with respect to earthly standards – they are born with temperatures $\sim 10^{11}$ K and cool down to $\sim 10^9$ K (~ 0.1 MeV) – the Fermi energy is much higher than the thermal one due to the high occupation number of Fermion states (i.e. high densities) [2, 3].

The core, for example, has densities ranging from $\sim \rho_{\mathrm{sat}}/2$ up to somewhere in the range 4 to $10\,\rho_{\mathrm{sat}}$, depending on the NS mass. The core begins when nuclear matter dissolves into homogeneous uniform matter: the outer part is composed of neutrons, protons, electrons, and muons, but the inner core ($\gtrsim 2\rho_{\mathrm{sat}}$) composition is highly uncertain. Many different proposals exist in the literature, such as the appearance of excited baryon states (hyperons and Δs), condensation of pions and/or kaons, and the occurrence of a deconfinement phase transition to quark matter [4–12]. Being a highly magnetized and cold system, particles in the NS are also prone to pairing, forming superconducting and superfluid states [13–15]. The microscopic composition of the core is the main component in determining the maximum mass a NS can have, and this constraint is important to determine how stiff the equation of state (EOS) of nuclear matter is[1].

The crust is also separated into outer and inner parts. The composition of the outer part is fairly simple, consisting of neutron-rich heavy ions with baryon numbers up to ~ 120 [16, 17] and a strongly degenerate electron gas. The inner crust begins at the neutron drip line [2], so a neutron gas is additionally present, which can be in a superfluid state by undergoing Cooper

[1] The equation of state refers to the relation between pressure and energy density of cold nuclear matter in β–equilibrium.

[2] The point where some neutrons start to become unbound from nuclei: $\rho_{\mathrm{drip}} = 4.3 \times 10^{11}\ \mathrm{g\ cm}^{-3} \approx 0.00028\ \mathrm{fm}^{-3}$.

pairing [18–20], and the ions become extremely deformed, giving rise to the nuclear pasta phase [21–23].

The crust is essential in the determination of the radius of the neutron star, e.g. in the analysis of canonical 1.4 $M_\odot$ NS. Thus a good knowledge of its composition, along with simultaneous measurements of mass and radius, such as those currently being provided by NICER, will result in important constraints on the EOS [24–27]. Additionally, the crust properties are also important in determining the dynamic properties of the star, such as the thermo-magnetic evolution [28–33], the continuous emission of gravitational waves due to "mountains" [34–37], quasi-periodic oscillations [38], quasi-persistent sources of soft-γ ray transients and giant flares due to the relaxation of the crust after heat deposition and neutrino emissivity in a proto-neutron star (PNS) [39–43]. Additionally, the superfluid neutrons in the crust are related to pulsar glitches, a sudden change in the rotation period of stable pulsars [19, 20, 44].

These macroscopic features of the NS crust are controlled by the microscopic properties: conductivities, viscosity, breaking strain, lattice structure, defects, impurities, etc. [45]. Such transport properties are determined by the scattering of electrons by other electrons, ionic impurities, and phonons in the crystal lattice. Electron-ion scattering dominates over other mechanisms, and at the lowest densities, it has been extensively studied [46–52]. But in the inner crust at temperatures $T < 10^7$ K, thermal conductivity due to degenerate electron-electron Coulomb scattering becomes competitive with the electron conductivity due to the scattering of electrons by impurity ions [53] and dominates over the contribution due to electron-phonon scattering [54]. In the innermost part of the crust, where the anisotropic pasta appears, the situation is much more complicated.

The existence of nuclear pasta was proposed in the early 1980s by Ranvehall, Pethick, and Wilson [21] and independently by Hashimoto, Seki, and Yamada [22]. The shapes of nuclei proposed in these articles were assumed a priori as cylindrical (rod and tubes) or planar (slab). Bubble shapes could also be formed. These specific shapes were picked due to their symmetries, which allow an analytic calculation of the associated Coulomb and surface energy. The reason for their appearance is that the small lattice spacing in the inner crust makes the Coulomb energy of the ions competitive with its nuclear surface energy, which is otherwise dominant. This competition frustrates the system and allows the pasta to appear. The name pasta phase was coined due to their resemblance with pasta meals: gnocchi (droplet), spaghetti (rod), lasagna

(slabs), bucatini (tubes), and swiss cheese (bubble). These structures appear in this respective order as density increases and the latter two are also known as "inverse" pasta: the dense nuclei form a quasi-continuous medium with neutron-filled holes [53,55]. The difficulties associated with pasta are that they are anisotropic and form an amorphous system, so the determination of its transport properties is a highly non-trivial problem. It has been argued that their amorphous nature is related to the maximum period of 12 s for isolated X-ray pulsars, since the high impurity would raise the resistivity, making the magnetic field have a steep decay after a certain age, thus limiting the NS spin period [56,57].

The calculation of the pasta properties can only be performed with a reliable nuclear model at hand. Since the 1950's many nuclear relativistic and non-relativistic models have been proposed to describe nuclear phenomena, since the fundamental theory of the strong force, quantum chromodynamics, can be applied only in very specific situations: high energy scattering and high temperature and low chemical potential via lattice simulations [58,59]. The earliest calculations regarding the pasta applied the compressible liquid drop (CLD) formalism [21], which assumes constant particle densities (or particle number) to the ions and idealized shapes for the pasta, and then the equilibrium is found via minimization of the free energy. This same approach has been used within relativistic mean field (RMF) models, with the simple difference that the nuclear energy functional comes from a relativistic theory. The RMF is an approximation for effective relativistic theories of nuclear interactions where the meson fields responsible for the interaction are assumed to be static and isotropic. More robust models have also been used to study the pasta, such as the Thomas-Fermi approximations for relativistic models [60–62], where meson fields are no longer isotropic as in the RMF; molecular dynamics (MD) [42,63,64], where interactions are described by short (long) range two-body potentials; and three-dimension Skyrme-Hartree-Fock (3DHF) [65–68], where the ground state is approximated by a Slatter determinant and the nuclear force is described by one-body potentials (Skyrme forces).

Relativistic models are interesting due to the freedom in the determination of their coupling constants, which allow the description of nuclear matter bulk parameters, and astrophysical phenomena. Additionally, the freedom in adding covariant interactions to the Lagrangian permits one to understand the correlations between bulk and astrophysical measurements by changing single bulk parameters. For example, the well-known correlation between the symmetry energy and its slope with the point of the crust–core transition and the NS radius [69–76]. However, the simplicity of the RMF does not allow for robust calculations of the pasta, and we are obliged

to assume the idealized shapes aforementioned and work with a sharp pasta-gas interface, as in the CLD. In contrast, MD has only four free parameters that are fitted to describe the saturation density and binding energies of symmetric matter, neutron matter, and some selected finite nuclei, and 3DHF has 10 free parameters that are fitted with focus either on ground states, fission barriers, and surface energies or in neutron-rich matter, with astrophysical applications [77,78]. But, since they allow the simulation of single particle interactions, it is possible to follow a system of nucleons, starting from an out-of-equilibrium state, evolving into an equilibrium one, and forming pasta.

These simulations are done without the assumption of specific shapes, and it has been shown by both MD and 3DHF that more exotic shapes of pasta can be formed, such as waffle-like, gyroid, sponge-like and "parking-garage" [28,79–83]. CLD calculations have also corroborated that the gyroid phase can appear as a metastable state [84]. Moreover, these models have shown the inner crust is a very impure system [28,29,85] and MD, in particular, has been used to estimate the transport properties of the pasta [34,55,86,87]. One drawback of MD is that high temperatures and proton fractions must be used, which are thermodynamic conditions better suited for a proto-neutron star, where the presence of the pasta is still a topic of discussion due to the very high temperatures present [88]. Additionally, these simulations require a very large computational power, and the study of a single thermodynamic condition is already very costly.

Conversely, the RMF is not costly numeric, it allows the calculation of the EOS and pasta properties in a couple of minutes. The goal of this thesis is to, within an RMF model:

1 give a preliminar calculation of the pasta impurity parameter $Q_{\rm imp}$;
2 provide the analytical expressions for the pasta collision rates and use them to calculate the pasta conduction transport properties.

For the first goal, we must acknowledge that, in the RMF, the pasta phase is commonly calculated in the one-component plasma approximation (OCP), which assumes the presence of a single ion/pasta structure at a fixed thermodynamic condition [88–97]. The ions in the crust start as a liquid in the proto-neutron star, and they turn into a solid when the ion melting temperature T_m is achieved. The energy difference between ions of different proton numbers and geometries is much smaller than the thermal energy in a NS, so we should expect that a multi-component plasma (MCP) is formed [3,57,98–104], as already ratified by MD calculations of the impurity. In Ref. [98] a statistical approach was developed in order to account for the different ions that can

coexist at finite temperatures. This MCP formalism is valid for an arbitrary EOS and provides a framework for calculating cluster abundances. It improves on older statistical approaches by accounting for interactions and in-medium effects [105], and it has been applied to liquid drop [99, 101, 106] and relativistic models [107]. Furthermore, it recovers the OCP in the zero temperature limit, where a crystalline structure is in fact expected. In Refs. [99, 101] the charge-impurity was calculated in the crust, but only for spherical clusters, while Ref. [107] presents a calculation of pasta distributions only for symmetric matter. However, the calculation of [107]does not minimize the full energy density, making their results inconsistent with the OCP.

The different pasta structures in the system certainly modify the transport properties, and thus the magneto-thermal evolution of the catalyzed neutron star, since they break long-range order. This was our starting motivation for the second goal. Nevertheless, we have realized that no formalism had been fully developed in the literature to calculate the pasta transport properties with a general nuclear model. Indeed, transport calculations considering spherical nuclei have been performed with the relaxation time approximation since the 1970s [46–48], but this cannot be straightforwardly applied to the pasta, as it is founded on the assumption of isotropic scattering. Therefore, based on the proposition of Yakovlev in [33] that the pasta conduction is described by two collision rates, contrary to the unique one in isotropic scattering, we show from simple assumptions that electron-pasta scattering is, in indeed, described by Yakovlev proposal and we provide analytical equations for them. Then we use the non-linear Walecka RMF model [108, 109] to provide quantitative values for the pasta conduction properties. Though the quantitative properties of the pasta are model dependent, the qualitative behavior of our results should remain valid for any realistic nuclear model [110, 111].

In order to make this thesis self-contained we introduce, in Section 2, the non-linear Walecka model in the mean-field approximation. We discuss the bulk properties of the parametrization we choose to work with, the IUFSU [112], as well as some other models for a wider context. We calculate its thermodynamic properties and discuss how the pasta is built in the OCP. In Section 3 we introduce the MCP formalism; we show how it obeys ensemble equivalence, being in accordance with the OCP. We show that a rearrangement term has to be introduced due to the constraint of charge neutrality and that it is essential for ensemble equivalence between OCP and MCP formalisms. Then we calculate the distribution of pasta structures at different thermodynamic conditions accounting for density and geometry fluctu-

ations and estimate the impurity parameter in the inner crust. In Section 4 we introduce the basic concepts of transport theory: the Boltzmann equation, the collision time approximation, and the calculation of the scattering transition rate. Afterwards we generalize the collision time approximation to anisotropic scattering and, using spherical harmonics expansion, we derive analytical expressions for the complex collision rates. Finally, using the pasta symmetries, and restricting ourselves to the pasta conductivity we are able to give expressions for the physical collision rates of the pasta. We give quantitative estimates of the electric conductivity related to electron-pasta scattering in the high-temperature regime, where long-range ion correlations are smaller. Finally, in Section 5 we briefly summarize different works that were developed by the author during his doctorate, but that are not directly related to the main topic of the thesis: deconfinement phase transition in magnetars; presence and effect of heavy baryons in proto–neutron stars and in magnetars; the effect of short-range correlations in the pasta and the correlation between the deconfinement phase transition and the slope parameter.

Natural and gaussian units are used throughout this thesis: $\hbar = c = k_B = 1$ and $\epsilon_0 = 1/4\pi$.

2 Relativistic mean field theory and the pasta phase

In this section, we introduce the non-linear Walecka model and the mean-field approximation, discuss different parametrizations and their predictions, and show how to build the pasta phase. We obtain the equilibrium equations of the mixed pasta-gas phase with a variational calculation, we discuss the pasta properties and the thermodynamic conditions under which it may appear. The formalism developed in this section is the basis for subsequent section.

2.1 Non-linear Walecka model

The fundamental theory of strong interacting particles is quantum chromodynamics [113], from which it is possible to describe high-energy quark interactions, but not interactions at the nucleon level. The majority of phenomena involving nuclear matter occur with nucleons, thus effective models become essential in order to describe them. These models come in many forms: liquid drop [91, 100, 114], molecular dynamics [64], relativistic models [112, 115, 116], Skyrme functionals [67], etc., with their parameters adjusted to describe selected nuclear data, such as decay rates, astrophysical data, resonances, binding energies of finite nuclei, bulk parameters, etc. The selected data the model describe depend on the author's choice. For example, binding energies of finite nuclei are not so commonly used in relativistic models since the description of finite nuclei requires calculations beyond the mean-field approximation, so they tend to be more focused on bulk and astrophysical properties. In this thesis, we will focus solely on one relativistic model: the non-linear Walecka model. Firstly we will describe the model, then the nuclear bulk properties commonly used to fit its parameters.

In nuclear relativistic models, the baryons are described by a Dirac spinor ψ_q. The protons and neutrons ($q = p, n$) can be written in a SU(2) doublet as

$$\Psi = \begin{pmatrix} \psi_p \\ \psi_n \end{pmatrix}, \tag{2.1}$$

and they are distinguished only by their isospin (I_3) and electric charge (e_q). Other baryons, such as hyperons and Δ resonances can be added to the model, but these particles do not appear in the NS crust, and we shall discuss them only in Section 5. The baryons interactions occur via meson and pion exchanges. In the non-linear version we use in this thesis, the interactions occur via the

exchange of σ, ω, and ρ mesons. Nevertheless, other parametrizations of the Walecka model can additionally consider δ and ϕ mesons [117–119]. The ϕ meson is considered only when hyperons are present. Pions are not considered in the Walecka model because their contribution to the energy averages out to zero in the mean-field and Hartree level calculations [120, 121]. Chiral models also consider the ζ meson that acts as a strange condensate and χ dilaton field representing a gluon condensate [116]. Even though the Walecka model is an effective one, these mesons have a counterpart in nature, and their properties are studied through proton-proton and pion-pion collisions [122–132]. The fields that describe the nucleons and mesons relevant to this work and their properties are shown in Tab. 1.

Multiplet	Field	Spin (S)	Isospin (I_3)	Electric charge (e_q)
p, n	ψ_q	1/2	1/2	1, 0
σ	σ	0	0	0
ω	V_μ	1	0	0
$\rho^0, \rho^\pm$	$b^3_\mu,\ b^1_\mu \pm i b^2_\mu$	1	1	(0, ±1)

Table 1: Particles in the QHD and their respective fields, spin, isospin and electric charge.

The Lagrangian of the model can be written as

$$\mathcal{L} = \mathcal{L}_N + \mathcal{L}_\sigma + \mathcal{L}_\omega + \mathcal{L}_\rho + \mathcal{L}_{\omega\rho}. \tag{2.2}$$

The nucleon part (N) contains the usual Dirac kinematics, and couples minimally to the meson fields

$$\mathcal{L}_N = \bar{\Psi}\left[\gamma^\mu\left(i\partial_\mu - g_v V_\mu - g_b I_a b^a_\mu\right) + g_s\sigma - M_N\right]\Psi, \tag{2.3}$$

as traditionally done to enforce invariance by local phase transformations. Here γ^μ are the Dirac matrices, defined by the Clifford algebra $\{\gamma^\mu, \gamma^\nu\} = 2\eta^{\mu\nu}$ and the adjoint spinor is $\bar{\psi} = \psi^\dagger\gamma_0$. The scalar isoscalar σ-meson and the vector isoscalar ω-meson interactions have no isospin charge, so they produce identical interactions for protons and neutrons, but the vector isovector ρ-meson has isospin charge 1, being essential to describe the highly asymmetric neutron star matter. When considering only nucleons, the ρ-meson can be seen as an element of the fundamental representation of $SU(2)$ due to its isospin charge, so we can write $b_\mu = b^a_\mu I_a$ with the index a

summed over $a = 1, 2, 3$. The isospin I_a can be identified with half of the Pauli matrices τ_a

$$I_1 = \frac{1}{2}\begin{pmatrix} 0 & 1 \\ 1 & 0 \end{pmatrix}, \quad I_2 = \frac{1}{2}\begin{pmatrix} 0 & -i \\ i & 0 \end{pmatrix}, \quad I_3 = \frac{1}{2}\begin{pmatrix} 1 & 0 \\ 0 & -1 \end{pmatrix}, \tag{2.4}$$

that obey $[I_a, I_b] = i\epsilon_{abc}I_c$, with ϵ_{abc} being the completely antisymmetric unit tensor, with $\epsilon_{123} = +1$.

The σ-meson describes a long-range attractive force, and its Lagrangian is given by

$$\mathcal{L}_\sigma = \frac{1}{2}\partial_\mu\sigma\partial^\mu\sigma - \frac{1}{2}m_s^2\sigma^2 + \frac{\kappa}{3!}\sigma^3 + \frac{\lambda}{4!}\sigma^4, \tag{2.5}$$

where the third and fourth-order self-couplings were not present in the original Walecka model, being firstly added in order to reproduce measurements of the nuclear incompressibility at saturation density [133]. The Lagrangian for the ω and ρ-mesons are

$$\mathcal{L}_\omega = -\frac{1}{4}\Omega^{\mu\nu}\Omega_{\mu\nu} + \frac{1}{2}m_v^2V_\mu V^\mu + \frac{\xi g_v^4}{4!}(V_\mu V^\mu)^2, \tag{2.6}$$

$$\mathcal{L}_\rho = -\frac{1}{4}B^a_{\mu\nu}B_a^{\mu\nu} + \frac{1}{2}m_b^2b^a_\mu b^\mu_a, \tag{2.7}$$

with kinetic terms defined by the field strength tensors

$$\Omega_{\mu\nu} = \partial_\mu V_\nu - \partial_\nu V_\mu, \tag{2.8}$$

$$B^a_{\mu\nu} = \partial_\mu b^a_\nu - \partial_\nu b^a_\mu - \epsilon^{abc}b^b_\mu b^c_\nu. \tag{2.9}$$

The ω-meson is responsible for short-range repulsion and, in conjunction with long-range interaction of the σ, they reproduce the saturation property of the nuclear force. The fourth-order ω self-interaction is introduced to soften the high-density EOS, and it has only a small effect on bulk properties at saturation density [112, 134, 135]. The vector isovector $\rho-$mesons are essential in the description of asymmetric matter ($N \neq Z$): if they were not present in the model, symmetric matter ($N = Z$) and a pure neutron system ($N = A, Z = 0$) would have the same properties. The charge neutral meson (ρ^0) is described by the fields b^3_μ, and the charged mesons ($\rho_\pm$) are described by the combination $b^\pm_\mu = b^1_\mu \pm ib^2_\mu$.

An ω-ρ interaction term is also typically added:

$$\mathcal{L}_{\omega\rho} = \Lambda_v g_v^2 g_b^2 (V^\mu V_\mu)(b_\nu^a b_a^\nu), \tag{2.10}$$

which, like the fourth-order interaction of the ω-meson, only weakly affects properties at saturation density. Its main impact is on the high-density behavior of the symmetry energy, which measures the difference between a pure neutron system and a completely symmetric one. It can also partly explain the mass difference in mirror nuclei [136, 137].

The equations of motion can be obtained by finding the extremes of the action, leading to an Euler-Lagrange equation for each field

$$\delta \int d^4x \mathcal{L}\left[\Phi_k, \partial_\mu \Phi_k\right] = 0 \quad \Rightarrow \quad \frac{\partial \mathcal{L}}{\partial \Phi_k} - \partial_\mu \frac{\partial \mathcal{L}}{\partial\left(\partial_\mu \Phi_k\right)} = 0, \tag{2.11}$$

therefore, applying it to eq. (2.2) leads to a set of field equations

$$\left[\gamma^\mu\left(i\partial_\mu - g_v V_\mu - \frac{g_b}{2}\tau_a b_\mu^a\right) + g_s\sigma - M\right]\Psi = 0 \tag{2.12}$$

$$\partial_\mu\partial^\mu\sigma + m_s^2\sigma + \frac{\kappa}{2}\sigma^2 + \frac{\lambda}{6}\sigma^3 = g_s\bar{\Psi}\Psi \tag{2.13}$$

$$\partial_\mu\Omega^{\mu\nu} + m_v^2 V^\nu + \frac{\xi g_v^4}{6}(V_\mu V^\mu)V^\nu + 2\Lambda_v g_v^2 g_b^2 (b_c^\mu b_\mu^c)V^\nu = g_v\bar{\Psi}\gamma^\nu\Psi \tag{2.14}$$

$$\partial_\mu B_a^{\mu\nu} + m_b^2 b_a^\nu + 2\Lambda_v g_v^2 g_b^2 (V^\mu V\mu) b_a^\nu = g_b\bar{\Psi}\gamma^\nu I_a\Psi - g_b\epsilon_{abc} b_\mu^b B_c^{\nu\mu}. \tag{2.15}$$

It is complicated to solve this system of equations. In the static case – the Thomas Fermi approximation, they can be solved numerically, but this is quite costly computationally and only necessary if one is interested in finite nuclei. Furthermore, the boundary conditions are taken from the relativistic mean-field approximation, where the meson fields are replaced by their expectation values

$$\sigma \to \langle\sigma\rangle = \sigma_0, \qquad V_\mu \to \left\langle V_\mu\right\rangle = (V_0, \mathbf{0}), \qquad b_\mu^a \to \left\langle b_\mu^3\right\rangle = (b_0, \mathbf{0}). \tag{2.16}$$

In this approximation, we assume isotropic meson fields, which implies that vector components of the 4-vectors vanish and charged mesons are averaged to zero. To calculate bulk parameters and static compact star properties, the RMF is a great approximation. Indeed, many parametrizations are derived only within this approximation, and we will use it from now on.

The Dirac equation (2.12) in the RMF becomes

$$\left[\gamma^0\left(i\partial_0 - g_v V_0 - g_b I_3 b_0\right) + i\boldsymbol{\gamma}\cdot\boldsymbol{\nabla} + g_s\sigma_0 - M_N\right]\Psi = 0, \tag{2.17}$$

and, since the meson fields are homogeneous, and thus take constant values at a fixed density and temperature, it can be solved exactly as if the nucleons were free particles with effective mass

$$M_N^* = M_N - g_s\sigma_0 \tag{2.18}$$

and energy

$$\epsilon_q^{\pm} = \pm E^* + g_v V_0 + I_{3q} g_b b_0. \tag{2.19}$$

where $E^* = \sqrt{\boldsymbol{k}^2 + M_N^{*\,2}}$, and the isospin projections are $I_{3p} = +1/2$ and $I_{3n} = -1/2$. The full solution can be written as a superposition of plane waves $u(\boldsymbol{k},s)e^{-ik\cdot x}$ and $v(\boldsymbol{k},s)e^{ik\cdot x}$ for particles and anti-particles multiplied by their respective creation operators:

$$\psi_q(x) = \sum_s \int \frac{d^3k}{(2\pi)^3}\left[a^q_{\boldsymbol{k},s}u^q_{\boldsymbol{k},s}e^{-i\epsilon_q^+ t + i\boldsymbol{k}\cdot\boldsymbol{x}} + b^{q\,\dagger}_{\boldsymbol{k},s}v^q_{\boldsymbol{k},s}e^{-i\epsilon_q^- t - \boldsymbol{k}\cdot\boldsymbol{x}}\right], \quad q = p,n. \tag{2.20}$$

The reader interested in the complete derivation is referred to [108, 109]. The positive energy solutions, associated with the spinor $u^q_{\boldsymbol{k},s}$ and the creation operator $a^q_{\boldsymbol{k},s}$, represent protons and neutrons, while the negative energy solutions, related to the spinor $\mathrm{v}^q_{\boldsymbol{k},s}$ and the operator $b^q_{k,s}$, represent anti-protons and anti-neutrons. The spin polarization is represented by the label $s = \pm 1$ and $\boldsymbol{k}$ is the 3-momentum. We neither show the explicit form of spinors nor specify a representation of the γ-matrices, since to calculate the EOS it is only necessary to have a few independent relations among them, namely

$$u^\dagger_{\boldsymbol{k},s}u_{\boldsymbol{k},s'} = v^\dagger_{\boldsymbol{k},s}v_{\boldsymbol{k},s'} = \delta_{s\,s'} \tag{2.21}$$

$$\bar{u}_{\boldsymbol{k},s}u_{\boldsymbol{k}',s'} = -\bar{v}_{\boldsymbol{k},s}v_{\boldsymbol{k}',s'} = \frac{M_N^*}{E^*}\delta_{s\,s'}, \tag{2.22}$$

$$\{a^q_{\boldsymbol{k},s}, a^{q\,\dagger}_{\boldsymbol{k}',s'}\} = (2\pi)^3\delta(\boldsymbol{k}-\boldsymbol{k}')\delta_{ss'}, \tag{2.23}$$

$$\{b^q_{\boldsymbol{k},s}, b^{q\,\dagger}_{\boldsymbol{k}',s'}\} = (2\pi)^3\delta(\boldsymbol{k}-\boldsymbol{k}')\delta_{ss'}, \tag{2.24}$$

The first line is a choice of normalization on the spinors, and the second is a property that can be proven quite straightforwardly using eq. (2.17). The third and fourth lines are the imposed commutation relation on the fermionic creation operators at equal times, also known as second

quantization [138].

The meson equations, eqs. (2.13), (2.14) and (2.15), in the RMF become

$$m_s^2\sigma_0 + \frac{\kappa}{2}\sigma_0^2 + \frac{\lambda}{6}\sigma_0^3 \quad = g_s\rho_s = g_s\langle\bar{\Psi}\Psi\rangle, \tag{2.25}$$

$$m_v^2 V_0 + \frac{1}{6}\xi g_v^4 V_0^3 + 2\Lambda_v g_v^2 g_b^2 V_0 b_0^2 \quad = g_v\rho_B = g_v\langle\Psi^\dagger\Psi\rangle \tag{2.26}$$

$$m_b^2 b_0 + 2\Lambda_v g_v^2 g_b^2 V_0^2 b_0 \quad = g_b\rho_3 = g_b\langle\bar{\Psi}I_3\Psi\rangle, \tag{2.27}$$

where the baryon, scalar, and isospin densities are defined as products of the spinor Ψ as:

$$\rho_B = \langle\Psi^\dagger\Psi\rangle = \langle\psi_p^\dagger\psi_p\rangle + \langle\psi_n^\dagger\psi_n\rangle = \rho_p + \rho_n, \tag{2.28}$$

$$\rho_s = \langle\bar{\Psi}\Psi\rangle = \langle\bar{\psi}_p\psi_p\rangle + \langle\bar{\psi}_n\psi_n\rangle = \rho_{sp} + \rho_{sn} \tag{2.29}$$

$$\rho_3 = \langle\Psi^\dagger I_3\Psi\rangle = \langle\psi_p^\dagger I_{3p}\psi_p\rangle + \langle\psi_n^\dagger I_{3n}\psi_n\rangle = \frac{1}{2}\left(\rho_p - \rho_n\right), \tag{2.30}$$

whereas expressions for the proton and neutron number and scalar densities can be obtained with the aid of eqs. (2.21) – (2.24). We write them as

$$\rho_q = \langle\psi_q^\dagger\psi_q\rangle = \gamma_q\int\frac{d^3k}{(2\pi)^3}\left[f_{q+}(\boldsymbol{k}) - f_{q-}(\boldsymbol{k})\right], \qquad q = p, n \tag{2.31}$$

and

$$\rho_{sq} = \langle\bar{\psi}_q\psi_q\rangle = \gamma_q\int\frac{d^3k}{(2\pi)^3}\frac{M_N^*}{\sqrt{\boldsymbol{k}^2 + M^{*2}}}\left[f_{q+}(\boldsymbol{k}) + f_{q-}(\boldsymbol{k})\right]. \tag{2.32}$$

where degeneracy is accounted for with the factor γ_q, which is equal to 2 due to spin, and the functions $f_{q\pm}$ are the Fermi-Dirac distribution [139], defined as

$$\begin{aligned} f_{q+}(\boldsymbol{k}) &= \left\langle a_{\boldsymbol{k},s}^{q\dagger} a_{\boldsymbol{k},s}^{q}\right\rangle = \frac{1}{1+\exp\left[(E^* - \mu_q^*)/T\right]} \\ f_{q-}(\boldsymbol{k}) &= \left\langle b_{\boldsymbol{k},s}^{q\dagger} b_{\boldsymbol{k},s}^{q}\right\rangle = \frac{1}{1+\exp\left[(E^* + \mu_q^*)/T\right]}, \end{aligned} \tag{2.33}$$

where μ_q^* is the effective chemical potential, related to the true one $\mu_q = \partial\mathcal{E}_q/\partial\rho_q$, by

$$\mu_q^* = \mu_q - g_v V_0 - \frac{g_b}{2}\tau_{3,q} b_0. \tag{2.34}$$

At $T = 0$, they relate to the Fermi momentum k_{Fq} via $\mu_q^* = \sqrt{k_{F\,q}^2 + M_N^{*\,2}}$, defining the occupied

energy levels of the Fermi sea. The factor M_N^*/E^* in the scalar density (2.32) represents a Lorentz contraction, so as nucleons become more relativistic the ratio of scalar to number density becomes smaller than unity.

Finally, energy and pressure can be calculated from the energy-momentum tensor

$$T_{\mu\nu} = \sum_{\{\Phi\}} \frac{\partial \mathcal{L}}{\partial\left(\partial_\mu \Phi\right)} \partial_\nu \Phi - \eta_{\mu\nu}\mathcal{L}, \tag{2.35}$$

$$\partial_\mu T^{\mu\nu} = 0, \tag{2.36}$$

which can be derived from Noether's theorem. The theorem states that continuous symmetries of the Lagrangian give rise to conserved currents. Energy and momentum conservation are related to invariance in space-time translation ($x \to x + \epsilon$). In the RMF only spinors are dynamic, thus the meson contribution comes solely from the averaged Lagrangian. The energy density is given by the 00-component

$$\begin{aligned}
\mathcal{E}_\mathrm{b} &= \int \frac{d^3x}{V} \langle T_{00} \rangle = i \sum_{q=p,n} \int \frac{d^3x}{V} \psi_q^\dagger \partial_t \psi_q - \langle \mathcal{L} \rangle \\
&= \sum_{q=n,p} \gamma_q \int \frac{d^3k}{(2\pi)^3} E^* \left(f_{q+} + f_{q-}\right) + \frac{m_v^2}{2} V_0^2 + \frac{\xi g_v^4}{8} V_0^4 \\
&\quad + \frac{m_s^2}{2}\sigma_0^2 + \frac{\kappa}{6}\sigma_0^3 + \frac{\lambda}{24}\sigma_0^4 + \frac{m_b^2}{2} b_0^2 + 3\Lambda_v g_v^2 g_b^2 V_0^2 b_0^2,
\end{aligned} \tag{2.37}$$

and the pressure is given by the average of the spatial components

$$\begin{aligned}
P_b &= \frac{1}{3}\langle T_{ii} \rangle = \frac{-i}{3} \sum_{q=p,n} \int \frac{d^3x}{V} \bar{\psi}_q \boldsymbol{\gamma} \cdot \nabla \psi_q + \langle \mathcal{L} \rangle \\
&= \frac{1}{3} \sum_{q=n,p} \gamma_q \int \frac{d^3k}{(2\pi)^3} \frac{k^2}{E^*} \left(f_{q+} + f_{q-}\right) + \frac{m_v^2}{2} V_0^2 + \frac{\xi g_v^4}{24} V_0^4 \\
&\quad + \frac{m_b^2}{2} b_0^2 - \frac{m_s^2}{2}\sigma_0^2 - \frac{\kappa}{6}\sigma_0^3 - \frac{\lambda}{24}\sigma_0^4 + \Lambda_v g_v^2 g_b^2 V_0^2 b_0^2.
\end{aligned} \tag{2.38}$$

The entropy is given by the classical expression

$$S_b = -\sum_{q=n,p} \gamma_q \sum_{k=+,-} \int \frac{d^3k}{(2\pi)^3} \left[f_{qk} \ln f_{qk} + (1 - f_{qk}) \ln\left(1 - f_{qk}\right) \right], \tag{2.39}$$

and we are now able to calculate the free energy density

$$\mathcal{F}_b = \mathcal{E}_b - TS_b, \tag{2.40}$$

which is the relevant quantity at a finite temperature.

Since protons are charged particles, leptons must also be taken into account to make the system charge neutral. On the leptonic sector, we include only electrons, which obey the free Dirac Lagrangian [140]

$$\mathcal{L}_e = \bar{\psi}_e \left(i\gamma^\mu \partial_\mu - m_e\right) \psi_e, \tag{2.41}$$

with $m_e = 0.511$ MeV [141]. We do not account for muons because they become significant only at densities above saturation, and the interactions of strongly degenerate electrons are negligible [3]. Following the same steps as in the baryonic case, we calculate the electron density

$$\rho_e = \gamma_e \int \frac{d^3k}{(2\pi)^3} \left[f_{e+}(\boldsymbol{k}) - f_{e-}(\boldsymbol{k})\right], \tag{2.42}$$

with the Fermi-Dirac distribution given by Eq. (2.33), but with the substitutions $E^* \to E_e = \sqrt{k^2 + m_e^2}$ and $\mu_q^* \to \mu_e$. The energy density, pressure, and entropy are given by

$$\mathcal{E}_e = \gamma_e \int \frac{d^3k}{(2\pi)^3} E_e \left(f_{e+} + f_{e-}\right), \tag{2.43}$$

$$P_e = \frac{\gamma_e}{3} \int \frac{d^3k}{(2\pi)^3} \frac{k^2}{E_e} \left(f_{e+} + f_{e-}\right), \tag{2.44}$$

and

$$S_e = -\gamma_e \sum_{k=+,-} \int \frac{d^3k}{(2\pi)^3} \left[f_{ek} \ln f_{ek} + (1 - f_{ek}) \ln(1 - f_{ek}).\right]. \tag{2.45}$$

The total energy and pressure are then given by the sum of baryon and lepton contributions. In catalyzed neutron stars, matter is in β-equilibrium and the baryon and electron chemical potentials are related by

$$\mu_q = \mu_B - e_q \mu_e, \tag{2.46}$$

where μ_B is the chemical potential related to baryon number. If we consider nucleons only this

B/A (MeV)	J (MeV)	L (MeV)	K (MeV)	M_N^*	$\rho_{\rm sat}$ (fm^{-3})
15.8 - 16.5	28.6 - 34.4	30.6 -86.8 *	220 - 260	0.6 - 0.8	0.15 - 0.16

Table 2: Current constraints on nuclear matter parameters, based on the values reported in [142, 143]. The value in parenthesis for the slope, marked by $*$ is due to the recent analysis of PREX-II data [144]. See text for details.

is simply $\mu_n = \mu_B$ and $\mu_p = \mu_n - \mu_e$. Throughout the rest of this section and in section 3 we do not work in β-equilibrium, rather we fix the proton fraction Y_p, to understand how our results are dependent on this quantity. In neutron stars, the typical proton fraction is ~ 0.1 and in newly born proto-neutron stars it can range between 0.05 and ~ 0.3 in the densities of interest. To give quantitative values to the quantities obtained in this section we must specify values for the couplings of the baryon Lagrangian, i.e. define a parametrization.

2.2 RMF parametrizations and constraints

Several parametrizations for the Lagrangian (2.2) exist throughout the literature, differing in the bulk and astrophysical properties they yield. Bulk properties are defined by expanding the energy per nucleon around the saturation density ($\rho_{\rm sat}$) and half proton fraction ($Y_p = \rho_p/\rho_B = 0.5$), i.e. symmetric matter. $\rho_{\rm sat}$ is the point where the energy density of symmetric matter is minimal, and thus the pressure is zero. It is also the average density of nuclei. The energy per nucleon expansion is

$$\frac{E}{A} = \frac{\mathcal{E}_b}{\rho_B} = E_0 + \frac{1}{2}K\left(\frac{\rho_B - \rho_0}{3\rho_0}\right)^2 + \left(1 - 2Y_p\right)^2 \mathcal{S}\left(\rho_B\right), \tag{2.47}$$

where $\mathcal{S}$ is the symmetry energy

$$\mathcal{S}\left(\rho_B\right) = \frac{1}{8}\frac{\partial^2\left(\mathcal{E}/\rho_B\right)}{\partial Y_p^2}\bigg|_{Y_p\approx 0.5} = J + L\left(\frac{\rho_B - \rho_0}{3\rho_0}\right). \tag{2.48}$$

The expansion defines the binding energy per nucleon, incompressibility, symmetry energy at saturation, and slope at saturation density as

$$\frac{B}{A} = E_0 - M_N, \quad K_0 = \left[9\rho^2\frac{\partial^2\mathcal{E}/\rho_B}{\partial\rho^2}\right]_{\rho_B=\rho_0} = 9\left.\frac{\partial P}{\partial\rho_B}\right|_{\rho_B=\rho_0}, \tag{2.49}$$

Par.	B/A (MeV)	J (MeV)	L (MeV)	K (MeV)	M_N^*/M_N	$M_{\max}/M_\odot$
IUFSU	-16.40	31.3	47.2	231.2	0.6	1.94
NL3$\omega\rho$	-16.30	31.7	55.2	272.0	0.6	2.75
FSU2	-16.30	31.6	112.8	238.0	0.6	2.07
L3$\omega\rho$	-16.30	31.2	74.3	254.3	0.7	2.30
NL3$\omega\rho^*$	-16.30	30.7	41.2	258.5	0.6	2.75

Table 3: Bulk properties of infinite nuclear matter of a few selected RMF parametrizations.

	IUFSU	NL3$\omega\rho$	FSU2	L3$\omega\rho$	NL3$\omega\rho^*$
m_s (MeV)	491.5	508.194	497.479	512.0	502.574
m_v (MeV)	782.5	782.5	782.500	783.0	782.600
m_b (MeV)	763.0	763.0	763.000	770.0	763.000
g_s	9.971	10.217	10.397	9.029	10.0944
g_v	13.032	12.868	13.557	10.584	12.8065
g_b	13.590	11.2766	8.970	8.550	14.4410
κ	3.5695	4.384	3.594	6.092	4.543
λ	2.926	-173.31	-6.228	-155.52	-180.892
ξ	0.03	0.00	0.0256	0.00	0.00
Λ	0.046	0.03	0.000823	0.0185	0.045
ρ_{sat} (fm^{-3})	0.155	0.148	0.1505	0.1555	0.150

Table 4: Selected RMF parametrizations.

$$J = \mathcal{S}(\rho_0) \quad L = \left[3\rho\frac{\partial \mathcal{S}}{\partial \rho}\right]_{\rho_B=\rho_0}. \tag{2.50}$$

The constraints to each of these parameters come from different experiments: saturation density and binding energy data come from simple nuclear masses and density distributions [142, 145]; results for the incompressibility of infinite nuclear matter come mainly from isoscalar giant monopole and isovector giant dipole resonances [146–149]; the symmetry energy and its density dependence can also be obtained from giant resonances, but additionally from experimental data of pigmy dipole resonances [150, 151], neutron skin radii [144, 152–154], heavy-ion collisions [152, 153], and isobaric analog states [155, 156]. For an extensive and comprehensible review of the current constraints to bulk properties, see [142]. We summarize the constraints present in [142] in Tab. 2. The values of the slope are marked with an asterisk due to the recent PREX-II result of the neutron thickness in ^{208}Pb, which yielded a slope inconsistent with previous measurements ($L = 106 \pm 37$) [144]. Further measurements are necessary to resolve this tension, though a lower slope value have been hinted at CREX [157, 158], and it has also been argued that, considering the PREX-II data with other constraints, such high slope values cannot be realized [159, 160] and must stay within the bound present in Tab. 2.

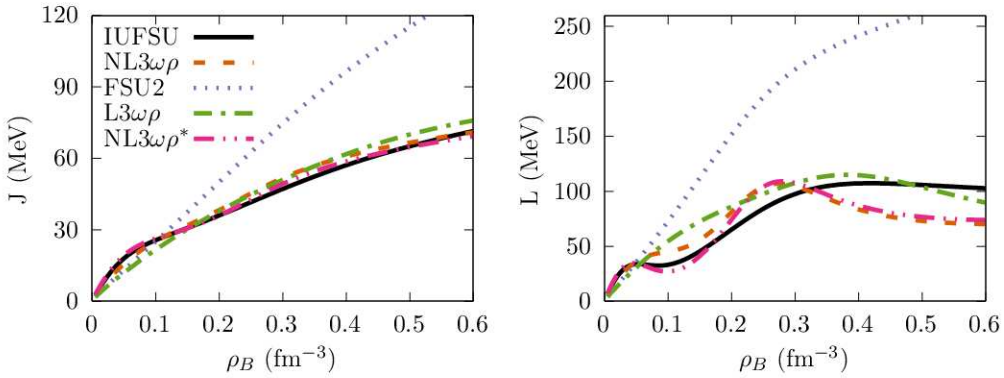

Figure 1: Symmetry energy (left) and symmetry energy slope (right) for the parametrizations shown in Tab. 3.

Astrophysical constraints are also important in the physics of dense nuclear matter. Some important measurements of the maximum mass of massive pulsars have also aided in constraining the EOS in the last decade, such a PSR J0348+0432 [161] and PSR J1614-2230 [162,163], with masses $(2.01 \pm 0.4)M_\odot$ and $(1.97 \pm 0.04)M_\odot$ at the 68% confidence level. More recently, the NICER mission (Neutron Star Interior Composition Explorer), launched in 2017, reported the determination of the pulsar PSR J0740+6620 mass to be $(2.08 \pm 0.07)\ M_\odot$, with a simultaneous radius measurement of $R = 12.35 \pm 0.75$ [164]. Other three simultaneous measurements of mass and radius have been provided by NICER [24–26]. Simultaneous mass and radius measurements are essential in constraining the high-density behavior of the EOS, around 2 and 3 times the saturation density [165]. Before NICER, the NS radii were constrained to be between $10-14$ km through accretion-powered millisecond pulsars, X-ray thermonuclear bursts, and X-ray emission of quiescent neutron stars, but these had very large systematic errors [166–169]. Furthermore, the symmetry energy (2.48) is closely related to the NS radius, proton fraction, and fraction of hyperons, and thus can be further constrained by future mass-radius measurements [170].

In Tab. 3 we show the bulk parameters of the IUFSU [112], NL3$\omega\rho$ [171–173], FSU2 [174], L3$\omega\rho$ [175] and NL3$\omega\rho^*$ [176,177] parameterizations, and in Tab. 4 we show the meson couplings and masses related to them. Due to the yet poor constraints on the density dependence of the symmetry energy, the curve of the slope is quite different for all these models, as shown on the right of Fig. 1. At densities above saturation, all bulk parameters are poorly constrained, and the macroscopic properties of a NS can be quite different when obtained with the different parametrizations. Indeed, the mass-radius diagram curves of these parametrizations, shown in fig. 2, exhibit very different maximum mass and radii predictions.

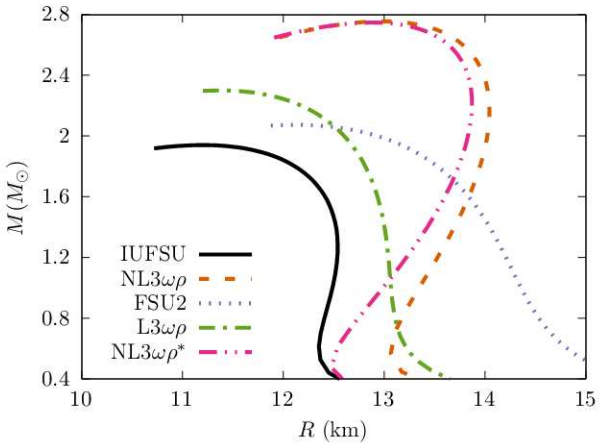

Figure 2: Mass-radius diagram for different parametrizations.

In this thesis, we choose to work with the IUFSU parametrization. It is a very appealing parametrization to study the pasta since simulations within the Thomas-Fermi approximation were performed with it [115], and a ready-to-use surface tension fit was made available to be used in the RMF. On the other hand, the parametrization is at the lower end of the error bar of the NICER measurements at 2σ confidence level. Additionally, hyperons and Δ baryons cannot be added to this model, since their addition softens the EOS and diminishes the NS maximum mass [178]. Therefore, in Section 5 we will use parametrizations L3$\omega\rho$ and NL3$\omega\rho^*$ to study the NS core. The first one was built to constrain NICER data and the second was built to describe the very high mass measured in the GW190814 event, though is not known to be a neutron star or a black hole [179]. Now, with a defined parametrization and an understanding of the model bulk properties, we now turn to the nuclear pasta.

2.3 Nuclear pasta: one-component plasma

In the outer crust of a NS there are nuclei arranged as a Coulomb crystal and degenerate electrons, and in the core, there is homogeneous matter, independent of the particle composition. But in the inner crust, beyond the neutron drip line, there is a coexistence of two phases of nuclear matter: ions and a very neutron-rich nuclear gas. Indeed at zero temperature, the gas is purely made of neutrons, and protons appear only due to thermal excitations. The presence of this mixed phase can be understood from the negative values of the baryonic pressure at sub-saturation densities, in the right of Fig. 3, which indicate the existence of an instability that culminates in a mixed phase with separately conserved charges [180, 181]. We will label the dense phase, consisting of bound nucleons, as I and the gas phase as II. Equilibrium is commonly established

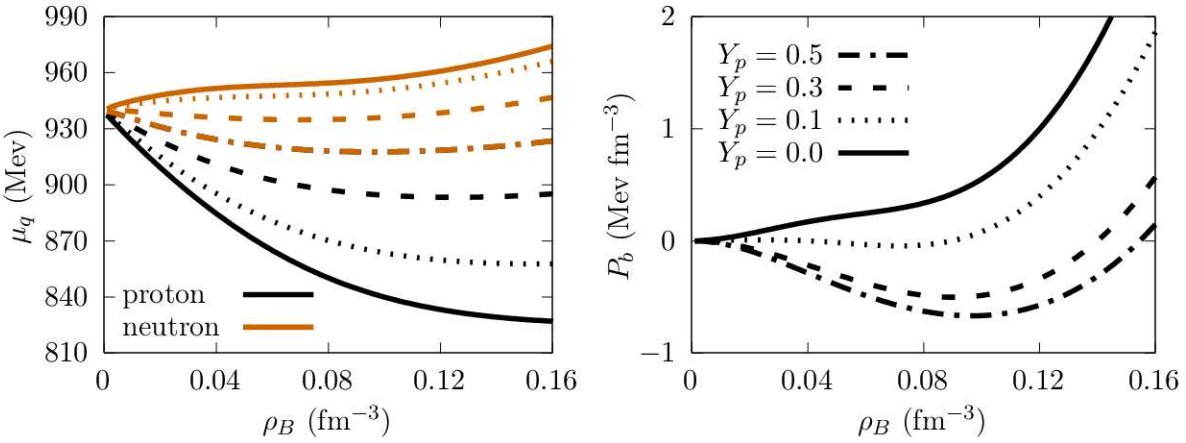

Figure 3: Chemical potential of protons (black) and neutrons (orange) and baryon pressure (right) for proton fractions $Y_p = 0.5, 0.3, 0.1$ and pure neutron matter using the IUFSU parametrization.

through the Gibbs conditions

$$\mu_p^I = \mu_p^{II}, \tag{2.51}$$

$$\mu_n^I = \mu_n^{II}, \tag{2.52}$$

$$P^I = P^{II}. \tag{2.53}$$

On the left of Fig. 3, we show the proton and neutron chemical potentials of homogeneous matter at zero temperature. All curves are drawn using the IUFSU parametrization.

Moreover, the spacing between nuclei becomes smaller when the densities get higher increasing Coulomb self (pp) and lattice (pe and ee) interactions, which become more similar. Competition between the total Coulomb and the nuclear surface energy leads to a deformation of the clustered nuclei: from spherical to cylindrical and then to rectangular shapes. These are collectively called pasta phase, and we denote these geometries by the integers $d = 3, 2, 1$ [21, 22, 56]. Inverse pasta structures further appear as densities increase such as tubes and bubbles, with the dense phase forming a continuum containing 'holes' filled with neutron gas. These holes become smaller as density continues growing, up to the point where matter becomes completely homogeneous. This overall picture does not hold in all models: some geometries might not appear and it might also happen that from rods or slabs the system changes directly to homogeneous matter.

The pasta occupies a volume f inside a Wigner-Seitz (WS) cell and the dripped nucleons occupy the excluded volume $(1 - f)$ in the WS cell. Each cell has volume V_{WS} and its geometry

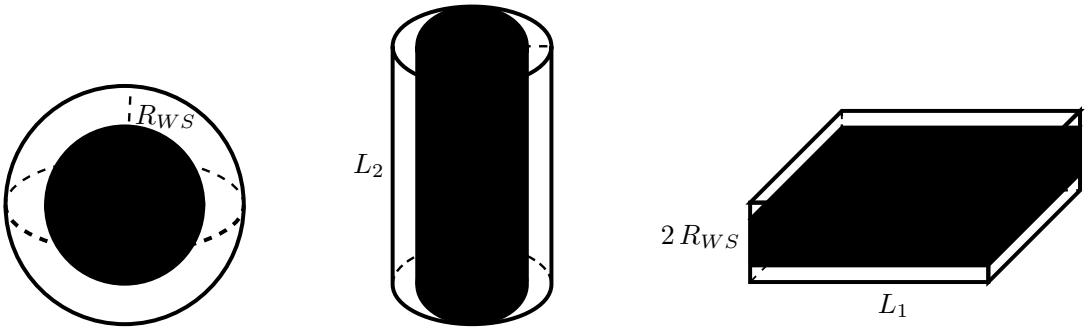

Figure 4: Illustration of Wigner-Seitz cells containing droplets, rods, and slabs.

corresponds to the one of the pasta inside, which occupies a volume V^I. The WS volume is given by

$$V_{\rm WS} = \begin{cases} \frac{4\pi}{3} R_{\rm WS}^2, & \text{d=3} \\ \pi R_{\rm WS}^2 L_2 & \text{d=2} \\ 2 R_{\rm WS} L_1^2 & \text{d=1} \end{cases} \tag{2.54}$$

whereas geometry has a characteristic radius R_d ($R_{\rm WS}$) corresponding to the pasta (WS cell) radius, and the cylindrical and planar shapes have an additional length L_d, which is the same for cluster and for the WS cell. In Fig. 4 we show what each of these lengths signifies. In order to compare the free energy density of the different geometries, the volumes of rods and slabs must be normalized to one of the droplets, i.e.

$$\frac{4\pi}{3} R_{3\,\rm WS}^2 = \pi R_{2\,\rm WS}^2 L_2 = 2 R_{1\,\rm WS} L_1^2. \tag{2.55}$$

While the tube is normalized to the bubble. For simplicity we define the volume fraction $f = V^I/V_{WS}$, with $0 < f \leq 1$, which can be written as

$$f = \left(\frac{R_d}{R_{\rm WS}} \right)^d . \tag{2.56}$$

The cell must obey the constraints of mass and charge conservation and charge neutrality:

$$\rho_n = f(\rho_n^I - \rho_n^{II}) + \rho_n^{II}, \tag{2.57}$$

$$\rho_p = f(\rho_p^I - \rho_p^{II}) + \rho_p^{II}. \tag{2.58}$$

$$\rho_p = \rho_e. \tag{2.59}$$

The total baryon density of a cell is $\rho_B = \rho_p + \rho_n$ and its proton fraction is $Y_p = \rho_p/\rho_B$. The free energy density of the WS cell receives bulk contributions from the pasta and the gas, from the electron that makes the cell charge neutral, from the Coulomb energy due to pp, pe, and ee interactions, and from surface terms, i.e.

$$\mathcal{F}_{\rm WS} = f\mathcal{F}_b^I + (1-f)\mathcal{F}_b^{II} + \beta\mathcal{F}_{sc,d} + \mathcal{F}_e, \tag{2.60}$$

where the bulk free energy density of the cluster and gas is given by Eq. (2.40), and $\mathcal{F}_{sc,d}$ is the sum of surface and Coulomb energies [21,88,92]. The surface energy of the cell is given by the surface tension times the surface area

$$F_s = \sigma(Y_p,T)A = \begin{cases} 4\sigma\pi R_3^2, & \text{for spheres (d=3)} \\ 2\sigma\pi R_2 L_2, & \text{for rods (d=2)} \\ \sigma L_1^2, & \text{for slabs (d=1)} \end{cases} \tag{2.61}$$

so eq. (2.54) allows us to write the surface energy density as

$$\beta\mathcal{F}_{s,d} = \frac{F_s}{V_{WS}} = \frac{\beta d\ \sigma(Y_p,T)}{R_d}, \tag{2.62}$$

where $\beta = f$ for droplets, rods and slabs and $\beta = 1-f$ for tubes and bubbles. The surface tension σ is a function of isospin asymmetry $\delta = 1-2Y_p$ and temperature T, and the appearance of the pasta is largely sensitive to its value [61,70,92,182,183]. Next, we use the surface tension fit provided in Ref. [115] which reproduces the value obtained in a Thomas-Fermi calculation, where meson fields are not homogeneous and, in the thin-wall approximation [93]

$$\sigma = \int dz \left[(\partial_r\sigma_0)^2 - (\partial_r V_0)^2 - (\partial_r b_0)^2\right]. \tag{2.63}$$

The fit was made to the functional

$$\sigma(x,T) = \tilde{\sigma}(x)\left[1 - a(T)xT - b(T)T^2 - c(T)x^2T\right], \tag{2.64}$$

where $x = \delta^2$ stands for the squared relative neutron excess. $\tilde{\sigma}(x)$ is the surface tension at $T = 0$

IUFSU	$\tilde{\sigma}(x)$	$a(T)$	$b(T)$	$c(T)$
σ_0	1.16473	-	-	-
σ_1	-0.659167	-	-	-
a_0	-	0.00404325	0.00767923	0.0066774
a_1	-2.25482	0.00828207	-8.58068×10^{-5}	-0.0514285
a_2	-5.64237	-0.00153301	4.43918×10^{-7}	0.00949505
a_3	37.8471	7.26763×10^{-5}	-5.44453×10^{-7}	- 0.000427613
a_4	-81.6617	-	-	-
a_5	81.2696	-	-	-
a_6	-31.0227	-	-	-

Table 5: Surface tension coefficient parameters fitted within the Thomas-Fermi approximation. The coefficients are for T in MeV and σ_0 is in MeV/fm^{-2}.

and a, b and c are functions of the temperature:

$$\begin{aligned}
\tilde{\sigma}(x) &= \sigma_0 \exp\left(-\sigma_1 x^{3/2}\right)(1 + a_1 x + a_2 x^2 \\
&\quad + a_3 x^3 + a_4 x^4 + a_5 x^5 + a_6 x^6) \\
a(T) &= a_0 + a_1 T + a_2 T^2 + a_3 T^3 + a_4 T^4 + a_5 T^5 \\
b(T) &= a_0 + a_1 T + a_2 T^2 + a_3 T^3 + a_4 T^4 + a_5 T^5 \\
c(T) &= a_0 + a_1 T + a_2 T^2 + a_3 T^3 + a_4 T^4 + a_5 T^5,
\end{aligned} \tag{2.65}$$

where σ_0 is the surface coefficient at $T = 0$ for symmetric matter. In Table 5 the parameters of the surface tension fit for the IUFSU parametrization are given. In Ref. [115] one can also find the surface tension for the NL3, NL3$\omega\rho$, and FSUGold parametrizations. In Fig 5 we show the surface tension as a function of proton fraction for two different parametrizations at $T = 0$ (left) and temperatures (right) with the IUFSU parametrization. As $Y_p \to 0$ the surface tension goes to zero since ion and gas matter become more alike. The rise in temperature reduces the surface tension due to the extra kinetic energy of particles, which reduces particle interactions.

The Coulomb energy can be exactly calculated for the idealized pasta geometries by integrating the expression

$$dE_c = \frac{1}{2}\phi dQ \tag{2.66}$$

in the WS cell. In Appendix A the main steps of the calculation are presented. The result can

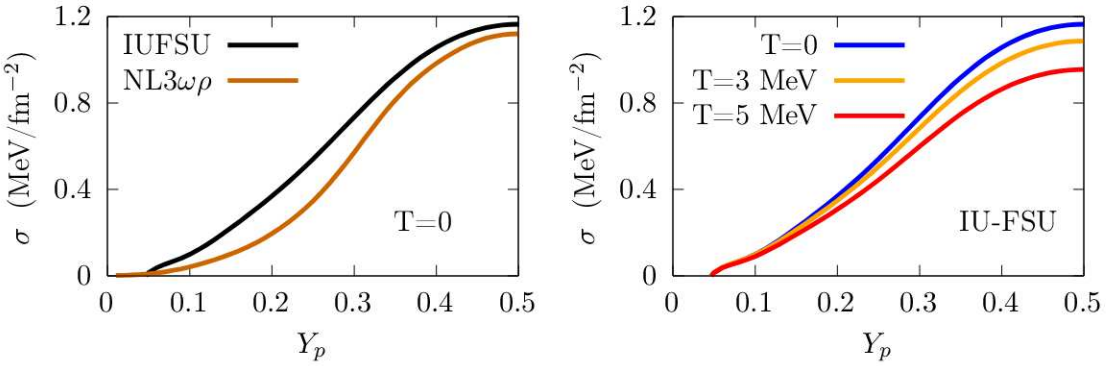

Figure 5: Surface tension for different parametrizations at T=0 (Left) and for different temperatures in the IUFSU parametrization (Right).

be compactly written as:

$$\beta\mathcal{F}_{c,d} = \frac{E_c}{V_W} = 2\pi\beta e^2 R_d^2 \left(\rho_p^I - \rho_p^{II}\right)^2 \Phi_d(\beta), \tag{2.67}$$

whereas the geometry dependence is encoded in the function Φ_d, given by

$$\Phi_d(\beta) = \begin{cases} \left(\dfrac{2 - d\beta^{1-2/d}}{d-2} + \beta\right)\dfrac{1}{d+2}, & \text{if d = 1, 3;} \\ \dfrac{-1 - \ln(\beta) + \beta}{d+2}, & \text{if d = 2;} \end{cases} \tag{2.68}$$

The first term on the Φ_d function comes from the nuclei self-energy, while the second and third are from pe and ee interactions [21, 184]. The sum of surface and Coulomb energies (S+C) is

$$\mathcal{F}_{sc,d} = \mathcal{F}_{s,d} + \mathcal{F}_{c,d} = \frac{\sigma\, d}{R_d} + \pi e^2 R_d^2 \left(\rho_p^I - \rho_p^{II}\right)^2 \Phi_d(\beta), \tag{2.69}$$

and its minimization yields the equilibrium radius R_d of the pasta

$$R_d = \left(\frac{\sigma d}{4\pi e^2 (\rho_p^I - \rho_p^{II})^2 \Phi_d(\beta)}\right)^{1/3} \tag{2.70}$$

and the virial relation $\mathcal{F}_{s,d} = 2\mathcal{F}_{c,d}$.

Notice though that the Gibbs conditions can be obtained by minimizing the free energy density (2.60) if the S+C energy is neglected. Indeed the overall strategy followed in the RMF literature is this: to minimize the free energy density and later introduce the S+C energy [92, 93, 115, 181, 182]. This approach is usually called coexistence phases approximation (CPA).

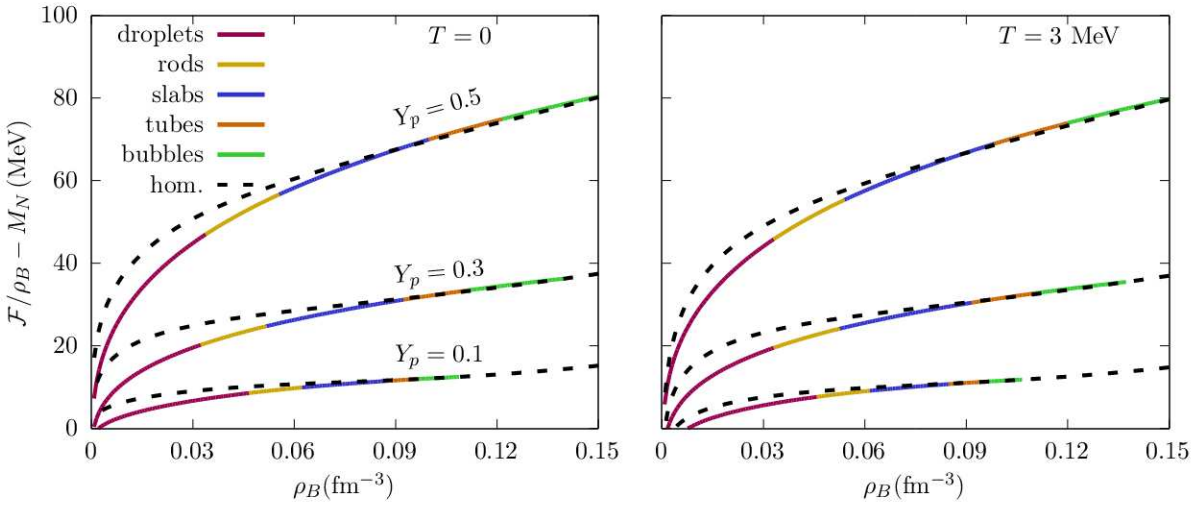

Figure 6: Free energy density per baryon for T=0 (3) MeV at the left (right) for $Y_p = 0.5, 0.3$ and 0.1 for homogeneous matter and for the pasta phase, obtained with the CPA.

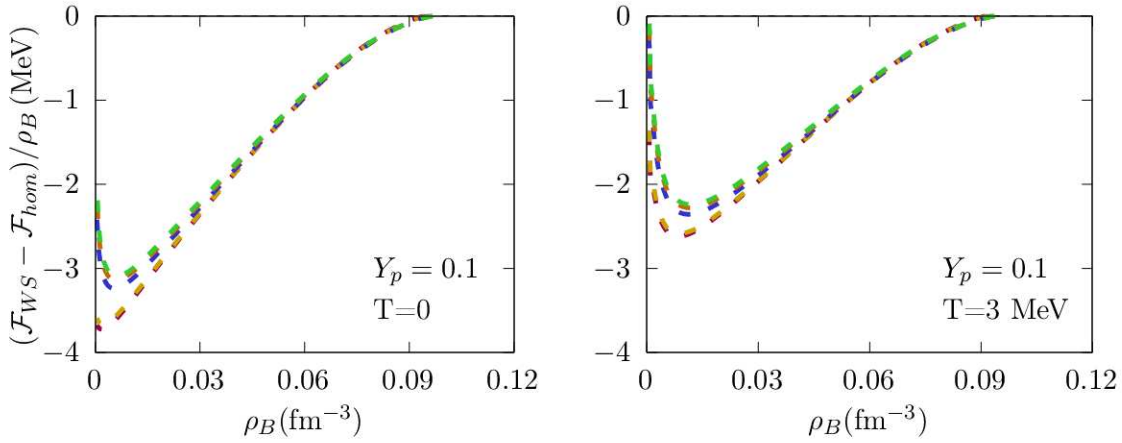

Figure 7: Difference between pasta and homogeneous free energy density per baryon for T=0 (3) MeV on the left (right) for $Y_p = 0.1$. The different colors represent the pasta geometries, as in Fig. 6.

In Fig. 6 we show the free energy density of the pasta obtained with the CPA along with the free energy density of homogeneous matter for different proton fractions and temperatures. The pasta appears when it becomes energetically favorable, that is $\mathcal{F}_{\text{pasta}} < \mathcal{F}_{\text{homog}}$. The difference between T=0 and T=3 MeV is very small in the geometry transitions and in free energy value. Indeed, at such temperatures, the thermal effect in the bulk energy is very small, and its main contribution comes from the S+C term.

This method of minimizing the free energy density in a WS cell and finding the equilibrium leads to a unique configuration at a thermodynamic condition, so this is known as one component plasma approximation (OCP). The OCP is used in various tabled EOS, e.g. the Lattimer and Swesty, based on the compressible liquid drop model, the Shen EOS, based on

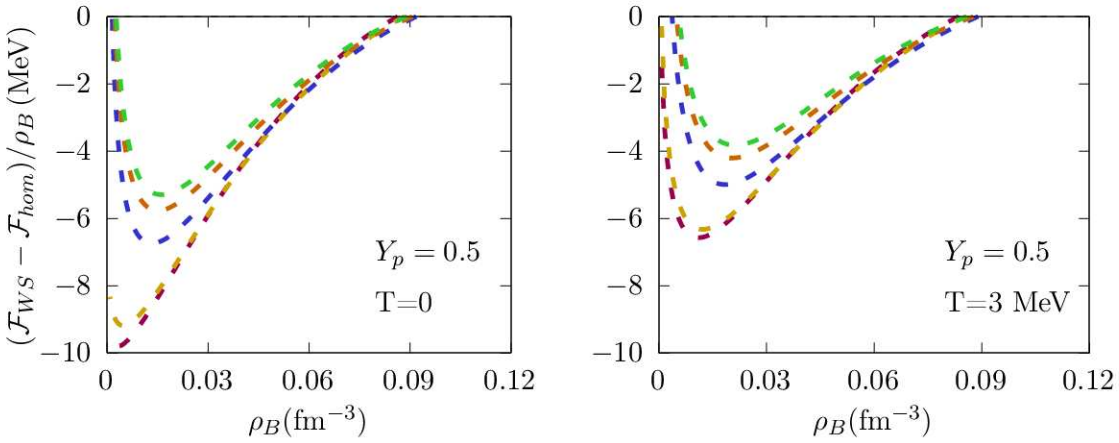

Figure 8: Same as Fig. 7 for $Y_p = 0.5$.

the RMF [89, 95, 184] and also in several other mean-field studies of the pasta [92, 93, 96, 97]. This is a common approach to astrophysical applications, but the presence of different ions in a macroscopic system can modify transport properties, for example. In the outer and inner crust of a NS, a distribution of ions with different proton numbers was obtained in [98–101].

In the case of the pasta, the small energy difference between the geometries implies that they can also coexist at a given depth of the star. We confirm this in Figs. 7 and 8, where we show the difference in energy between the pasta geometries and homogeneous matter for T=0 (left) and T=3 MeV (right). For a proton fraction of 0.1 the energy between geometries is of only a few keV even at low densities. The energy difference is reduced even more by a rise in temperature. Thus, the pasta is formed in a warm NS, with a very amorphous crust, and as the star continues to cool down, the crust is not expected to reach the full ground state, but rather to freeze out with different metastable states coexisting, due to this very small energy barrier separating the pasta geometries. More sophisticated simulations [85] indeed corroborate the idea of coexisting pasta structures. This is the topic of the next section, but before, we must use a more consistent way of finding the ground state of the pasta: minimizing the free energy density accounting for the S+C term.

This can be done in a variational fashion, by minimizing eq. (2.60) with the constraints of mass and charge, eqs. (2.57) and (2.58), with respect to the linear radius, volume fraction and cluster and gas number densities: $\{\rho_p^I, \rho_n^I, \rho_p^{II}, \rho_n^{II}, f, R_d\}$. [185, 186]. To do so we define the thermodynamic potential

$$\Omega = \mathcal{F}_{WS} - \mu_n \rho_n - \mu_p \rho_p, \tag{2.71}$$

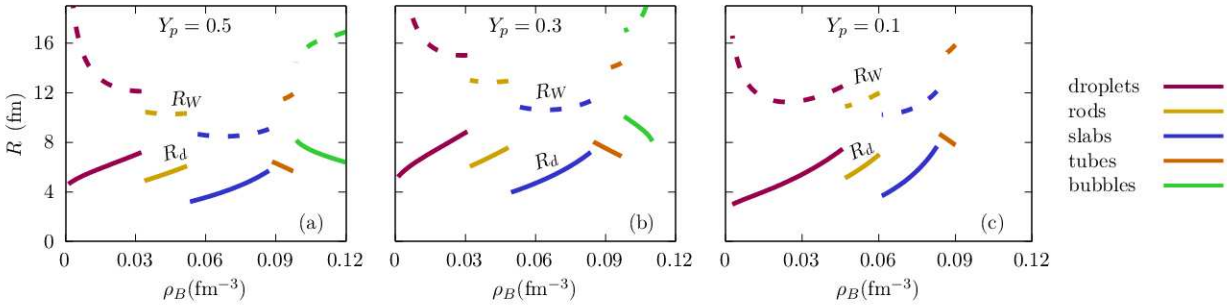

Figure 9: Linear radius for nuclear matter at zero temperature with proton fractions $Y_p = 0.5, 0.3$ and 0.1.

Here, μ_q are the thermodynamic chemical potentials that act as Lagrange multipliers and are to be determined by the minimization. We should expect that the S+C term enters as an extra contribution to the thermodynamic chemical potentials. This method is necessary to calculate the coexistence of pasta geometries in Section 3 and we refer to it as the compressible-liquid drop (CLD) approach. This is in contrast to Ref. [107], where the authors applied the CPA to calculate the pasta distribution to study the symmetric nuclear matter.

We begin by noticing that the only dependence on the linear radius is on the S+C energy, therefore

$$\frac{\partial \Omega}{\partial R_d} = 0 \Rightarrow \frac{\partial \mathcal{F}_{sc,d}}{\partial R_d} = 0, \tag{2.72}$$

leading to the linear radius equilibrium equation (2.70). The linear radius for the pasta configuration that minimizes the energy is plotted in Fig 9 for $Y_p = 0.3$ and 0.5 at T=3 MeV. With these we can also obtain the pasta WS length L_d from the volume conservation (2.55). These are shown in Fig. 10, and the pattern we see is that from rods to slabs and then from slabs to tubes, the length L jumps to a lower value, as expected from the radii shown in Fig. 9.

Taking the derivative of the thermodynamic potential w.r.t. the particle densities leads

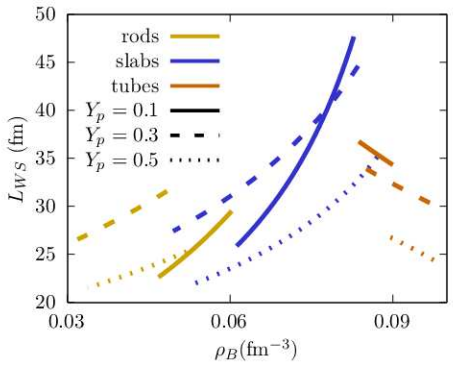

Figure 10: Lenght L_d for nuclear pasta at zero temperature with proton fractions $Y_p = 0.5, 0.3$ and 0.1.

to

$$\frac{\partial\Omega}{\partial\rho_q^I} = f\mu_q^I + \beta\frac{\partial\mathcal{F}_{sc,d}}{\partial\rho_q^I} - f\,\mu_q = 0, \tag{2.73}$$

$$\frac{\partial\Omega}{\partial\rho_q^{II}} = (1-f)\mu_p^{II} + \beta\frac{\partial\mathcal{F}_{sc,d}}{\partial\rho_q^{II}} - (1-f)\,\mu_q = 0 \tag{2.74}$$

combining these, we can write thermodynamic chemical potentials μ_q as

$$\begin{aligned}\mu_q &= \mu_q^I + \frac{\beta}{f}\frac{\partial\mathcal{F}_{sc,d}}{\partial\rho_q^I} \\ &= \mu_q^{II} + \frac{\beta}{1-f}\frac{\partial\mathcal{F}_{sc,d}}{\partial\rho_q^{II}},\end{aligned} \tag{2.75}$$

where we defined the bare chemical potentials

$$\mu_q^I = \frac{\partial\mathcal{F}_b^I}{\partial\rho_q^I} \qquad\qquad \mu_q^{II} = \frac{\partial\mathcal{F}_b^{II}}{\partial\rho_q^{II}}. \tag{2.76}$$

This is equivalent to the Gibbs conditions (2.81) and (2.82) but with corrected chemical potentials, now given by the right-hand side of the upper (lower) part of eq. (2.75) for phase I (II). Using the explicit expression for the S+C energy we can write the derivatives as

$$\frac{\partial\mathcal{F}_{sc,d}}{\partial\rho_p^I} = \frac{df(1-Y_p)}{\rho_B R_d}\frac{\partial\sigma}{\partial Y_p} + \frac{2\mathcal{F}_{c,d}}{(\rho_p^I - \rho_p^{II})} \tag{2.77}$$

$$\frac{\partial\mathcal{F}_{sc,d}}{\partial\rho_p^{II}} = \frac{d(1-f)\,(1-Y_p)}{\rho_B R_d}\frac{\partial\sigma}{\partial Y_p} - \frac{2\mathcal{F}_{c,d}}{(\rho_p^I - \rho_p^{II})}, \tag{2.78}$$

$$\frac{\partial\mathcal{F}_{sc,d}}{\partial\rho_n^I} = -\frac{dfY_p}{\rho_B R_d}\frac{\partial\sigma}{\partial Y_p} \tag{2.79}$$

$$\frac{\partial\mathcal{F}_{sc,d}}{\partial\rho_n^{II}} = -\frac{d(1-f)Y_p}{\rho_B R_d}\frac{\partial\sigma}{\partial Y_p}, \tag{2.80}$$

and arrive at the following equations for the bare chemical potentials

$$\mu_p^I = \mu_p^{II} - \frac{2\beta\mathcal{F}_{c,d}}{f(1-f)(\rho_p^I - \rho_p^{II})}, \tag{2.81}$$

$$\mu_n^I = \mu_n^{II}. \tag{2.82}$$

The proton chemical equilibrium condition is modified by the Coulomb force while the neutron one is unaltered, as expected since only the proton is charged. In Figs. 11 and 12 we show the thermodynamic, cluster, and gas chemical potentials obtained within the CLD, the thinner curve

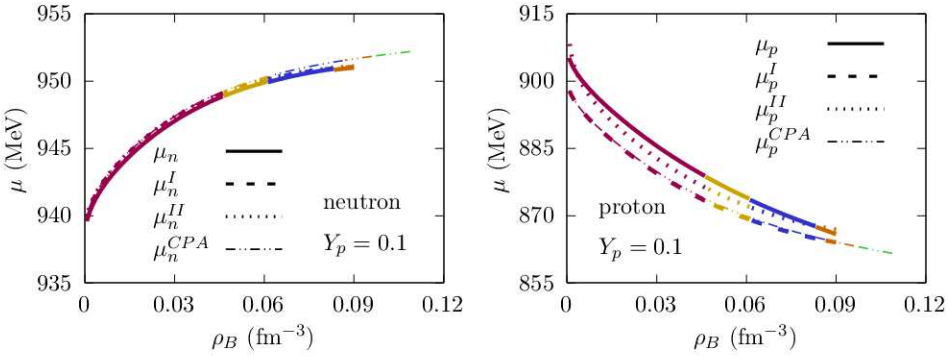

Figure 11: Thermodynamic, cluster and gas chemical potential of neutrons (left) and protons (right) at $Y_p = 0.1$ and T=0.

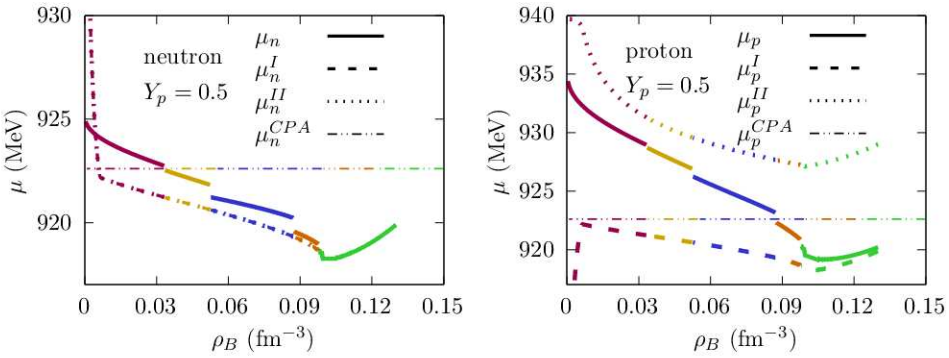

Figure 12: Same as Fig. 11 for $Y_p = 0.5$.

shows the CPA result. The cluster and gas bare chemical potentials differ more at higher proton fractions, both from each other and from the CPA result, due to the increasing Coulomb energy with proton number. For a proton fraction of 0.1 there is not a big difference, even from the CPA result.

The equation for pressure equilibrium is obtained by minimizing eq. (2.71) w.r.t. the volume fraction f:

$$\frac{\partial \Omega}{\partial f} = \mathcal{F}_b^I - \mathcal{F}_b^{II} - \mu_p(\rho_p^I - \rho_p^{II}) - \mu_n(\rho_n^I - \rho_n^{II}) + \frac{\partial \beta}{\partial f}\mathcal{F}_{sc} + \beta\frac{\partial \mathcal{F}_{sc}}{\partial f} = 0. \tag{2.83}$$

By substituting the thermodynamic potentials, eqs. (2.75), and using the thermodynamic relation $P_b^K = -\mathcal{F}_b^K + \mu_p^K \rho_p^K + \mu_n^K \rho_n^K$, K=I,II, the expression above can be written as

$$-P_b^I + P_b^{II} + \frac{d\beta}{df}\left(\mathcal{F}_{sc,d} + \beta\mathcal{F}_{c,d}\,\frac{1}{\Phi_d}\frac{d\Phi_d}{d\beta}\right) - \frac{2\beta\mathcal{F}_c\left(\rho_p^I - f(\rho_p^I - \rho_p^{II})\right)}{f(1-f)\left(\rho_p^I - \rho_p^{II}\right)} = 0. \tag{2.84}$$

All the equilibrium equations are in agreement with those presented in Refs. [185, 186].

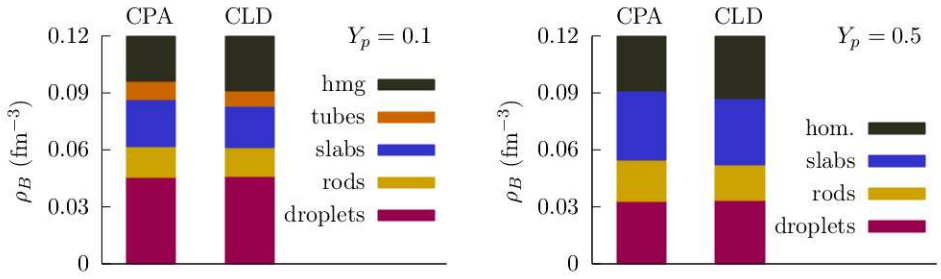

Figure 13: Histograms comparing the densities where each pasta geometry appears in the CPA and CLD approaches.

In Fig. 13 we see there is almost no difference in the densities where each geometry appears between the CLD and CPA approaches. The CPA approach is enough to determine the thermodynamic properties of the crust, but the CLD is necessary for the multi-component approach presented in the next section.

The numerical recipe to find equilibrium is to guess the effective chemical potentials μ_q^* and nucleon masses M_N^* in each phase (I and II), and then use an iterative method to search for the true solution while simultaneously solving the meson fields – eqs.(2.25), (2.26), (2.27) – and obeying the mass and charge constraints – eqs. (2.57) and (2.58). For this a reasonable first guess is essential, and the properties of homogeneous matter can be a guide in the process. For this numerical purpose, we use the Ceres Solver [187] to solve the system of non-linear equations and the GSL library to perform integrations and interpolations [188]. The code written to obtain all results in this thesis is publicly available [189].

Computationally, the cost of finding the equilibrium conditions is higher with the CLD rather than with the CPA: the latter is independent of the geometries, so it is only necessary to find one solution for each thermodynamic condition, while the CLD requires solving Eqs. (2.81) – (2.84) for each geometry, each yielding different chemical potentials. Furthermore, the $1/(1-f)$ terms imply that divergences might be reached when searching for the solution. Now we turn to the multi-component approach.

3 Fluctuations in the pasta phase

In this section, we introduce the formalism of the multi-component plasma for the pasta phase. We use the RMF model discussed in the last section to calculate the abundance of pasta geometries at a certain thermodynamic condition and calculate the pasta impurity parameter for the first time with an RMF model. Fluctuations are made on the geometry and on the proton and neutron densities of the pasta. To account for the geometric anisotropy of the pasta in the impurity parameter, we define an effective proton number that depends on the pasta surface area in a given direction.

3.1 Multi-component plasma

In the previous section, we discussed the OCP approach, which is reasonable to determine thermodynamic quantities such as energy, entropy and pressure [90]. Nevertheless, transport properties and reaction rates can be modified by system impurities. To calculate the pasta abundances and estimate its impurity using an RMF model we turn to the multi-component plasma (MCP) formalism developed in Ref. [98], which has been applied to supernovae [106] and to the NS crust [99, 101, 107], and extend it to the pasta phase.

Consider a system of macroscopic volume V composed of WS cells, each occupying a volume V_{WS}^{N}. Inside the cell, there is a pasta structure, a nucleon gas, composed mainly of neutrons, and an electron gas. The gases are assumed to have constant density throughout the entire system, to avoid interface discontinuities in the chemical potentials of different cells. The constancy of the electron density is further justified by its high incompressibility [182]. The grand partition function is defined as

$$Z = \sum_{\{n\}} \exp\left[-\beta \sum_{N,d} \mathcal{N}^{N,d} \tilde{\Omega}_{WS}^{N,d}\right]. \tag{3.1}$$

The sum over $\{n\}$ indicates the different system configurations, $\mathcal{N}^{N,d}$ is the total number of cells with clusters in a configuration (N, d), $\tilde{\Omega}_{WS}^{N,d}$ is the cell thermodynamic potential, and $\beta = 1/T$ is the inverse temperature. The superscript N is used to denote quantities that vary between different WS cells due to proton and neutron density fluctuations, and it substitutes the I that was utilized in Section 2. The sum over $d = 3, 2, 1$ accounts for droplets, rods, and slabs. We do not

consider the tubes and bubbles, since cluster and gas are exchanged and this would introduce the extra complication of discontinuities between cells. The nucleon gas is now denoted by the subscript g instead of the superscript II, thus changing our notation to:

$$\begin{aligned} &\rho_q^I \to \rho_q^N \quad ,\mathcal{F}_b^I \to \mathcal{F}_b^N, \quad f \to f^N, \quad R_d \to R_d^N \\ &\rho_q^{II} \to \rho_{qg} \quad \mathcal{F}_b^{II} \to \mathcal{F}_{b,g} \quad \mu_q^{II} \to \mu_{qg}, \quad \mu_q^I \to \mu_q^N. \end{aligned}$$

The one-cell thermodynamic potential, introduced in eq. (3.1), is given by [98]

$$\tilde{\Omega}_{WS}^{N,d} = V_{WS}^N \mathcal{F}_{WS}^{N,d} + \delta F^N - \mu_n \rho_{n,WS}^N - \mu_p \rho_{p,WS}^N - \mu_e \rho_e, \tag{3.2}$$

with the free energy density of the cell $\mathcal{F}_{WS}^{N,d}$ defined as in the SNA case – Eq. (2.60),

$$\mathcal{F}_{WS}^{N,d} = f^N \mathcal{F}_b^N + (1 - f^N)\mathcal{F}_{b,g} + f^N \mathcal{F}_{sc,d}^N + \mathcal{F}_e, \tag{3.3}$$

and a total proton and neutron densities of

$$\rho_{p,WS}^N = f^N(\rho_p^N - \rho_{pg}) + \rho_{pg}, \tag{3.4}$$

$$\rho_{n,WS}^N = f^N(\rho_n^N - \rho_{ng}) + \rho_{ng}, . \tag{3.5}$$

in each cell. We allow the densities ρ_p^N, ρ_n^N to fluctuate between different WS cells but in principle, both linear radius and volume fraction could also fluctuate independently of the densities. However, we choose to constrain them. The reason is that if both densities and volume fraction were to fluctuate, local net charge fluctuations would exist, leading to long-range Coulomb terms that would violate the hypothesis of linear mixing between the different cells, i.e. the additivity of free energies [98, 190]. We impose charge neutrality by assuming that the global proton density ρ_p is equal to the fixed electron density ρ_e. In practice we must impose this locally: $\rho_{p,WS}^N = \rho_p = \rho_e$ by fixing f^N from Eq. (3.4), such that

$$f^N = \frac{\rho_p - \rho_{pg}}{\rho_p^N - \rho_{pg}}. \tag{3.6}$$

The price to be paid is the introduction of the rearrangement term δF^N in the free energy. We discuss how to calculate it in Sec.3.2. Finally, μ_q are the thermodynamic chemical potentials derived in Eq. (2.75) which we take as input from the CLD solution.

Regarding the linear radius, we assume it to be determined from the equilibrium of the S+C energy in each cell

$$R_d^N = \left(\frac{\sigma d}{4\pi e^2 (\rho_p^N - \rho_{pg})^2 \Phi_d(f^N)} \right)^{1/3}, \tag{3.7}$$

as in Eq. (2.70), but it will vary in each cell due to fluctuating densities. The volume of slabs, rods and droplets are

$$V_1^N = 2R_1^N \left(L_1^N\right)^2, \quad V_2^N = \pi \left(R_2^N\right)^2 L_2^N, \quad V_3^N = 4\pi \left(R_3^N\right)^3 /3, \tag{3.8}$$

respectively. The length parameters L_d^N are determined as in eq. (2.55)

$$V^N \equiv V_1^N = V_2^N = V_3^N, \tag{3.9}$$

and values were shown in Fig. 10. The proton and baryon numbers in the pasta are independent of the pasta geometry and are given by

$$Z^N = V^N \left(\rho_p^N - \rho_{pg}\right), \qquad A^N = V^N \left(\rho^N - \rho_g\right). \tag{3.10}$$

Now that the main variables of the WS cell are defined we turn to the grand partition function, eq. (3.1), which we rewrite in terms of the number density $n^{N,d} = \mathcal{N}^{N,d}/V$, in the spirit of RMF, which deals with quantities per volume:

$$Z = \sum_{\{n\}} \exp\left[-\beta V \sum_N n^{N,d} \tilde{\Omega}_{WS}^{N,d} \right]. \tag{3.11}$$

The number densities are normalized as

$$\sum_{N,d} n^{N,d} V_{WS}^N = 1. \tag{3.12}$$

By substituting the densities given by eqs.(2.57) and (2.58) in the thermodynamic potential, eq. (3.2), we are able to factorize the partition function into cluster, nucleon gas and electron components

$$Z = Z_{\rm cl} z_g^V z_e^V, \tag{3.13}$$

with

$$z_e = \exp\left[-\beta\left(\mathcal{F}_e - \mu_e\rho_e\right)\right], \tag{3.14}$$

$$z_g = \exp\left[-\beta\left(\mathcal{F}_{b,g} - \mu_n\rho_{ng} - \mu_p\rho_{pg}\right)\right], \tag{3.15}$$

$$Z_{\rm cl} = \sum_{\{n\}} \exp\left[-\beta V \sum_{N,d} n^{N,d}\tilde{\Omega}^{N,d}\right]. \tag{3.16}$$

The cluster partition function is simply that of an ideal classical gas, and a factorial factor must be introduced to enforce indistinguishability of clusters [98,106,191]. Since the number of occurrences for the different configurations $\mathcal{N}^{N,d}$ can be any positive integer, we can analytically calculate the sum as:

$$Z_{cl} = \prod_{N,d}\sum_{\mathcal{N}=0}^{\infty}\frac{\left(\exp\left[-\beta\tilde{\Omega}^{N,d}\right]\right)^{\mathcal{N}}}{\mathcal{N}!} = \prod_{N,d}\exp\omega^{N,d}, \tag{3.17}$$

where we define

$$\omega^{N,d} = \exp\left(-\beta\tilde{\Omega}^{N,d}\right) \tag{3.18}$$

and the cluster thermodynamic potential

$$\tilde{\Omega}^{N,d} = V^N\left[\mathcal{F}_b^N - \mathcal{F}_{b,g} + \mathcal{F}_{sc,d}^N - \mu_n\left(\rho_n^N - \rho_{ng}\right) - \mu_p\left(\rho_p^N - \rho_{pg}\right)\right] + \delta F^N. \tag{3.19}$$

The chemical potential of the cluster is

$$\mu^N = V^N\left[\mu_n(\rho_n^N - \rho_{ng}) + \mu_p(\rho_p^N - \rho_{pg})\right], \tag{3.20}$$

and the free energy is

$$F_{cl}^{N,d} = V^N\left[\mathcal{F}^N - \mathcal{F}_{b,g} + \mathcal{F}_{sc,d}^N\right]. \tag{3.21}$$

Finally, the equilibrium number density for a fluctuation $\left(\rho_p^N,\rho_n^N\right)$ is readily found from the cluster partition function to be

$$n^N = \frac{1}{V}\frac{\partial\ln Z_{cl}}{\partial\beta\mu^N} = \sum_{d=1}^{3} n^{N,d} = \sum_{d=1}^{3}\frac{\omega^{N,d}}{V}, \tag{3.22}$$

while the probability of cell with pasta density $\left(\rho_p^N, \rho_n^N\right)$ and geometry d is

$$p^{N,d} = \frac{n^{N,d}}{\sum_{N,d} n^{N,d}} = \frac{\exp\left(-\beta\tilde{\Omega}^{N,d}\right)}{\sum_{N,d} \exp\left(-\beta\tilde{\Omega}^{N,d}\right)}. \tag{3.23}$$

an the probability that a pasta structure of dimension d is dominant in a cell is obtained by summing eq. (3.23) over N:

$$P^d = \sum_N p^{N,d} \tag{3.24}$$

The results are shown for proton fractions Y_p =0.1 and 0.3 and temperatures T=1, 3 and 5 MeV in Fig. 14, where we see that there is a larger mixing of pasta geometries at higher temperatures and for more asymmetric matter, that is, these are more impure. Particularly for T=5 MeV and $Y_p = 0.1$, the fraction of droplets at the onset density is already about 40%. The high predominance of slabs when the density goes beyond 0.06 fm^{-3} may be due to our negligence of tubes and bubbles that may already exist at such densities. In some cells, it is possible that the pasta even dissolves and the cell contains purely homogeneous matter, even though we do not take this into account in the calculation.

3.2 Ensemble equivalence: the rearrangement term

For standard Poissonian fluctuations as the ones we are modeling, we expect that the most probable configuration (optimal) coincides with the average one. Moreover, ensemble equivalence at the thermodynamic limit implies that this optimal MCP configuration should

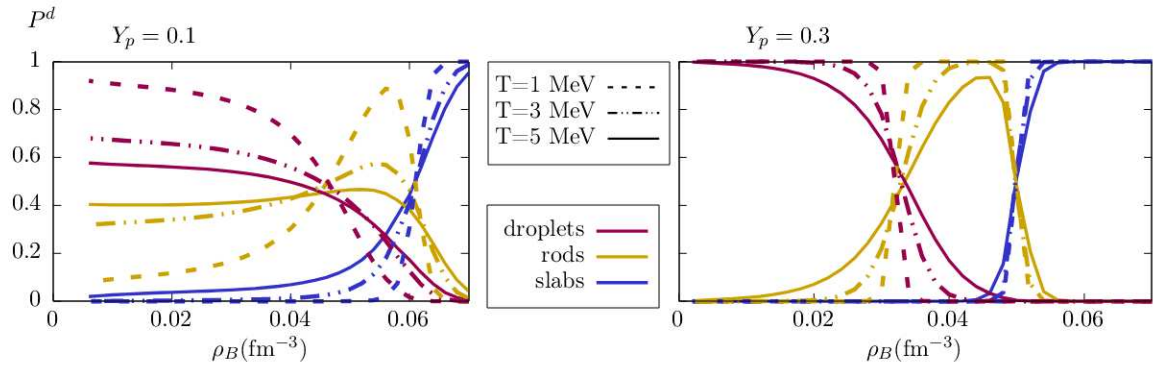

Figure 14: Abundances of pasta structures at proton fractions Y_p = 0.1 (left) and 0.3 (right) and temperatures T=5, 3, 1 MeV plotted with solid, dash-double-dotted and dashed lines, respectively. Geometries are plotted with different colors: droplets are in magenta, rods in yellow and slabs in blue.

coincide with the unique one obtained in the OCP, where the Wigner-Seitz free energy density is minimized. In this section we will analytically show that our calculation respects ensemble equivalence and that taking the chemical potentials from the CLD, instead of the CPA, is essential.

We begin by calculating and discussing the rearrangement term, an essential quantity in this context [101, 106]. The rearrangement was introduced in eq. (3.2) and to understand its origin we notice that, had we allowed ρ_p^N, ρ_n^N, f^N and R_d^N to fluctuate, the total proton fraction of the system, given by

$$\rho_p = \sum_{N,d} n^{N,d} V^N \left(\rho_p^N - \rho_{pg}\right) + \rho_{pg}, \tag{3.25}$$

would be different from the total electron density ρ_e, which is fixed from the OCP, and the system would have a net charge. Microscopically, each cell would also have a net charge, leading to long-range Coulomb interactions. In order to avoid these issues, we fix the global proton cell by imposing that it is equal to the electron one: $\rho_p = \rho_e$. Moreover, the WS cell proton density is equal to the global one by constraining volume fraction f^N via eq. (3.6). By doing so, the assumption of independent fluctuations in different cells is broken. Now the volume fraction becomes a function of the global proton density, and thus of the number densities $n^{N,d}$, i.e. $f^N = f^N(\rho_p(n^{N,d}))$. In turn, this implies that the thermodynamic potential (3.2) also acquires a dependency on the number densities. To be mathematically precise, we write the average cluster free energy density as

$$\langle \mathcal{F}_{cl} \rangle = \sum_{N,d} n^{N,d} F_{cl}^{N,d}, \tag{3.26}$$

where the cluster free energy is given in eq. (3.21) and the single-cluster thermodynamic potential is [98, 106]

$$\tilde{\Omega}^{N,d} = V^N \left[\frac{\partial \langle \mathcal{F}_{cl} \rangle}{\partial n^{N,d}} - \sum_q \mu_q \left(\rho_q^N - \rho_{qg}\right) \right]. \tag{3.27}$$

Substitution of Eq. (3.26) gives us the derivative inside the brackets:

$$\tilde{F}_{cl}^{N,d} \equiv \frac{\partial \langle \mathcal{F}_{cl} \rangle}{\partial n^{N,d}} = F_{cl}^{N,d} + \sum_{M,d'} n^{M,d'} \frac{\partial F_{cl}^{M,d'}}{\partial n^{N,d}}, \tag{3.28}$$

where we identify the rearrangement with

$$\delta F^N = \sum_{M,d'} n^{M,d'} \frac{\partial F_{cl}^{M,d'}}{\partial n^{N,d}}. \tag{3.29}$$

The calculation can be done straightforwardly with a change of variables. Using Eqs. (3.4) and (3.25):

$$\begin{aligned}\delta F^N &= \frac{\partial \rho_p}{\partial n^{N,d}} \sum_{L,M,d'} n^{M,d'} \frac{\partial F_{cl}^{M,d'}}{\partial f^L} \frac{\partial f^L}{\partial \rho_p} \\ &= V^N \left(\rho_p^N - \rho_{pg}\right) \sum_{M,d'} n^{M,d'} \frac{\partial F^{M,d'}}{\partial f^M} \frac{1}{\rho_p^M - \rho_{pg}}.\end{aligned} \tag{3.30}$$

If we additionally assume that the different averaged quantities are not correlated, such that the average commutes with the product – $\langle x\rangle\langle y\rangle = \langle xy\rangle$ – then we can divide the cluster volume coming from the free energy by WS cell average, appearing in the denominator of $n^{N,d} = p^{N,d}/\langle V_{WS}\rangle$, and the rearrangement becomes

$$\delta F^N = V^N \left(\rho_p^N - \rho_{pg}\right) \left\langle \frac{f^M}{\rho_p^M - \rho_{pg}} \frac{\partial \mathcal{F}_{sc,d}^M}{\partial f^M} \right\rangle, \tag{3.31}$$

which is an expression similar to the ones proposed in Refs. [101, 106, 107]. Nevertheless, in those, the average was introduced by hand due to a missing sum over M, d in the calculation. We have shown that the average appears directly from the calculation if the change of variables is done properly (with the extra assumption of uncorrelated averages). The notation $\langle X\rangle$ indicates ensemble average.

Nevertheless, a complete determination of the pasta probabilities becomes numerically challenging with the rearrangement, since we must determine the number densities and the rearrangement term simultaneously and self-consistently. To avoid this complication we identify the average value of the rearrangement with its value calculated in the OCP with optimal geometry d_0:

$$\left\langle \frac{f^M}{\rho_p^M - \rho_{pg}} \frac{\partial \mathcal{F}_{sc,d}^M}{\partial f^M} \right\rangle = \frac{\mathcal{F}_{c,d_0}}{\Phi} \frac{d\Phi}{df} + \frac{d_0 f}{R_{d_0}\rho_B} \frac{\left(\rho_p^I - \rho_{pg}\right) - Y_p\left(\rho^I - \rho_g\right)}{\rho_p^I - \rho_{pg}} \frac{\partial \sigma}{\partial Y_p}.$$

Now we analytically prove that ensemble equivalence is respected by demonstrating that

the equilibrium equations of the MCP are equivalent to those of the OCP – eqs. (2.82), (2.81) and (2.84). We characterize the most probable cluster by the superscript $N_0 = \{\rho_p^{N_0}, \rho_n^{N_0}, V^{N_0}\}$, and we find the conditions by taking the derivative of the one-cell cluster thermodynamic potential (3.27) w.r.t. to these variables at the point where it is equal to zero.

We begin with the derivative w.r.t. the proton cluster density, with cluster volume and neutron density kept fixed

$$\begin{aligned}\left.\frac{\partial\tilde{\Omega}^{N,d}}{\partial\rho_p^N}\right|_{\rho_n^N,V^N} &= V^N\left[\frac{\partial\mathcal{F}_b^N}{\partial\rho_p^N}+\left.\frac{\partial\mathcal{F}_{sc,d}^N}{\partial\rho_p^N}\right|_{\rho_n^N,V^N}-\mu_p+\left\langle\frac{f^M}{\rho_p^M-\rho_{pg}}\frac{\partial\mathcal{F}_{sc,d}^M}{\partial f^M}\right\rangle\right]\\ &= V^N\left[\mu_p^N+\left.\frac{\partial\mathcal{F}_{sc,d}^N}{\partial\rho_p^N}\right|_{f^N,\rho_n^N,V^N}+\frac{f^N}{\rho_p^N-\rho_{pg}}\left.\frac{\mathcal{F}_{sc,d}^N}{\partial f^N}\right|_{\rho_p^N,\rho_n^N,V^N}\right.\\ &\qquad\left.-\mu_p+\left\langle\frac{f^M}{\rho_p^M-\rho_{pg}}\frac{\mathcal{F}_{sc,d}^M}{\partial f^M}\right\rangle\right],\end{aligned}\tag{3.32}$$

and rewrite it at equilibrium – when the derivative is zero – as

$$\mu_p^{N_0}+\frac{\partial\mathcal{F}_{sc,d}^{N_0}}{\partial\rho_p^{N_0}}+\frac{f^{N_0}}{\rho_p^{N_0}-\rho_{pg}}\frac{\mathcal{F}_{sc,d}^{N_0}}{\partial f^{N_0}}=\mu_p+\frac{f}{\rho_p^I-\rho_p^{II}}\left.\frac{\mathcal{F}_{sc,d}}{\partial f}\right|_{OCP}.\tag{3.33}$$

The terms with derivatives of the S+C energy w.r.t. f^N cancel out exactly when the MCP solution coincides with the OCP – see eq. (2.75). For the neutron density, we take the derivative

$$\begin{aligned}\left.\frac{\partial\tilde{\Omega}^{N,d}}{\partial\rho_n^N}\right|_{\rho_p^N,V^N} &= V^N\left[\frac{\partial\mathcal{F}_b^N}{\partial\rho_n^N}+\frac{\partial\mathcal{F}_{sc,d}^N}{\partial\rho_n^N}-\mu_n\right]\\ &= V^N\left[\mu_n^N+\frac{\partial\mathcal{F}_{sc,d}^N}{\partial\rho_n^N}-\mu_n\right],\end{aligned}\tag{3.34}$$

which is the minimum when neutron density is $\rho_n^N = \rho_n^I$, as can be seen by comparison with eqs. (2.75) and (2.82).

Finally, to complete the proof, we turn to pressure equilibrium by taking the derivative

w.r.t. V^N, which is a function of R_d^N:

$$\left.\frac{\partial \Omega_N}{\partial V^N}\right|_{\rho_p^N,\rho_n^N} = \mathcal{F}_b^N - \mathcal{F}_{b,g} - \mu_p(\rho_p^N - \rho_{pg}) - \mu_n(\rho_n^N - \rho_{ng}) + \mathcal{F}_{sc,d}^N + V^N \frac{\partial \mathcal{F}_{sc,d}^N}{\partial R_d^N}\frac{\partial R_d^N}{\partial V^N} + \left(\rho_p^N - \rho_{pg}\right)\left\langle \frac{1}{\rho_p^M - \rho_{pg}}\frac{\partial \mathcal{F}_{sc,d}^M}{\partial f^M}\right\rangle. \tag{3.35}$$

This is exactly equivalent to eq. (2.83), and thus to the OCP equilibrium condition. This is only true due to our assumption that the S+C energy is minimized in each cell.

To illustrate the importance of the rearrangement term we show the probabilities calculated both with and without it in Fig. 15. The vertical dashed line is drawn over the OCP solution. The rearrangement is clearly more important at higher proton fractions, due to the larger contribution of the Coulomb energy, nevertheless, even at $Y_p = 0.1$ there are differences between the most probable cluster with and without the rearrangement. For simplicity, these probabilities were calculated by fluctuating only the cluster proton density and pasta geometry, while maintaining the neutron one fixed ($\rho_n^N = \rho_n^I$).

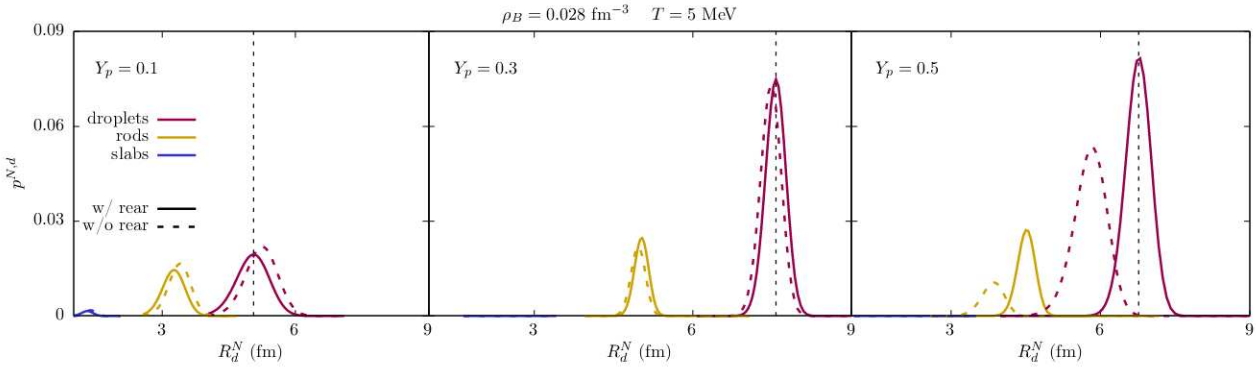

Figure 15: Pasta probabilities calculated with (continuous lines) and without (dashed lines) the rearrangement term. The vertical dashed line is drawn over the OCP linear radius. The plots are for $\rho_B = 0.028$ fm^{-3}, T=5 MeV and $Y_p = 0.1, 0.3$ and 0.5.

Additionally, in Fig. 16 we show the average linear radius

$$\langle R^N \rangle = \sum_{N,d} p^{N,d} R_d^N \tag{3.36}$$

along with the OCP value for T=3 MeV. On the left we show the curves for proton fractions $Y_p = 0.3$ and 0.5, where the optimal geometry is much more abundant than the others– see Fig. 14– and on the right side, we show $Y_p = 0.1$. For the higher proton fractions, which are less impure systems, the average radii coincide with the OCP, while for a large mixing of geometries,

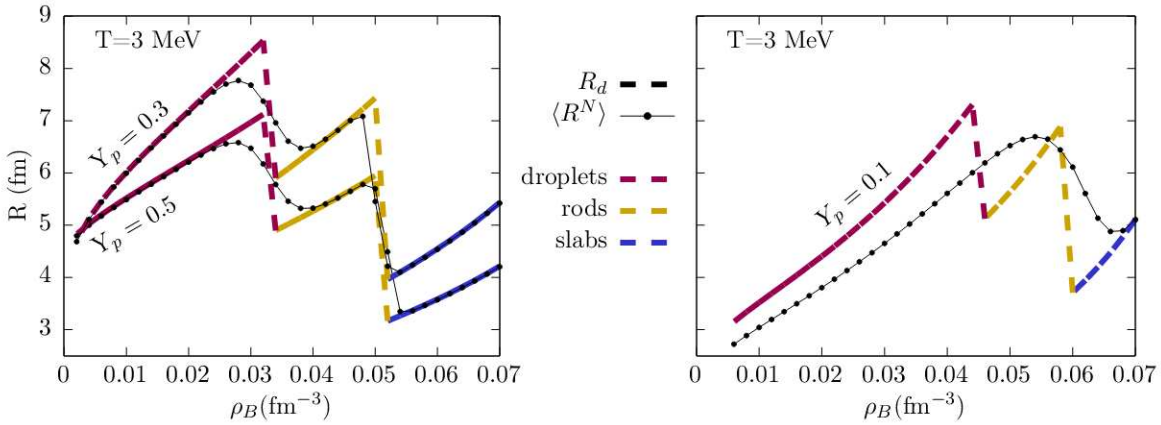

Figure 16: Average linear radius (line-points) and radius obtained by minimizing the S+C energy for the optimal geometry (dashed lines) for $Y_p = 0.3, 0.5$ on the left and $Y_p = 0.1$ on the right. Both for T=3 MeV.

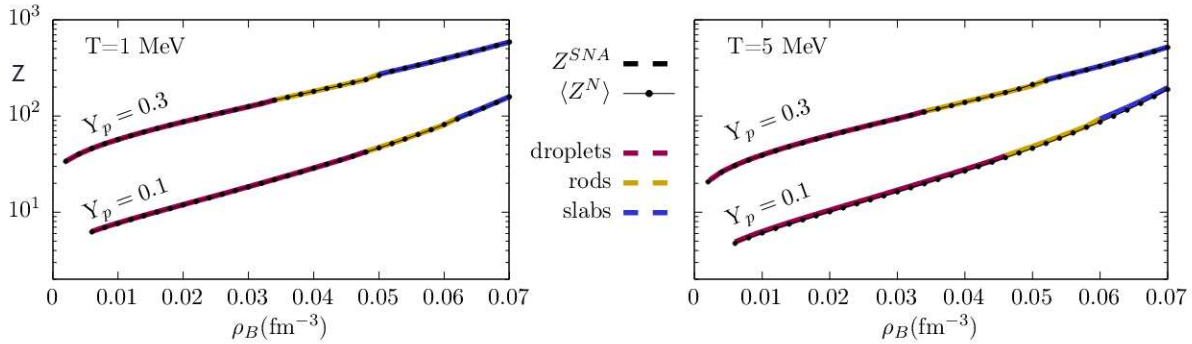

Figure 17: Average proton number (line-points) compared to the OCP value (dashed lines) for $Y_p = 0.1, 0.3$ and T=1 and 3 MeV on the left and right, respectively.

this is not the case. Thus, the linear size of the pasta seems to be a good quantity to quantify the geometric impurity.

3.3 Impurities

Lattice impurities are quantified by the charge variance, that is an increasing function of the baryonic density and temperature [101, 192–194]:

$$Q_{\mathrm{imp}} = \langle (\Delta Z)^2 \rangle = \sum_{N,d} p^{N,d} \left(Z^N - \langle Z^N \rangle \right)^2 \tag{3.37}$$

$$= \langle (Z^N)^2 \rangle - \langle Z^N \rangle^2 \tag{3.38}$$

Of course the average proton number

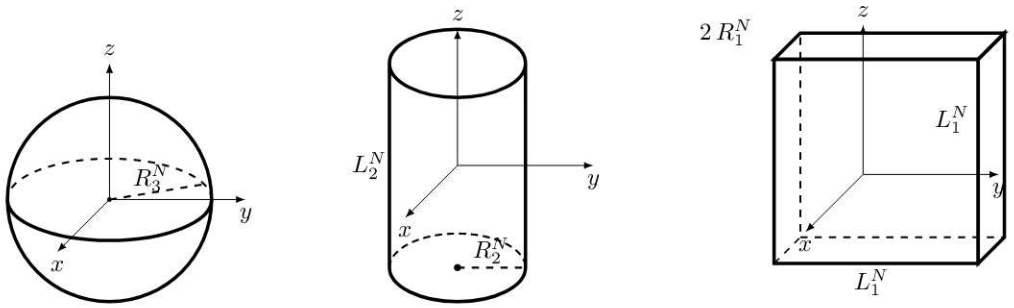

Figure 18: Illustration of the symmetry axis, linear radius, and length of the pasta geometries.

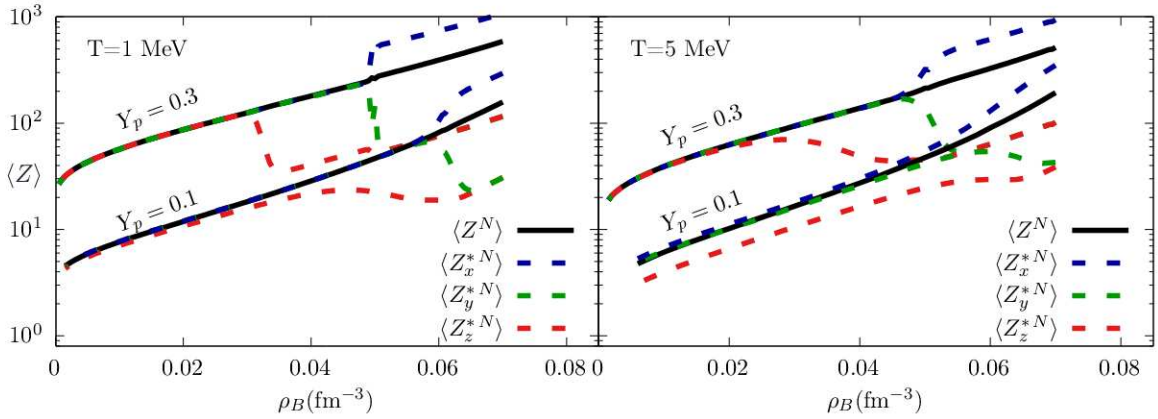

Figure 19: Average proton number (continuous line) and effective proton number in the x, y and z axis (red, green and blue dashed lines) for $Y_p = 0.1, 0.3$ and T=1 (left) and 5 MeV (right).

$$\langle Z^N \rangle = \sum_{N,d} p^{N,d} Z^N \tag{3.39}$$

is independent of the pasta geometries, as shown in Fig. 17. But the pasta geometric anisotropy implies that, if it is "seen" from different angles, its effective proton number will change. We state this in the same spirit that transport and elastic properties are sensitive to the pasta geometrical anisotropy [33, 40]. Thus, in order to quantify these directional changes we define an effective proton number according to the ratio of the pasta surface area in a certain direction to the droplet surface area.

Axis	$S_{2,k}^N$	$S_{1,k}^N$
x	$\pi R_2^N L_2^N$	$\left(L_1^N\right)^2$
y	$\pi R_2^N L_2^N$	$R_1^N L_1^N$
z	$\pi (R_2^N)^2$	$R_1^N L_1^N$

Table 6: Effective surface of the pasta structure in the axis of motion of an incident probe. The rods are considered to have length $L_{2,WS}$ in the x-axis, and the slabs have length $L_{1,WS}$ in the x and y directions.

We consider that the pasta structures are oriented as illustrated in Fig. 18: the cross-sectional area of rods is in the z and L_2^N defines their length in the z direction. Slabs have length L_1^N in both y and z directions, and size $2\,R_1^N$ in the x axis. An incident probe moving in the $k-$direction sees a surface area $S_{d,k}^N$, perceiving a larger number of protons $Z^{*N} > Z^N$, if the area is larger than that of droplets, and a smaller number, if there is a smaller area. The surface areas for rods and slabs are summarized in Tab. 6. Droplets have $S_3^N = 2\pi(R_3^N)^2$, which is half of the droplet total surface, as seen by an object moving towards it.

In this point of view, we define the effective proton number seen by a probe moving in the k-axis as

$$Z_{d,k}^{*N} = Z^N \frac{S_{d,k}^N}{S_3^N}. \tag{3.40}$$

and we show their values in Fig. 19 for $Y_p = 0.1, 0.3$ and T=1 and 5 MeV. As more rods or slabs are present, the effective number of protons seen by a probe moving in the z direction decreases, and as rods turn to slabs the y proton number also decreases, but in x it increases.

Using eq. (3.40) we define the orientation-dependent variances in the same spirit as eq. (3.37)

$$(\Delta Z_k^*)^2 = \sum_{N,d} p^{N,d} \left(Z_{dk}^{*N} - \langle Z_k^{*N} \rangle \right)^2, \tag{3.41}$$

which are shown in Figs. 20 and 21 for T=1 and 5 MeV, respectively, along with the one defined by eq. (3.37), which is displayed as a solid line. The order of magnitude is consistent with previously proposed values: in ref. [57], Pons proposes curves with the impurity ranging from 0.1 and 100, while in [29] they calculate a value ranging between 30 and 40 in molecular dynamics simulations, and in [28] they calculate the average impurity of the crust to be 29. In our results, larger anisotropic fluctuations occur near changes in dominant geometry. The results of this section were published in [195].

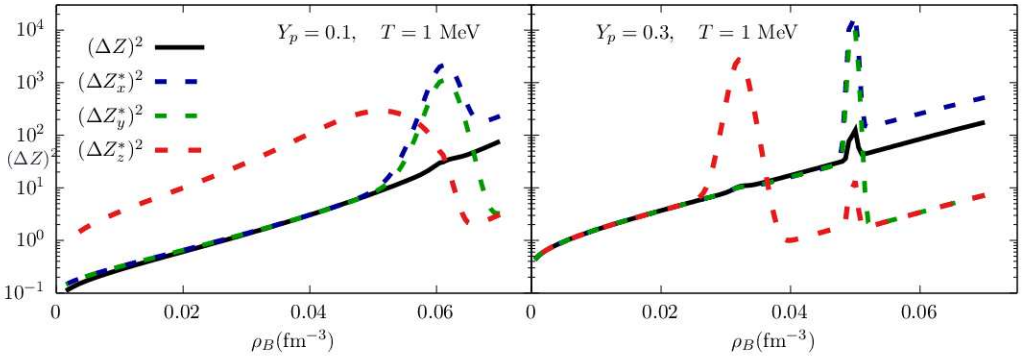

Figure 20: Total (solid line) and orientation-dependent (dashed) proton number variances for T=1 MeV, $Y_p = 0.1$ (left) and 0.3 (right). The x, y and z axis denote the direction of motion of the probe, and are represented by the colors red, green and blue, respectively. We assume local domains of different geometries aligned along a common symmetry axis x.

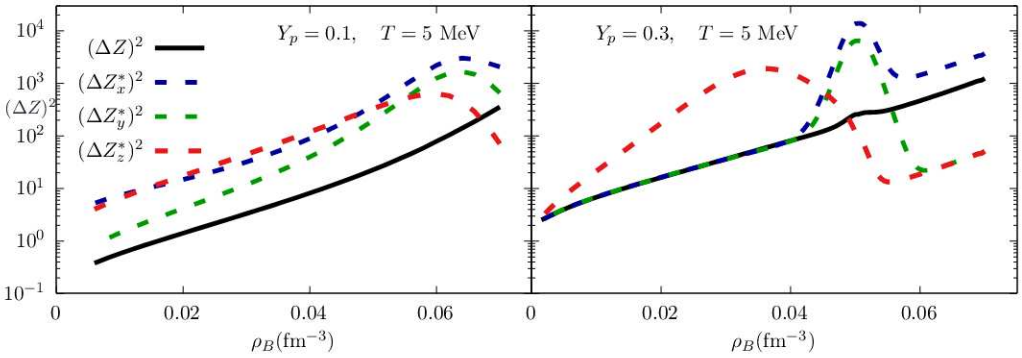

Figure 21: Same as Fig. 20 for T=5 MeV.

4 Conductivity of nuclear pasta

In this section, we introduce the formalism of transport theory via the Boltzmann equation and the relaxation time approximation. We generalize the formalism of elastic isotropic electron-ion scattering to the elastic electron-pasta scattering and calculate the anisotropic collision frequencies that arise due to the pasta anisotropic geometry. The RMF model is used to give quantitative estimations of the conductivity and collision rates.

4.1 Transport coefficients and the Boltzmann equation

Transport phenomena occur when some conserved physical quantity in a system, such as charge or momentum, changes position. These changes are induced by out-of-equilibrium conditions, such as temperature gradients, non-homogeneous chemical composition, or the presence of electric potentials, which modify the particle distribution functions $f(\boldsymbol{r}, \boldsymbol{p}, t)$ and give rise to currents of charge, heat and momentum. These are respectively defined as

$$J_{e\,i} = q \sum_s \int \frac{d^3\boldsymbol{p}}{(2\pi)^3}\, v_i\, f(\boldsymbol{r}, \boldsymbol{p}, t), \tag{4.1}$$

$$J_{Q\,i} = \sum_s \int \frac{d^3\boldsymbol{p}}{(2\pi)^3}\, \left(\epsilon_p - \mu\right)\, v_i\, f(\boldsymbol{r}, \boldsymbol{p}, t), \tag{4.2}$$

$$\Pi_{ij} = \sum_s \int \frac{d^3\boldsymbol{p}}{(2\pi)^3}\, p_i\, v_j\, f(\boldsymbol{r}, \boldsymbol{p}, t), \tag{4.3}$$

where the variables $\boldsymbol{r}$, $\boldsymbol{p}$, $\boldsymbol{v}$, q, ϵ_p and μ are the position, momentum, velocity, charge, energy, and chemical potential of the particle affected by the out-of-equilibrium conditions. The function $f(\boldsymbol{r}, \boldsymbol{p}, t)$ is the probability distribution of the particle. At equilibrium, it is simply given by the Fermi-Dirac expression, eq. (2.33), which we will denote hereafter as $f^{(0)}$.

The main transport coefficients are electric ($\hat{\boldsymbol{\sigma}}$) and thermal ($\hat{\boldsymbol{\kappa}}$) conductivity and shear ($\hat{\boldsymbol{\eta}}$) and bulk ($\hat{\boldsymbol{\zeta}}$) viscosity, which are respectively defined as a linear response to an effective electric field $E_j^* = E_j + q^{-1}\nabla\mu$, temperature gradient ∇T, and to variations in the center of mass

velocity $\boldsymbol{V}(\boldsymbol{r}, t)$, i.e.

$$J_{e,i} = \sigma_{ij} E_j^* \tag{4.4}$$

$$J_{Q,i} = \kappa_{ij} \left(-\frac{\partial T}{\partial x_j} \right), \tag{4.5}$$

$$\Pi_{ij} = \eta_{ij\,kl} \left[\partial_k V_l + \partial_l V_k - \frac{2}{3} \delta_{kl} \nabla \cdot \boldsymbol{V} \right] + \zeta_{ij} \nabla \cdot \boldsymbol{v}. \tag{4.6}$$

The values of these coefficients are dependent on microscopic particle collisions and flavor-changing processes that occur, which modify the particle distribution function. The distribution function obeys the Boltzmann equation, which can be derived by taking the time derivative of f as:

$$\frac{\partial f}{\partial t} + \boldsymbol{v} \cdot \frac{\partial f}{\partial \boldsymbol{r}} + \boldsymbol{F} \cdot \frac{\partial f}{\partial \boldsymbol{p}} = \frac{df}{dt} = I[f] \tag{4.7}$$

where $\boldsymbol{v} = \dot{\boldsymbol{r}}$, $\boldsymbol{F} = \dot{\boldsymbol{p}}$ are the external forces and $I[f]$ is the collision integral that takes into account the microscopic processes.

Astronomical observations related to the thermal, magnetic, and spin evolution of neutron stars can provide us with indirect information on the transport properties of dense matter [29, 102, 196]. These observations must be compared with simulations by properly modeling the coupled magneto-thermal evolution. Hence, models are necessary for the microscopic processes that give rise to the conductivities and viscosity throughout the star [53, 197, 198], which are then used as inputs to the macroscopic simulations, see [199–201].

In the crust, electrons, are the primary carriers of heat, charge, and momentum. Their scattering with ions, lattice phonons, and other electrons determines the rate at which these quantities are transported. The dominant contribution depends on the state and composition of the system: electron-electron collisions become relevant only at very small temperatures and densities or in a low Z plasma, which may be interesting in the context of the NS surface or in white dwarfs [202, 203] and electron-ion contributions are the dominant ones both in liquid ($T > T_m$) and in solid ($T < T_m$) ions [50]. In the solid phase, the main contribution comes from the scattering with lattice vibrations of the ions (phonons), while in the liquid it comes from the direct electron-ion scattering [47, 49, 198]. The free neutrons in the inner crust can also contribute to the heat and momentum transport via scattering with magnetic moments of electrons or phonons, though their contribution is likely relevant only close to the crust-core transition [46, 204, 205].

In compact stars, electrons are strongly degenerate ($T \ll T_F = \mu_e - m_e$), so microscopic processes are restricted to excitations near the Fermi surface. This greatly simplifies calculations since the electron energy in (4.7) can be taken as the Fermi energy itself. The reader interested in the non-degenerate case should refer to the appendix of ref. [206], which is a reference that also provides an interesting review of NS cooling. In principle to determine the transport coefficients one must have full knowledge of the collision integral and solve the Boltzmann transport equation to find the particle distribution, and then rewrite eqs. (4.1), (4.2) and (4.3) as a linear response to the gradient fields. Nevertheless, this is a very ambitious program. Solutions are usually found in a variational fashion or with the relaxation time approximation, which can be used as long as the temperature is sufficiently high so that quantum corrections to the scattering can be ignored ($\omega = \epsilon_p - \epsilon_{p'} \ll T$). We will follow this path.

In the relaxation time approximation, we assume the distribution function to be slightly out of equilibrium, such that

$$f(\boldsymbol{r}, \boldsymbol{p}, t) = f^0(\boldsymbol{r}, \boldsymbol{p}, t) + \delta f(\boldsymbol{p}), \tag{4.8}$$

with the position and time dependence in the equilibrium term coming from the temperature and chemical potential fields $T(\boldsymbol{r}, t)$ and $\mu(\boldsymbol{r}, t)$. The collision integral is written as

$$I[f] = -\frac{\delta f}{\tau}, \tag{4.9}$$

where τ is the relaxation time of electrons, thus the approximation name. For simplicity, we shall use the collision rate $\nu = 1/\tau$ from now on. We shall assume the electrons are in an external force $\boldsymbol{F}$ and have a center of mass velocity $\boldsymbol{V}(\boldsymbol{r}, t)$, such that the dispersion relation becomes a function $\epsilon_p(\boldsymbol{v}, \boldsymbol{V}(\boldsymbol{r}, t))$.

By using eq. (4.8) we can linearize the Boltzmann equation (4.7). To do so we begin by taking the differential of the equilibrium component

$$\begin{aligned} df_0 &= \frac{\partial f_0}{\partial t} dt + \left(-\frac{\partial f_0}{\partial \epsilon_p}\right) \left[\left(\frac{\partial \mu}{\partial \boldsymbol{r}} + p_k \frac{\partial V_k}{\partial \boldsymbol{r}} + \left(\frac{\epsilon_p - \mu}{T}\right) \frac{\partial T}{\partial \boldsymbol{r}} \right) \cdot d\boldsymbol{r} - \frac{\partial \epsilon_p}{\partial \boldsymbol{p}} \cdot d\boldsymbol{p} \right] \\ &= \frac{\partial f_0}{\partial t} dt + \frac{\partial f_0}{\partial \boldsymbol{r}} \cdot d\boldsymbol{r} + \frac{\partial f_0}{\partial \boldsymbol{p}} \cdot d\boldsymbol{p} \end{aligned} \tag{4.10}$$

such that we can now use eqs. (4.8) and (4.10) in eq. (4.7). By keeping only first-order terms in

δf we arrive at the linearized Boltzmann equation

$$\left(-\frac{\partial f_0}{\partial \epsilon_p}\right) v_k \left[\frac{\partial \mu}{\partial x_k} - F_k + \frac{\epsilon_p - \mu}{T}\frac{\partial T}{\partial x_k}\right] + \frac{1}{2}\left(-\frac{\partial f_0}{\partial \epsilon_p}\right) p_j v_k \left[\frac{\partial V_j}{\partial x_k} + \frac{\partial V_k}{\partial x_j} - \frac{2}{3}\delta_{jk}\nabla\cdot\boldsymbol{V}\right] + \left[\frac{\partial f_0}{\partial t} + \left(-\frac{\partial f_0}{\partial \epsilon_p}\right)\frac{1}{3}u_k p_j \delta_{jk}\nabla\cdot\boldsymbol{V}\right] + F_k\frac{\partial \delta f}{\partial p_k} = I[f]. \tag{4.11}$$

The first term contains the temperature gradient and electric field that give rise to the conductivities, and it is first order in the momentum ($\propto v_k$). The second term contains the mathematical structure of the bulk viscosity definition, eq. (4.6), and it is of second order in the momentum ($\propto p_j v_k$). The third term is related to the shear viscosity, which is due to flavor-changing processes.

Our main interest in this thesis is the conductivity, so we'll simply ignore the terms related to the viscosity by keeping only linear terms in $\boldsymbol{v}$,

$$\left(-\frac{\partial f_0}{\partial \epsilon_p}\right)\boldsymbol{v}\cdot\left[\frac{\partial \mu}{\partial \boldsymbol{x}} + e\boldsymbol{E} + \frac{\epsilon_p - \mu}{T}\frac{\partial T}{\partial \boldsymbol{x}}\right] - e(\boldsymbol{v}\times\boldsymbol{B})\frac{\partial \delta f}{\partial \boldsymbol{p}} = I[f], \tag{4.12}$$

where we used $\boldsymbol{F} = -e\,(\boldsymbol{E} + \boldsymbol{v}\times\boldsymbol{B})$. Let's also ignore the magnetic field momentarily. By using the relaxation time approximation, eq (4.9) we straightforwardly find a solution for δf:

$$\delta f = \frac{1}{\nu}\left(-\frac{\partial f_0}{\partial \epsilon_p}\right)\boldsymbol{v}\cdot\left[\frac{\partial \mu}{\partial \boldsymbol{x}} + e\boldsymbol{E} + \frac{\epsilon_p - \mu}{T}\frac{\partial T}{\partial \boldsymbol{x}}\right]. \tag{4.13}$$

To find the electric conductivity we take $\nabla T = 0$ and substitute the solution in eq. (4.1), and for the thermal one we take $\boldsymbol{E}^* = 0$ and substitute it in eq. (4.2). We get

$$\boldsymbol{J}_e = \frac{e^2 p_F^2 v_F}{3\pi^2\nu}\boldsymbol{E}^* = \frac{e^2 n_e}{m_e^*\nu}\boldsymbol{E}^* \tag{4.14}$$

and

$$\boldsymbol{J}_q = \frac{T\,p_F^2 v_F}{9\nu}\,(-\nabla T) = \frac{\pi^2 T n_e}{3m_e^*\nu}\,(-\nabla T) \tag{4.15}$$

where we have performed a direct integration in the solid angle Ω_p

$$\int d\Omega_p v_i v_j = \frac{4\pi v^2}{3}\delta_{ij} \tag{4.16}$$

and used the Sommerfeld expansion [207]

$$\int_0^\infty d\epsilon\; G(\epsilon)\left(-\frac{\partial f^0}{\partial \epsilon}\right) \approx G(\epsilon_F) + \frac{\pi^2}{6}T^2 G''(\epsilon_F) + \frac{7\pi^4}{180}G''''(\epsilon_F) + \cdots \tag{4.17}$$

to first order by making the change of variable $dp = d\epsilon/v$. Thus we find, in the relaxation time approximation, the conductivities [47,48,51]

$$\sigma_{ij} = \frac{e^2 n_e}{m_e^* \nu_\sigma}\delta_{ij} \qquad\qquad \kappa_{ij} = \frac{\pi^2 T n_e}{3 m_e^* \nu_\kappa}\delta_{ij} \tag{4.18}$$

where m_e^* is the effective electron mass and p_F (v_F) the Fermi momentum (velocity). The collision frequencies are the same only in the case that no quantum effects are taken into account, otherwise, there are different kinematic factors entering ν_σ and ν_κ [47,50].

The case of viscosity is a bit more complicated. Its expression is very similar to eqs. (4.18)

$$\eta_{ij} = \frac{n_e p_F v_F}{5\nu_\eta}\delta_{ij} \tag{4.19}$$

but to determine this expression and calculate the collision frequency it is necessary to introduce a full expansion of the collision integral in spherical harmonics

$$I[f] = -\sum \delta f_{lm}(\epsilon_p)\nu_l(\epsilon_p)Y_l^m(\Omega_p), \tag{4.20}$$

from which we can determine that the $l = 1$ term corresponds to the simple eq. (4.9), from which we got the conductivities, while the viscosity is related to $l = 2$ ($\nu_\eta = \nu_{l=2}$) by writing the (complex) spherical harmonics in terms of real coefficients, i.e. an expansion in homogeneous harmonic polynomials [198,208–210],

$$\begin{aligned} f(\boldsymbol{p}) &= \sum_{l\,m} f_{lm}Y_l^m(\Omega_p) \\ &= f_0 + \frac{p_i}{p}f_i + \frac{p_i p_j}{p^2}f_{ij} + \ldots \end{aligned}$$

This can be done by making linear combinations of the spherical harmonics to produce real coefficients $f_{i_1 i_2 \ldots i_k}$, with the power of l corresponding to the power of p_i. By orthogonality, we can identify the first order power p_i in the left-hand side of the Boltzmann eq. (4.11) with $l = 1$ and the second order $p_i p_j$ with $l = 2$, such that each one contributes to a different multipole of

δf_{lm} coefficients, defined by

$$\delta f(\boldsymbol{p}) = \sum_{l>0\,m} \delta f_{lm}\left(\epsilon_p\right) Y_l^m(\Omega_p). \tag{4.21}$$

where $l = 0$ is left out because it corresponds to the equilibrium distribution f^0. By direct substitution of eq. (4.21) into the transport coefficients, eqs. (4.1), (4.2) and (4.3) we see that $l = 1$ contributes to the conductivity and $l = 2$ to the viscosity because the angular integral is different from zero only if it is performed on even powers of momentum p_i, as in eq. (4.16).

Because of the isotropy assumption, the collision frequencies only depend on the modulus of the electron momentum transfer $\boldsymbol{q} = \boldsymbol{p} - \boldsymbol{p'}$ according to the general expression [46–48]:

$$\nu_l = \frac{4\pi e^4 Z^2}{v_F p_F^2} \int_0^{2p_F} \frac{dq}{q} \left(1 - \frac{q^2}{4\epsilon_F^2}\right) R_l(q) \frac{F^2(q)}{\varepsilon^2(q)} S(q)\,, \tag{4.22}$$

where $F(q)$ is the ion form factor, $\varepsilon(q)$ is the dielectric function, $S(q)$ is the effective structure factor that accounts for particle correlations, $R_l(q)$ is a kinetic factor

$$R_1(q) = 1, \qquad R_2(q) = 3\left(1 - \frac{q^2}{4p_F^2}\right) \tag{4.23}$$

and v_F, p_F, and ϵ_F are the Fermi velocity, momentum and energy respectively. Unfortunately, eq. (4.22) cannot be straightforwardly generalized to the case of anisotropic scatterings. To better understand the meaning of each term in this expression, and how to generalize it to the pasta, let's discuss how to calculate the collision integral for elastic electron–pasta scattering.

4.2 The collision integral

The term collision integral $I[f]$ on the right-hand side of the Boltzmann equation (4.11) accounts for the microscopic processes that give rise to transport phenomena such as scatterings and decays. It can be written as [211,212]

$$I[f] = \int \frac{d^3\boldsymbol{p}'}{(2\pi)^3} \left[P\left(\boldsymbol{p}' \to \boldsymbol{p}\right) - P\left(\boldsymbol{p} \to \boldsymbol{p}'\right)\right] \tag{4.24}$$

where $P\left(\boldsymbol{p}' \to \boldsymbol{p}\right)$ is the probability that a process changes the electron momentum from $\boldsymbol{p'}$ to $\boldsymbol{p}$. We will assume the electrons conserve energy in the collision, and since they are strongly

degenerate we can approximate $\epsilon_p \approx \epsilon_{p'} = \epsilon_F$. Thus, the collision is elastic, and the degenerate electrons scatter with the electric potential generated by the localized pasta. The probability of an electron changing momentum is given by the Fermi-rule

$$P\left(\boldsymbol{p} \to \boldsymbol{p}'\right) = 2\pi\ \delta(\epsilon_p - \epsilon_{p'})\frac{1}{2}\sum_{s,s'} |\langle 0|H_I|0\rangle|^2 \tag{4.25}$$

where we average over the spin states s' and sum over s, the δ-function ensures energy conservation, and the electromagnetic interaction Hamiltonian is

$$H_I(t) = -e\int d^3\boldsymbol{x}\ \bar{\psi}(\boldsymbol{x})\gamma^\mu A_\mu(\boldsymbol{x})\psi(\boldsymbol{x}), \tag{4.26}$$

where A_μ is the photon field and ψ is the electron spinor. Now we can substitute plane wave solution for electrons, as discussed in the nuclear RMF model in Section 2 – see eq. (2.20). For the second term of eq. (4.24), with initial and final momenta respectively given by $\boldsymbol{p}$ and $\boldsymbol{p}'$ we have

$$|\langle 0|H_I|0\rangle|^2 = \left|\frac{e}{\sqrt{2\epsilon_p 2\epsilon_{p'}}}\langle a^\dagger_{p's'}a_{p,s}\rangle\bar{u}_{p's'}\gamma^0 u_{ps}\int d^3\boldsymbol{x}A_0(\boldsymbol{x})e^{-i(\boldsymbol{p}-\boldsymbol{p}')\cdot\boldsymbol{x}}\right|^2. \tag{4.27}$$

The distinction between the two terms in eq. (4.24) is due to the order of the creation/destruction operators. We can write the electron distribution function in terms of these operators as

$$\langle a^\dagger_{p\,s}a_{p',s'}a^\dagger_{p's'}a_{p,s}\rangle = f(\boldsymbol{p})\left(1 - f(\boldsymbol{p}')\right), \tag{4.28}$$

such that eq. (4.25) can be written as

$$P\left(\boldsymbol{p} \to \boldsymbol{p}'\right) = 2\pi\ \delta(\epsilon_p - \epsilon_{p'})f(\boldsymbol{p})\left(1 - f(\boldsymbol{p}')\right)W_{pp'}, \tag{4.29}$$

with the transition rate defined as

$$W_{pp'} = W(\boldsymbol{p},\boldsymbol{p}') = \frac{e^2}{8\epsilon_p^2}\sum_{s,s'}\left|\bar{u}_{p's'}\gamma^0 u_{ps}\int d^3\boldsymbol{x}A_0(\boldsymbol{x})e^{-i(\boldsymbol{p}-\boldsymbol{p}')\cdot\boldsymbol{x}}\right|^2. \tag{4.30}$$

We can contract the Dirac spinors using trace properties of the gamma matrices [138,213]

$$\begin{aligned}\sum_{s\,s'} |\bar{u}_{p's'}\gamma^0 u_{ps}|^2 &= \mathrm{Tr}\left[\gamma^0(\gamma^\mu p'_\mu + m_e)\gamma^0(\gamma^\nu p_\nu + m_e)\right] \\ &= 8\epsilon_p^2\left(1 - \frac{q^2}{4\epsilon_p^2}\right),\end{aligned} \tag{4.31}$$

to write the transition rate as

$$W_{pp'} = e^2\left(1 - \frac{q^2}{4\epsilon_p^2}\right)\left|\int d^3\boldsymbol{x} A_0(\boldsymbol{x}) e^{-i(\boldsymbol{p}-\boldsymbol{p'})\cdot\boldsymbol{x}}\right|^2, \tag{4.32}$$

which is symmetric in the initial and final momentum, i.e.

$$W_{pp'} = W_{p'p}. \tag{4.33}$$

By exchanging $\boldsymbol{p}$ and $\boldsymbol{p'}$ in eq. (4.29) and the symmetry of the transition rate, the collision integral can be written as

$$I[f] = 2\pi\int \frac{d^3\boldsymbol{p}'}{(2\pi)^3}\delta(\epsilon_p - \epsilon_{p'})W_{pp'}\left[f(\boldsymbol{p'})\left(1 - f(\boldsymbol{p})\right) - f(\boldsymbol{p})\left(1 - f(\boldsymbol{p'})\right)\right], \tag{4.34}$$

such that the product of distributions cancel out, and the use of eq. (4.8) leads to

$$I[f] = 2\pi\int \frac{d^3\boldsymbol{p}'}{(2\pi)^3}\delta(\epsilon_p - \epsilon_{p'})W_{pp'}\left[\delta f(\boldsymbol{p'}) - \delta f(\boldsymbol{p})\right], \tag{4.35}$$

due to elasticity assumption.

The complete information about the scattering is in the transition rate. We restrict ourselves to the scattering with an electric potential $A_\mu = (A_0, \boldsymbol{0})$, given by

$$A_0(\boldsymbol{x}) = \int d^3\boldsymbol{x'}\rho_p^{\mathrm{tot}}(\boldsymbol{x'})U(\boldsymbol{x} - \boldsymbol{x'}), \tag{4.36}$$

where ρ_p^{tot} is the proton density of a macroscopic volume V and U is the potential of a proton in $\boldsymbol{x}$ acting at $\boldsymbol{x'}$

$$U(\boldsymbol{x} - \boldsymbol{x'}) = \frac{e}{|\boldsymbol{x} - \boldsymbol{x'}|}. \tag{4.37}$$

Equations with the mathematical structure of (4.36) are known as convolutions. This allows

the application of the convolution theorem of Fourier transforms to the transform of the electric potential [214] in eq. (4.30)

$$\int d^3\boldsymbol{x} A_0(\boldsymbol{x}) e^{-i\boldsymbol{q}\cdot\boldsymbol{x}} = \rho_p^{\text{tot}}(\boldsymbol{q}) U(\boldsymbol{q}) \tag{4.38}$$

where we recall that $\boldsymbol{q} = \boldsymbol{p} - \boldsymbol{p}'$ is the transferred momentum. The functions $\rho_p^{\text{tot}}(\boldsymbol{q})$ and $U(\boldsymbol{q})$ are the Fourier transforms of the system proton charge density and of the proton electric potential, respectively. We begin with the potential: to calculate the Fourier transformation we add a decaying exponential with a controlling parameter α to contour the divergence we would obtain otherwise

$$\begin{aligned} U(\boldsymbol{q}) = e \int d^3\boldsymbol{x}\; e^{i\boldsymbol{q}\cdot\boldsymbol{x}} \frac{e^{-\alpha x}}{x} &= 2\pi e \int r^2 dr \int d(\cos\theta) e^{iqr\cos\theta - \alpha r} \\ &= 2\pi e \int r^2 dr \left[\frac{e^{iqr} - e^{-iqr}}{i\,qr}\right] e^{-\alpha r} = \frac{4\pi e}{q^2 + \alpha^2} \end{aligned} \tag{4.39}$$

$$\overset{\alpha\to 0}{=} \frac{4\pi e}{q^2}. \tag{4.40}$$

Though the α parameter we added was spurious and should be taken to be zero in the end, the final result, eq. (4.40) is divergent at $q \to 0$. This is due to the long-range nature of the Coulomb interactions. Nevertheless, this is not a physical divergence: electrons in the plasma tend to repel their neighbors, creating a ball around them where no other electrons are found – a density fluctuation. This hole moves along with the electron, carrying inertia and acting as a positively charged particle that gives rise to a screening function that regularizes the divergence. The static screening functions $\varepsilon(q)$ modifies the potential as

$$U(q) = \frac{4\pi e}{q^2 \varepsilon(q)}. \tag{4.41}$$

and it has been calculated for the strongly degenerate electron gas in ref. [215],

$$\begin{aligned} \varepsilon(q) = 1 + \frac{k_{TF}^2}{q^2} \Bigg\{ \frac{2}{3} - \frac{2}{3}\frac{y x_r}{\gamma_r} \log(x_r + \gamma_r) + \frac{x_r^2 + 1 - 3x_r^2 y^2}{6 y x_r^2} \log\left|\frac{1+y}{1-y}\right| \\ + \frac{2y^2 x_r^2 - 1}{6 y x_r^2} \frac{\sqrt{1 + x_r^2 y^2}}{\gamma_r} \log\left|\frac{y\gamma_r + \sqrt{1 + x_r^2 y^2}}{y\gamma_r - \sqrt{1 + x_r^2 y^2}}\right| \Bigg\} \end{aligned} \tag{4.42}$$

where $y = q/(2p_F)$, $x_r = p_F/m_e$, $\gamma_r = \sqrt{1+x_r^2}$ and k_{TF} is the Thomas-Fermi momentum

$$k_{TF} = \sqrt{4\pi e^2 \partial n_e/\partial \mu_e} = 2\sqrt{\alpha_{em}\gamma_r/(\pi x_r)}p_F. \tag{4.43}$$

In the limit $y \ll 1$ this equation reduces to

$$\varepsilon(q) \overset{y\ll 1}{=} 1 + \frac{k_{TF}^2}{q^2}, \tag{4.44}$$

which is simply the potential calculated with the screening exponential in eq. (4.39) by identifying $\alpha = k_{TF}$. This correction can be calculated using the Poisson equation for the electric potential by accounting for the density screening due to the corrected chemical potential $\delta\rho_p = \rho_p(\mu + eA_0) - \rho_p(\mu)$ [211]. The interested reader should read section 3 of ref. [211] for an in-depth theoretical description of screening, or section 2.1 of [3] for a concise discussion. We should explicitly mention that, while in this work we utilize a static isotropic screening, strong magnetic fields can lead to anisotropic behavior producing Friedel oscillations [216, 217] and a dynamic dielectric function is necessary in case the projectile electron has a velocity smaller than the average plasma velocity, which is never the case for strongly degenerate matter [3, 218].

Now we turn to the Fourier transform of the system proton density. In position space, the density can be written as a sum over the centers of mass of different clusters in positions $\boldsymbol{R}_k$

$$\rho_p^{\text{tot}}(\boldsymbol{r}) = \sum_k \rho_p(\boldsymbol{r} - \boldsymbol{R_k}) \tag{4.45}$$

$$= \int d^3\boldsymbol{R} \sum_k \rho_p(\boldsymbol{r} - \boldsymbol{R})\delta^3(\boldsymbol{R} - \boldsymbol{R_k}) \tag{4.46}$$

$$\rho_p^{\text{tot}}(\boldsymbol{r}) = \int d^3\boldsymbol{R}\, \rho_p(\boldsymbol{r} - \boldsymbol{R})\rho_{CM}(\boldsymbol{R}) \tag{4.47}$$

where in the second line we have added a δ function so that this equation can be written as a convolution in the third line. Here we define the pasta center of mass density as

$$\rho_{CM}(\boldsymbol{R}) = \sum_k \delta^3(\boldsymbol{R} - \boldsymbol{R_k}) \tag{4.48}$$

and the charge density of a single pasta structure

$$\rho_p(\boldsymbol{r}) = \begin{cases} \rho_p^I\ \Theta(R_3 - r), & \text{d=3} \\ \rho_p^I\ \Theta(R_2 - r)\ \Theta(L_2 - 2|z|), & \text{d=2} \\ \rho_p^I\ \Theta(R_1 - |z|)\ \Theta(L_1 - 2|x|)\ \Theta(L_1 - 2|y|), & \text{d=1} \end{cases} \tag{4.49}$$

whereas the ρ_p^I on the right-hand side is the constant charge density of the pasta, as calculated in chap. 2. The convolution (4.47) allows the Fourier transform of the total proton density to be written as

$$\rho_q^{\text{tot}}(\boldsymbol{q}) = \rho_{CM}(\boldsymbol{q})\,\rho_p(\boldsymbol{q}), \tag{4.50}$$

as in the case of the electric potential.

Whenever we are dealing with a macroscopic system, in order to account for all its possible configurations, the thermal average $\langle\ldots\rangle_T$ must be taken into account. In principle, this is done at the level of the transition rate, but now we have factorized all macroscopic information into the center of mass density, so the average is made only in the product $\rho_{CM}(\boldsymbol{q})\rho_{CM}(-\boldsymbol{q})$ entering eq. (4.30), which we define as the static structure factor

$$\begin{aligned} S(\boldsymbol{q}) &= \langle \rho_{CM}(-\boldsymbol{q})\rho_{CM}(\boldsymbol{q})\rangle \\ &= \frac{1}{V}\int d^3\boldsymbol{r}d^3\boldsymbol{r'}e^{i\boldsymbol{q}\cdot(\boldsymbol{r}-\boldsymbol{r'})}\langle \rho_{CM}(\boldsymbol{r})\rho_{CM}(\boldsymbol{r'})\rangle_T. \end{aligned} \tag{4.51}$$

Additionally, we define the form factor as the Fourier transform of the one-pasta density normalized by its proton number:

$$F_d(\boldsymbol{q}) = \frac{1}{Z}\int_{\text{WS}} d^3\boldsymbol{r}e^{i\boldsymbol{q}\cdot\boldsymbol{r}}\rho_p(\boldsymbol{r}), \tag{4.52}$$

where we add the subscript d to denote its dependence on the pasta dimension. The matrix element is now written as:

$$W_{pp'} = e^2\left(1 - \frac{q^2}{4\,\epsilon_p^2}\right)\left|\frac{4\pi Ze\,F_d(\boldsymbol{q})}{q^2\varepsilon(q)}\right|^2 S(\boldsymbol{q}), \tag{4.53}$$

whereas both $F_d(\boldsymbol{q})$ and $S(\boldsymbol{q})$ are sources of anisotropy in the scattering with pasta, the form factor accounts for the geometric anisotropy from the finite size of a single pasta structure, while the structure factor accounts for the lattice anisotropies due to correlations and for out-of-

equilibrium particle excitations [198, 219–222].

In the liquid phase, the static structure factor can be obtained with OCP simulations of Coulomb plasma with Monte-Carlo calculations, e.g. refs. [223–225], or via the classic theory Landau-de Gennes model of liquid crystals that accounts for thermal density fluctuations in liquid-crystals [219, 220, 226, 227]. In the solid phase, electrons start to interact with lattice phonons of the system, which are accounted for via the structure factor by considering the ion center-of-mass displacements. $S(\boldsymbol{q})$ will depend on the lattice structure and on the phonons energy spectrum and polarization, which will depend on the $\boldsymbol{q}$ orientation, leading to essential differences between scatterings perpendicular and parallel to the pasta symmetry axis. To the best of our knowledge, the structure factor of the nuclear pasta has not been calculated yet. This is a non-trivial task and a work in progress.

The structure factor can also account for particle excitations within a single-pasta structure, as discussed in [221] for the pasta. Nevertheless, since those are due to single-particle-excitations within the scatterer, they are relevant for high-energy scatterings (high q), which essentially hides the structure of the scatterer, which is more relevant at lower q, thus the contributions of particle excitations in the pasta and in the homogeneous matter are identical. We do not consider these thermal particle excitations here, since they are not a source of anisotropy. They are equivalent to the homogeneous structure factor, which was analytically calculated at zero temperature [228].

Due to the lack of calculations of the structure factor we consider the pasta structures are completely uncorrelated, so scatterings occur with a static pasta structure. Substitution of eq. (4.48) considering a unique $\boldsymbol{R}_k$ leads to

$$S(\boldsymbol{q}) = \rho_i \tag{4.54}$$

where ρ_i is the ion density [46–48]. In this case the anisotropy is fully due to the pasta geometry, accounted for in the form factor.

For $F_d(\boldsymbol{q})$, analytic expressions can be found by direct integration of eq. (4.52) for the spherical, cylindrical, and planar geometries

- **Droplet:** For droplets the proton density is $\rho_p^I = \frac{3Z}{4\pi R_3^3}$ and due to the rotational symmetry

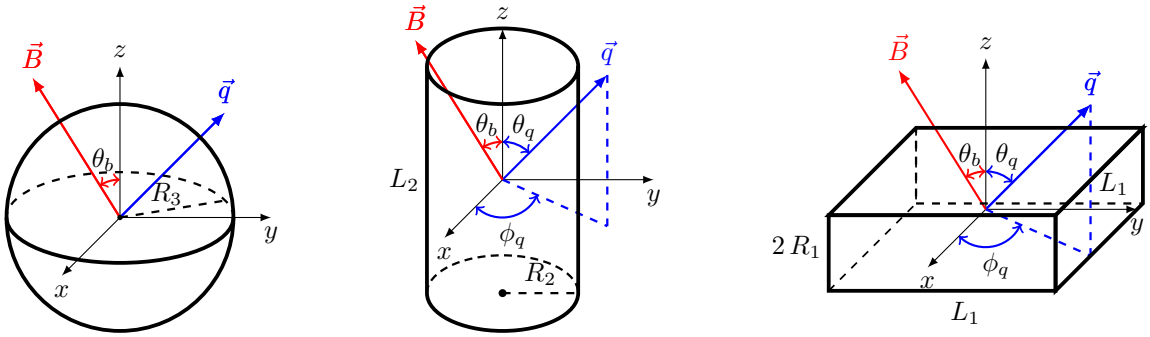

Figure 22: Cluster geometries (droplets, rods and slabs, respectively), the transferred momentum of electrons $\boldsymbol{q}$ and the magnetic field $\boldsymbol{B} = B_x\hat{\boldsymbol{x}} + B_z\hat{\boldsymbol{z}}$ are also shown.

we can choose $\boldsymbol{q}$ to lie in the z–axis, such that

$$\begin{aligned} F_3(\boldsymbol{q}) &= \frac{3}{4\pi R_3^3}\int_0^{2\pi} d\phi \int_{-1}^{1} d(\cos\theta) \int_0^{R_3} r^2\, dr\; e^{iq\,r\cos\theta} \\ &= \frac{3}{2R_3^3}\int_0^{R_3} r^2\, dr\, \left[\frac{e^{iq\,r} - e^{-iq\,r}}{iqr}\right] \\ &= \frac{3}{(qR_3)^3}\left[\cos(qR_3) - qR_3\sin(qR_3)\right]. \end{aligned} \tag{4.55}$$

In this case, the scattering depends only on the exchanged momentum absolute value $|\boldsymbol{q}|$, which is equivalent to a dependence in the angle between incoming and outgoing momentum only, since

$$q^2 = 2\,p_F^2(1 - \cos\xi), \tag{4.56}$$

where $\cos\xi = \hat{\boldsymbol{p}}\cdot\hat{\boldsymbol{p}}'$, meaning the scattering is isotropic. For the rods and slabs, the form factor additionally depends on the angle formed between the pasta symmetry axis (and its parallel plane) with the transferred momentum. By choosing the symmetry axis of the geometries to coincide with the z-axis, this dependence turns out to be in the vector $\boldsymbol{q}$ itself. This is depicted in Fig. 22.

- **Rod**: For rods the proton density is $\rho_p = \frac{Z}{\pi R_2^2 L_2}$ and we choose z as the symmetry axis,

leaving $\boldsymbol{q}$ to point in an arbitrary direction. The form factor can be calculated as:

$$\begin{aligned} F_2(\boldsymbol{q}) &= \frac{1}{\pi R_2^2 L_2} \int_{-L_2/2}^{L_2/2} d\,z \int_0^{2\pi} d\phi \int_0^{R_2} \rho\, d\rho\; e^{iq(z\cos\theta+\rho\cos\phi\sin\theta)} \\ &= \frac{1}{\pi R_2^2 L_2} \left[\frac{e^{iqL\cos\theta/2} - e^{-iqL\cos\theta/2}}{iq\cos\theta}\right] \int_0^{R_2} \rho\, d\rho \int_0^{2\pi} d\phi\, e^{iq\rho\cos\phi\sin\theta} \\ &= \frac{2}{R_2^2 L_2 q\cos\theta} \sin\left(\frac{qL\cos\theta}{2}\right) \int_0^{R_2} \rho\, d\rho J_0\left(q\rho\sqrt{1-\sin^2\theta}\right) \\ &= \frac{2}{L_2 q_z} \sin\left(\frac{q_z L}{2}\right) \frac{2}{q_\perp R_2} J_1\left(q_\perp \rho\right) \end{aligned} \tag{4.57}$$

where $q_z = q\cos\theta$, $q_\perp = \sqrt{q_x^2 + q_y^2} = q|\sin\theta|$, J_0 is the zero-th order cylindrical Bessel function

$$J_0(x) = \frac{1}{\pi}\int_0^{\pi} d\phi e^{ixcos(\phi)}. \tag{4.58}$$

and J_1 is the first-order cylindrical Bessel function

$$J_1(x) = \frac{1}{i\pi}\int_0^{\pi} d\phi e^{ixcos(\phi)}cos(\phi). \tag{4.59}$$

- **Slab:** We choose the slab to be oriented such that in the xy–plane it has lengths L_1, and in the z axis it has length $2R_1$. The proton density of the slab is $\rho_p = Z/2R_1L_1^2$. The form factor is

$$\begin{aligned} F_1(\boldsymbol{q}) &= \frac{1}{2R_1^2 L_1^2} \int_{-L_1/2}^{L_1/2} dx \int_{-L_1/2}^{L_1/2} dy \int_{-R_1}^{R_1} e^{q_x x + q_y y + q_z z} \\ &= \left(\frac{2\sin\left(L_1 q_x/2\right)}{L_1 q_x}\right)\left(\frac{2\sin\left(L_1 q_y/2\right)}{L_1 q_y}\right)\left(\frac{\sin\left(R_1 q_z\right)}{R_1 q_z}\right) \end{aligned} \tag{4.60}$$

where $q_x = q\sin\theta\cos\phi$, $q_y = q\sin\theta\sin\phi$ and $q_z = q\cos\theta$.

We write compactly for future reference:

$$F_d(\boldsymbol{q}) = \begin{cases} \dfrac{3}{(qR_3)^3}\left[\sin(qR_3) - qR_3\cos(qR_3)\right], & \text{d=3} \\ \dfrac{2}{q_z L_2}\sin\left(\dfrac{q_z L_2}{2}\right)\dfrac{2}{q_\perp R_2}J_1\left(q_\perp R_2\right), & \text{d=2} \\ \dfrac{2}{L_1 q_x}\sin\left(\dfrac{L_1 q_x}{2}\right)\dfrac{2}{L_1 q_y}\sin\left(\dfrac{L_1 q_y}{2}\right)\dfrac{1}{R_1 q_z}\sin\left(R_1 q_z\right), & \text{d=1} \end{cases} \tag{4.61}$$

Recall that the radius R_d can be calculated from the RMF model from eq. (2.70), but the length

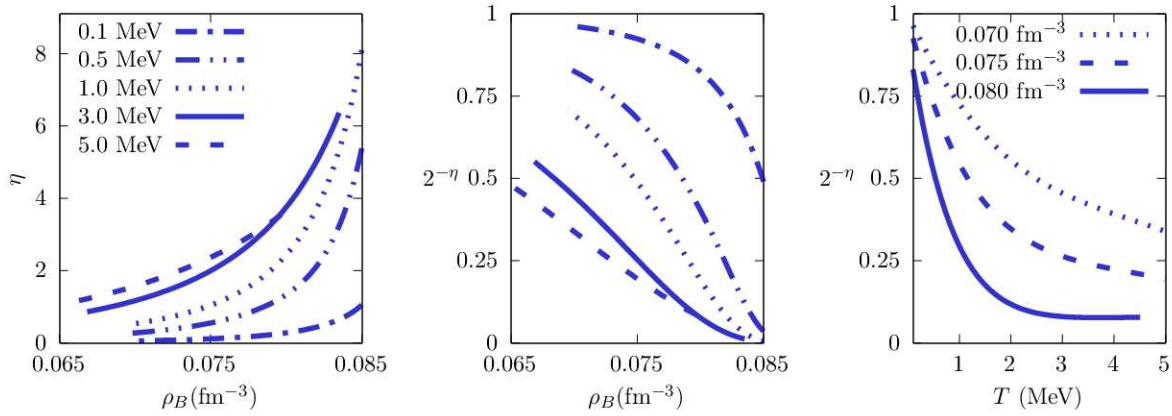

Figure 23: Left panel: correlation function decay parameter η for slabs. Middle (right) panel: estimation of the correlation between neighboring slab structures as a function of density (temperature), see text for details. Curves for T =0.1, 0.5, 1, 3, and 5 MeV are shown on the left and center, and for ρ_B = 0.07, 0.075 and 0.08 fm^{-3} on the right.

L_d of rods and slabs is unconstrained by nuclear theory. Indeed, the length will depend on the temperatures analyzed and on the strength of the thermal fluctuations that disrupt long-range order, which is related to the structure factor.

These fluctuations have been calculated in the axis perpendicular to the size L_d for the pasta [88, 229] within the aforementioned Landau-de Gennes model of liquid crystals [219]. For slabs, the thermal displacement presents a logarithmic divergence with the linear dimension of the sample, reflecting the Landau-Peierls instability that destroys one-dimensional order in a three-dimensional system. This is quantified by a critical temperature at which the thermal displacement becomes as large as the cell radius, so thermal fluctuations of slabs in the z direction can become larger than R_{WS} [88, 226]. Concerning the rod phase, the thermal displacement is finite and the long-range order in the transverse plane is in principle preserved. The critical temperature was shown to strongly decrease with increasing baryonic density and, for fiducial values of the surface tension, to be of the order of a few MeV both for slabs and for rods [88]. Above such temperatures, it is reasonable to expect that the pasta is fully destroyed, even if complex deformed disordered cluster structures may still be present, as suggested by MD simulations [29, 32, 79, 85].

Nonetheless, even though complete calculations of the structure factor are lacking, there exists asymptotic results for the density correlation of slabs [219, 230] $\langle n_p(\boldsymbol{r}) n_p(\boldsymbol{r'}) \rangle_T \equiv$

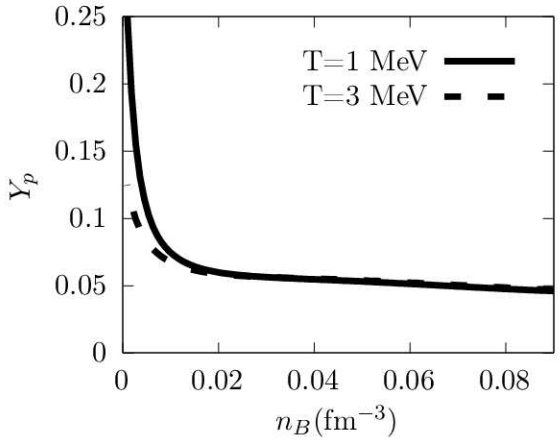

Figure 24: Total proton number as a function of density for temperatures of $T = 1$ and 3 MeV.

$\langle \delta n^2(\boldsymbol{r} - \boldsymbol{r}') \rangle_T$ showing the power law behavior:

$$\langle \delta n^2(\boldsymbol{r}) \rangle_T \propto |z|^{-\eta} \quad |z| \to \infty \tag{4.62}$$

$$\propto r_\perp^{-2\eta} \quad r_\perp \to \infty, \tag{4.63}$$

where

$$\eta = \frac{q_0^2 T}{8\pi\lambda C_0}, \tag{4.64}$$

with $q_0 = \pi/R_{W1}$, $\lambda^2 = R_{W1}^2(1 + 2f - 2f^2)/45$, $f = R_1/R_{W1}$ and $C_0 = 6\varepsilon_C$, where ε_C is the average Coulomb energy density in the slab-cell [229]. More recently, the calculations of elastic constants were improved by [231]. We limit ourselves in this paper to temperatures high enough for the hypothesis of uncorrelated scatterers to be realistic. To this aim, we plot in the center and right parts of Fig. 23 the quantity $2^{-\eta}$ as an estimation of the ratio between the correlation function at $z = 2R_{W1}$, corresponding to a distance containing two different slabs, and the same quantity at $z = R_{W1}$, such that a single slab is accounted for, i.e.

$$2^{-\eta} \approx \frac{\delta n^2(2R_{W1})}{\delta n^2(R_{W1})}. \tag{4.65}$$

Even if these distances might be small to justify the use of the asymptotic behavior given by eq. (4.62), the quantity $2^{-\eta}$ can be taken as an estimation of the correlation reduction due to thermal effects. The numerical values of the η parameter itself are displayed in the left part of Fig. 23 for different temperatures as a function of the baryonic density. These results are numerically obtained from the pasta configuration predicted by the RMF model described in Section 2. As expected, the correlation decreases with temperature and density. We can see

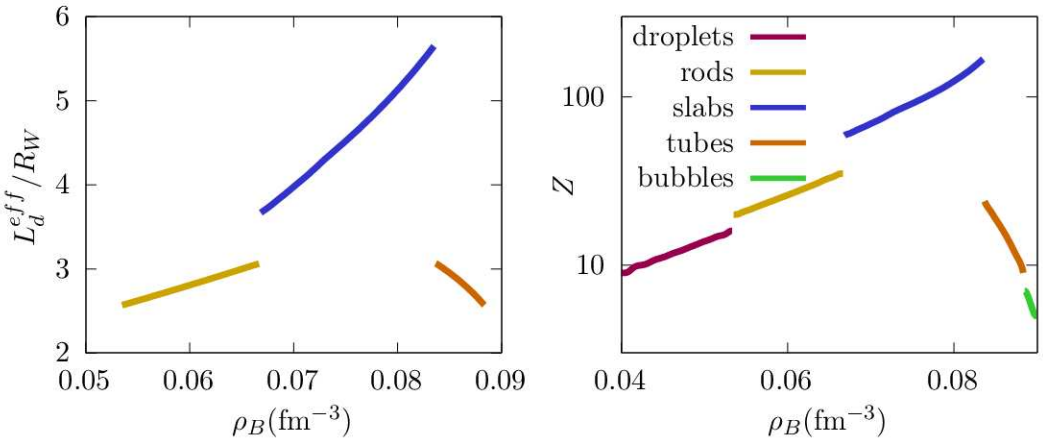

Figure 25: Left: Effective length of the pasta transverse to the symmetry axis, normalized to the Wigner-Seitz radius. Right: Proton number of the pasta as a function of density. The different pasta geometries are indicated with different colors. The temperature is fixed to $T = 3$ MeV.

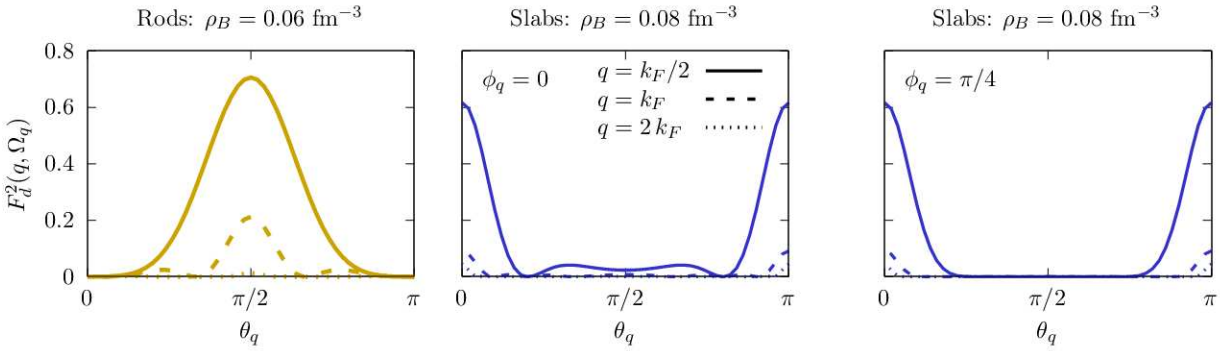

Figure 26: Squared form factor for rods at the representative density $\rho_B = 0.06$ fm^{-3} (left, yellow) and slabs at $\rho_B = 0.08$ fm^{-3} (middle and right, blue) as a function of the azimuthal angle, for different transferred momenta $q = k_F/2$, k_F and $2k_F$ shown as continuous, dashed and dotted curves, respectively. For slabs we fix $\phi_q = 0$ (middle) and $\pi/4$ (right). The effective lengths L are taken from Figure 25. The temperature is fixed as $T = 3$ MeV.

that only at very high temperatures – above 1 MeV – the hypothesis of incoherent scattering appears justified. For the following numerical applications, we will focus on $T = 1$ and 3 MeV as a representative temperature value. The proton fraction is now constrained by β-equilibrium ($\mu_p = \mu_n - \mu_e$), and it is shown in Fig. 24.

Since the correlation (4.63) asymptotically follows the same power law in the transverse and in the longitudinal plane, we define the effective length of the slab L_1 from the same order-of-magnitude consideration:

$$\frac{\delta n^2(L_1^{eff})}{\delta n^2(L_{W1})} \approx 2^{-\eta} \tag{4.66}$$

where L_{W1} is defined by normalizing the slab WS volume to the droplet volume at identical

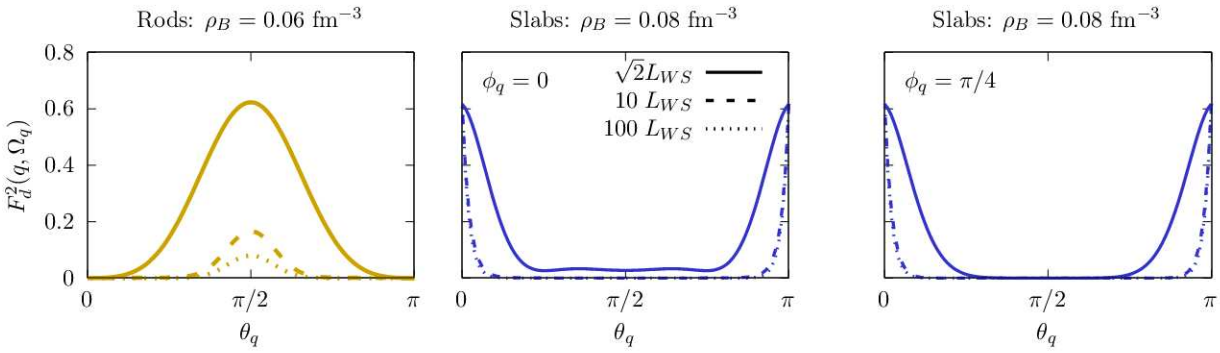

Figure 27: Squared form factor for rods at the representative density $\rho_B = 0.06$ fm^{-3} (left, yellow) and slabs at $\rho_B = 0.08$ fm^{-3} (middle and right, blue) at $q = k_F/2$ as a function of the azimuthal angle, for different pasta lengths momenta $L = \sqrt{2}, 10, 100\ L_{\rm WS}$ shown as continuous, dashed and dotted curves, respectively. For slabs we fix $\phi_q = 0$ (middle) and $\pi/4$ (right). The temperature is fixed to $T = 3$ MeV.

thermodynamic conditions, as done in the MCP calculation of Section 3. Comparing eqs (4.65) and (4.66), we consider that the effective length of the slabs is

$$L_1^{eff} = \sqrt{2} L_{1W}. \tag{4.67}$$

For the rods, in the absence of an analogous calculation of $S(\boldsymbol{q})$, we assume the length of interest to be equal to the slabs one if they were dominant at the same density

$$L_2^{eff} = L_1^{eff}. \tag{4.68}$$

The resulting numerical values of the pasta length and proton number at $T = 3$ MeV are shown in Fig. 25. Due to the fiducial nature of our length estimation, we will still discuss how our results are sensitive to the pasta size.

The relation between the size probed by a particle and the momentum are inverse, therefore low momentum interactions probe the pasta as a whole, whereas higher momentum would probe the excitations of its constituents [221]. Since we account for the pasta as a whole through the form factor, we expect them to be larger at lower q and lower at higher q. Indeed, in figs. 26 we show the structure factors of rods and slabs calculated at different q as a function of the azimuthal angle θ_q, and we confirm that, while the shape of the form factor is the same for different q, its absolute value diminishes as q increases. The same is true if we fix q and increase the size of the pasta: as the length increases the form factor becomes more concentrated at lower q, as shown in Fig. 27. Additionally, the form factors are peaked in the elongated direction of the pasta: at $\theta_q = \pi/2$ for the rods and $\theta_q = 0$ and π for the slabs.

4.3 Isotropic case

In the isotropic case the matrix element $W_{pp'}$ is a function of the absolute value of $\boldsymbol{q}$ or, equivalently, of the angle between the electron initial and final momentum $\cos\xi = \hat{\boldsymbol{p}} \cdot \hat{\boldsymbol{p}'}$, therefore we can make an expansion in Legendre polynomials

$$W_{pp'}(q) = \sum_l w_l P_l(\cos\xi) = \frac{4\pi}{2l+1} \sum_l \sum_{m=-l}^{l} w_l \, Y_l^m(\Omega_p) Y_l^{m*}(\Omega_{p'}), \tag{4.69}$$

then we substitute eq. (4.69) and the expansion of the variation of the distribution function, eq. (4.21) into the collision integral, eq. (4.35), such that

$$\begin{aligned} I[f] &= 2\pi \int \frac{d^3\boldsymbol{p}'}{(2\pi)^3} \delta(\epsilon_p - \epsilon_{p'}) W_{pp'} \left[\delta f(\boldsymbol{p}') - \delta f(\boldsymbol{p})\right], \\ &= -\frac{p^2}{4\pi^2 v} \sum_{lm\,LM} \frac{4\pi}{2L+1} w_L \, \delta f_{lm} \int d\Omega_{p'} Y_L^M(\Omega_p) Y_L^{M*}(\Omega_{p'}) \left[Y_l^m(\Omega_p) - Y_l^m(\Omega_{p'})\right], \end{aligned} \tag{4.70}$$

where we have used that

$$\int d\,p\; p^2\, \delta(\epsilon_p - \epsilon_{p'}) = \int \frac{d\epsilon_p\; p^2}{|dv_p/dp|}\, \delta(\epsilon_p - \epsilon_{p'}) = \frac{p^2}{v}. \tag{4.71}$$

By using the orthogonality property of spherical harmonics

$$\int d\Omega\, Y_l^m(\Omega) Y_{l'}^{m'*}(\Omega) = \delta_{ll'}\delta_{mm'} \tag{4.72}$$

and noticing that

$$\int d\Omega\, Y_l^m(\Omega) = \sqrt{4\pi} \int d\Omega\, Y_l^m(\Omega) Y_0^{0*}(\Omega) = \sqrt{4\pi}\delta_{l0}\delta_{m0} \tag{4.73}$$

the collision integral is simplified to

$$I[f] = -\frac{p^2}{4\pi^2 v} \sum_{lm} 4\pi\, \delta f_{lm} Y_l^m(\Omega_p) \left[w_0 - \frac{w_l}{2l+1}\right]. \tag{4.74}$$

From this expression, we are able to define the isotropic collision time, defined in eq. (4.20), to be

$$\nu_l = \frac{p^2}{\pi} \left[w_0 - \frac{w_l}{2l+1}\right]. \tag{4.75}$$

By inverting the matrix element expansion (4.69)

$$w_l = \frac{2l+1}{2}\int_{-1}^{1} d\cos\xi \; W_{pp'} \; P_l\left(\cos\xi\right), \tag{4.76}$$

we get the well-known result

$$\nu_l = \frac{p^2}{2\pi v}\int_{-1}^{1} d\cos\xi W_{pp'}\left[1 - P_l\left(\cos\xi\right)\right], \tag{4.77}$$

which can also be found in eq. 3.135 of [211].

To get the result commonly used in the literature of transport [32, 46–48] we make a change of variable using $q^2 = 2p^2(1-\cos\xi)$:

$$\int_{-1}^{1} d\cos\xi = \int_{0}^{2p_F} \frac{q^2 d\,q}{p^2} \tag{4.78}$$

such that for $l = 1$ we have

$$\begin{aligned}\nu_{l=1} &= \frac{1}{4\pi p^2 v}\int_0^{2p_F} q^3 dq\, W_{pp'} \\ &= \frac{4\pi e^4 Z^2}{p^2 v}\int_0^{2p_F}\frac{dq}{q}\left(1-\frac{q^2}{4\,\epsilon_p^2}\right)\frac{F^2(q)}{\varepsilon^2(q)}S(q).\end{aligned} \tag{4.79}$$

which is exactly eq. (4.22) if evaluated at the Fermi energy. Likewise, for $l = 2$

$$\begin{aligned}\nu_{l=2} &= \frac{3}{4\pi p^2 v}\int_0^{2p_F} q^3 dq\left(1-\frac{q^2}{4p^2}\right) W_{pp'} \\ &= \frac{12\pi e^4 Z^2}{p^2 v}\int_0^{2p_F}\frac{dq}{q}\left(1-\frac{q^2}{4\,\epsilon_p^2}\right)\left(1-\frac{q^2}{4p^2}\right)\frac{F^2(q)}{\varepsilon^2(q)}S(q)\end{aligned} \tag{4.80}$$

which can also be confirmed by eqs. (2) and (3) of [51].

4.4 Anisotropic collision rates

Now we turn to the calculation of the pasta collision rates by generalizing the isotropic calculation shown in 4.3. We will show that the pasta is described by two collision rates, an axial (ν_a) and a perpendicular one (ν_p), and will derive analytical expressions for them. Our results are in agreement with the intuitive proposal of [33] to generalize the collision time

approximation (eq. (4.9)) to the pasta as

$$I[f] = -\mathbf{\Phi}_\perp \cdot \boldsymbol{v}_\perp \nu_p - \Phi_z v_z \nu_a \tag{4.81}$$

where $\boldsymbol{v}$ is the electron velocity and $\mathbf{\Phi}(\epsilon_p)$ is defined by $\delta f = \boldsymbol{v} \cdot \mathbf{\Phi}$. While in [33] the expression for the pasta conductivity was obtained using (4.81), the collision rates were treated as free parameters and no analytical expressions for them were derived.

To do so we will make use of the spherical harmonics expansion one more time. The collision integral expansion is now written as as [198]

$$I[f] = -\sum_{lm\, l'm'} \delta f_{lm}\left(\epsilon_p\right) \nu_{lm}^{l'm'} Y_{l'}^{m'}(\Omega_p), \tag{4.82}$$

differing from the isotropic case as now the multiplicities l and l' can be mixed and there is an explicit dependence on m and m'. The coefficients δf_{lm} are the ones defined in eq. (4.21)

To obtain analytical expressions for the collision rates we must use expansions of the variation of the distribution, eq. (4.21), and of the transition rate (4.30) in (4.35). However, the matrix element $W_{pp'}$ for electron-pasta scattering is a function of the vector $\boldsymbol{q}$, not of its absolute value $|\boldsymbol{q}|$, so the expansion in Legendre polynomials (4.69) of the isotropic case can no longer be used. To proceed we consider the transition rate to be a function of the solid angles of the incoming and outgoing electrons, $W_{pp'} = W_{p\,p'}\left(\Omega_p, \Omega_{p'}, \epsilon_p\right)$ such that its expansion in spherical harmonics is

$$W_{p\,p'}\left(\Omega_p, \Omega_{p'}, \epsilon_p\right) = \sum_{lm\, l'm'} \mathcal{W}_{lm\, l'm'}(\epsilon_p) Y_l^m(\Omega_p) Y_{l'}^{m'}(\Omega_{p'}). \tag{4.83}$$

This expansion does not assume the nature of the anisotropy, being valid for any scattering. Nevertheless, the pasta geometric symmetries and the assumption of elastic collision will simplify our calculation later by constraining the coefficients $\mathcal{W}_{lm\, l'm'}$: in the $xy-$plane rods are invariant under arbitrary rotations $\phi \longrightarrow \phi + \delta\phi$ and slabs under $\pi/2$ rotations: $\phi \longrightarrow \phi' = \phi + \pi/2$. Imposing these symmetries to the matrix element, a constraint on the sum $m + m'$ can be applied. In the z-axis both are invariant under reflections in the $z-$axis, $\theta \longrightarrow \pi - \theta$, such that $l + l'$ is

constrained. The constraints due to the pasta symmetry in the coefficients $\mathcal{W}_{lm\,l'm'}$ are

$$\text{Rods}\begin{cases} l+l'=2k \\ m+m'=0 \end{cases} \qquad \text{Slabs}\begin{cases} l+l'=2k \\ m+m'=4k' \end{cases} \tag{4.84}$$

with $k, k' \in \mathbb{Z}$. Furthermore, elasticity implies that $\boldsymbol{p}$ and $\boldsymbol{p}'$ are interchangeable, such that

$$W_{pp'} = W_{p'p} \implies \mathcal{W}_{lm\,l'm'} = \mathcal{W}_{l'm'\,lm}. \tag{4.85}$$

Now we can substitute eqs. (4.21) and (4.83) into eq. (4.35) such that'

$$\begin{aligned} I[f] &= 2\pi \int \frac{d^3\boldsymbol{p}'}{(2\pi)^3}\delta(\epsilon_p - \epsilon_{p'})W_{pp'}\left[\delta f(\boldsymbol{p}') - \delta f(\boldsymbol{p})\right], \\ &= -\frac{p^2}{4\pi^2}\sum_{lm\,LM\,ab}\mathcal{W}_{LM\,ab}\,\delta f_{lm}\int d\Omega_{p'}Y_L^M(\Omega_p)Y_a^b(\Omega_{p'})\left[Y_l^m(\Omega_p) - Y_l^m(\Omega_{p'})\right] \\ &= -\frac{p^2}{4\pi^2}\sum_{lm\,LM\,ab}\mathcal{W}_{LM\,ab}\,\delta f_{lm}Y_L^M(\Omega_p)\left[\sqrt{4\pi}\delta_{a0}\delta_{b0}Y_l^m(\Omega_p) - (-1)^m\delta_{al}\delta_{bm}\right] \\ &= -\frac{p^2}{4\pi^2}\sum_{lm\,LM}\delta f_{lm}Y_L^M(\Omega_p)\left[\sqrt{4\pi}\mathcal{W}_{LM\,00}Y_l^m(\Omega_p) - (-1)^m\mathcal{W}_{LM\,l-m}\right], \end{aligned} \tag{4.86}$$

where from the second to third line we used that $Y_l^{m*}(\Omega) = (-1)^m Y_l^{-m}(\Omega)$, the orthogonality of spherical harmonics (4.72), and simplified the p integral with the δ function using eq. (4.71). From the third to the fourth line, we simplified the Kronecker-δs with the summations. In the first term inside brackets we have a product of spherical harmonics of equal arguments, so we use the contraction property

$$\begin{aligned} Y_l^m(\Omega)Y_L^M(\Omega) = \sum_{l'm'}(-1)^{m'}\sqrt{\frac{(2l+1)(2L+1)(2l'+1)}{4\pi}} \\ \begin{pmatrix} l & l' & L \\ 0 & 0 & 0 \end{pmatrix}\times\begin{pmatrix} l & l' & L \\ m & -m' & M \end{pmatrix}Y_a^b(\Omega) \end{aligned} \tag{4.87}$$

to write it in terms of a unique one. Here, $\begin{pmatrix} l_1 & l_2 & l_3 \\ m_1 & m_2 & l_3 \end{pmatrix}$ are the 3-j Wigner symbols, which are not zero only if $m_1 + m_2 + m_3 = 0$, $|l_1 - l_2| < l_3 < l_1 + l_2$ and the sum $l_1 + l_2 + l_3$ is an integer.

They also obey the symmetry property

$$\begin{pmatrix} l_1 & l_2 & l_3 \\ m_1 & m_2 & m_3 \end{pmatrix} = \begin{pmatrix} l_2 & l_3 & l_1 \\ m_2 & m_3 & m_1 \end{pmatrix} = \begin{pmatrix} l_3 & l_1 & l_2 \\ m_3 & m_1 & m_2 \end{pmatrix}, \tag{4.88}$$

and their values can be read off tables or calculated via their connection to Clebsch–Gordan coefficients $\langle l_1 m_1, l_2 m_2 | l_3 - m_3 \rangle$ [232, 233]

$$\begin{pmatrix} l_1 & l_2 & l_3 \\ m_1 & m_2 & m_3 \end{pmatrix} = \frac{(-1)^{l_1 - l_2 - m_3}}{\sqrt{2l_3 + 1}} \langle l_1 m_1, l_2 m_2 | l_3 - m_3 \rangle. \tag{4.89}$$

Using eq. (4.87) the collision integral (4.86) is written as

$$\begin{aligned} I[f] = -\frac{p^2}{4\pi^2} \sum_{lm\, LM} \delta f_{lm} \Bigg[\mathcal{W}_{LM\,00} \sum_{l'm'} (-1)^{m'} \sqrt{(2l+1)(2L+1)(2l'+1)} \\ \times \begin{pmatrix} l & l' & L \\ 0 & 0 & 0 \end{pmatrix} \begin{pmatrix} l & l' & L \\ m & -m' & M \end{pmatrix} Y_{l'}^{m'}(\Omega_p) - (-1)^m \mathcal{W}_{LM\,l-m} Y_L^M(\Omega_p) \Bigg]. \end{aligned} \tag{4.90}$$

Now we have a unique spherical harmonic and we are able to identify eqs. (4.82) and (4.90) with each other. We can obtain the collision rates either by renaming the dummy indices or by multiplying both equations by $Y_a^{b\,*}(\Omega_p)$ and integrating them in Ω_p, such that the orthogonality relation (4.72) can be used to write

$$\begin{aligned} \nu_{lm}^{l'm'} = \frac{p^2}{4\pi^2 v} \Bigg[(-1)^{m'} \sqrt{(2l+1)(2l'+1)} \sum_{LM} \mathcal{W}_{LM\,00} \sqrt{2L+1} \\ \times \begin{pmatrix} l & l' & L \\ 0 & 0 & 0 \end{pmatrix} \begin{pmatrix} L & l & l' \\ M & m & -m' \end{pmatrix} - (-1)^m \mathcal{W}_{l'm'\,l-m} \Bigg]. \end{aligned} \tag{4.91}$$

As a side note, we notice that a more compact form can be obtained for his expression by using the Wigner–Eckart theorem and the spherical harmonics representation of irreducible tensor operators of rank l [234, 235],

$$C_m^l = \sqrt{\frac{4\pi}{2l+1}} Y_{lm}(\Omega)\,, \tag{4.92}$$

such that eq. (4.91) becomes

$$\nu_{lm}^{l'm'} = \frac{p^2}{4\pi^2 v} \left[\sum_{LM} \mathcal{W}_{LM\,00} \sqrt{2L+1} \langle l'm' | C_M^L | lm \rangle - (-1)^m \mathcal{W}_{l'm'\,l-m} \right]. \tag{4.93}$$

To further progress, we restrict ourselves to the case of conductivities. Recall that, since only odd powers of momentum in a δf expansion will contribute to the currents (4.1), (4.2), meaning that only odd l terms in the expansion (4.21) contribute. The left-hand side of eq. (4.12) is linear in $\boldsymbol{p}$, implying that only the coefficient $l' = 1$ in eq. (4.82) contributes to the currents. Nevertheless mixing between the $l' = 1$ of the spherical harmonics and $l = 1, 3, 5...$ of δf_{lm} can occur. This is different from the isotropic case, where no mixing of multiplicities occurs and only δf_{1m} contributes to the conductivities. Nevertheless, these mixings are expected to be corrections, and to this first calculation, we neglect them and restrict ourselves to the most important contribution (see also [198]) by writing $\nu_{lm}^{l'm'} = \nu_{1m}^{1m'}\delta_{l1}\delta_{l'1}$ in eq. (4.82). Due to the symmetry rules in (4.84), this approximation is probably better justified in the case of pasta.

Since spherical harmonics are complex functions, so are the associated coefficients of the expansion, namely δf_{lm} and $\nu_{lm}^{l'm'}$. To obtain physical collision rates we must rewrite the expansions eqs. (4.21) and (4.82) in terms of real coefficients. To this goal, we define the real spherical harmonics

$$\mathcal{Y}_{lm} = \begin{cases} \dfrac{i}{\sqrt{2}}\left(Y_l^m - (-1)^m Y_l^{-m}\right) & m < 0 \\ Y_l^0 & m = 0 \\ \dfrac{1}{\sqrt{2}}\left(Y_l^{-m} + (-1)^m Y_l^m\right) & m > 0 \end{cases} \tag{4.94}$$

The $l = 1$ term of eq. (4.21) is now written as

$$\delta f(\boldsymbol{p})\Big|_{l=1} = \mathcal{Y}_{11}\delta f_x + \mathcal{Y}_{1-1}\delta f_y + \mathcal{Y}_{10}\delta f_z \tag{4.95}$$

where the real (physical) coefficients are

$$\delta f_x = \frac{\delta f_{1-1} - \delta f_{11}}{\sqrt{2}}, \quad \delta f_y = \frac{\delta f_{1-1} + \delta f_{11}}{\sqrt{2}i}, \quad \delta f_z = \delta f_{10}, \tag{4.96}$$

and substituting eqs. (4.94) and (4.96) in the collision integral expansion, eq. (4.82), we get

$$I[f] = \begin{pmatrix} \mathcal{Y}_{11} & \mathcal{Y}_{1-1} & \mathcal{Y}_{10} \end{pmatrix} \begin{pmatrix} \nu_{xx} & \nu_{xy} & \nu_{xz} \\ \nu_{yx} & \nu_{yy} & \nu_{yz} \\ \nu_{zx} & \nu_{zy} & \nu_{zz} \end{pmatrix} \begin{pmatrix} \delta f_x \\ \delta f_y \\ \delta f_z \end{pmatrix} \tag{4.97}$$

with the physical collision rates $\hat{\boldsymbol{\nu}}$ given by:

$$\hat{\boldsymbol{\nu}} = \begin{pmatrix} \frac{1}{2}\left(\nu_{11}^{11} + \nu_{1-1}^{1-1} - \nu_{11}^{1-1} - \nu_{1-1}^{11}\right) & \frac{i}{2}\left(\nu_{11}^{11} - \nu_{1-1}^{1-1} + \nu_{11}^{1-1} - \nu_{1-1}^{11}\right) & \frac{1}{\sqrt{2}}\left(\nu_{1-1}^{10} - \nu_{11}^{10}\right) \\ \frac{i}{2}\left(-\nu_{11}^{11} + \nu_{1-1}^{1-1} + \nu_{11}^{1-1} + \nu_{1-1}^{11}\right) & \frac{i}{2}\left(\nu_{11}^{11} + \nu_{1-1}^{1-1} + \nu_{11}^{1-1} + \nu_{1-1}^{11}\right) & \frac{i}{\sqrt{2}}\left(\nu_{1-1}^{10} + \nu_{11}^{10}\right) \\ \frac{1}{\sqrt{2}}\left(\nu_{10}^{1-1} - \nu_{10}^{11}\right) & \frac{-i}{\sqrt{2}}\left(\nu_{10}^{11} + \nu_{10}^{1-1}\right) & \nu_{10}^{10} \end{pmatrix} \tag{4.98}$$

The constraint of elasticity in the coefficients $\mathcal{W}_{lm\,l'm'}$ given in eq. (4.85) can be expressed in the complex collision frequencies as $\nu_{1m}^{1m'} = (-1)^{m+m'}\nu_{1-m'}^{1-m}$, making them matrix $\hat{\boldsymbol{\nu}}$ symmetric: $\nu_{ij} = \nu_{ji}$. Additionally, the pasta symmetries given in eq. (4.84) imply

$$\begin{aligned} \nu_{1-1}^{11} = \nu_{11}^{1-1} = \nu_{10}^{1\pm1} = \nu_{1\pm1}^{10} = 0 \quad &\Rightarrow \quad \nu_{xy} = \nu_{xz} = \nu_{yz} = 0 \\ \nu_{11}^{11} = \nu_{1-1}^{1-1} \quad &\Rightarrow \quad \nu_{xx} = \nu_{yy}. \end{aligned} \tag{4.99}$$

That is, off-diagonal terms vanish and the collision rates perpendicular to the symmetry axis, xx and yy, are equal [3], so our collision rate matrix is

$$\hat{\boldsymbol{\nu}} = \begin{pmatrix} \nu_{xx} & \nu_{xy} & \nu_{xz} \\ \nu_{yx} & \nu_{yy} & \nu_{yz} \\ \nu_{zx} & \nu_{zy} & \nu_{zz} \end{pmatrix} = \begin{pmatrix} \nu_p & 0 & 0 \\ 0 & \nu_p & 0 \\ 0 & 0 & \nu_a \end{pmatrix} \tag{4.100}$$

Whereas we have finally obtained the axial and perpendicular collision rates, which can be calculated from eq. (4.91) using the symmetries of the 3j-Wigner symbols to be

$$\nu_a(\epsilon_p) = \nu_{10}^{10} = \frac{p^2}{4\pi^2 v}\left[\mathcal{W}_{00,00} - \mathcal{W}_{10,10} + \frac{1}{\sqrt{5}}\left(W_{20,00} + \mathcal{W}_{00,20}\right)\right] \tag{4.101}$$

and

$$\nu_p(\epsilon_p) = \nu_{11}^{11} = \frac{p^2}{4\pi^2 v}\left[\mathcal{W}_{00,00} - \frac{1}{2\sqrt{5}}\left(\mathcal{W}_{20,00} + \mathcal{W}_{00,20}\right) + \frac{1}{2}\left(\mathcal{W}_{11,1-1} + \mathcal{W}_{1-1,11}\right)\right]. \tag{4.102}$$

To be certain that this is equivalent to the collision rates proposed in [33] we write, without any loss of generality, $\delta f_k = \sqrt{4\pi/3}\Phi_k(\epsilon_p)|\boldsymbol{v}|$, $k = x, y, z$, which is equivalent to

$$\delta f|_{l=1} = \boldsymbol{v} \cdot \boldsymbol{\Phi}, \tag{4.103}$$

[3] In the case of slabs this is valid only because $L_{1x} = L_{1y} = L_1$

such that the $l' = l = 1$ term of the collision integral expansion, eq. (4.82), can be rewritten as

$$I[f] = -v_z \Phi_z \nu_a - \boldsymbol{v}_p \cdot \boldsymbol{\Phi}_p \nu_p, \tag{4.104}$$

which is exactly Eq. (8) of [33].

To write the collision rates in terms of eq. (4.30) we invert the expansion of eq. (4.83)

$$\mathcal{W}_{lm\,l'm'} = \int d\Omega_p d\Omega_{p'} W_{pp'} Y_l^{m*}(\Omega_p) Y_{l'}^{m'*}(\Omega_{p'}), \tag{4.105}$$

such that

$$\nu_a\left(\epsilon_p\right) = \frac{3}{32\pi^3 v} \int d\Omega_p d\Omega_{p'} W_{pp'}\, q^2\, \cos^2\theta_q \tag{4.106}$$

$$\nu_p\left(\epsilon_p\right) = \frac{3}{32\pi^3 v} \int d\Omega_p d\Omega_{p'}\, W_{pp'}\, q^2 \frac{1}{2} \sin^2\theta_q .. \tag{4.107}$$

These expressions could apply to any elastic collision with cylindrical or planar symmetry, not necessarily the electron–pasta we are dealing with. To write this in a form that can be compared with the isotropic eq. (4.22) we make a change of variable

$$\int d\Omega_p d\Omega'_p = \frac{2\pi}{p^2} \int \frac{d^3\boldsymbol{q}}{q}\,, \tag{4.108}$$

and we use eq. (4.30) to write the anisotropic collision rates as:

$$\nu_a\left(\epsilon_p\right) = \frac{12\pi\rho_i e^4 Z^2}{v p^2} \int_0^{2p} \frac{dq}{q} \frac{1}{\varepsilon^2(q)} \left(1 - \frac{q^2}{4\epsilon_p^2}\right) \int \frac{d\Omega_q}{4\pi} |F_d(\boldsymbol{q})|^2 \cos^2\theta_q \tag{4.109}$$

$$\nu_p\left(\epsilon_p\right) = \frac{12\pi\rho_i e^4 Z^2}{v p^2} \int_0^{2p} \frac{dq}{q} \frac{1}{\varepsilon^2(q)} \left(1 - \frac{q^2}{4\epsilon_p^2}\right) \int \frac{d\Omega_q}{4\pi} |F_d(\boldsymbol{q})|^2 \frac{1}{2} \sin^2\theta_q\,. \tag{4.110}$$

Comparing these to the isotropic collision frequency, eq. (4.22), we notice the difference to be the presence of a multiplicative factor of 3 in both expressions and an angular average in Ω_q, which weights the form factors by $\cos\theta_q$ and $\sin^2\theta_q/2$ in the axial and perpendicular components, respectively. These equations are the main results we have obtained.

Following the spirit of calculations in the isotropic regime we write the collision rates

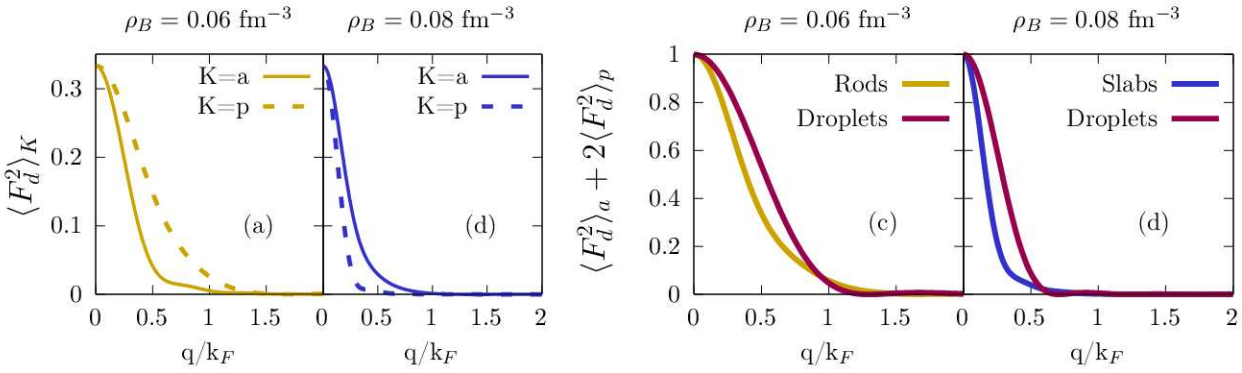

Figure 28: Left panels (a,b): axial (full) and perpendicular (dashed) squared form factor of rods (yellow) and slabs (blue) at $\rho_B = 0.06$ (a) and 0.08 (b) fm^{-3}. Right panels (c,d): average squared form factors of rods (yellow, c panel) and slabs (blue, d panel) are compared to the ones of droplets (magenta) at the same density. The representative temperature T=3 MeV is chosen.

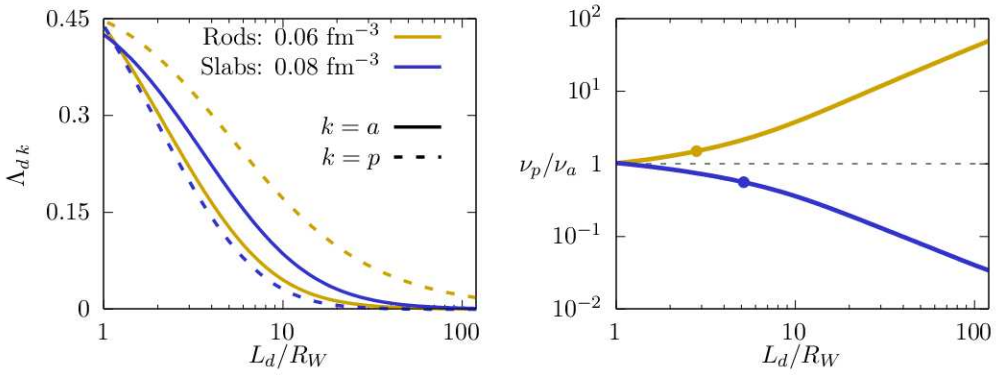

Figure 29: The Coulomb logarithms (left) and the ratio of perpendicular to axial collision frequency (right) are shown as a function of the pasta length normalized to the Wigner-Seitz radius, L_d/R_W. Quantities for rods (slabs) are calculated at $\rho_B = 0.06$ fm^{-3} ($\rho_B = 0.08$ fm^{-3}) and plotted in yellow (blue). In the upper panel, the perpendicular (axial) component are displayed as dashed (continuous) lines. The points in the lower plot indicate the estimated effective length $L_1^{eff} = \sqrt{2}\, L_{1W}$ (see text). The representative temperature $T = 3$ MeV is chosen.

in terms of adimensional functions named Coulomb logarithms

$$\nu_k = \frac{12\pi\rho_i e^4 Z^2}{v p^2}\Lambda_{d,k} \tag{4.111}$$

with

$$\Lambda_{d,k} = \int_0^{2p_F} \frac{dq}{q}\frac{1}{\varepsilon^2(q)}\left(1-\frac{q^2}{4\epsilon_F^2}\right)\langle F_d^2(q)\rangle_k \tag{4.112}$$

for which we defined the weighted averages

$$\langle F_d^2(q)\rangle_a = \int \frac{d\Omega_q}{4\pi}|F_d(\boldsymbol{q})|^2\cos^2\theta_q, \tag{4.113}$$

$$\langle F_d^2(q)\rangle_p = \int \frac{d\Omega_q}{4\pi}|F_d(\boldsymbol{q})|^2\frac{1}{2}\sin^2\theta_q \tag{4.114}$$

$$\tag{4.115}$$

that are shown in (a) and (b) of Fig. 28 with $L_d^{\rm eff} = \sqrt{2}L_{1\,WS}$. For the rods the perpendicular average is larger than the axial one, as expected intuitively from its geometry. The opposite is true for the slab. In panels (c) and (d) of the same figure we show the angular averaged form factor

$$\langle F_d^2(q)\rangle_a + 2\langle F_d^2(q)\rangle_p = \int \frac{d\Omega_q}{4\pi}|F_d(\boldsymbol{q})|^2 \tag{4.116}$$

of rods and slabs compared to the form factor of the droplet, with its radius calculated at the same density as the pasta. The difference is essentially at low q, where the average form factor of the pasta is smaller than the one of spherical droplets.

To evaluate the effect of the uncertainty on the estimation of L_d, in Fig. 29 we show the axial and perpendicular Coulomb logarithms eq.(4.112) and the ratio of perpendicular to axial collision frequency eq.(4.111) as a function of the ratio of the pasta length L_d to the WS-radius R_{Wd} for rods and slabs. For rods (slabs), the perpendicular component of the Coulomb logarithm is larger (smaller) than the axial one, and the difference between them increases with the growing length of the pasta, varying up to 100 (0.01) when $L_d \approx 150\ R_W$. This shows that a precise estimation of the length of the structures is important for the quantitative determination of the collision frequencies, as it affects in a considerable way the difference between the two scattering directions. In particular, the deviation from an isotropic scattering is small only for small values of L_d/R_W, corresponding to the high-temperature regime. At smaller temperatures, as correlations become more important, a larger transverse length will contribute

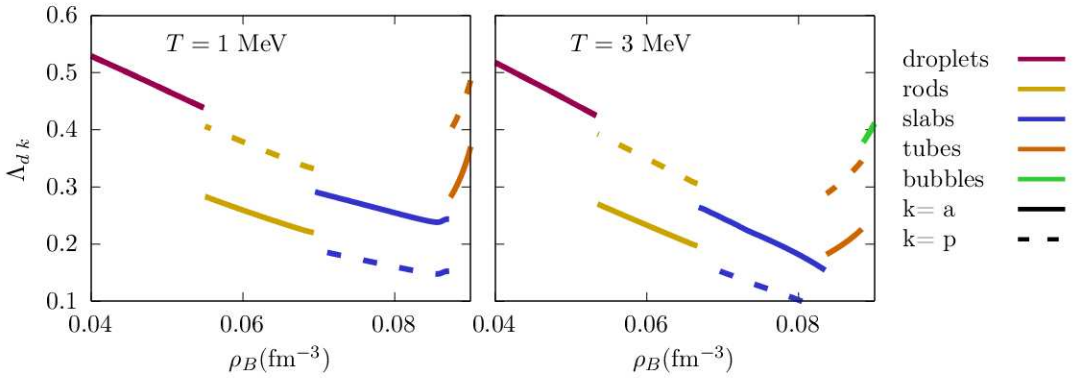

Figure 30: Axial (continuous) and perpendicular (dashed) Coulomb logarithms as a function of baryon density, for $T = 1$ MeV (left panel) and $T = 3$ MeV (right panel). The different pasta geometries are indicated with different colours.

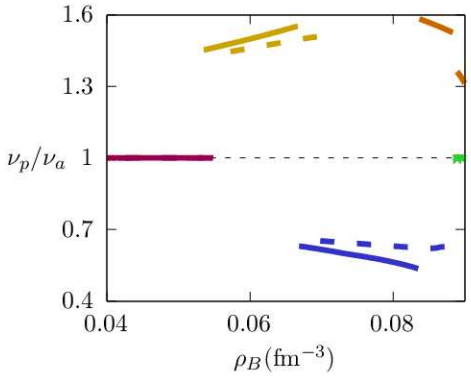

Figure 31: Top: ratio of perpendicular to axial relaxation time. Bottom: Average electric conductivity. Curves are shown as a function of density for the representative temperatures of $T = 1$ (dashed) and 3 (continuous) MeV. The different pasta geometries are indicated with different colours.

to the scattering, and the difference in the anisotropic frequencies will be more pronounced, likely reaching those expected in [33].

In Fig. 30 the Coulomb logarithms, eqs. (4.112) are shown as a function of the density for T=1 and 3 MeV. In both cases, we can see that the abrupt change of favored geometry leads to slight discontinuities in the Coulomb logarithms, and both overall decrease with density. This can be understood from the increase in length, shown in Fig. 25, and from Fig. 29. The ratio of perpendicular to axial collision frequency – eqs (4.111) is shown in Fig. 31 for the same temperatures. The slight increase in the ratio with density is due to the increasing length. It is important to note that, at the temperatures and lengths we are considering, the different collision frequencies differ by a factor smaller than two, so there is only a small deviation from isotropic scattering at high temperatures.

4.5 Pasta conductivity

Now we turn to connect our calculation of the pasta collision rates to the conductivities by calculating the electron distribution function variation δf, which amounts to finding $\mathbf{\Phi}$. This calculation was first made in [33], and we reproduce it in detail. We assume an external magnetic field lying on the xz-plane $\boldsymbol{B} = B\,(\cos\theta_b \hat{\boldsymbol{x}} + \sin\theta_b \hat{\boldsymbol{z}})$ and a weak electric field $\boldsymbol{E}$ such that $\boldsymbol{F} = -e(\boldsymbol{E} + \boldsymbol{v} \times \boldsymbol{B})$, and can start our discussion from eqs. (4.12) and (4.81)

$$\left(-\frac{\partial f_0}{\partial \epsilon_p}\right) \boldsymbol{v} \cdot \left[\frac{\partial \mu}{\partial \boldsymbol{x}} + e\boldsymbol{E} + \frac{\epsilon_p - \mu}{T}\frac{\partial T}{\partial \boldsymbol{x}}\right] - e(\boldsymbol{v} \times \boldsymbol{B}) \cdot \frac{\partial \delta f}{\partial \boldsymbol{p}} = -v_z \Phi_z \nu_a - \boldsymbol{v}_p \cdot \mathbf{\Phi}_p \nu_p, \tag{4.117}$$

For simplicity, we define the electron gyrofrequency $\omega = eB/\epsilon_p$, the unity vector $\boldsymbol{b}$ that points in the direction of the magnetic field $\boldsymbol{b} = \boldsymbol{B}/B$ and the vector

$$\boldsymbol{F} = \left(-\frac{\partial f_0}{\partial \epsilon_p}\right) \left[\frac{\partial \mu}{\partial \boldsymbol{x}} + e\boldsymbol{E} + \frac{\epsilon_p - \mu}{T}\frac{\partial T}{\partial \boldsymbol{x}}\right]. \tag{4.118}$$

Note that, by substituting $\delta f \approx \delta f|_{l=1} = \mathbf{\Phi} \cdot \boldsymbol{v}$ in eq. (4.117), our problem amounts to determining the vector $\mathbf{\Phi}$ and application of linear algebra techniques become straightforward. Using the relations above and writing the derivative in the term with magnetic field as $\partial \delta f/\partial \boldsymbol{p} = \mathbf{\Phi}/\epsilon_p$, eq. (4.117) can be written as

$$\boldsymbol{v} \cdot \boldsymbol{F} - \omega \mathbf{\Phi} \cdot (\boldsymbol{v} \times \boldsymbol{b}) = -v_z \Phi_z \nu_a - \boldsymbol{v}_p \cdot \mathbf{\Phi}_p \nu_p, \tag{4.119}$$

Using $\mathbf{\Phi} \cdot (\boldsymbol{v} \times \boldsymbol{b}) = \boldsymbol{v} \cdot (\boldsymbol{b} \times \mathbf{\Phi})$ and $I[f] = \boldsymbol{v} \cdot \hat{\nu} \cdot \mathbf{\Phi}$ we are able to completely factorize the vector $\boldsymbol{v}$

$$\boldsymbol{v} \cdot \boldsymbol{F} = \boldsymbol{v} \cdot \Big[\hat{\boldsymbol{\nu}} \cdot \mathbf{\Phi} + \omega b \times \mathbf{\Phi})\Big], \tag{4.120}$$

and now we can write this equation in matrix form as

$$\boldsymbol{F} = \hat{\mathbf{\Pi}} \mathbf{\Phi} \tag{4.121}$$

where

$$\hat{\mathbf{\Pi}} = \begin{pmatrix} -\nu_p & -\omega b_z & 0 \\ \omega b_z & -\nu_p & -\omega b_x \\ 0 & \omega b_x & -\nu_a \end{pmatrix}, \tag{4.122}$$

and the task of determining Φ amounts to finding the inverse of $\hat{\mathbf{\Pi}}$ such that

$$\mathbf{\Phi} = \hat{\mathbf{\Pi}}^{-1} \boldsymbol{F}. \tag{4.123}$$

We can confirm that the matrix is indeed invertible by assuring the determinant is not zero:

$$\Delta = -\det \hat{\mathbf{\Pi}} = \nu_p^2 \nu_a + \omega^2 b_x^2 \nu_p + \omega^2 b_z^2 \nu_a \neq 0 \tag{4.124}$$

and to find the solution we need the adjoint of the $\hat{\mathbf{\Pi}}$ matrix, $\hat{\mathbf{\Pi}}^*$, since the inverse can be written as [236]

$$\hat{\mathbf{\Pi}}^{-1} = -\frac{1}{\Delta} \hat{\mathbf{\Pi}}^* \tag{4.125}$$

which can be readily obtained by calculating the minors of $\hat{\mathbf{\Pi}}$. The result is

$$\hat{\mathbf{\Pi}}^* = \begin{pmatrix} \nu_a \nu_p + \omega^2 b_x^2 & -\omega b_z \nu_a & \omega^2 b_x b_z \\ \omega b_z \nu_a & \nu_a \nu_p & -\omega b_x \nu_p \\ \omega^2 b_x b_z & \omega b_x \nu_p & \nu_p^2 + \omega^2 b_z^2 \end{pmatrix}. \tag{4.126}$$

To calculate the conductivity we can take $\partial_{\boldsymbol{x}} T = 0$, such that, from eq. (4.1)

$$J_{e\,i} = -e^2 \int \frac{d^3\boldsymbol{p}}{(2\pi)^3} v_i v_j \left(-\frac{\partial f_0}{\partial \epsilon_p}\right) \left(-\frac{1}{\Delta} \Pi^*_{jk}\right) E^*_k, \tag{4.127}$$

which leads to

$$J_{e\,i} = \frac{e^2}{3\pi^2 \Delta} \int_0^\infty d\epsilon p^2 v \left(-\frac{\partial f_0}{\partial \epsilon_p}\right) \Pi^*_{ij} E^*_j. \tag{4.128}$$

The use of eqs. (4.16) and of the Sommerfeld expansion, eq. (4.17), which in our case implies

$$J_{e\,i} = \frac{e^2 p_F^2 v_F}{3\pi^2 \Delta} \Pi^*_{ij}\,(\epsilon_F)\, E^*_j. \tag{4.129}$$

leads to the expression for the electric conductivity via the linear response definition (4.4):

$$\sigma_{ij} = \frac{e^2 p_F^3}{3\pi^2 m_e^* \Delta} \Pi^*_{ij} = \frac{e^2 n_e}{m_e^* \Delta} \Pi^*_{ij}, \tag{4.130}$$

where we use $m_e^* = \epsilon_F$ since this is a more standard notation in the literature when natural units

are not used ($m_e^* = \epsilon_F/c^2$). In the limit of $B \to 0$ we get

$$\sigma_{ij} = \frac{e^2 n_e}{m_e^*} \begin{pmatrix} \nu_p^{-1} & 0 & 0 \\ 0 & \nu_p^{-1} & 0 \\ 0 & 0 & \nu_a^{-1} \end{pmatrix}, \tag{4.131}$$

that is, we get a perpendicular and an axial conductivity, given by

$$\sigma_{0p} = \frac{e^2 n_e}{m_e^* \nu_p}, \qquad \sigma_{0a} = \frac{e^2 n_e}{m_e^* \nu_a}. \tag{4.132}$$

The thermal conductiviy can be found using the Wiedemann-Franz law

$$\hat{\boldsymbol{\kappa}} = \frac{\pi^2 k_B^2 T}{3e^2} \hat{\boldsymbol{\sigma}}. \tag{4.133}$$

The behavior of both conductivities is identical as a function of pasta length and density, thus it would be interesting to study the thermal conductivity as a function of temperature. Nevertheless, our high-temperature limit is very restrictive, so we restrain ourselves to analyzing only the electric conductivity.

Though we have provided a complete formalism to the calculation of the conduction, the collision rates depend on the proton number as Z^2 and Z depends on the pasta length as $\propto L_2$ ($\propto L_1^2$) for rods (slabs). Therefore, even though we have fixed the effective scattering length as $L_d = \sqrt{2} L_{1\,WS}$, there is a very large uncertainty associated with this choice. The dependence of $\langle \sigma_0 \rangle$ with the choice of L is shown on the left-hand side of Fig. 32, where we see a variation of four orders of magnitude. On the right-hand side, however, we show the average conductivity as a function of density using the effective lengths eq. (4.67). In the high-temperature regime assumed here, there is a discontinuity when the abrupt change of geometry happens. Even though the collision rates are not dramatically different from the isotropic one, this discontinuity can be attributed to the discontinuity in the proton number, since the discontinuities in the Coulomb logarithms are not as pronounced – see fig. 30. The anomalously high resistivity of the pasta layer reported in the literature [40] is nicely reproduced by our calculations, and it is seen to be essentially due to the high Z value of the clusters close to the crust-core transition, more than to the specific geometry of the pasta phases.

We now turn to the effect of the magnetic field on the conductivities. When including the

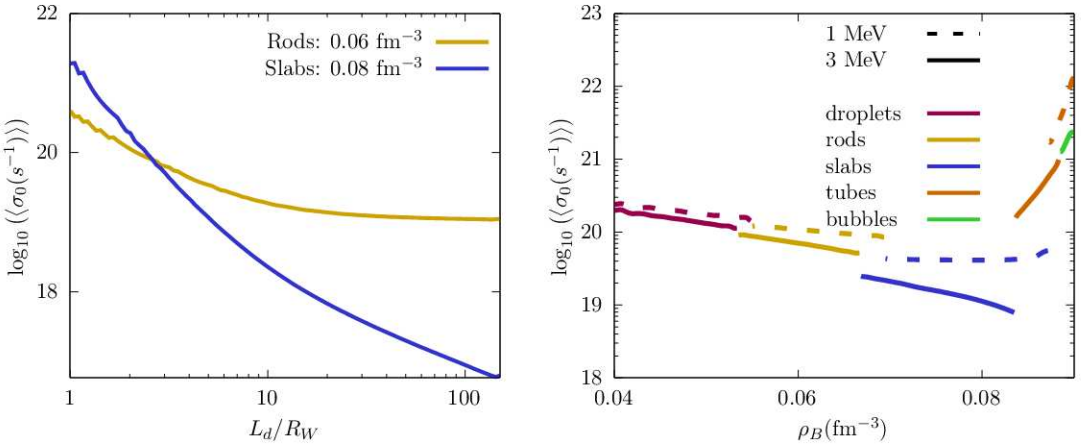

Figure 32: Average electric conductivity is shown as a function of pasta size (left) and of density (right). The right panel shows two representative temperatures of $T = 1$ (dashed) and 3 (continuous) MeV. The different pasta geometries are indicated with different colors.

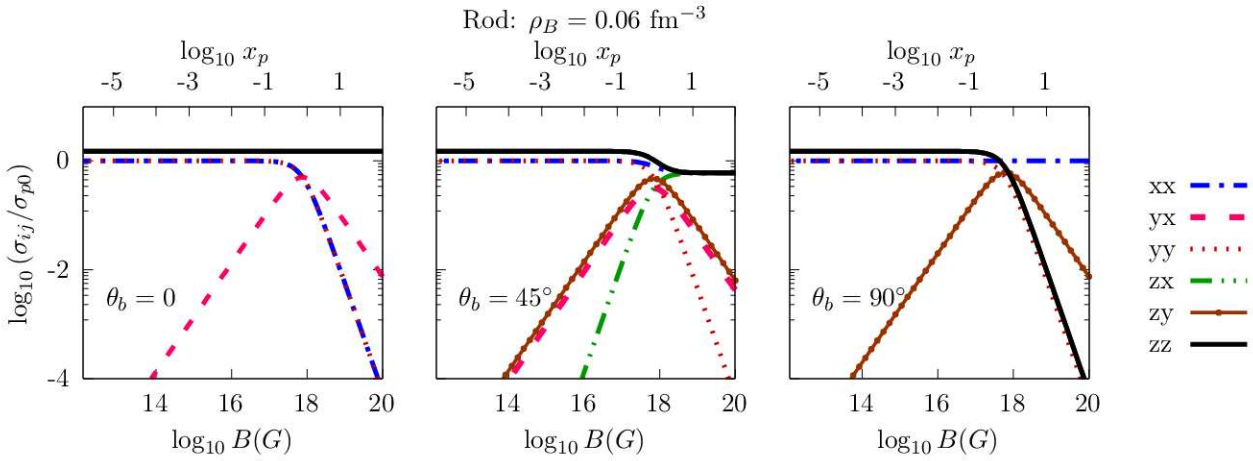

Figure 33: Components of the electric conductivity in units of the perpendicular conductivity at $B = 0$, as a function of the magnetic field for rods at $\rho_B = 0.06$ fm^{-3}. The angle between the pasta symmetry axis and the magnetic field is fixed at 0 (left), 45º (center) and 90º (right). In the top axis, we show the variable $x_p = eB/(\epsilon_F \nu_p)$.

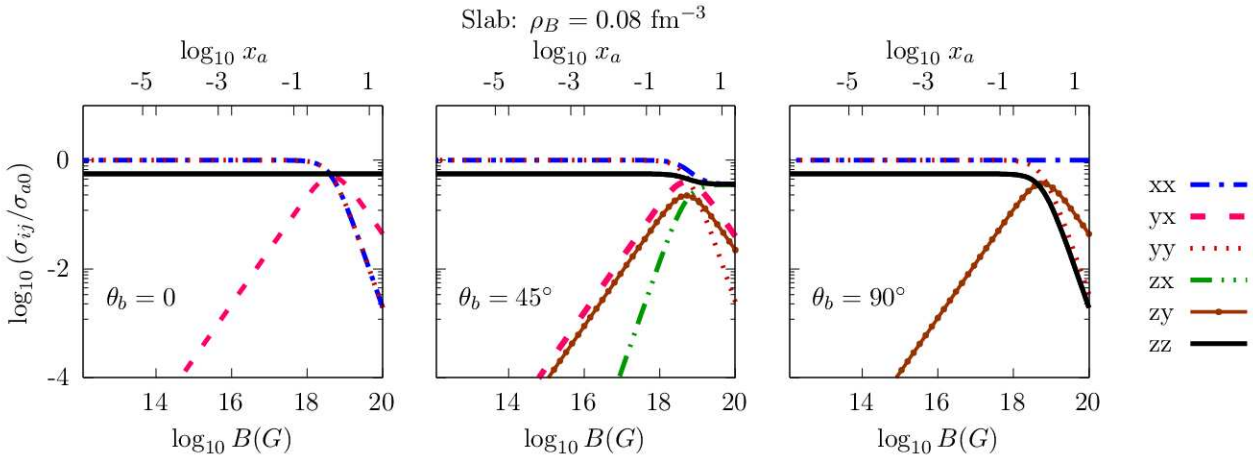

Figure 34: Components of the electron conductivity in units of the axial conductivity at $B = 0$, as a function of the magnetic field for slabs at $\rho_B = 0.08$ fm^{-3}. The angle between the pasta symmetry axis and the magnetic field is fixed at 0 (left), 45º (center) and 90º (right). In the top axis, we show the variable $x_a = \omega/\nu_a$.

magnetic field, we show all components of the conductivity in units of the dominant conductivity at zero magnetic field, i.e. the perpendicular (axial) conductivity for rods (slabs). In Figs. 33 (34) we show the conductivity components when the magnetic field forms an angle $\theta_b = 0, 45º$, and 90º with the symmetry axis of the pasta. Different off-diagonal components appear depending on the angle of the magnetic field: if it lies on the symmetry axis of the pasta, only the perpendicular xy component is not zero, the zz component depends only on ν_a, and the perpendicular xx and yy components are determined by both ν_p and $\boldsymbol{B}$. If it lies perpendicularly to the symmetry axis, only zy is not zero, the zz component is determined by ν_a and $\boldsymbol{B}$ and $xx = yy$ only by ν_p. At magnetic fields $B < 10^{18}$ G, the difference between components parallel and perpendicular to the magnetic field are due to the pasta length, with transverse components smaller (larger) for rods (slabs), meanwhile off-diagonal terms increase steadily with the magnetic field. At $\sim 10^{18}$ G, the components parallel to the magnetic field are unaffected, but the perpendicular and off-diagonal ones start to decrease. A magnetic field of this order is not far from the one expected at the very bottom of the inner crust of magnetars, which is about 20% of the field in the core [237, 238].

For the average conductivity, we follow [33] once more, and assume the pasta takes random orientations with respect to the magnetic field since up to date there is no information regarding its orientation or prevalence of domains. To calculate the average parallel, perpendicular, and Hall terms we define a plane orthogonal to the magnetic field with the vectors $\boldsymbol{e}_1$, $\boldsymbol{e}_2 = \boldsymbol{e}_1 \times \boldsymbol{b}$ (i.e. $\boldsymbol{e}_1 \cdot \boldsymbol{b} = \boldsymbol{e}_2 \cdot \boldsymbol{b} = 0$) and make the projections: $\sigma_\perp = \boldsymbol{b} \cdot \hat{\sigma} \cdot \boldsymbol{b}$, $\sigma_\parallel = \boldsymbol{e}_1 \cdot \hat{\sigma} \cdot \boldsymbol{e}_1$

and $\sigma_H = \boldsymbol{e}_1 \cdot \hat{\sigma} \cdot \boldsymbol{e}_2$, such that

$$\begin{pmatrix} \sigma_\perp \\ \sigma_\parallel \\ \sigma_H \end{pmatrix} = \frac{e^2 n_e}{m_e^* \Delta} \begin{pmatrix} \nu_p \nu_a b_x^2 + \nu_p^2 b_z^2 + \omega^2 \\ \nu_a \nu_p (e_{1x}^2 + e_{1y}^2) + \nu_p^2 e_{1z}^2 \\ \omega(\nu_a b_z^2 + \nu_p b_x^2) - e_{1z} e_{1y} b_x (\nu_p^2 - \nu_a \nu_p) \end{pmatrix} \tag{4.134}$$

and we can average the coefficients over all possible directions of the magnetic field, which is equivalent to assuming random pasta directions with a constant magnetic field. Making the average

$$\langle \sigma_x \rangle = \frac{1}{4\pi} \int d\cos\theta_b d\phi_b \sigma_x \tag{4.135}$$

leads to the average perpendicular, parallel, and Hall conductivities

$$\begin{pmatrix} \langle \sigma_\perp \rangle \\ \langle \sigma_\parallel \rangle \\ \langle \sigma_H \rangle \end{pmatrix} = \frac{e^2 n_e}{m_e^* \omega^2} \begin{pmatrix} (\omega^2 + \nu_p \nu_a)(\nu_p^2 + \omega^2) H - \nu_p \\ \frac{1}{2}[\nu_a \nu_p (\omega^2 - \nu_p^2) H + \nu_p] \\ \omega(1 - \nu_a \nu_p H) \end{pmatrix} \text{ with } H = \begin{cases} (sr)^{-1} \arctan(s/r) & \nu_a > \nu_p \\ (sr)^{-1} \operatorname{arctanh}(s/r) & \nu_a < \nu_p \\ (\nu_a^3 + \omega^2 \nu_a)^{-1} & \nu_a = \nu_p \end{cases} \tag{4.136}$$

$s = \omega\sqrt{|\nu_a - \nu_p|}$ and $r = \sqrt{\nu_p(\omega^2 + \nu_a \nu_p)}$. For $B \to 0$ we get

$$\langle \sigma_\perp \rangle = \langle \sigma_\parallel \rangle = \frac{e^2 n_e}{m_e^*} \langle \nu^{-1} \rangle, \quad \langle \nu^{-1} \rangle = \frac{1}{3} \left(\frac{2}{\nu_p} + \frac{1}{\nu_a} \right) \tag{4.137}$$

and the Hall parameters is zero $\langle \sigma_H \rangle \to 0$. One must notice that the average conductivity is proportional to the average of the inverse of $\langle \nu \rangle$, and not $\langle \nu \rangle$ itself, therefore its calculation does not amount to averaging the matrix element over Ω_q. In Fig. 35 we show the average conductivities for rods and slabs, respectively, in units of the average conductivity with $B = 0$. To conclude this discussion, it is important to note that for all the calculations reported in this thesis, the inner crust structure was computed without accounting for the magnetic field. Numerous studies exist in the literature addressing this point, using CLD or Thomas-Fermi techniques with different nuclear models, see e.g. [239–242]. The general result of these works is that only extreme magnetic fields of the order of $B = 10^{18}$ G affect the density profiles of the Wigner-Seitz cells, with an increased average proton fraction, particularly in the outer part of the inner crust dominated by spherical nuclei, and an increase of the charge of the pasta structures, that however does not exceed $\approx 10 - 20\%$. These modifications would not affect the results presented in Figs. 34 and 35, and would lead to an extra decrease of the conductivity

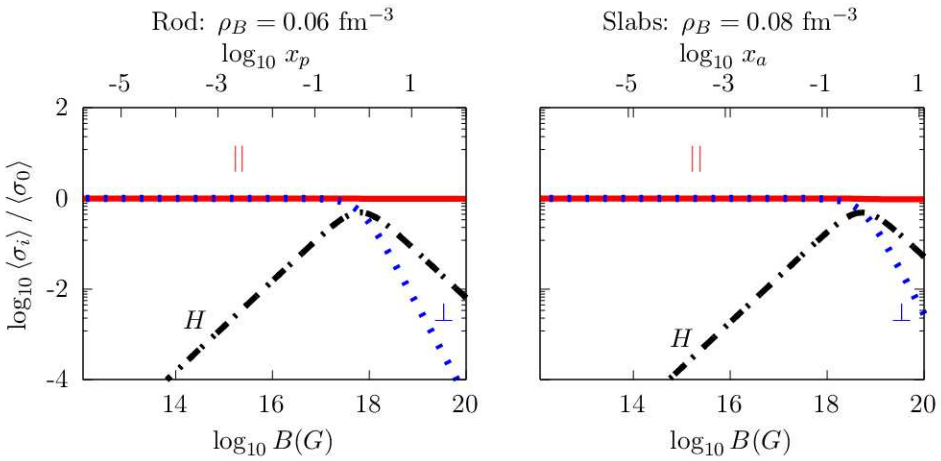

Figure 35: Average parallel, perpendicular and Hall conductivities for randomly oriented rods (left) and slabs (right) at $\rho_B = 0.06$ fm^{-3} and $\rho_B = 0.08$ fm^{-3}, respectively. In the top axis, we show the variable $x_i = \omega/\nu_i$, with $i = p$ (a) on the left (right).

in Fig. 32, since $\sigma \propto Z^{-2}$, see eq.(4.111). This calculation has been accepted for publication in the Monthly Notices of the Royal Astronomical Society [243].

The calculation presented here to calculate the anisotropic collision frequencies is novel, to the best of our knowledge. Our calculation can be made more realistic if a better estimate of the pasta lengths $L_{1,2}$ and the inclusion of density correlations due to thermal fluctuations is made. Moreover, we expect to use this method to calculate the pasta viscosity, related to $l' = 2$ in eq. (4.82), and to analyze the size of corrections due to the mixing of multiplicities in Eq. (4.82).

5 Digression: related work

In this section, we briefly discuss other works I have either published or submitted during the period of my doctorate but which did not fit the main scope of the thesis.

5.1 Effect of short-range correlations in nuclear pasta

In this section, we examine how short-range nucleon correlations can impact the appearance of the nuclear pasta. Pairs of nucleons are strongly correlated in nuclei, leading to a high momentum tail in the single nucleon distributions that decays as k^{-4}. Such short-range correlations (SRCs) can modify many of the nuclear properties [244–248]. To construct an equation of state with SRC included, the Lagrangian density is still given by Eq. (2.2), but with the Fermi-Dirac distribution (2.33) replaced by a new momentum distribution function, namely,

$$f_{n,p}(k) = \begin{cases} \Delta_{n,p}, & 0 < k < k_{F\,n,p} \\ \dfrac{C_{n,p}\, k_{F\,n,p}^4}{k^4}, & k_{F\,n,p} < k < \phi_{n,p} k_{F\,n,p}, \end{cases} \tag{5.1}$$

with $\Delta_{n,p} = 1 - 3C_{n,p}(1 - 1/\phi_{n,p})$, $C_p = C_0[1 - C_1(1 - 2Y_p)]$, $C_n = C_0[1 + C_1(1 - 2Y_p)]$, $\phi_p = \phi_0[1 - \phi_1(1 - 2Y_p)]$ and $\phi_n = \phi_0[1 + \phi_1(1 - 2Y_p)]$. The values of the constants $C_{0,1}$, $\phi_{0,1}$ we use are $C_0 = 0.161$, $C_1 = -0.25$, $\phi_0 = 2.38$ and $\phi_1 = -0.56$. All these numbers were extracted from Ref. [244]. The idea is that the SRCs reduce the Fermi-Dirac step function up to k_F, which is done by the multiplicative factor $\Delta_q < 1$, and a high-momentum tail $\propto k^{-4}$ is added between k_F and $\phi_q k_F > k_F$, for the density to be kept constant. The modifications introduced in the momentum distribution function then affect all thermodynamic quantities of the system, namely the scalar densities (2.32), chemical potentials of protons and neutrons, the energy (2.37), and the pressure (2.38).

When SRCs are included, the Lagrangian parametrization changes. The new parametrization is obtained by imposing that it reproduces the same bulk parameters of their versions without SRC, namely, saturation density (ρ_0), binding energy, effective mass, incompressibility, symmetry energy, and symmetry energy slope, all of them evaluated at ρ_0, as shown in Tab. 3. In Tab. 7 we show the IUFSU-SRC parametrization, which reproduces the IUFSU parameters. While the original parametrizations might have been constructed to correctly describe some features of

	IUFSU-SRC
m_s (MeV)	491.5
m_v (MeV)	782.5
m_b (MeV)	763.0
g_s	10.132
g_v	11.867
g_b	15.551
κ	5.9113
λ	-179.28
ξ	0.03
Λ	0.0055
$\rho_{\rm sat}$ (fm^{-3})	0.155

Table 7: Parametrization that reproduces the IUFSU bulk properties when accounting for SRCs.

finite nuclei such as the neutron skin thickness, as in the case of the IUFSU, for instance, these are not taken into account when obtaining the SRC parametrization.

In Figs. 36 we show the chemical potentials and pressure of the IUFSU parametrization with and without short-range correlations. The effect of SRCs is much more prominent in asymmetric matter, which leads to a smaller (larger) proton (neutron) chemical potential. In Fig.

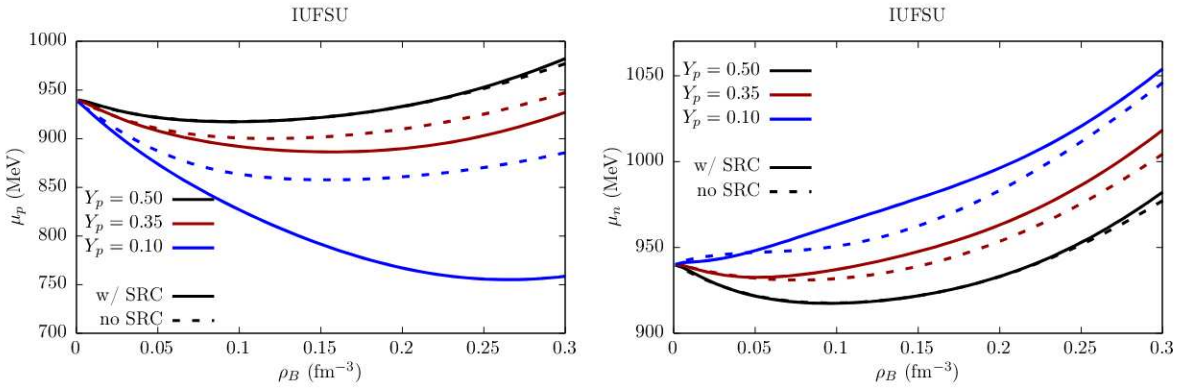

Figure 36: Chemical potential of protons (left) and neutrons (right)for homogeneous matter with the IUFSU parametrization for different proton fractions, both without (dashed curves) and with (full curves) short range correlations.

37 we also show how the pressure behaves as a function of the density. The differences at very low densities, the region important in the present study, are shown in the inset, corroborating the statement that very asymmetric matter feels the effect of SRC more strongly.

In Figs. 38 our results are shown for the pasta, respectively without (left) and with (right) SRC. We use the same surface tension of the IUFSU from [115]. As a consequence of the already observed differences in homogeneous matter, the larger the asymmetry, the stronger the

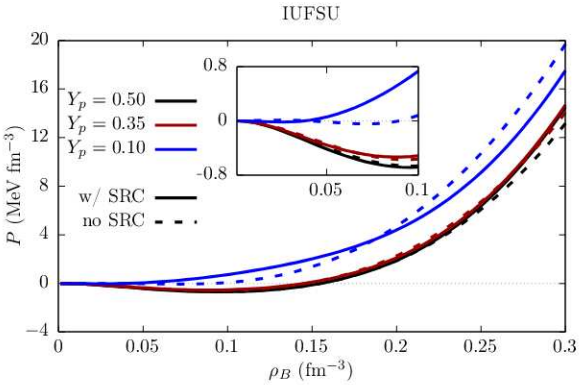

Figure 37: Pressure of homogeneous baryon matter for different proton fractions with IUFSU without (dashed curves) and with (full curves) short range correlations for different proton fractions.

effects of the SRC. For symmetric matter, the results are very similar, both as far as the size of the pasta phase as well as its internal structure. For $Y_p = 0.35$, the similarities disappear: not only the pasta phase shrinks when SRC are included, but one of its internal structure, the tubes, vanishes. When we analyze $Y_p = 0.1$, the most important result for the NS inner crust, the pasta phase diminishes even more and spherical nuclei survive. We have further used the NL3 [176] and FSU2R [119] parametrizations to test the model dependence of our results, but they were the same: the pasta disappears at low proton fractions.

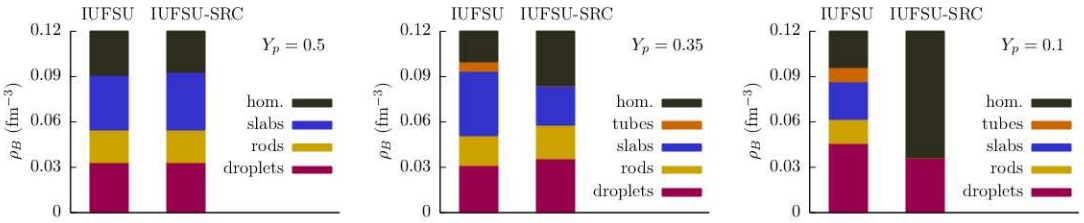

Figure 38: Baryon densities where each pasta geometry is dominant for the IUFSU (left) and IUFSU-SRC (right) for proton fractions Y_p =0.5, 0.35 and 0.1 (left, center and right, respectively).

Even though the bulk parameters are kept fixed at saturation point in the models with and without SRC, at different densities they can be completely different. Thus, the disappearance of the pasta is likely related to the change in the symmetry energy and its slope at low densities, as depicted in Fig. 39. Nevertheless, more robust calculations in which the surface tension can be self-consistently calculated, as explained in [61, 115], must be carried out when the SRC are included. A manuscript containing these results [249] is currently under review in Physical Review C.

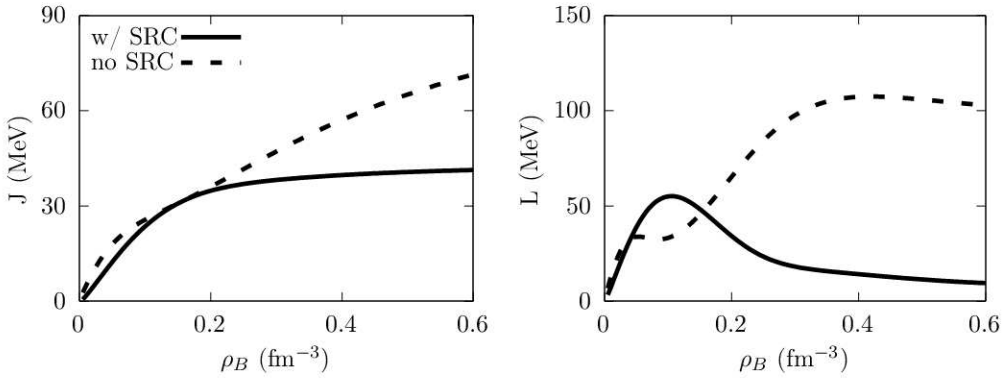

Figure 39: Symmetry energy (left) and symmetry energy slope (right) for the IUFSU with (full) and without (dashed) SRCs.

5.2 Delta baryons in magnetars

In this section, we examine the role of Δ baryons in magnetars and the impact of anomalous magnetic moments (AMMs) and strong magnetic fields in particle densities. Δ baryons are nucleon excitations with spin 3/2, and they are expected to appear in the core of NSs, along baryons of spin 1/2 containing strange quarks, the hyperons [250, 251]. The high magnetic field of a NS modifies the particle content of the core, and, in consequence, its macroscopic properties. Accounting for the particles AMMs can further modify the particle populations, specially for the Δ baryons due to their extra isospin projections ($I_\Delta = 3/2, 1/2, -1/2, -3/2$) and the electric charge of the Δ^{++}. The AMM (κ_b) is a deviation from the magnetic moment of that particle, as predicted by the "classical" tree-level calculation. Historically, the term *anomalous* was used to describe the deviation from the Dirac equation prediction for a system of fermions under the influence of a magnetic field, the magnetic moment, and thus, refers to fundamental particles. *Dipole* moment, on the other hand, is used for composite particles, such as baryons, since their value depends on the configuration of quarks and gluons inside it, and thus, are not *anomalous* in the strict sense. As commonly used in the literature and for simplicity, we use the term AMM in all cases. The AMM coefficients κ_b are related to the magnetic moments μ_b through the relation

$$\kappa_b = \mu_b - e_b \mu_N \frac{M_p}{M_b} \,. \tag{5.2}$$

The AMMs of nucleons are measured to a very high precision, with errors of the order of 10^{-9} [252, 253], but the same does not apply to heavier baryons. Measurements of the hyperon AMMs are precise to an order of 10^{-2} [254], while Δs are experimentally determined only for the positively charged Δ^{++} and Δ^{+}. For the Δ^{+}, there is a single measurement of $\mu_{\Delta^+}/\mu_N =$

Table 8: Vacuum mass, electric charge, isospin 3[rd] component, spin, normalized magnetic moment, and normalized anomalous magnetic moment of baryons considered in this work. Electric charge is shown in units of the electron charge and μ_N is the nuclear magneton.

	M_b (MeV)	$e_b(e)$	$I_{3\,b}$	S_b	μ_b/μ_N	κ_b/μ_N
p	939	+1	$+\frac{1}{2}$	1/2	2.79	1.79
n	939	0	$-\frac{1}{2}$	1/2	−1.91	−1.91
Λ	1116	0	0	1/2	−0.61	−0.61
Σ^+	1193	+1	+1	1/2	2.46	1.67
Σ^0	1193	0	0	1/2	1.61	1.61
Σ^-	1193	−1	−1	1/2	−1.16	−0.37
Ξ^0	1315	0	$+\frac{1}{2}$	1/2	−1.25	−1.25
Ξ^-	1315	−1	$-\frac{1}{2}$	1/2	−0.65	0.06
Δ^{++}	1232	+2	$+\frac{3}{2}$	3/2	4.99	3.47
Δ^+	1232	+1	$+\frac{1}{2}$	3/2	2.49	1.73
Δ^0	1232	0	$-\frac{1}{2}$	3/2	0.06	0.06
Δ^-	1232	−1	$-\frac{3}{2}$	3/2	−2.45	−1.69

$2.7^{+1.0}_{-1.3} \pm 1.5$ that comes from the $\gamma p \to p\pi\gamma'$ reaction [255], while for the Δ^{++} there are several measurements coming from the $\pi^+ p \to \pi^+ p\gamma$ bremsstrahlung cross section, with values in the range $\mu_{\Delta^{++}}/\mu_N = 3.7 - 7.5$ [254]. These measurements include systematic uncertainties, but additional theoretical uncertainties lead to errors $\approx \pm 3$. Complementary to experimental results, lattice quantum chromodynamics (LQCD) has been able to extract AMM values for Δ baryons. The values utilized in this paper are based on the predictions from LQCD provided in [256] that lie within the experimental uncertainties of the experimentally measured AMMs. Although the expression (5.2) is derived for spin-1/2 fermions in the non-relativistic regime, it is still commonly employed in the description of the Δ baryonsç [257, 258]. This subject is controversial, as the Rarita-Schwinger equation with minimal coupling predicts a gyromagnetic ratio of 2/3, while low energy/optical theorems predict a value of 2. For a more in-depth discussion, we refer to [259], which studies a generic non-minimal electromagnetic coupling in the Rarita-Schwinger formalism. In this work, we also account for the leptons (electron and muon) AMMs, given by $\kappa_e/\mu_{B_e} = 1.15965 \times 10^{-3}$ and $\kappa_\mu/\mu_{B_\mu} = 1.16592 \times 10^{-3}$, respectively, with $\mu_{B_l} = e/2M_l$, for $l = \{e,\mu\}$. Different properties of the baryons considered in this study are shown in Tab. 8.

To describe magnetized baryons with AMMs we add the hyperons and Δs to the Lagrangian by adding a sum over baryons $b = N, H, \Delta$ instead of the nucleon Lagrangian (2.3),

i.e.

$$\mathcal{L}_N \Longrightarrow \sum_b \mathcal{L}_b \tag{5.3}$$

with

$$\mathcal{L}_b = \bar{\psi}_b \left[\gamma^\mu \left(i\partial_\mu - \frac{1}{4}\kappa_b \sigma_{\mu\nu} F^{\mu\nu} \right) - \gamma^0 \left(g_{vb} V_0 + g_{\phi b}\phi_0 + g_{bb} I_{3b} b_0 \right) + g_{sb}\sigma_0 - M_b \right] \psi_b, \tag{5.4}$$

in the RMF, and $F_{\mu\nu} = \partial_\mu A_\nu - \partial_\nu A_\mu$, $\sigma^{\mu\nu} = \frac{i}{2}\left[\gamma^\mu, \gamma^\nu\right]$, and the vector potential $A_\mu = (0, 0, Bx, 0)$ is chosen such that the magnetic field is parallel to the z-axis. We additionally introduce the strange ϕ-meson that couples to hyperons. Since Δs are spin 3/2 particles, they are in fact described by the Rarita-Schwinger equation, but in the mean field approximation its Lagrangian can be written as if it were a spin 1/2 particle, thus the index b includes nucleons, hyperons and Δs [260]. A dynamic term to the photon field also has to be added

$$\mathcal{L}_{EM} = -\frac{1}{4} F^{\mu\nu} F_{\mu\nu}. \tag{5.5}$$

A solution to the equations of motion can be found by choosing a representation of the Dirac matrices [261, 262]. The main effect in the thermodynamic quantities is that the 3-momentum integrals are changed: while the z-component is still integrated as a continuum, in the plane perpendicular to the magnetic field the momentum integral turns to a summation in discrete Landau levels ν [263],

$$\int d^3\boldsymbol{k} \rightarrow \frac{|e_b B|}{2\pi} \sum_\nu \int_{-\infty}^{\infty} \frac{dk_z}{2\pi} \tag{5.6}$$

which are given by

$$\nu = n + \frac{1}{2} - \frac{s}{2}\frac{e_b}{|e_b|}\,, \tag{5.7}$$

with n = 0,1,2.... For particles with spin 1/2, the first Landau level ($\nu = 0$) is occupied by a single spin projection: $s = +1$ for $q_b > 0$ and $s = -1$ for $q_b < 0$. The second level ($\nu = 1$) and above are occupied by both spin projections $s = \{\pm 1\}$. For the spin-3/2 positively charged Δs, the first level ($\nu = 0$) is occupied by the spin projections s= $\{+3, +1\}$, the second level ($\nu = 1$) by $s = \{+3, \pm 1\}$, and hereafter all spin states are occupied. For the negatively charged Δ^- spin projection, signs are reversed for the lowest levels. At zero temperature, there is a maximum Landau level

$$\nu_{\max b}(s) = \left\lfloor \frac{\left(E^*_{F\,b} + s\kappa_b B\right)^2 - M^{*2}_b}{2|e_b|B} \right\rfloor . \tag{5.8}$$

where the Fermi energy is

$$E^*_{F\,b} = \mu_b - g_{vb}\omega_0 - g_{bb}I_{3b}\rho_0 - g_{\phi b}\phi_0\,, \tag{5.9}$$

The maximum Landau level is determined by the point where the Fermi momentum is zero. The Fermi momentum squared is given by

$$k^2_{F\,b} = \begin{cases} {E^*_{F\,b}}^2 - \left(M^*_b - s\kappa_b B\right)^2 & e_b = 0 \\ {E^*_{F\,b}}^2 - \left(\sqrt{M^{*2}_b + 2\nu|e_b|B} - s\kappa_b B\right)^2 & e_b \neq 0 \end{cases} \tag{5.10}$$

so for charged particles, it diminishes as ν increases. Furthermore, we assume particles are in β-equilibrium, so relation (2.46) is valid. With all this information, we can calculate particle densities, energy, and pressure from eqs. (2.31)(2.32) (2.37), (2.38).

Now we notice that the meson couplings g_{Mb} depend on the baryons b. It is usual to determine them from the ratio of the baryon-meson coupling to the nucleon-meson one

$$x_{Mb} = \frac{g_{Mb}}{g_{MN}}. \tag{5.11}$$

The scalar meson couplings are fitted to reproduce the hyperon potential depth $U_\Lambda = -28$ MeV for symmetric matter at saturation density, thus fixing the parameter α_s,

$$x_{s\Lambda} = \frac{10 + 6\alpha_s}{13 + 12\alpha_s}, \quad x_{s\Sigma} = \frac{22 - 6\alpha_s}{13 + 12\alpha_v}, \quad x_{s\Xi} = \frac{13 - 6\alpha_s}{13 + 12\alpha_v}. \tag{5.12}$$

The remaining relative strength of the coupling constants are determined by SU(3) symmetry group arguments, as proposed by [251], determining the complete hyperon-meson vector coupling scheme from a single free parameter, α_v. For the ω-meson

$$x_{v\Lambda} = \frac{4 + 2\alpha_v}{5 + 4\alpha_v}, \quad x_{v\Sigma} = \frac{8 - 2\alpha_v}{5 + 4\alpha_v}, \quad x_{v\Xi} = \frac{5 - 2\alpha_v}{5 + 4\alpha_v}, \tag{5.13}$$

for the ϕ-meson

$$x_{\phi\Lambda} = \sqrt{2}\left(\frac{2\alpha_v - 5}{5 + 4\alpha_v}\right), \quad x_{\phi\Sigma} = \sqrt{2}\left(\frac{-2\alpha_v - 1}{5 + 4\alpha_v}\right), \quad x_{\phi\Xi} = \sqrt{2}\left(\frac{-2\alpha_v - 4}{5 + 4\alpha_v}\right), \tag{5.14}$$

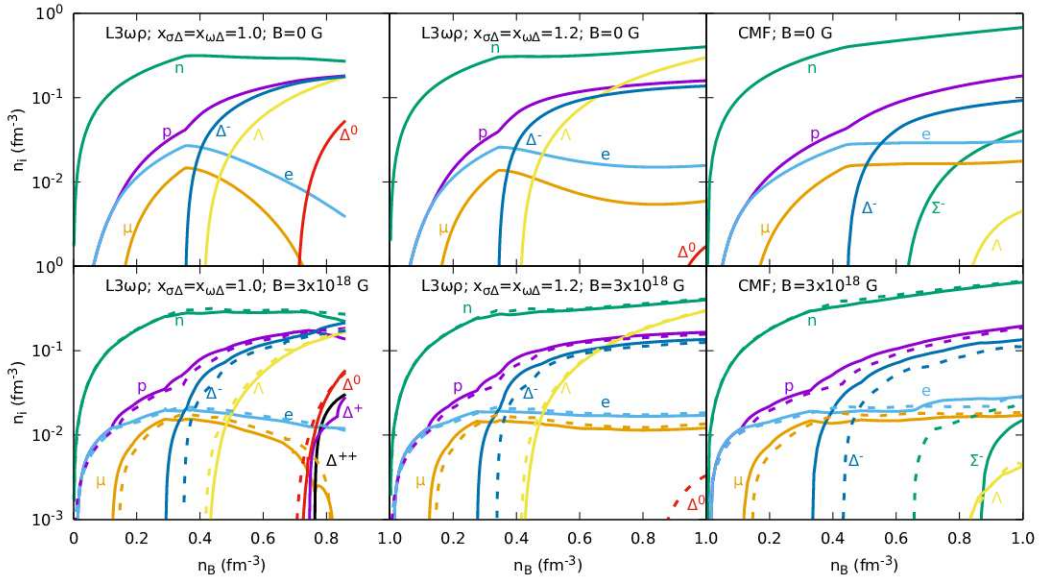

Figure 40: Particle composition of neutron-star matter with hyperons and Δs, with $B = 0$ (top panels) and magnetic field $B = 3 \times 10^{18}$ G (bottom panels), when considering (solid lines) or not (dashed lines) the effects of the anomalous magnetic moment. The left and middle panels show results for the L3$\omega\rho$ model with different interactions, while the right panel shows results for the CMF model.

and, finally, for the ρ-meson

$$x_{\rho\Lambda} = 0 \quad x_{\rho\Sigma} = \alpha_v, \quad x_{\rho\Xi} = -(1 - 2\alpha_v). \tag{5.15}$$

Despite the value of α_v, hyperons are always present in the neutron-star matter and the sequence of hyperon thresholds is always the same, with an inversely proportional relationship between α_v and the stiffness of the EoS. In this work, we choose to use $\alpha_v = 0.5$, which results in values for the additional potentials $U_\Sigma = +21.8$ MeV and $U_\Xi = +35.3$ MeV. Though the potential for the Ξ^-mesons is repulsive in the parametrization used, recent observational constraints predict it to be attractive [264–266], but to reproduce such an attractive potential we would need an extra free parameter in the meson couplings [175].

The Δ couplings are treated more freely, as their behavior is not well known. The scarce information present in the literature, such as transport models [267] and quasi-elastic scattering of electrons off nuclei [268], allows us to infer that the nucleon-Δ potential is slightly more attractive than the nucleon-nucleon one, so that, $U_N - 30\,\text{MeV} \lesssim U_\Delta \lesssim U_N$, which implies $x_{\sigma\Delta}$ is greater than 1. Also, the vector coupling is constrained by LQCD results as respecting the relation $0 \lesssim x_{\sigma\Delta} - x_{\omega\Delta} \lesssim 0.2$, and no constraint is put in the $x_{\rho\Delta}$ value [269–271]. Early

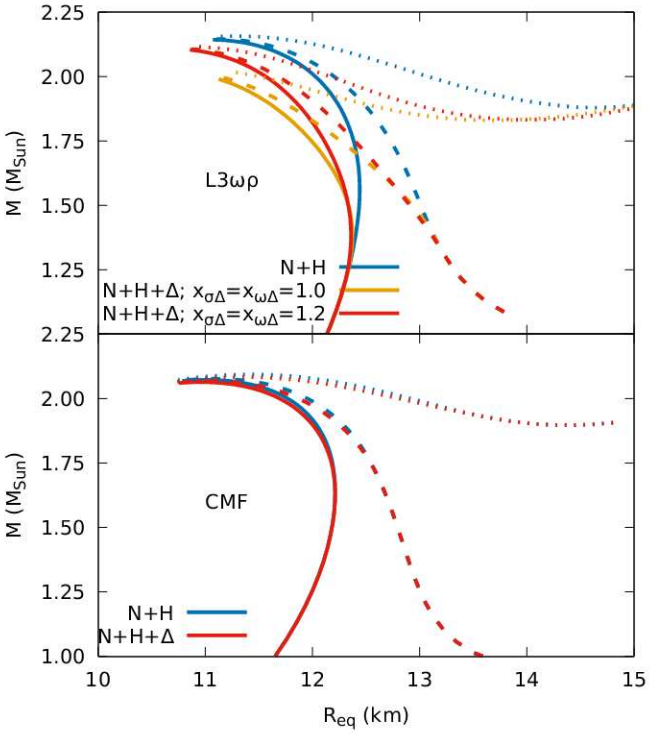

Figure 41: Stellar mass as a function of equatorial radius for different compositions and interaction strengths, for central magnetic fields $B = 0$ (solid lines), $B = 5 \times 10^{17}$ G (dashed lines), and $B = 10^{18}$ G (dotted lines). The top and bottom panels show results for the L3$\omega\rho$ and CMF models, respectively.

investigations on the effect of these parameters were made in [272, 273] and their role in the stellar particle composition and maximum-mass was studied considering $x_{\sigma\Delta} = 1.0$ and 1.1, within two classes of relativistic mean-field models in [274]. Following the previous study, we analyse the scenarios with $x_{\sigma\Delta} = x_{\omega\Delta} = 1.0$ and $x_{\sigma\Delta} = x_{\omega\Delta} = 1.2$, keeping $x_{\rho\Delta} = 1.0$, that generates, respectively, potentials $U_\Delta = -66.25$ MeV (equal to the nucleon potential) and -79.50 MeV. We also show results for the chiral mean-field (CMF) model [116].

In Fig. 40 we show the particle densities at $B = 0$ (top row) and $B = 3 \times 10^{18}$ G (bottom row) with (full lines) and without (dashed lines) AMMs. We can see that some of the charged particles are favored when magnetic field effects without AMMs are considered, an effect that is more pronounced for protons, whose onset density is pulled to very low densities for both models. As a consequence, their population becomes more similar to the neutron one in densities below ≈ 0.05 fm^{-3}. The inclusion of AMM enhances this effect. The Δ^- threshold (at densities around 0.3 fm^{-3}) coincides with the region at intermediate densities beyond which the N+H+Δ EoSs are softer than the respective N+H EoSs. The Λ (and the Σ in the CMF model) hyperons appear at larger densities than the Δ^-s. The remaining Δs appear at much larger densities and in amounts that depend on the interactions in the L3$\omega\rho$ model. For $x_{s\Delta} = x_{s\Delta} = 1.0$, including the

AMM makes the positively charged Δs appear at realistic NS core densities.

For magnetic fields larger than $\approx 10^{16}$ G, the deformation of the stellar geometry away from spherical symmetry is above 2% [275]. Therefore, the usual relativistic hydrostatic equations usually employed when describing non-magnetized stars, i.e., the Tolman-Oppenheimer-Volkoff equations [276, 277], which assume spherical symmetry as part of their derivation from the general relativity equations, cease to be adequate. For this reason, we make use of anisotropic solutions from the Einstein and Maxwell equations to explore the macroscopic structure of magnetars with strong internal magnetic fields. Beyond accounting for the non-spherical configurations of stars and anisotropies introduced by magnetic fields, this approach allows us to obtain an *ab initio* magnetic field profile in the interior of a given star [278,279]. to compute the effect of the strong magnetic fields on the structure of the magnetars, one must solve the coupled Einstein–Maxwell equations with the equations of state. For the chosen poloidal field geometry, we solve the Einstein–Maxwell equations within the numerical library LORENE[4] using a multi-domain spectral method.

In Fig. 41, any differences between the mass-radius curves for the $B = 0$ case (solid lines) arise from the differences in the (non-magnetic) EoS, while the differences with magnetic field come from the pure electromagnetic field contribution. We know that the Lorentz force originating from the pure electromagnetic field affects the low-density part of the EoS. This is why the maximum mass of very massive stars does not change with increasing magnetic field strength, but the mass and radius of less massive stars increase significantly. For the $L3\omega\rho$ model, the inclusion of Δs decreases modestly the maximum stellar mass, especially for the larger coupling. However, for the CMF model, we do not see meaningful changes on the mass-radius diagram with the inclusion of Δs.

Using the full numerical solution, we also study the effect of the EoS on the magnetic field configurations inside a given star. We decompose the magnetic field norm in terms of spherical harmonics

$$B(r,\theta) \approx \sum_{l=0}^{l_{max}} B_l(r) Y_l^0(\theta) \,, \tag{5.16}$$

and plot the first four even multipoles ($l = 0,2,4,6$) as function of coordinate radius for both the EoS models and coupling strengths in the left of Fig 42. We also plot the profile of the dominant monopolar, spherically symmetric, term ($l = 0$) inside the star in the right of Fig 42. For $L3\omega\rho$

[4] <http://www.lorene.obspm.fr>

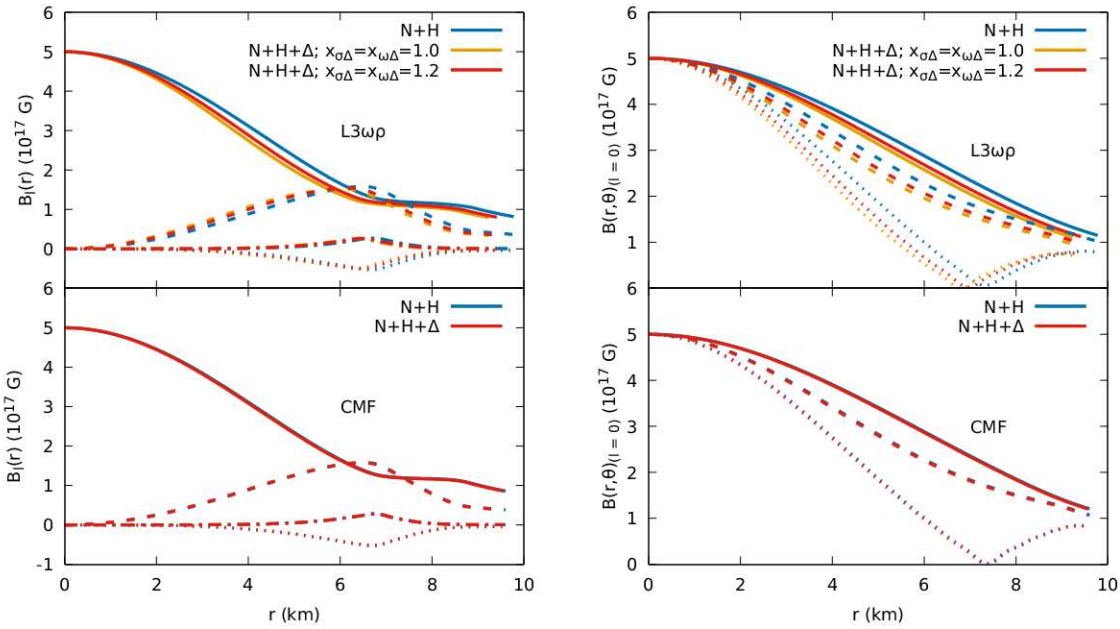

Figure 42: Magnetic field distribution inside a neutron star of mass $1.8M_{\odot}$ and central magnetic field of $B = 5 \times 10^{17}$ G for different compositions and interaction strengths. Left: Solid, dashed, dashed-dotted and dotted are, respectively, the first four even multipoles of the magnetic field norm (l = 0,2,4,6), shown as functions of the coordinate radius. Right: Solid, dashed and dotted are the dominant monopolar ($l = 0$) term at the polar ($\theta = 0$), intermediate ($\theta = \pi/4$) and equatorial ($\theta = \pi/2$) orientations, respectively, shown as functions of the coordinate radius. The top and bottom panels show results for the L3$\omega\rho$ and CMF models, respectively.

model, especially if we include Δs, the magnetic field norm decreases slightly inside the star but, for CMF model, we do not see any considerable changes. These results are published in Physical Review C [280] and was one of the Editor's choice of the issue.

5.3 Deconfinement phase transition in magnetars

In this section, we study the effects of strong magnetic fields on the deconfinement phase transition using the non–linear Walecka model with a modified version of the NL3* [176] parametrization, proposed in [177], the NL3$\omega\rho^*$. For the quark phase we use the MIT bag model with vector interactions (vMIT) [281–284]. A complete analysis of thermodynamic consistency, stability window, phase diagrams, and astrophysical consequences in the vMIT can be found in [177, 285, 286]. To find the point of the phase transition we follow [287], where the authors argue that the phase transition does not occur with both phases in β-equilibrium, but rather with only the hadronic phase in β-equilibrium. The quark phase is determined such that the fractions

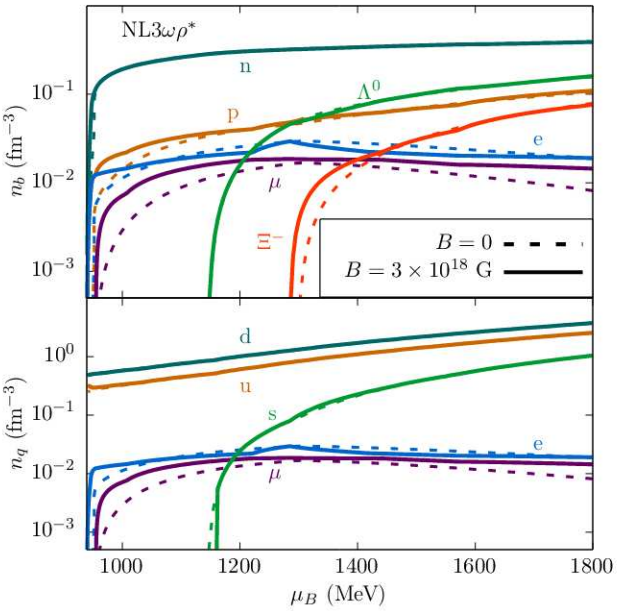

Figure 43: Density of baryons (top) and quarks (bottom) as a function of the chemical potential. Full lines are densities with $B = 0$ and dashed lines are densities calculated with $B = 3 \times 10^{18}$ G.

of quark flavors

$$Y_q = \sum_b \frac{1}{3} N_{qb} Y_b \tag{5.17}$$

are conserved during the transition, because the time scale over which the strong interaction acts is much shorter than the electroweak scale. After the phase transition occurs then β-equilibrium settles in. Here N_{qb} is the number of quarks of flavor q on the hadron b and $Y_b = n_b/n_B$.

The Lagrangian density of the vMIT model is given by

$$\mathcal{L}_Q = \sum_q \left\{ \bar{\psi}_q \left[i\gamma_\mu \partial^\mu - \gamma_0 g_{vq} \omega_0 - M_q \right] \psi_q - \mathcal{B} \right\} \Theta(\bar{\psi}_q \psi_q) + \frac{1}{2} m_v^2 \omega_0^2 + \frac{\xi}{4!} g_{vu}^4 \omega_0^4. \tag{5.18}$$

The quark densities n_q, energy density ε_q and pressure can be deduced in the same manner as those for hadrons in Section 2 and Section 5.2, with the substitutions $M_b^* \to M_q$ and $E_{F\,b}^* \to E_{F\,q}^* = \mu_q - g_{vq}\omega_0$. The quark degeneracy must be multiplied by 3 in order to include the color degree of freedom, so now the first Landau level has degeneracy $\gamma(0) = 3$ and levels above have $\gamma(\nu > 0) = 6$. The bag parameter $\mathcal{B}$ can be interpreted as the pressure exerted pointing to the center of the hadron, balancing the outward pressure due to quarks on the hadronic surface [288]. In order to study the parameter dependence we define the variables

$$G_V = \left(\frac{g_{vu}}{m_v} \right)^2, \quad X_V = \frac{g_{vs}}{g_{vu}}, \tag{5.19}$$

and to analyze how the magnetic field alters the phase transition, we consider the deconfinement to be a first-order transition

$$\mu_B = \mu_Q = \mu_0 \quad P_B = P_Q = P_0 \quad T_H = T_Q = 0. \tag{5.20}$$

with flavor conservation.

The densities of hadrons and quarks are shown as a function of the chemical potential in Fig. 43 for $B = 0$ and 3×10^{18} G. The magnetic field favors the appearance of negatively charged particles at lower chemical potentials. In order to find the point of the phase transition, the flavor fraction is fixed at equal chemical potentials. Another possibility would be to fix the quark fractions at equal pressures, which would lead to the same transition point, but to different quark densities and thermodynamic properties at points distinct from the transition point. Numerically it is simpler to fix the flavor fraction in the chemical potential, since the pressure of the quark phase can be negative but not the hadronic one, so one might exclude a large portion of chemical potential by fixing the flavor fraction at equal pressures and make it difficult to find the phase transition at very low chemical potentials.

Firstly we examine how the chemical potentials of the transition are altered with the magnetic field for values of $\mathcal{B}^{1/4}$ ranging between 148 and 205 MeV, with G_V =0, 0.1, 0.2 and 0.3 fm^2. As shown in Fig. 44, increasing values of the bag parameter and of the ω-coupling G_V increase the chemical potential, and thus also the pressure of the phase transition. For values of G_V larger than 0.3 the deconfinement phase transition occurs at chemical potentials larger

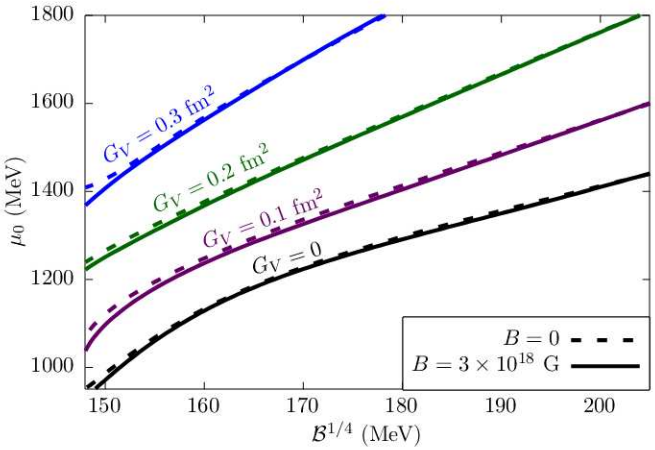

Figure 44: Chemical potential of the phase transition as a function of the bag parameter with $G_V = 0$, 0.1, 0.2 and 0.3 fm^2 (black, purple, red and blue curves, respectively) and $X_V = 1.0$. Dashed lines are curves with $B = 0$ and solid ones with $B = 3 \times 10^{18}$ G.

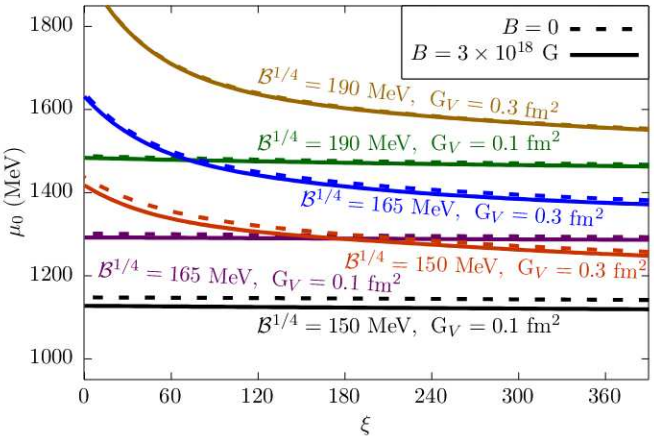

Figure 45: Chemical potential of the phase transition as a function of fourth order coupling parameter ξ, with varying values for the $\mathcal{B}^{1/4}$ and $G_V =$ and $X_V = 1.0$. Dashed lines are curves with $B = 0$ and solid ones with $B = 3 \times 10^{18}$ G

than 1800 MeV, which are beyond those expected in neutron stars [177]. The difference in the phase transition in magnetized and demagnetized matter is larger for lower values of the bag parameter, with the magnetic field favoring a slightly smaller chemical potential. As the bag parameter is increased, the effect of the magnetic field becomes less noticeable because the bag term dominates the pressure.

The addition of a fourth-order self-interaction for the ω-meson stiffens the EoS and reduces the chemical potential of the phase transition, with its importance being more pronounced at large chemical potentials and for higher values of the ω-coupling G_V. In Fig. 45 we show how the chemical potential of the phase transition is changed as a function of ξ, for both magnetized and demagnetized matter. As we turn on the fourth-order interaction the chemical potential decreases rapidly, and as ξ grows larger the chemical potential varies less. This is more attenuated for larger G_V, since the fourth-order interactions are weighted by G_V^2. The magnetic field slightly reduces the transition chemical potential, with the effect pronounced at lower chemical potentials.

In Fig. 46, we show the relativistic latent heat, given by

$$L\big|_{\varepsilon} = P_H \frac{\varepsilon_Q - \varepsilon_H}{\varepsilon_Q \varepsilon_H}, \tag{5.21}$$

as a function of the magnetic field. This expression was proposed in [289] to quantify the intensity of the phase transition, i.e., the discontinuity in the energy density between phases. The latent heat diminishes in magnetized matter, more prominently for smaller bag values. The

magnetic field becomes important on the latent heat for magnetic fields of the order of 10^{18} G only. where the latent heat is shown as a function of the magnetic field. This work is published in The European Physical Journal A [290].

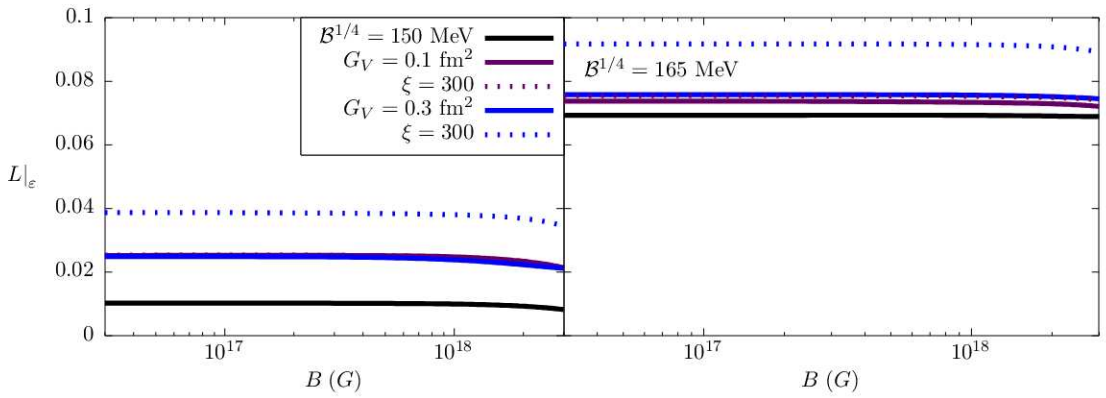

Figure 46: Latent heat as a function of the magnetic field for bag values of 150 and 165 (left and right, respectively), with G_V =0, 0.1 and 0.3 fm^2 and ξ =0 and 300.

Conclusions and Perspectives

In this thesis, in Section 2 I have introduced the non-linear Walecka model in the mean-field approximation, the bulk and mass-radius constraints, and a few parametrizations. Then I showed how to build the pasta phase in the one-component approach and discussed some pasta properties. The energy functional and the pasta properties throughout the thesis were calculated with the IUFSU parametrization which obeys most up-to-date constraints on the equation of state. The surface tension utilized to calculate the surface and Coulomb energies was fitted to reproduce a Thomas-Fermi calculation, where it is calculated consistently.

In Section 3 I have used the nuclear statistical equilibrium to calculate the distributions of pasta structures with geometry d and densities ρ_p^N, ρ_n^N, as well as pasta impurities that are quantified by charge variance. In order to also quantify geometric impurities, an effective proton number was proposed, varying according to the ratio of the pasta surface area relative to the droplet area and to the pasta orientation. Results show that charge impurities grow with temperature and baryonic density, and are larger for more symmetric matter due to the higher fraction of proton number. Geometric impurities become larger as isospin asymmetry or temperature rise, as can be reasoned from Fig. 14. We also demonstrated that our calculations obey ensemble equivalence, given the input thermodynamic chemical potentials (2.75) obtained with the variational approach and the inclusion of the rearrangement term.

In Section 4 I have calculated the anisotropic collision rates corresponding to elastic electron-pasta scattering, that were proposed in [33], using an expansion in spherical harmonics. I was able to give quantitative predictions for the electric conductivity in the magnetized and non-magnetized crust of a NS by estimating the pasta length from asymptotic expressions for the structure factor and restricting the calculation to the high-temperature regime, where pasta correlations can be neglected. In Section 5 other manuscripts produced during my doctorate were discussed.

In the future, I hope the large variances obtained in Section 3 are used in conjunction with the transport calculation of Section 4 to estimate the impact of the pasta impurities in the conductivity within a RMF model. Additionally, I expect to expand this calculation to derive expressions for the pasta viscosity; to calculate density correlations due to thermal fluctuations; and to estimate the impact of the mixing of multiplicity in the transport coefficients. These calculations can then be applied to astrophysical phenomena, such as to neutrino opacity in

supernovas and to the thermo-magnetic evolution of NSs.

The results presented in this thesis are either published or under review in international journals [195, 243, 249, 280, 290].

References

[1] SCHMITT, A. *Dense matter in compact stars: A pedagogical introduction*. [S.l.]: Springer, 2010. v. 811.

[2] GLENDENNING, N. *Compact Stars: Nuclear Physics, Particle Physics and General Relativity*. Springer New York, 2012. (Astronomy and Astrophysics Library). ISBN 9781468404913. Disponível em: <https://books.google.fr/books?id=cCDlBwAAQBAJ>.

[3] HAENSEL, P.; POTEKHIN, A. Y.; YAKOVLEV, D. G. *Neutron stars 1: Equation of state and structure*. [S.l.]: Springer Science & Business Media, 2007. v. 326.

[4] IVANENKO, D. D.; KURDGELAIDZE, D. F. Hypothesis concerning quark stars. *Astrophysics*, v. 1, p. 251–252, 1965.

[5] ITOH, N. Hydrostatic Equilibrium of Hypothetical Quark Stars. *Prog. Theor. Phys.*, v. 44, p. 291, 1970.

[6] LEE, C.-H.; RHO, M. Kaon condensation in dense stellar matter. In: *YITP Workshop: From Hadronic Matter to Quark Matter: Evolving View of Hadronic Matter*. [S.l.: s.n.], 1994. p. 0283–297.

[7] KAPLAN, D.; NELSON, A. Strange goings on in dense nucleonic matter. *Physics Letters B*, v. 175, n. 1, p. 57–63, 1986. ISSN 0370-2693. Disponível em: <https://www.sciencedirect.com/science/article/pii/037026938690331X>.

[8] GEZERLIS, A.; PETHICK, C. J.; SCHWENK, A. Pairing and superfluidity of nucleons in neutron stars. 6 2014.

[9] KURKELA, A.; ROMATSCHKE, P.; VUORINEN, A. Cold Quark Matter. *Phys. Rev. D*, v. 81, p. 105021, 2010.

[10] CLEVINGER, A. et al. Hybrid equations of state for neutron stars with hyperons and deltas. *Eur. Phys. J. A*, v. 58, n. 5, p. 96, 2022.

[11] DEXHEIMER, V. et al. Phase Transitions in Neutron Stars. *Int. J. Mod. Phys. E*, v. 27, n. 11, p. 1830008, 2018.

[12] MA, F.; WU, C.; GUO, W. Kaon Meson Condensation and Δ resonance of Hyperonized Star with relativistic mean-field model. 11 2022.

[13] LANDER, S. K. Magnetic fields in superconducting neutron stars. *Phys. Rev. Lett.*, American Physical Society, v. 110, p. 071101, Feb 2013. Disponível em: <https://link.aps.org/doi/10.1103/PhysRevLett.110.071101>.

[14] TANIMOTO, T.; BENTZ, W.; CLOËT, I. C. Massive neutron stars with a color superconducting quark matter core. *Phys. Rev. C*, American Physical Society, v. 101, p. 055204, May 2020. Disponível em: <https://link.aps.org/doi/10.1103/PhysRevC.101.055204>.

[15] BLASCHKE, D.; HANU, E.-O.; LIEBING, S. Neutron stars with crossover to color superconducting quark matter. *Phys. Rev. C*, American Physical Society, v. 105, p. 035804, Mar 2022. Disponível em: <https://link.aps.org/doi/10.1103/PhysRevC.105.035804>.

[16] GORIELY, S. et al. The decompression of the outer neutron star crust and r-process nucleosynthesis. *Astronomy and Astrophysics Journal*, v. 531, p. A78, jul. 2011.

[17] RÜSTER, S. B.; HEMPEL, M.; SCHAFFNER-BIELICH, J. Outer crust of nonaccreting cold neutron stars. *Phys. Rev. C*, American Physical Society, v. 73, p. 035804, Mar 2006. Disponível em: <https://link.aps.org/doi/10.1103/PhysRevC.73.035804>.

[18] SEDRAKIAN, A.; CLARK, J. W. Superfluidity in nuclear systems and neutron stars. *Eur. Phys. J. A*, v. 55, n. 9, p. 167, 2019.

[19] SAULS, J. A. Superfluidity in the Interiors of Neutron Stars. In: . [S.l.: s.n.], 2019.

[20] ANTONELLI, M.; MONTOLI, A.; PIZZOCHERO, P. Insights into the physics of neutron star interiors from pulsar glitches. In: ____. [S.l.: s.n.], 2023.

[21] RAVENHALL, D. G.; PETHICK, C. J.; WILSON, J. R. Structure of matter below nuclear saturation density. *Phys. Rev. Lett.*, American Physical Society, v. 50, p. 2066–2069, Jun 1983. Disponível em: <https://link.aps.org/doi/10.1103/PhysRevLett.50.2066>.

[22] HASHIMOTO, M.-a.; SEKI, H.; YAMADA, M. Shape of Nuclei in the Crust of Neutron Star. *Progress of Theoretical Physics*, v. 71, n. 2, p. 320–326, 02 1984. ISSN 0033-068X. Disponível em: <https://doi.org/10.1143/PTP.71.320>.

[23] OYAMATSU, K. Nuclear shapes in the inner crust of a neutron star. *Nuclear Physics A*, v. 561, n. 3, p. 431–452, 1993. ISSN 0375-9474. Disponível em: <https://www.sciencedirect.com/science/article/pii/037594749390020X>.

[24] MILLER, M. C. et al. PSR J0030+0451 mass and radius from NICER Data and implications for the properties of neutron star matter. *The Astrophysical Journal Letters*, The American Astronomical Society, v. 887, n. 1, p. L24, dec 2019. Disponível em: <https://dx.doi.org/10.3847/2041-8213/ab50c5>.

[25] RILEY, T. E. et al. A NICER View of PSR J0030+0451: Millisecond pulsar parameter estimation. *The Astrophysical Journal Letters*, The American Astronomical Society, v. 887, n. 1, p. L21, dec 2019. Disponível em: <https://dx.doi.org/10.3847/2041-8213/ab481c>.

[26] RILEY, T. E. et al. A NICER View of the Massive Pulsar PSR J0740+6620 Informed by Radio Timing and XMM-Newton Spectroscopy. *Astrophys. J. Lett.*, v. 918, n. 2, p. L27, 2021.

[27] FERREIRA, M.; PROVIDÊNCIA, C. m. c. Constraints on high density equation of state from maximum neutron star mass. *Phys. Rev. D*, American Physical Society, v. 104, p. 063006, Sep 2021. Disponível em: <https://link.aps.org/doi/10.1103/PhysRevD.104.063006>.

[28] SCHNEIDER, A. S. et al. Effect of topological defects on "nuclear pasta" observables. *Phys. Rev. C*, American Physical Society, v. 93, p. 065806, Jun 2016. Disponível em: <https://link.aps.org/doi/10.1103/PhysRevC.93.065806>.

[29] HOROWITZ, C. J. et al. Disordered nuclear pasta, magnetic field decay, and crust cooling in neutron stars. *Phys. Rev. Lett.*, American Physical Society, v. 114, p. 031102, Jan 2015. Disponível em: <https://link.aps.org/doi/10.1103/PhysRevLett.114.031102>.

[30] DEIBEL, A. et al. Late-time cooling of neutron star transients and the physics of the inner crust. *The Astrophysical Journal*, American Astronomical Society, v. 839, n. 2, p. 95, apr 2017. Disponível em: <https://doi.org/10.3847/1538-4357/aa6a19>.

[31] BROWN, E. F.; CUMMING, A. Mapping crustal heating with the cooling light curves of quasi-persistent transients. *The Astrophysical Journal*, American Astronomical Society, v. 698, n. 2, p. 1020–1032, may 2009. Disponível em: <https://doi.org/10.1088/0004-637x/698/2/1020>.

[32] NANDI, R.; SCHRAMM, S. Transport properties of the nuclear pasta phase with quantum molecular dynamics. *The Astrophysical Journal*, American Astronomical Society, v. 852, n. 2, p. 135, jan 2018. Disponível em: <https://doi.org/10.3847/1538-4357/aa9f12>.

[33] YAKOVLEV, D. G. Electron transport through nuclear pasta in magnetized neutron stars. *Monthly Notices of the Royal Astronomical Society*, v. 453, n. 1, p. 581–590, 08 2015. ISSN 0035-8711. Disponível em: <https://doi.org/10.1093/mnras/stv1642>.

[34] HOROWITZ, C. J. Gravitational Waves From Low Mass Neutron Stars. *Phys. Rev. D*, v. 81, p. 103001, 2010.

[35] GEARHEART, M. et al. Upper limits on the observational effects of nuclear pasta in neutron stars. *Monthly Notices of the Royal Astronomical Society*, v. 418, n. 4, p. 2343–2349, 12 2011. ISSN 0035-8711. Disponível em: <https://doi.org/10.1111/j.1365-2966.2011.19628.x>.

[36] ABBOTT, B. P. et al. Gw170817: Measurements of neutron star radii and equation of state. *Phys. Rev. Lett.*, American Physical Society, v. 121, p. 161101, Oct 2018. Disponível em: <https://link.aps.org/doi/10.1103/PhysRevLett.121.161101>.

[37] ABBOTT, B. P. et al. All-sky search for continuous gravitational waves from isolated neutron stars using advanced ligo o2 data. *Phys. Rev. D*, American Physical Society, v. 100, p. 024004, Jul 2019. Disponível em: <https://link.aps.org/doi/10.1103/PhysRevD.100.024004>.

[38] SOTANI, H. Effect of Pasta Phase on Oscillations in Neutron Stars. In: *21st Workshop on General Relativity and Gravitation in Japan*. [S.l.: s.n.], 2012. p. 100–103.

[39] SOTANI, H. Constraints on pasta structure of neutron stars from oscillations in giant flares. *Monthly Notices of the Royal Astronomical Society: Letters*, v. 417, n. 1, p. L70–L73, 10 2011. ISSN 1745-3925. Disponível em: <https://doi.org/10.1111/j.1745-3933.2011.01122.x>.

[40] CAPLAN, M. E.; SCHNEIDER, A. S.; HOROWITZ, C. J. Elasticity of nuclear pasta. *Phys. Rev. Lett.*, American Physical Society, v. 121, p. 132701, Sep 2018. Disponível em: <https://link.aps.org/doi/10.1103/PhysRevLett.121.132701>.

[41] ALLOY, M. D.; MENEZES, D. P. Nuclear "pasta phase" and its consequences on neutrino opacities. *Phys. Rev. C*, American Physical Society, v. 83, p. 035803, Mar 2011. Disponível em: <https://link.aps.org/doi/10.1103/PhysRevC.83.035803>.

[42] HOROWITZ, C. J. et al. Nonuniform neutron-rich matter and coherent neutrino scattering. *Phys. Rev. C*, American Physical Society, v. 70, p. 065806, Dec 2004. Disponível em: <https://link.aps.org/doi/10.1103/PhysRevC.70.065806>.

[43] LIN, Z. et al. Fast neutrino cooling of nuclear pasta in neutron stars: molecular dynamics simulations. *Phys. Rev. C*, v. 102, n. 4, p. 045801, 2020.

[44] PIEKAREWICZ, J.; FATTOYEV, F. J.; HOROWITZ, C. J. Pulsar Glitches: The Crust may be Enough. *Phys. Rev. C*, v. 90, n. 1, p. 015803, 2014.

[45] DALIGAULT, J.; GUPTA, S. Electron–ion scattering in dense multi-component plasmas: Application to the outer crust of an accreting neutron star. *The Astrophysical Journal*, American Astronomical Society, v. 703, n. 1, p. 994–1011, sep 2009. Disponível em: <https://doi.org/10.1088/0004-637x/703/1/994>.

[46] FLOWERS, E.; ITOH, N. Transport properties of dense matter. *The Astrophysical Journal*, v. 206, p. 218–242, maio 1976.

[47] YAKOVLEV, D. G.; URPIN, V. A. Thermal and Electrical Conductivity in White Dwarfs and Neutron Stars. *Soviet Astronomy*, v. 24, p. 303, jun. 1980.

[48] NANDKUMAR, R.; J., P. C. Transport coefficients of dense matter in the liquid metal regime. *Monthly Notices of the Royal Astronomical Society*, v. 209, p. 511–524, ago. 1984.

[49] BAIKO, D. A. et al. Ion structure factors and electron transport in dense Coulomb plasmas. *Phys. Rev. Lett.*, v. 81, p. 5556–5559, 1998.

[50] POTEKHIN, A. Y. et al. Transport properties of degenerate electrons in neutron star envelopes and white dwarf cores. *Astron. Astrophys.*, v. 346, p. 345, 1999.

[51] CHUGUNOV, A. I.; YAKOVLEV, D. G. Shear viscosity and oscillations of neutron star crusts. *Astron. Rep.*, v. 49, p. 724–738, 2005.

[52] AGUILERA, D. N. et al. Superfluid heat conduction and the cooling of magnetized neutron stars. *Phys. Rev. Lett.*, American Physical Society, v. 102, p. 091101, Mar 2009. Disponível em: <https://link.aps.org/doi/10.1103/PhysRevLett.102.091101>.

[53] CHAMEL, N.; HAENSEL, P. Physics of Neutron Star Crusts. *Living Rev. Rel.*, v. 11, p. 10, 2008.

[54] SHTERNIN, P. S.; YAKOVLEV, D. G. Electron thermal conductivity owing to collisions between degenerate electrons. *Phys. Rev. D*, American Physical Society, v. 74, p. 043004, Aug 2006. Disponível em: <https://link.aps.org/doi/10.1103/PhysRevD.74.043004>.

[55] SCHNEIDER, A. S. et al. Nuclear “pasta” formation. *Phys. Rev. C*, v. 88, n. 6, p. 065807, 2013.

[56] NEWTON, W. G. A taste of pasta? *Nature Physics*, Nature Publishing Group, v. 9, n. 7, p. 396–397, 2013.

[57] PONS, J.; VIGANÓ, D.; REA, N. A highly resistive layer within the crust of x-ray pulsars limits their spin periods. *Nature Physics*, p. 431–434, 2013.

[58] PHILIPSEN, O. Lattice QCD at finite temperature and density. *Eur. Phys. J. ST*, v. 152, p. 29–60, 2007.

[59] RATTI, C. Lattice QCD and heavy ion collisions: a review of recent progress. *Rept. Prog. Phys.*, v. 81, n. 8, p. 084301, 2018.

[60] FURTADO, U. J.; AVANCINI, S. S.; MARINELLI, J. R. Pairing effects in nuclear pasta phase within the relativistic Thomas–Fermi formalism. *J. Phys. G*, v. 49, n. 2, p. 025202, 2022.

[61] AVANCINI, S. S. et al. Warm “pasta” phase in the thomas-fermi approximation. *Phys. Rev. C*, American Physical Society, v. 82, p. 055807, Nov 2010. Disponível em: <https://link.aps.org/doi/10.1103/PhysRevC.82.055807>.

[62] SHCHECHILIN, N. N. et al. Pasta phases in neutron star mantle: Extended thomas-fermi vs. compressible liquid drop approaches. *Universe*, v. 8, n. 11, 2022. ISSN 2218-1997. Disponível em: <https://www.mdpi.com/2218-1997/8/11/582>.

[63] IIDA, K.; WATANABE, G.; SATO, K. Formation of Nuclear “Pasta” in Cold Neutron Star Matter. *Progress of Theoretical Physics*, v. 106, n. 3, p. 551–559, set. 2001.

[64] HOROWITZ, C. J.; PÉREZ-GARCÍA, M. A.; PIEKAREWICZ, J. Neutrino-“pasta” scattering: The opacity of nonuniform neutron-rich matter. *Phys. Rev. C*, American Physical Society, v. 69, p. 045804, Apr 2004. Disponível em: <https://link.aps.org/doi/10.1103/PhysRevC.69.045804>.

[65] MAGIERSKI, P.; HEENEN, P.-H. Structure of the inner crust of neutron stars: Crystal lattice or disordered phase? *Phys. Rev. C*, American Physical Society, v. 65, p. 045804, Apr 2002. Disponível em: <https://link.aps.org/doi/10.1103/PhysRevC.65.045804>.

[66] GÖGELEIN, P. et al. Nuclear matter in the crust of neutron stars derived from realistic *NN* interactions. *Phys. Rev. C*, American Physical Society, v. 77, p. 025802, Feb 2008. Disponível em: <https://link.aps.org/doi/10.1103/PhysRevC.77.025802>.

[67] NEWTON, W. G.; STONE, J. R. Modeling nuclear “pasta” and the transition to uniform nuclear matter with the 3d skyrme-hartree-fock method at finite temperature: Core-collapse supernovae. *Phys. Rev. C*, American Physical Society, v. 79, p. 055801, May 2009. Disponível em: <https://link.aps.org/doi/10.1103/PhysRevC.79.055801>.

[68] PAIS, H. et al. Core-collapse supernova matter: light clusters, pasta phase and phase transitions. In: *Compact Stars in the QCD Phase Diagram IV*. [S.l.: s.n.], 2015.

[69] PAIS, H.; PROVIDÊNCIA, C. Vlasov formalism for extended relativistic mean field models: The crust-core transition and the stellar matter equation of state. *Phys. Rev. C*, American Physical Society, v. 94, p. 015808, Jul 2016. Disponível em: <https://link.aps.org/doi/10.1103/PhysRevC.94.015808>.

[70] XU, J. et al. Locating the inner edge of the neutron star crust using terrestrial nuclear laboratory data. *Phys. Rev. C*, American Physical Society, v. 79, p. 035802, Mar 2009. Disponível em: <https://link.aps.org/doi/10.1103/PhysRevC.79.035802>.

[71] LOPES, L. L.; MENEZES, D. P. Hyperon threshold and stellar radii. *JCAP*, v. 05, p. 038, 2018.

[72] LOPES, L. L.; MENEZES, D. P. Role of vector channel in different classes of (non) magnetized neutron stars. *Eur. Phys. J. A*, v. 56, n. 4, p. 122, 2020.

[73] BAO, S. S.; SHEN, H. Impact of the symmetry energy on nuclear pasta phases and crust-core transition in neutron stars. *Phys. Rev. C*, American Physical Society, v. 91, p. 015807, Jan 2015. Disponível em: <https://link.aps.org/doi/10.1103/PhysRevC.91.015807>.

[74] CHAMEL, N. et al. Role of the Symmetry Energy on the Structure of Neutron Stars with Unified Equations of State. *AIP Conf. Proc.*, v. 2127, n. 1, p. 020021, 2019.

[75] SALINAS, M.; PIEKAREWICZ, J. Bayesian refinement of covariant energy density functionals. 1 2023.

[76] TSANG, M. B. et al. Constraints on the symmetry energy and neutron skins from experiments and theory. *Phys. Rev. C*, v. 86, p. 015803, 2012.

[77] CHABANAT, E. et al. A skyrme parametrization from subnuclear to neutron star densities part ii. nuclei far from stabilities. *Nuclear Physics A*, v. 635, n. 1, p. 231–256, 1998. ISSN 0375-9474. Disponível em: <https://www.sciencedirect.com/science/article/pii/S0375947498001808>.

[78] BARTEL, J. et al. Towards a better parametrisation of skyrme-like effective forces: A critical study of the skm force. *Nuclear Physics A*, v. 386, n. 1, p. 79–100, 1982. ISSN 0375-9474. Disponível em: <https://www.sciencedirect.com/science/article/pii/0375947482904031>.

[79] SCHNEIDER, A. S. et al. Nuclear "waffles". *Phys. Rev. C*, American Physical Society, v. 90, p. 055805, Nov 2014. Disponível em: <https://link.aps.org/doi/10.1103/PhysRevC.90.055805>.

[80] BERRY, D. K. et al. "parking-garage" structures in nuclear astrophysics and cellular biophysics. *Phys. Rev. C*, American Physical Society, v. 94, p. 055801, Nov 2016. Disponível em: <https://link.aps.org/doi/10.1103/PhysRevC.94.055801>.

[81] DORSO, C. O.; MOLINELLI, P. A. G.; LÓPEZ, J. A. Topological characterization of neutron star crusts. *Phys. Rev. C*, American Physical Society, v. 86, p. 055805, Nov 2012. Disponível em: <https://link.aps.org/doi/10.1103/PhysRevC.86.055805>.

[82] WATANABE, G. et al. Simulation of transitions between "pasta" phases in dense matter. *Phys. Rev. Lett.*, American Physical Society, v. 94, p. 031101, Jan 2005. Disponível em: <https://link.aps.org/doi/10.1103/PhysRevLett.94.031101>.

[83] LI, B.-A. Tasting nuclear pasta made with classical molecular dynamics simulations. *Front. Phys. (Beijing)*, v. 16, n. 2, p. 24302, 2021.

[84] NAKAZATO, K.; OYAMATSU, K.; YAMADA, S. Gyroid phase in nuclear pasta. *Phys. Rev. Lett.*, American Physical Society, v. 103, p. 132501, Sep 2009. Disponível em: <https://link.aps.org/doi/10.1103/PhysRevLett.103.132501>.

[85] NEWTON, W. G. et al. Glassy quantum nuclear pasta in neutron star crusts. *Phys. Rev. C*, v. 105, n. 2, p. 025806, 2022.

[86] ABBAR, S. et al. Quantum monte carlo calculations of the thermal conductivity of neutron star crusts. *Phys. Rev. C*, American Physical Society, v. 92, p. 045809, Oct 2015. Disponível em: <https://link.aps.org/doi/10.1103/PhysRevC.92.045809>.

[87] CHUGUNOV, A. I.; HOROWITZ, C. J. Breaking stress of neutron star crust. *Mon. Not. Roy. Astron. Soc.*, v. 407, p. L54–L58, 2010.

[88] WATANABE, G.; IIDA, K.; SATO, K. Thermodynamic properties of nuclear "pasta" in neutron star crusts. *Nuclear Physics A*, v. 676, n. 1, p. 455 – 473, 2000. ISSN 0375-9474. Disponível em: <http://www.sciencedirect.com/science/article/pii/S0375947400001974>.

[89] LATTIMER, J. M.; Douglas Swesty, F. A generalized equation of state for hot, dense matter. *Nuclear Physics A*, v. 535, n. 2, p. 331 – 376, 1991. ISSN 0375-9474. Disponível em: <http://www.sciencedirect.com/science/article/pii/037594749190452C>.

[90] BURROWS, A.; LATTIMER, J. M. On the accuracy of the single-nucleus approximation in the equation of state of hot, dense matter. *The Astrophysical Journal*, v. 285, p. 294–303, out. 1984.

[91] BAYM, G.; BETHE, H. A.; PETHICK, C. J. Neutron star matter. *Nuclear Physics A*, v. 175, n. 2, p. 225 – 271, 1971. ISSN 0375-9474. Disponível em: <http://www.sciencedirect.com/science/article/pii/0375947471902818>.

[92] AVANCINI, S. S. et al. Warm and cold pasta phase in relativistic mean field theory. *Phys. Rev. C*, American Physical Society, v. 78, p. 015802, Jul 2008. Disponível em: <https://link.aps.org/doi/10.1103/PhysRevC.78.015802>.

[93] AVANCINI, S. S. et al. α particles and the "pasta" phase in nuclear matter. *Phys. Rev. C*, American Physical Society, v. 82, p. 025808, Aug 2010. Disponível em: <https://link.aps.org/doi/10.1103/PhysRevC.82.025808>.

[94] MENEZES, D. P.; PROVIDÊNCIA, C. Nucleation process in asymmetric hot nuclear matter. *Phys. Rev. C*, American Physical Society, v. 60, p. 024313, Jul 1999. Disponível em: <https://link.aps.org/doi/10.1103/PhysRevC.60.024313>.

[95] SHEN, H. et al. Relativistic equation of state of nuclear matter for supernova and neutron star. *Nuclear Physics A*, v. 637, n. 3, p. 435 – 450, 1998. ISSN 0375-9474. Disponível em: <http://www.sciencedirect.com/science/article/pii/S037594749800236X>.

[96] JI, F. et al. Nuclear pasta in hot and dense matter and its influence on the equation of state for astrophysical simulations. *Phys. Rev. C*, American Physical Society, v. 102, p. 015806, Jul 2020. Disponível em: <https://link.aps.org/doi/10.1103/PhysRevC.102.015806>.

[97] GRAMS, G. et al. Nuclear pasta phases within the quark-meson coupling model. *Phys. Rev. C*, American Physical Society, v. 95, p. 055807, May 2017. Disponível em: <https://link.aps.org/doi/10.1103/PhysRevC.95.055807>.

[98] GULMINELLI, F.; RADUTA, A. R. Unified treatment of subsaturation stellar matter at zero and finite temperature. *Physical Review C*, American Physical Society (APS), v. 92, n. 5, Nov 2015. ISSN 1089-490X. Disponível em: <http://dx.doi.org/10.1103/PhysRevC.92.055803>.

[99] FANTINA, A. F. et al. Crystallization of the outer crust of a non-accreting neutron star. *Astronomy and Astrophysics Journal*, v. 633, p. A149, 2020. Disponível em: <https://doi.org/10.1051/0004-6361/201936359>.

[100] CARREAU, T. et al. Crystallization of the inner crust of a neutron star and the influence of shell effects. *Astron. Astrophys.*, v. 635, p. A84, 2020.

[101] CARREAU, T.; FANTINA, A. F.; GULMINELLI, F. Inner crust of a neutron star at the point of crystallization in a multicomponent approach. *A&A*, v. 640, p. A77, 2020. Disponível em: <https://doi.org/10.1051/0004-6361/202038347>.

[102] POTEKHIN, A. Y.; CHABRIER, G. Crust structure and thermal evolution of neutron stars in soft x-ray transients. *A&A*, v. 645, p. A102, 2021. Disponível em: <https://doi.org/10.1051/0004-6361/202039006>.

[103] ZEMLYAKOV, N. A.; CHUGUNOV, A. I. Stability of Spherical Nuclei in the Inner Crust of Neutron Stars. *Particles*, v. 5, n. 3, p. 225–234, 2022.

[104] XIA, C.-J. et al. Nuclear pasta structures at high temperatures. *Phys. Rev. D*, v. 106, n. 6, p. 063020, 2022.

[105] PHILLIPS, A. C. *The physics of stars*. [S.l.]: John Wiley & Sons, 2013.

[106] GRAMS, G. et al. Distribution of nuclei in equilibrium stellar matter from the free-energy density in a wigner-seitz cell. *Phys. Rev. C*, American Physical Society, v. 97, p. 035807, Mar 2018. Disponível em: <https://link.aps.org/doi/10.1103/PhysRevC.97.035807>.

[107] BARROS, C. C.; MENEZES, D. P.; GULMINELLI, F. Fluctuations in the composition of nuclear pasta in symmetric nuclear matter at finite temperature. *Phys. Rev. C*, American Physical Society, v. 101, p. 035211, Mar 2020. Disponível em: <https://link.aps.org/doi/10.1103/PhysRevC.101.035211>.

[108] WALECKA, J. D. The relativistic nuclear many-body problem. In: ____. *New Vistas in Nuclear Dynamics*. Boston, MA: Springer US, 1986. p. 229–271. ISBN 978-1-4684-5179-5. Disponível em: <https://doi.org/10.1007/978-1-4684-5179-5_8>.

[109] FETTER, A.; WALECKA, J. *Quantum Theory of Many-particle Systems*. Dover Publications, 2003. (Dover Books on Physics). ISBN 9780486428277. Disponível em: <https://books.google.com.br/books?id=ZA7jDAAAQBAJ>.

[110] THI, H. D.; FANTINA, A. F.; GULMINELLI, F. The effect of the energy functional on the pasta-phase properties of catalysed neutron stars. *Eur. Phys. J. A*, v. 57, n. 10, p. 296, 2021.

[111] PARMAR, V. et al. Pasta properties of the neutron star within effective relativistic mean-field model. *Phys. Rev. D*, American Physical Society, v. 106, p. 023031, Jul 2022. Disponível em: <https://link.aps.org/doi/10.1103/PhysRevD.106.023031>.

[112] FATTOYEV, F. J. et al. Relativistic effective interaction for nuclei, giant resonances, and neutron stars. *Phys. Rev. C*, American Physical Society, v. 82, p. 055803, Nov 2010. Disponível em: <https://link.aps.org/doi/10.1103/PhysRevC.82.055803>.

[113] MUTA, T. *Foundations of quantum chromodynamics: an introduction to perturbative methods in gauge theories*. [S.l.]: World Scientific, 1998.

[114] GRAMS, G. et al. Properties of the neutron star crust: Quantifying and correlating uncertainties with improved nuclear physics. *Phys. Rev. C*, American Physical Society, v. 105, p. 035806, Mar 2022. Disponível em: <https://link.aps.org/doi/10.1103/PhysRevC.105.035806>.

[115] AVANCINI, S. S. et al. Light clusters in nuclear matter and the “pasta” phase. *Phys. Rev. C*, American Physical Society, v. 85, p. 035806, Mar 2012. Disponível em: <https://link.aps.org/doi/10.1103/PhysRevC.85.035806>.

[116] DEXHEIMER, V.; SCHRAMM, S. Proto-Neutron and Neutron Stars in a Chiral SU(3) Model. *Astrophys. J.*, v. 683, p. 943–948, 2008.

[117] LIU, B. et al. Asymmetric nuclear matter: The role of the isovector scalar channel. *Phys. Rev. C*, American Physical Society, v. 65, p. 045201, Mar 2002. Disponível em: <https://link.aps.org/doi/10.1103/PhysRevC.65.045201>.

[118] KUBIS, S.; KUTSCHERA, M. Nuclear matter in relativistic mean field theory with isovector scalar meson. *Physics Letters B*, v. 399, n. 3, p. 191–195, 1997. ISSN 0370-2693. Disponível em: <https://www.sciencedirect.com/science/article/pii/S0370269397003067>.

[119] TOLOS, L.; CENTELLES, M.; RAMOS, A. The equation of state for the nucleonic and hyperonic core of neutron stars. *Publications of the Astronomical Society of Australia*, Cambridge University Press, v. 34, p. e065, 2017.

[120] WALECKA, J. D. A Theory of highly condensed matter. *Annals Phys.*, v. 83, p. 491–529, 1974.

[121] MILLER, L. D.; GREEN, A. E. S. Relativistic self-consistent meson field theory of spherical nuclei. *Phys. Rev. C*, American Physical Society, v. 5, p. 241–252, Jan 1972. Disponível em: <https://link.aps.org/doi/10.1103/PhysRevC.5.241>.

[122] NARISON, S. On the quark and gluon substructure of the sigma and other scalar mesons. *Soryushiron Kenkyu*, v. 102, n. 5, p. 123–132, 2000.

[123] AGABABYAN, N. M. et al. Charged rho meson production in neutrino induced reactions at E(nu) approx. 10-GeV. *Phys. Atom. Nucl.*, v. 74, p. 221–228, 2011.

[124] ARNALDI, R. et al. First measurement of the ρ spectral function in high-energy nuclear collisions. *Phys. Rev. Lett.*, American Physical Society, v. 96, p. 162302, Apr 2006. Disponível em: <https://link.aps.org/doi/10.1103/PhysRevLett.96.162302>.

[125] MASERA, M.; COLLABORATION, H. et al. Dimuon production below mass 3.1 gev/c2 in pw and sw interactions at 200 gev/c/a. *Nuclear Physics A*, Elsevier, v. 590, n. 1-2, p. 93–102, 1995.

[126] WESSELS, J. P. et al. Latest results from CERES / NA45. *Nucl. Phys. A*, v. 715, p. 262–271, 2003.

[127] HIBOU, F. et al. Near-threshold production of ω mesons in the $pp \rightarrow pp\omega$ reaction. *Phys. Rev. Lett.*, American Physical Society, v. 83, p. 492–495, Jul 1999. Disponível em: <https://link.aps.org/doi/10.1103/PhysRevLett.83.492>.

[128] BALESTRA, F. et al. φ and ω meson production in pp reactions at $p_{\mathrm{lab}} = 3.67\mathrm{GeV}/c$. *Phys. Rev. C*, American Physical Society, v. 63, p. 024004, Jan 2001. Disponível em: <https://link.aps.org/doi/10.1103/PhysRevC.63.024004>.

[129] BARSOV, S. et al. Study of omega-meson production in pp collisions at ANKE. *Eur. Phys. J. A*, v. 31, p. 95–104, 2007.

[130] KUNIHIRO, T. Significance of the sigma meson in hadron physics (QCD) and possible experiments to observe it. *Frascati Phys. Ser.*, v. 15, p. 143–150, 1999.

[131] KAMIŃSKI, R. What happened with the $f_0(500)/\sigma$ meson? Theory and experiment. *Acta Phys. Polon. Supp.*, v. 8, n. 1, p. 103–108, 2015.

[132] BYDZOVSKÝ, P.; KAMINSKI, R.; NAZARI, V. Modified $\pi\pi$ amplitude with σ pole. *Phys. Rev. D*, v. 90, n. 11, p. 116005, 2014.

[133] BOGUTA, J.; BODMER, A. Relativistic calculation of nuclear matter and the nuclear surface. *Nuclear Physics A*, v. 292, n. 3, p. 413 – 428, 1977. ISSN 0375-9474. Disponível em: <http://www.sciencedirect.com/science/article/pii/0375947477906261>.

[134] BODMER, A. Relativistic mean field theory of nuclei with a vector meson self-interaction. *Nuclear Physics A*, v. 526, n. 3, p. 703 – 721, 1991. ISSN 0375-9474. Disponível em: <http://www.sciencedirect.com/science/article/pii/037594749190439D>.

[135] MÜLLER, H.; SEROT, B. D. Relativistic mean-field theory and the high-density nuclear equation of state. *Nuclear Physics A*, v. 606, n. 3, p. 508 – 537, 1996. ISSN 0375-9474. Disponível em: <http://www.sciencedirect.com/science/article/pii/037594749600187X>.

[136] EPELE, L. et al. The Nolen-Schiffer anomaly and the $\rho_0 - \omega$ mixing. *Physics Letters B*, v. 277, n. 1, p. 33–37, 1992. ISSN 0370-2693. Disponível em: <https://www.sciencedirect.com/science/article/pii/037026939290952Z>.

[137] MENEZES, D. P.; PROVIDÊNCIA, C. ρ-ω mixing in the nonlinear walecka model. *Phys. Rev. C*, American Physical Society, v. 66, p. 015206, Jul 2002. Disponível em: <https://link.aps.org/doi/10.1103/PhysRevC.66.015206>.

[138] PESKIN, M. *An introduction to quantum field theory*. [S.l.]: CRC press, 2018.

[139] NIELSEN, M.; PROVIDÊNCIA, C.; PROVIDÊNCIA, J. da. Collective modes in hot and dense nuclear matter. *Phys. Rev. C*, American Physical Society, v. 47, p. 200–209, Jan 1993. Disponível em: <https://link.aps.org/doi/10.1103/PhysRevC.47.200>.

[140] MARUYAMA, T. et al. Pasta structures in compact stars. *Recent Res. Devel. Phys.*, v. 7, p. 1–57, 2006.

[141] ZYLA, P. et al. Review of Particle Physics. *PTEP*, v. 2020, n. 8, p. 083C01, 2020.

[142] OERTEL, M. et al. Equations of state for supernovae and compact stars. *Rev. Mod. Phys.*, v. 89, n. 1, p. 015007, 2017.

[143] DUTRA, M. et al. Relativistic mean-field hadronic models under nuclear matter constraints. *Phys. Rev. C*, American Physical Society, v. 90, p. 055203, Nov 2014. Disponível em: <https://link.aps.org/doi/10.1103/PhysRevC.90.055203>.

[144] REED, B. T. et al. Implications of PREX-2 on the equation of state of neutron-rich matter. *Phys. Rev. Lett.*, American Physical Society, v. 126, p. 172503, Apr 2021. Disponível em: <https://link.aps.org/doi/10.1103/PhysRevLett.126.172503>.

[145] Angeli, I.; Marinova, K. P. Table of experimental nuclear ground state charge radii: An update. *Atomic Data and Nuclear Data Tables*, v. 99, n. 1, p. 69–95, jan. 2013.

[146] PEARSON, J. M.; CHAMEL, N.; GORIELY, S. Breathing-mode measurements in Sn isotopes and isospin dependence of nuclear incompressibility. *Phys. Rev. C*, American Physical Society, v. 82, p. 037301, Sep 2010. Disponível em: <https://link.aps.org/doi/10.1103/PhysRevC.82.037301>.

[147] KHAN, E.; MARGUERON, J. Determination of the density dependence of the nuclear incompressibility. *Phys. Rev. C*, American Physical Society, v. 88, p. 034319, Sep 2013. Disponível em: <https://link.aps.org/doi/10.1103/PhysRevC.88.034319>.

[148] KHAN, E.; MARGUERON, J.; NA, I. V. Constraining the nuclear equation of state at subsaturation densities. *Phys. Rev. Lett.*, American Physical Society, v. 109, p. 092501, Aug 2012. Disponível em: <https://link.aps.org/doi/10.1103/PhysRevLett.109.092501>.

[149] VRETENAR, D.; NIKSIĆ, T.; RING, P. A microscopic estimate of the nuclear matter compressibility and symmetry energy in relativistic mean-field models. *Phys. Rev. C*, American Physical Society, v. 68, p. 024310, Aug 2003. Disponível em: <https://link.aps.org/doi/10.1103/PhysRevC.68.024310>.

[150] WIELAND, O. et al. Search for the pygmy dipole resonance in ^{68}Ni at 600 MeV/nucleon. *Phys. Rev. Lett.*, American Physical Society, v. 102, p. 092502, Mar 2009. Disponível em: <https://link.aps.org/doi/10.1103/PhysRevLett.102.092502>.

[151] CARBONE, A. et al. Constraints on the symmetry energy and neutron skins from pygmy resonances in ^{68}Ni and ^{132}Sn. *Phys. Rev. C*, American Physical Society, v. 81, p. 041301, Apr 2010. Disponível em: <https://link.aps.org/doi/10.1103/PhysRevC.81.041301>.

[152] KOHLEY, Z. et al. Transverse collective flow and midrapidity emission of isotopically identified light charged particles. *Phys. Rev. C*, American Physical Society, v. 83, p. 044601, Apr 2011. Disponível em: <https://link.aps.org/doi/10.1103/PhysRevC.83.044601>.

[153] TSANG, M. B. et al. Constraints on the density dependence of the symmetry energy. *Phys. Rev. Lett.*, American Physical Society, v. 102, p. 122701, Mar 2009. Disponível em: <https://link.aps.org/doi/10.1103/PhysRevLett.102.122701>.

[154] HOROWITZ, C. J.; PIEKAREWICZ, J. Neutron star structure and the neutron radius of ^{208}pb. *Phys. Rev. Lett.*, American Physical Society, v. 86, p. 5647–5650, Jun 2001. Disponível em: <https://link.aps.org/doi/10.1103/PhysRevLett.86.5647>.

[155] DANIELEWICZ, P.; LEE, J. Symmetry energy from systematic of isobaric analog states. *AIP Conference Proceedings*, v. 1423, n. 1, p. 29–34, 2012. Disponível em: <https://aip.scitation.org/doi/abs/10.1063/1.3688777>.

[156] DANIELEWICZ, P.; LEE, J. Symmetry Energy II: Isobaric Analog States. *Nucl. Phys. A*, v. 922, p. 1–70, 2014.

[157] ADHIKARI, D. et al. Precision Determination of the Neutral Weak Form Factor of Ca48. *Phys. Rev. Lett.*, v. 129, n. 4, p. 042501, 2022.

[158] REINHARD, P.-G.; ROCA-MAZA, X.; NAZAREWICZ, W. Information Content of the Parity-Violating Asymmetry in Pb208. *Phys. Rev. Lett.*, v. 127, n. 23, p. 232501, 2021.

[159] YUE, T.-G. et al. Constraints on the symmetry energy from PREX-II in the multimessenger era. *Phys. Rev. Res.*, v. 4, n. 2, p. L022054, 2022.

[160] ESSICK, R. et al. Astrophysical Constraints on the Symmetry Energy and the Neutron Skin of Pb208 with Minimal Modeling Assumptions. *Phys. Rev. Lett.*, v. 127, n. 19, p. 192701, 2021.

[161] ANTONIADIS, J. et al. A Massive Pulsar in a Compact Relativistic Binary. *Science*, v. 340, p. 6131, 2013.

[162] DEMOREST, P. et al. Shapiro Delay Measurement of A Two Solar Mass Neutron Star. *Nature*, v. 467, p. 1081–1083, 2010.

[163] FONSECA, E. et al. The nanograv nine-year data set: Mass and geometric measurements of binary millisecond pulsars. *The Astrophysical Journal*, The American Astronomical Society, v. 832, n. 2, p. 167, nov 2016. Disponível em: <https://dx.doi.org/10.3847/0004-637X/832/2/167>.

[164] MILLER, M. C. et al. The radius of PSR J0740+6620 from NICER and XMM-Newton Data. *The Astrophysical Journal Letters*, The American Astronomical Society, v. 918, n. 2, p. L28, sep 2021. Disponível em: <https://dx.doi.org/10.3847/2041-8213/ac089b>.

[165] RADUTA, A. R.; NACU, F.; OERTEL, M. Equations of state for hot neutron stars. *Eur. Phys. J. A*, v. 57, n. 12, p. 329, 2021.

[166] MILLER, M. C. et al. PSR J0030+0451 Mass and Radius from *NICER* Data and Implications for the Properties of Neutron Star Matter. *Astrophys. J. Lett.*, v. 887, n. 1, p. L24, 2019.

[167] STEINER, A. W. et al. Constraining the mass and radius of neutron stars in globular clusters. *Monthly Notices of the Royal Astronomical Society*, v. 476, n. 1, p. 421–435, 01 2018. ISSN 0035-8711. Disponível em: <https://doi.org/10.1093/mnras/sty215>.

[168] STEINER, A. W.; LATTIMER, J. M.; BROWN, E. F. The equation of state from observed masses and radii of neutron stars. *The Astrophysical Journal*, The American Astronomical Society, v. 722, n. 1, p. 33, sep 2010. Disponível em: <https://dx.doi.org/10.1088/0004-637X/722/1/33>.

[169] SALMI, T.; NÄTTILÄ, J.; POUTANEN, J. Bayesian parameter constraints for neutron star masses and radii using x-ray timing observations of accretion-powered millisecond pulsars. *Astronomy and Astrophysics Journal*, v. 618, p. A161, 2018. Disponível em: <https://doi.org/10.1051/0004-6361/201833348>.

[170] PROVIDÊNCIA, C. et al. Imprint of the symmetry energy on the inner crust and strangeness content of neutron stars. *Eur. Phys. J. A*, v. 50, p. 44, 2014.

[171] HOROWITZ, C. J.; PIEKAREWICZ, J. Neutron star structure and the neutron radius of ^{208}Pb. *Phys. Rev. Lett.*, American Physical Society, v. 86, p. 5647–5650, Jun 2001. Disponível em: <https://link.aps.org/doi/10.1103/PhysRevLett.86.5647>.

[172] HOROWITZ, C. J.; PIEKAREWICZ, J. Constraining urca cooling of neutron stars from the neutron radius of ^{208}Pb. *Phys. Rev. C*, American Physical Society, v. 66, p. 055803, Nov 2002. Disponível em: <https://link.aps.org/doi/10.1103/PhysRevC.66.055803>.

[173] HOROWITZ, C. J.; PIEKAREWICZ, J. Constraining urca cooling of neutron stars from the neutron radius of ^{208}Pb. *Phys. Rev. C*, American Physical Society, v. 66, p. 055803, Nov 2002. Disponível em: <https://link.aps.org/doi/10.1103/PhysRevC.66.055803>.

[174] CHEN, W.-C.; PIEKAREWICZ, J. Building relativistic mean field models for finite nuclei and neutron stars. *Phys. Rev. C*, American Physical Society, v. 90, p. 044305, Oct 2014. Disponível em: <https://link.aps.org/doi/10.1103/PhysRevC.90.044305>.

[175] LOPES, L. L. Hyperonic neutron stars: reconciliation between nuclear properties and NICER and LIGO/VIRGO results. *Commun. Theor. Phys.*, v. 74, n. 1, p. 015302, 2022.

[176] LALAZISSIS, G. A.; KÖNIG, J.; RING, P. New parametrization for the lagrangian density of relativistic mean field theory. *Phys. Rev. C*, American Physical Society, v. 55, p. 540–543, Jan 1997. Disponível em: <https://link.aps.org/doi/10.1103/PhysRevC.55.540>.

[177] LOPES, L. L.; MENEZES, D. P. On the Nature of the Mass-gap Object in the GW190814 Event. *Astrophys. J.*, v. 936, n. 1, p. 41, 2022.

[178] BHOWMICK, B. et al. Massive neutron stars with a hyperonic core: A case study with the IUFSU relativistic effective interaction. *Phys. Rev. C*, v. 89, n. 6, p. 065806, 2014.

[179] ABBOTT, R. et al. GW190814: Gravitational Waves from the Coalescence of a 23 Solar Mass Black Hole with a 2.6 Solar Mass Compact Object. *The Astrophysical Journal Letters*, v. 896, n. 2, p. L44, jun. 2020.

[180] MÜLLER, H.; SEROT, B. D. Phase transitions in warm, asymmetric nuclear matter. *Phys. Rev. C*, American Physical Society, v. 52, p. 2072–2091, Oct 1995. Disponível em: <https://link.aps.org/doi/10.1103/PhysRevC.52.2072>.

[181] AVANCINI, S. S. et al. Spinodal instabilities and the distillation effect in relativistic hadronic models. *Phys. Rev. C*, American Physical Society, v. 74, p. 024317, Aug 2006. Disponível em: <https://link.aps.org/doi/10.1103/PhysRevC.74.024317>.

[182] MARUYAMA, T. et al. Nuclear "pasta" structures and the charge screening effect. *Phys. Rev. C*, American Physical Society, v. 72, p. 015802, Jul 2005. Disponível em: <https://link.aps.org/doi/10.1103/PhysRevC.72.015802>.

[183] AVANCINI, S. S. et al. Nuclear "pasta" phase within density dependent hadronic models. *Phys. Rev. C*, American Physical Society, v. 79, p. 035804, Mar 2009. Disponível em: <https://link.aps.org/doi/10.1103/PhysRevC.79.035804>.

[184] LATTIMER, J. et al. Physical properties of hot, dense matter: The general case. *Nuclear Physics A*, v. 432, n. 3, p. 646 – 742, 1985. ISSN 0375-9474. Disponível em: <http://www.sciencedirect.com/science/article/pii/0375947485900065>.

[185] PAIS, H.; CHIACCHIERA, S.; PROVIDÊNCIA, C. Light clusters, pasta phases, and phase transitions in core-collapse supernova matter. *Phys. Rev. C*, American Physical Society, v. 91, p. 055801, May 2015. Disponível em: <https://link.aps.org/doi/10.1103/PhysRevC.91.055801>.

[186] PAIS, H. et al. Light and heavy clusters in warm stellar matter. *Nucl. Sci. Tech.*, v. 29, n. 12, p. 181, 2018.

[187] AGARWAL, S.; MIERLE, K.; The Ceres Solver Team. *Ceres Solver*. 2022. Disponível em: <https://github.com/ceres-solver/ceres-solver>.

[188] CONTRIBUTORS, G. P. *GSL - GNU Scientific Library - GNU Project - Free Software Foundation (FSF)*. 2010. Disponível em: <http://www.gnu.org/software/gsl/>.

[189] PELICER, M. *Nuclear astrophysics folder*. 2023. Disponível em: <https://github.com/mrpelicer>.

[190] GULMINELLI, F.; RADUTA, A. R. Ensemble inequivalence in supernova matter within a simple model. *Phys. Rev. C*, American Physical Society, v. 85, p. 025803, Feb 2012. Disponível em: <https://link.aps.org/doi/10.1103/PhysRevC.85.025803>.

[191] PATHRIA, R. *Statistical Mechanics*. Elsevier Science & Technology Books, 1972. (International series of monographs in natural philosophy). ISBN 9780080167473. Disponível em: <https://books.google.com.br/books?id=ejUVnQEACAAJ>.

[192] ITOH, N.; KOHYAMA, Y. Electrical and Thermal Conductivities of Dense Matter in the Crystalline Lattice Phase. II. Impurity Scattering. *The Astrophysical Journal*, v. 404, p. 268, fev. 1993.

[193] ITOH, N.; HAYASHI, H.; KOHYAMA, Y. Electrical and Thermal Conductivities of Dense Matter in the Crystalline Lattice Phase. III. Inclusion of Lower Densities. *The Astrophysical Journal*, v. 418, p. 405, nov. 1993.

[194] MEISEL, Z. et al. Nuclear Physics of the Outer Layers of Accreting Neutron Stars. *J. Phys. G*, v. 45, n. 9, p. 093001, 2018.

[195] PELICER, M. R. et al. Fluctuations in the nuclear pasta phase. *Phys. Rev. C*, v. 104, n. 2, p. L022801, 2021.

[196] MONTOLI, A. et al. Bayesian estimate of the superfluid moments of inertia from the 2016 glitch in the Vela pulsar. *Astronomy and Astrophysics Journal*, v. 642, p. A223, out. 2020.

[197] PAGE, D.; REDDY, S. Thermal and transport properties of the neutron star inner crust. *arXiv e-prints*, p. arXiv:1201.5602, jan. 2012.

[198] SCHMITT, A.; SHTERNIN, P. Reaction rates and transport in neutron stars. *Astrophys. Space Sci. Libr.*, v. 457, p. 455–574, 2018.

[199] BRANSGROVE, A.; LEVIN, Y.; BELOBORODOV, A. Magnetic field evolution of neutron stars - I. Basic formalism, numerical techniques and first results. *Monthly Notices of the Royal Astronomical Society*, v. 473, n. 2, p. 2771–2790, jan. 2018.

[200] PONS, J. A.; VIGANÒ, D. Magnetic, thermal and rotational evolution of isolated neutron stars. *Living Reviews in Computational Astrophysics*, Springer Science and Business Media LLC, v. 5, n. 1, dec 2019. Disponível em: <https://doi.org/10.1007\%2Fs41115-019-0006-7>.

[201] CAMELIO, G. et al. Simulating bulk viscosity in neutron stars I: formalism. *arXiv e-prints*, p. arXiv:2204.11809, abr. 2022.

[202] SHTERNIN, P. S.; YAKOVLEV, D. G. Electron thermal conductivity owing to collisions between degenerate electrons. *Phys. Rev. D*, v. 74, p. 043004, 2006.

[203] SHTERNIN, P. S. Shear viscosity of degenerate electron matter. *J. Phys. A*, v. 41, p. 205501, 2008.

[204] CHAMEL, N. Neutron conduction in the inner crust of a neutron star in the framework of the band theory of solids. *Phys. Rev. C*, American Physical Society, v. 85, p. 035801, Mar 2012. Disponível em: <https://link.aps.org/doi/10.1103/PhysRevC.85.035801>.

[205] DEIBEL, A. et al. Late time cooling of neutron star transients and the physics of the inner crust. *Astrophys. J.*, v. 839, n. 2, p. 95, 2017.

[206] POTEKHIN, A. Y.; PONS, J. A.; PAGE, D. Neutron stars - cooling and transport. *Space Sci. Rev.*, v. 191, n. 1-4, p. 239–291, 2015.

[207] ASHCROFT, N. W.; MERMIN, N. D. *Solid state physics*. [S.l.]: Cengage Learning, 2022.

[208] SYKES, J.; BROOKER, G. The transport coefficients of a fermi liquid. *Annals of Physics*, v. 56, n. 1, p. 1–39, 1970. ISSN 0003-4916. Disponível em: <https://www.sciencedirect.com/science/article/pii/0003491670900023>.

[209] FREIRE, A. *Partial differential equations*. [S.l.]: University of Tennessee, 2022.

[210] GALLIER, J. *Notes on Spherical Harmonics and Linear Representations of Lie Groups*. [S.l.]: University of Pennsylvania, 2013.

[211] PINES, D.; NOZIÈRES, P. *Theory of Quantum Liquids: Normal Fermi Liquids*. [S.l.]: CRC Press, 2018.

[212] LANDAU, L. D.; LIFSHITZ, E. M.; PITAEVSKI, L. P. *Course of theoretical physics: Physical Kinetics*. [S.l.]: Pergamon P., 1981.

[213] BERESTETSKII, V. B.; LIFSHITZ, E. M.; PITAEVSKII, L. P. *Quantum Electrodynamics: Volume 4*. [S.l.]: Butterworth-Heinemann, 1982. v. 4.

[214] HASSANI, S. *Mathematical physics: a modern introduction to its foundations*. [S.l.]: Springer Science & Business Media, 2013.

[215] JANCOVICI, B. On the relativistic degenerate electron gas. *Il Nuovo Cimento (1955-1965)*, Springer, v. 25, n. 2, p. 428–455, 1962.

[216] HORING, N. J. Friedel density oscillations about a coulombic impurity in a high magnetic field. *Phys. Rev.*, American Physical Society, v. 186, p. 434–442, Oct 1969. Disponível em: <https://link.aps.org/doi/10.1103/PhysRev.186.434>.

[217] SHARMA, R.; REDDY, S. Anisotropic electronic screening and damping in magnetars. *Phys. Rev. C*, American Physical Society, v. 83, p. 025803, Feb 2011. Disponível em: <https://link.aps.org/doi/10.1103/PhysRevC.83.025803>.

[218] JUNG, Y.-D. Dynamic screening effects on electron-ion coulomb bremsstrahlung in dense plasmas. *Phys. Rev. E*, American Physical Society, v. 55, p. 3369–3372, Mar 1997. Disponível em: <https://link.aps.org/doi/10.1103/PhysRevE.55.3369>.

[219] GENNES, P. G. de; PROST, J. *The physics of liquid crystals*. [S.l.]: Clarendon, Oxford, 1993.

[220] CHANDRASEKHAR, S. *Liquid crystals*. [S.l.]: Cambridge University Press, 1992.

[221] SCHUETRUMPF, B.; MARTÍNEZ-PINEDO, G.; REINHARD, P.-G. Survey of nuclear pasta in the intermediate-density regime: Structure functions for neutrino scattering. *Phys. Rev. C*, American Physical Society, v. 101, p. 055804, May 2020. Disponível em: <https://link.aps.org/doi/10.1103/PhysRevC.101.055804>.

[222] SCHMIDT, P. et al. Longitudinal and transversal collective modes in strongly correlated plasmas. *Phys. Rev. E*, American Physical Society, v. 56, p. 7310–7313, Dec 1997. Disponível em: <https://link.aps.org/doi/10.1103/PhysRevE.56.7310>.

[223] YOUNG, D. A.; COREY, E. M.; DEWITT, H. E. Analytic fit to the one-component-plasma structure factor. *Phys. Rev. A*, American Physical Society, v. 44, p. 6508–6512, Nov 1991. Disponível em: <https://link.aps.org/doi/10.1103/PhysRevA.44.6508>.

[224] HANSEN, J. P. Statistical mechanics of dense ionized matter. i. equilibrium properties of the classical one-component plasma. *Phys. Rev. A*, American Physical Society, v. 8, p. 3096–3109, Dec 1973. Disponível em: <https://link.aps.org/doi/10.1103/PhysRevA.8.3096>.

[225] SLATTERY, W. L.; DOOLEN, G. D.; DEWITT, H. E. Improved equation of state for the classical one-component plasma. *Phys. Rev. A*, American Physical Society, v. 21, p. 2087–2095, Jun 1980. Disponível em: <https://link.aps.org/doi/10.1103/PhysRevA.21.2087>.

[226] LANDAU, L. D.; LIFSHITZ, E. M. *Statistical Physics*. [S.l.]: Pergamon Press, Oxford, 1969.

[227] HANSEN, J.-P.; MCDONALD, I. R. *Theory of simple liquids: with applications to soft matter*. [S.l.]: Academic press, 2013.

[228] GORI-GIORGI, P.; SACCHETTI, F.; BACHELET, G. B. Analytic static structure factors and pair-correlation functions for the unpolarized homogeneous electron gas. *Phys. Rev. B*, American Physical Society, v. 61, p. 7353–7363, Mar 2000. Disponível em: <https://link.aps.org/doi/10.1103/PhysRevB.61.7353>.

[229] PETHICK, C.; POTEKHIN, A. Liquid crystals in the mantles of neutron stars. *Physics Letters B*, v. 427, n. 1, p. 7–12, 1998. ISSN 0370-2693. Disponível em: <https://www.sciencedirect.com/science/article/pii/S0370269398003414>.

[230] PONIEWIERSKI, A. et al. Dynamic correlation functions for finite and infinite smectic-a systems: theory and experiment. *Phys. Rev. E*, American Physical Society, v. 58, p. 2027–2040, August 1998.

[231] PETHICK, C. J.; ZHANG, Z.; KOBYAKOV, D. N. Elastic properties of phases with nonspherical nuclei in dense matter. *Phys. Rev. C*, v. 101, n. 5, p. 055802, 2020.

[232] BRINK, D.; SATCHLER, G. *Theory of Angular Momentum*. [S.l.]: Clarendon Press, Oxford, 1968.

[233] EDMONDS, A. R. *Angular momentum in quantum mechanics*. [S.l.]: Princeton university press, 2016.

[234] RACAH, G. Theory of complex spectra. I. *Phys. Rev.*, American Physical Society, v. 61, p. 186–197, Feb 1942. Disponível em: <https://link.aps.org/doi/10.1103/PhysRev.61.186>.

[235] RACAH, G. Theory of complex spectra. II. *Phys. Rev.*, American Physical Society, v. 62, p. 438–462, Nov 1942. Disponível em: <https://link.aps.org/doi/10.1103/PhysRev.62.438>.

[236] SHILOV, G. E. *Linear algebra*. [S.l.]: Courier Corporation, 2012.

[237] CHATTERJEE, D.; NOVAK, J.; OERTEL, M. Magnetic field distribution in magnetars. *Phys. Rev. C*, American Physical Society, v. 99, p. 055811, May 2019. Disponível em: <https://link.aps.org/doi/10.1103/PhysRevC.99.055811>.

[238] FUJISAWA, K.; KISAKA, S. Magnetic field configurations of a magnetar throughout its interior and exterior – core, crust and magnetosphere. *Monthly Notices of the Royal Astronomical Society*, v. 445, n. 3, p. 2777–2793, 10 2014. ISSN 0035-8711. Disponível em: <https://doi.org/10.1093/mnras/stu1911>.

[239] NANDI, R. et al. Inner crusts of neutron stars in strongly quantizing magnetic fields. *The Astrophysical Journal*, The American Astronomical Society, v. 736, n. 2, p. 156, jul 2011. Disponível em: <https://dx.doi.org/10.1088/0004-637X/736/2/156>.

[240] LIMA, R. C. R. de; AVANCINI, S. S.; PROVIDÊNCIA, C. Effect of strong magnetic fields on the nuclear "pasta" phase structure. *Phys. Rev. C*, American Physical Society, v. 88, p. 035804, Sep 2013. Disponível em: <https://link.aps.org/doi/10.1103/PhysRevC.88.035804>.

[241] BAO, S. S.; HU, J. N.; SHEN, H. Impact of strong magnetic fields on the inner crust of neutron stars. *Phys. Rev. C*, American Physical Society, v. 103, p. 015804, Jan 2021. Disponível em: <https://link.aps.org/doi/10.1103/PhysRevC.103.015804>.

[242] WANG, X. et al. Pasta phases in neutron stars under strong magnetic fields. *Phys. Rev. D*, American Physical Society, v. 105, p. 063004, Mar 2022. Disponível em: <https://link.aps.org/doi/10.1103/PhysRevD.105.063004>.

[243] PELICER, M. R. et al. Anisotropic electron transport in the nuclear pasta phase. *Mon. Not. Roy. Astron. Soc.*, v. 521, n. 1, p. 743–759, 2023.

[244] CAI, B.-J.; LI, B.-A. Symmetry energy of cold nucleonic matter within a relativistic mean field model encapsulating effects of high-momentum nucleons induced by short-range correlations. *Phys. Rev. C*, American Physical Society, v. 93, p. 014619, Jan 2016. Disponível em: <https://link.aps.org/doi/10.1103/PhysRevC.93.014619>.

[245] SOUZA, L. A. et al. Effects of short-range nuclear correlations on the deformability of neutron stars. *Phys. Rev. C*, American Physical Society, v. 101, p. 065202, Jun 2020. Disponível em: <https://link.aps.org/doi/10.1103/PhysRevC.101.065202>.

[246] LOURENÇO, O.; FREDERICO, T.; DUTRA, M. Dark matter component in hadronic models with short-range correlations. *Phys. Rev. D*, American Physical Society, v. 105, p. 023008, Jan 2022. Disponível em: <https://link.aps.org/doi/10.1103/PhysRevD.105.023008>.

[247] LOURENÇO, O. et al. Dark matter effects on tidal deformabilities and moment of inertia in a hadronic model with short-range correlations. *Phys. Rev. D*, American Physical Society, v. 106, p. 043010, Aug 2022. Disponível em: <https://link.aps.org/doi/10.1103/PhysRevD.106.043010>.

[248] DUTRA, M.; LENZI, C. H.; LOURENÇO, O. Dark particle mass effects on neutron star properties from a short-range correlated hadronic model. *Monthly Notices of the Royal Astronomical Society*, v. 517, n. 3, p. 4265–4274, 10 2022. ISSN 0035-8711. Disponível em: <https://doi.org/10.1093/mnras/stac2986>.

[249] PELICER, M. R. et al. Do short range correlations inhibit the appearance of the nuclear pasta? Nov 2022.

[250] GLENDENNING, N. K.; MOSZKOWSKI, S. A. Reconciliation of neutron-star masses and binding of the Λ in hypernuclei. *Phys. Rev. Lett.*, American Physical Society, v. 67, p. 2414–2417, Oct 1991. Disponível em: <https://link.aps.org/doi/10.1103/PhysRevLett.67.2414>.

[251] LOPES, L. L.; MENEZES, D. P. Hypernuclear matter in a complete SU(3) symmetry group. *Physical Review C*, v. 89, n. 2, p. 25805, 2014.

[252] GREENE, G. L. et al. Measurement of the neutron magnetic moment. *Phys. Rev. D*, American Physical Society, v. 20, p. 2139–2153, Nov 1979. Disponível em: <https://link.aps.org/doi/10.1103/PhysRevD.20.2139>.

[253] SCHNEIDER, G. et al. Double-trap measurement of the proton magnetic moment at 0.3 parts per billion precision. *Science*, v. 358, n. 6366, p. 1081–1084, 2017. Disponível em: <https://www.science.org/doi/abs/10.1126/science.aan0207>.

[254] ZYLA, P. A. et al. Review of Particle Physics. *PTEP*, v. 2020, n. 8, p. 083C01, 2020.

[255] KOTULLA, M. et al. The reaction $\gamma p \rightarrow \pi^0 \gamma' p$ and the magnetic dipole moment of the $\Delta^+(1232)$ resonance. *Phys. Rev. Lett.*, American Physical Society, v. 89, p. 272001, Dec 2002. Disponível em: <https://link.aps.org/doi/10.1103/PhysRevLett.89.272001>.

[256] CLOET, I.; LEINWEBER, D.; THOMAS, A. Delta baryon magnetic moments from lattice QCD. *Physics Letters B*, v. 563, n. 3, p. 157–164, 2003. ISSN 0370-2693. Disponível em: <https://www.sciencedirect.com/science/article/pii/S0370269303004180>.

[257] CASTRO, G. L.; MARIANO, A. Elastic and radiative π+p scattering and properties of the Δ++ resonance. *Nuclear Physics A*, v. 697, n. 1, p. 440–468, 2002. ISSN 0375-9474. Disponível em: <https://www.sciencedirect.com/science/article/pii/S0375947401012465>.

[258] CASTRO, G. L.; MARIANO, A. Determination of the Δ++ magnetic dipole moment. *Physics Letters B*, v. 517, n. 3, p. 339–344, 2001. ISSN 0370-2693. Disponível em: <https://www.sciencedirect.com/science/article/pii/S0370269301009807>.

[259] DESER, S.; WALDRON, A.; PASCALUTSA, V. Massive spin 3/2 electrodynamics. *Phys. Rev. D*, American Physical Society, v. 62, p. 105031, Oct 2000. Disponível em: <https://link.aps.org/doi/10.1103/PhysRevD.62.105031>.

[260] PAOLI, M. G. de et al. The Rarita-Schwinger Particles Under de Influence of Strong Magnetic Fields. *J. Phys. G*, v. 40, p. 055007, 2013.

[261] BRODERICK, A.; PRAKASH, M.; LATTIMER, J. M. The equation of state of neutron star matter in strong magnetic fields. *The Astrophysical Journal*, American Astronomical Society, v. 537, n. 1, p. 351–367, jul 2000. Disponível em: <https://doi.org/10.1086/309010>.

[262] MAO, G.-J.; IWAMOTO, A.; LI, Z.-X. A study of neutron star structure in strong magnetic fields that includes anomalous magnetic moments. *Chinese Journal of Astronomy and Astrophysics*, IOP Publishing, v. 3, n. 4, p. 359–374, aug 2003. Disponível em: <https://doi.org/10.1088/1009-9271/3/4/359>.

[263] STRICKLAND, M.; DEXHEIMER, V.; MENEZES, D. Bulk Properties of a Fermi Gas in a Magnetic Field. *Phys. Rev. D*, v. 86, p. 125032, 2012.

[264] FABBIETTI, L.; SARTI, V. M.; DOCE, O. V. Study of the strong interaction among hadrons with correlations at the lhc. *Annual Review of Nuclear and Particle Science*, v. 71, n. 1, p. 377–402, 2021. Disponível em: <https://doi.org/10.1146/annurev-nucl-102419-034438>.

[265] ACHARYA, S. et al. First observation of an attractive interaction between a proton and a cascade baryon. *Phys. Rev. Lett.*, American Physical Society, v. 123, p. 112002, Sep 2019. Disponível em: <https://link.aps.org/doi/10.1103/PhysRevLett.123.112002>.

[266] FRIEDMAN, E.; GAL, A. Constraints on Ξ− nuclear interactions from capture events in emulsion. *Phys. Lett. B*, v. 820, p. 136555, 2021.

[267] COZMA, M. D.; TSANG, M. B. In-medium Δ(1232) potential, pion production in heavy-ion collisions and the symmetry energy. *Eur. Phys. J. A*, v. 57, n. 11, p. 309, 2021.

[268] BODEK, A.; CAI, T. Comparison of optical potential for nucleons and Δ resonances: In electron scattering from nuclear targets. *Eur. Phys. J. C*, v. 80, n. 7, p. 655, 2020.

[269] WEHRBERGER, K.; BEDAU, C.; BECK, F. Electromagnetic excitation of the delta-baryon in quantum hadrodynamics. *Nuclear Physics A*, v. 504, n. 4, p. 797–817, 1989. ISSN 0375-9474. Disponível em: <https://www.sciencedirect.com/science/article/pii/0375947489900080>.

[270] RIBES, P. et al. Interplay between delta particles and hyperons in neutron stars. *The Astrophysical Journal*, American Astronomical Society, v. 883, n. 2, p. 168, oct 2019. Disponível em: <https://doi.org/10.3847/1538-4357/ab3a93>.

[271] RADUTA, A. R. Δ-admixed neutron stars: spinodal instabilities and dUrca processes. *Phys. Lett. B*, v. 814, p. 136070, 2021.

[272] OLIVEIRA, J. de et al. Delta matter formation in dense asymmetric nuclear medium. *Modern Physics Letters A*, World Scientific, v. 15, n. 24, p. 1529–1537, 2000.

[273] OLIVEIRA, J. de et al. Effects of δ-baryon interaction strength on neutron stars properties. *International Journal of Modern Physics D*, World Scientific, v. 16, n. 02n03, p. 175–183, 2007.

[274] DEXHEIMER, V.; MARQUEZ, K. D.; MENEZES, D. P. Delta baryons in neutron-star matter under strong magnetic fields. *Eur. Phys. J. A*, v. 57, n. 7, p. 216, 2021.

[275] GOMES, R. O. et al. Limiting magnetic field for minimal deformation of a magnetized neutron star. *Astron. Astrophys.*, v. 627, p. A61, 2019.

[276] TOLMAN, R. C. Static solutions of Einstein's field equations for spheres of fluid. *Phys. Rev.*, v. 55, p. 364–373, 1939.

[277] OPPENHEIMER, J. R.; VOLKOFF, G. M. On Massive neutron cores. *Phys. Rev.*, v. 55, p. 374–381, 1939.

[278] DEXHEIMER, V. et al. What is the magnetic field distribution for the equation of state of magnetized neutron stars? *Phys. Lett. B*, v. 773, p. 487–491, 2017.

[279] CHATTERJEE, D.; NOVAK, J.; OERTEL, M. Magnetic field distribution in magnetars. *Phys. Rev. C*, v. 99, n. 5, p. 055811, 2019.

[280] MARQUEZ, K. D. et al. Exploring the effects of Δ baryons in magnetars. *Phys. Rev. C*, v. 106, n. 3, p. 035801, 2022.

[281] KLAHN, T.; FISCHER, T. Vector interaction enhanced bag model for astrophysical applications. *Astrophys. J.*, v. 810, n. 2, p. 134, 2015.

[282] FRANZON, B.; GOMES, R. O.; SCHRAMM, S. Effects of the quark-hadron phase transition on highly magnetized neutron stars. *Mon. Not. Roy. Astron. Soc.*, v. 463, n. 1, p. 571–579, 2016.

[283] GOMES, R. O.; CHAR, P.; SCHRAMM, S. Constraining strangeness in dense matter with GW170817. *Astrophys. J.*, v. 877, n. 2, p. 139, 2019.

[284] ALBINO, M. B.; FARIELLO, R.; NAVARRA, F. S. Tidal Deformability of Quark Stars with Repulsive Interactions. *Phys. Rev. D*, v. 104, p. 083011, 2021.

[285] LOPES, L. L.; BIESDORF, C.; MENEZES, D. P. Modified MIT bag Models—part I: Thermodynamic consistency, stability windows and symmetry group. *Phys. Scripta*, v. 96, n. 6, p. 065303, 2021.

[286] LOPES, L. L. et al. Modified MIT Bag Models – part II: QCD phase diagram and hot quark stars. *Phys. Scripta*, v. 96, n. 6, p. 065302, 2021.

[287] BOMBACI, I.; LOGOTETA, D. Quark deconfinement in neutron stars and astrophysical implications. *International Journal of Modern Physics D*, v. 26, n. 2, p. 1730004, jan. 2017.

[288] BHADURI, R.; BHADURI, R. *Models of the Nucleon: From Quarks to Soliton*. Addison-Wesley, Advanced Book Program, 1988. (Advanced book program). ISBN 9780201156737. Disponível em: <https://books.google.com.br/books?id=7smBAAAAIAAJ>.

[289] LOPE-OTER, E.; LLANES-ESTRADA, F. J. Maximum latent heat of neutron star matter independent of general relativity. *Phys. Rev. C*, v. 105, n. 5, p. L052801, maio 2022.

[290] PELICER, M. R.; MENEZES, D. P. Phase transitions and latent heat in magnetized matter. *Eur. Phys. J. A*, v. 58, n. 9, p. 177, 2022.

A Coulomb energy

In this Appendix we outline the main steps in the calculation of the Coulomb energy density. Firstly we explicit the main steps of the derivation, and in the subsections we write the necessary expressions to make the calculation for each geometry.

To arrive at the energy density compactly written in Eq. (2.67) we must calculate the total coulomb energy of the cell for each case. We begin from energy

$$E_c = \frac{1}{2}\int d^3\boldsymbol{r}\rho_{ch}(\boldsymbol{r})\phi(\boldsymbol{r}) \tag{A.1}$$

where ϕ is the electrical potential, that satisfies the Laplace equation

$$\nabla^2\phi = 4\pi e\rho_{ch}, \tag{A.2}$$

and can be directly calculated by integrating the electric field as

$$\phi(r) = -\int_{R_w}^{r} \boldsymbol{E}\cdot d\boldsymbol{l}, \tag{A.3}$$

where we assume the vanishing of field at the boundary of the cell: $\phi(R_W) = 0$. This is direct in our case since the electric field can be calculated from Gauss' law:

$$\int d\boldsymbol{S}\cdot\boldsymbol{E} = 4\pi Q_{\text{in S}}, \tag{A.4}$$

if we consider the cylinders and slabs as sufficiently large ($L_d \gg R_d$) such that contributions from mirroring sides cancel out in $\boldsymbol{E}$.

The contribution to energy comes from the uneven distribution of protons and electrons, and possible contributions from the homogeneous gas ρ_p^{II} would cancel with the corresponding electron counterpart. This implies that we only need to consider the ion contribution to charge, and its electron counterpart. In this section we write:

$$\rho_p = \left(\rho_p^I - \rho_p^{II}\right) = \frac{Z}{V_N}, \tag{A.5}$$

and

$$\rho_e = \frac{Z}{V_W} = f\rho_p, \tag{A.6}$$

where $f = V_N/V_W$ is the volume fraction of the ions.

Regarding the notation, in the following we use $>$ to denote the values of a function in the region $R_N < r < R_W$, and and $>$ variables in the in $0 < r < R_N$. In this manner, the potential, for example, can be written as

$$\phi_> = -\int_{R_w}^{r} \boldsymbol{E}_> \cdot d\boldsymbol{l} \tag{A.7}$$

$$\phi_< = -\int_{R_w}^{R_N} \boldsymbol{E}_> \cdot d\boldsymbol{l} - \int_{R_N}^{r} \boldsymbol{E}_< \cdot d\boldsymbol{l}. \tag{A.8}$$

These are the information needed to calculate the Coulomb energy, in the following we show the main equations needed in the specific cases of droplets, rods and slabs, respectively.

A.1 Sphere

- Electric field:

$$E_r = \frac{q}{r^2}, \tag{A.9}$$

- Volumes:

$$V_N = \frac{4\pi R_N^3}{3}, \quad V_W = \frac{4\pi R_W^3}{3}, \tag{A.10}$$

- Charge distribution:

$$q_< = \frac{4\pi e r^3}{3}(\rho_p - \rho_e), \tag{A.11}$$

$$q_> = \frac{4\pi e}{3}(\rho_p R_N^3 - \rho_e r^3). \tag{A.12}$$

- Potential:

$$\phi_< = \frac{2\pi e}{3}\left[\rho_p\left(3R_i^2 - r^2\right) - \rho_e\left(3R_W^2 - r^2\right)\right], \tag{A.13}$$

$$\phi_> = \frac{2\pi e}{3}\left[2\rho_p\frac{R_N^3}{r} - \rho_e\left(R_W^2 - r^2\right)\right], \tag{A.14}$$

- Coulomb energy:

$$E_C = \frac{16\pi^2 e^2 \rho_p^2 R_N^5}{15}\left[1 - \frac{3}{2}\frac{R_N}{R_W} + \frac{1}{2}\left(\frac{R_N}{R_W}\right)^3\right], \tag{A.15}$$

- Coulomb energy density:

$$\frac{E_C}{V_W} = \frac{4\pi e^2 f \rho_p^2 R_N^2}{5}\left[1 - \frac{3}{2}f + \frac{1}{2}f\right], \tag{A.16}$$

A.2 Cylinder

The electric field of the cylinder in the direction perpendicular to its symmetry axis (z) is

- Electric field:

$$E_r = \frac{2Q}{rL_2} \tag{A.17}$$

- Volumes:

$$V_N = \pi L_2 R_N^2, \quad V_W = \pi L_2 R_W^3 \tag{A.18}$$

- Charge distribution:

$$q_< = \pi e L_2 r^2(\rho_p - \rho_e), \tag{A.19}$$

$$q_> = \pi e L_2(\rho_p R_N^2 - \rho_e r^2). \tag{A.20}$$

- Potential:

$$\phi_< = -\pi e\left[\rho_p\left(R_N^2 \log\left(\frac{R_N}{R_W}\right)^2 + r^2 - R_N^2\right) + \rho_e\left(R_W^2 - r^2\right)\right],, \tag{A.21}$$

$$\phi_> = -\pi e\left[\rho_p R_N^2 \log\left(\frac{r}{R_W}\right)^2 + \rho_e\left(R_W^2 - r^2\right)\right], \tag{A.22}$$

- Coulomb energy:

$$E_C = \frac{\pi^2}{2} L_2 e^2 \rho_p^2 R_N^4\left[-1 - \log\left(\frac{R_N}{R_W}\right)^2 + \left(\frac{R_N}{R_W}\right)^2\right] \tag{A.23}$$

- Energy density:

$$\frac{E_C}{V_W} = \frac{\pi}{2} e^2 \rho_p^2 R_N^2 \left[-1 - \log f + f\right] \tag{A.24}$$

A.3 Slab

For the slab, half its size ($0 < z < R_W$) and double the total Coulomb energy in the end. Considering z to be the symmetry axis, we obtian

- Electric field:

$$E_z = \frac{4\pi q}{L_1^2} \tag{A.25}$$

- Volumes:

$$V_N = 2R_N L_1^2, \quad V_W = 2R_N L_1^2 \tag{A.26}$$

- Charge distribution:

$$q_< = eL_1^2 z(\rho_p - \rho_e), \tag{A.27}$$

$$q_> = eL_1^2(\rho_p R_N - \rho_e z). \tag{A.28}$$

- Potential:

$$\phi_< = 4\pi e \left[\rho_p \left(R_W R_N - \frac{R_N^2}{2} - \frac{z^2}{2}\right) - \rho_e \left(\frac{R_W^2 - z^2}{2}\right)\right], \tag{A.29}$$

$$\phi_> = 4\pi e \left[\rho_p R_N \left(R_W - z\right) - \rho_e \left(\frac{R_W^2 - z^2}{2}\right)\right], \tag{A.30}$$

- Coulomb energy:

$$E_C = \frac{4\pi}{3} L_1^2 e^2 \rho_p^2 R_N^3 \left[-2 + \frac{R_N}{R_W} + \frac{R_W}{R_N}\right] \tag{A.31}$$

- Energy density:

$$\frac{E_C}{V_W} = \frac{2\pi}{3} e^2 \rho_p^2 R_N^2 \left[-2 + \frac{1}{f} + f\right] \tag{A.32}$$

B Publications

1. Pelicer, M. R., Menezes, D. P., Barros Jr., C. C. and Gulminelli, F., *Fluctuations in the nuclear pasta phase*. **Phys. Rev. C**, 104, L022801 (2021) [195].
2. Marquez, K. D., Pelicer, M. R., Ghosh, S., Peterson, J., Chatterjee D., Dexheimer V., and Menezes D. P., *Exploring the effects of Δ baryons in magnetars*. **Phys. Rev. C** 106, 035801 (2022) [280].
3. Pelicer, M. R., Menezes, D. P., *Phase transitions and latent heat in magnetized matter*. **The European Physical Journal A**, 58, 177 (2022) [290].
4. Pelicer, M. R., Menezes, D. P., Dutra, M., Lourenço, O., *Do short range correlations inhibit the appearance of the nuclear pasta?*, **arXiv**:2211.14002 (2022) [249].
5. Pelicer, M. R., Antonelli, M., Menezes, D. P., and Gulminelli, F., *Anisotropic electron transport in the nuclear pasta phase*. **Monthly Notices of the Royal Astronomical Society**, 521, 1 (2023) [243].

Fluctuations in the pasta phase

Mateus R. Pelicer,[1] Débora P. Menezes,[1] Celso C. Barros Jr.,[1] and Francesca Gulminelli[2]

[1]*Depto de Física - CFM - Universidade Federal de Santa Catarina Florianópolis - SC - CP. 476 - CEP 88.040 - 900 - Brazil*
[2]*CNRS and ENSICAEN, UMR6534, LPC, 14050 Caen cédex, France*

Baryonic matter close to the saturation density is very likely to present complex inhomogeneous structures collectively known under the name of pasta phase. At finite temperature, the different geometric structures are expected to coexist, with potential consequences on the neutron star crust conductivity and neutrino transport in supernova matter. In the framework of a statistical multi-component approach, we calculate the composition of matter in the pasta phase considering density, proton fraction, and geometry fluctuations. Using a realistic energy functional from relativistic mean field theory and a temperature and isospin dependent surface tension fitted from Thomas-Fermi calculations, we show that different geometries can coexist in a large fraction of the pasta phase, down to temperatures of the order of the crystallization temperature of the neutron star crust. Quantitative estimates of the charge fluctuations are given.

Introduction: It is known since the early '80s [1] that the equilibrium state of electrically neutral dense baryonic matter, close to the saturation density ($n_{sat} \approx 0.17$ fm^{-3}) of symmetric nuclear matter, may not correspond to a lattice of spherical nuclei, but rather to a spatially periodic distribution of inhomogeneities with cylindrical (rods) or planar (slabs) symmetry. These complex pasta phases could be present in the inner crust of neutron stars as well as in the central regions of core collapse supernovae during the infall and early post-bounce phase. Different studies suggest that they may have sizeable impact on different astrophysical phenomena, such as the magneto-thermal evolution of compact stars [2], neutrino opacity [3, 4], timing properties of X-ray pulsars [5], and the ellipticity of neutron stars that can be potentially probed by gravitational wave measurements [6]. The energy barrier between the different shapes being often of a few KeV only, it is expected that complex shapes including impurities and defects might appear even in the crust of catalyzed neutron stars [7–9] leading to an increased resistivity. Above the crystallization temperature, $T_m \approx 700$ KeV in the pasta region [10], pasta matter has to be seen as a liquid and the calculation of transport properties requires the evaluation of the electrical and thermal conductivity tensor averaged over finite domains. A rich phenomenology is expected depending on the orientation of the nuclear clusters [11] as well as their distribution.

In this paper, we make a first step towards the complex problem related to the anisotropic transport in the pasta phase at finite temperature, by calculating the distribution and charge variance of the different geometrical structures in a multi-component approach with a realistic microscopic energy functional.

Pasta phases in a Relativistic Mean Field Approach:

In the single nucleus approximation it is assumed that, at a given thermodynamical condition (ρ_B, Y_p, T), a crystalline structure of identical cells is formed. Each cell contains a dense cluster at baryonic density $\rho^I = \rho_p^I + \rho_n^I$, occupying a volume fraction f of the cell, and surrounded by a homogeneous gas of baryons at density $\rho^{II} = \rho_p^{II} + \rho_n^{II}$. The cell is neutralized by an electron gas of homogeneous density $\rho_e = Y_p \rho_B$, modelled as a free relativistic gas with free energy density $\mathscr{F}_e$, see Refs. [12, 13] for explicit expressions. The different shapes of the pasta structures is denoted by the integer $d = 3, 2, 1$, referring to droplets, rods and slabs, respectively.

The free energy density of a cell of total baryonic density $\rho_B = \rho_p + \rho_n$ and proton fraction $Y_p = \rho_p/\rho_B$ is given by [12]

$$\mathscr{F}_{WS} = f\mathscr{F}_b^I + (1-f)\mathscr{F}_b^{II} + \beta\mathscr{F}_{sc,d} + \mathscr{F}_e, \qquad (1)$$

with $\beta = f$ for droplets, rods and slabs, and $\beta = 1-f$ for tubes and bubbles. The constraints of mass and charge conservation are imposed on the cells, $\rho_q = f(\rho_q^I - \rho_q^{II}) + \rho_q^{II}$, with $q = n, p$.

For all our numerical applications, the bulk free energy densities $\mathscr{F}_b^{I(II)} = \mathscr{F}_b(\rho_p^{I(II)}, \rho_n^{I(II)})$ of the dense (dilute) fraction of the cell are calculated with the IUFSU parametrization [14] of the quantum hadrodynamics model in the mean field approximation (RMF) [15] which is consistent with a number of experimental and observational constraints [16–18]. This version of the RMF model includes σ, ω and ρ mesons with non-linear scalar and vector couplings, as well as an $\omega-\rho$ interaction term, with a coupling fitted such as to reproduce the experimental symmetry energy of nuclear matter [14].

The interface free energy density $\mathscr{F}_{sc,d}$ contains a surface and a Coulomb term and it is written as [1, 19]:

$$\mathscr{F}_{sc,d} = \mathscr{F}_{s,d} + \mathscr{F}_{c,d} = \frac{\sigma(Y_p, T)\, d}{R_d} + 2\pi e^2 R_d^2 \left(\rho_p^I - \rho_p^{II}\right)^2 \Phi_d(\beta), \qquad (2)$$

with the Φ_d function given by

$$\Phi_d(\beta) = \begin{cases} \left(\frac{2-d\beta^{1-2/d}}{d-2} + \beta\right)\frac{1}{d+2}, & d = 1, 3; \\ \frac{\beta-1-ln(\beta)}{d+2}, & d = 2. \end{cases} \qquad (3)$$

The temperature and proton fraction dependent surface tension coefficient σ is taken from Ref. [20], where a fit was obtained from Thomas-Fermi calculations employing the same IUFSU functional.

The equilibrium densities in the cells can be found by minimizing the thermodynamic potential Ω with respect to

the 6 independent variables, here chosen as the cluster and gas densities ρ_q^I, ρ_q^{II}, $q = n, p$, the volume fraction f, and the linear dimension of the pasta R_d:

$$\Omega = \mathscr{F} - \mu_p \rho_p - \mu_n \rho_n, \tag{4}$$

with the conservation laws imposed by the chemical potentials, μ_p and μ_n.

The equilibrium equations from the minimization of Eq. (4) are obtained as:

$$\mu_p^I = \mu_p^{II} - \frac{2\beta \mathscr{F}_{c,d}}{f(1-f)(\rho_p^I - \rho_p^{II})}, \tag{5}$$

$$\mu_n^I = \mu_n^{II}, \tag{6}$$

$$-P^I + P^{II} + \frac{d\beta}{df}\left(\mathscr{F}_{sc,d} + \beta \mathscr{F}_{c,d} \frac{1}{\Phi}\frac{d\Phi}{d\beta}\right) - \frac{2\beta \mathscr{F}_c \left(\rho_p^I - f(\rho_p^I - \rho_p^{II})\right)}{f(1-f)\left(\rho_p^{II} - \rho_p^{II}\right)} = 0, \tag{7}$$

$$R_d = \left(\frac{\sigma d}{4\pi e^2 (\rho_p^I - \rho_p^{II})^2 \Phi_d(\beta)}\right)^{1/3}, \tag{8}$$

where μ_q^K, P^K,q=n,p, K=I,II represent bulk chemical potentials and pressures, $\mu_q^K = \partial \mathscr{F}_b^K / \partial \rho_q^K$, $P^K = -\mathscr{F}_b^K + \sum_q \mu_q^K \rho_q^K$. Eqs.(5)-(8) are in agreement with those of Refs. [21, 22]. The variation of the thermodynamic potential additionnally allows us to determine the thermodynamic chemical potentials for the inhomogeneous system, given as:

$$\mu_q = \mu_q^I + \frac{\beta}{f}\frac{\partial \mathscr{F}_{sc,d}}{\partial \rho_q^I} = \mu_q^{II} + \frac{\beta}{1-f}\frac{\partial \mathscr{F}_{sc,d}}{\partial \rho_q^{II}}. \tag{9}$$

The minimization is done independently for the different geometries, and the one corresponding to the minimum value of the optimized $\mathscr{F}_{WS}$ is associated to the equilibrium configuration.

Fluctuations: distribution of pasta structures

The SNA is not realistic in the sense that different cluster sizes and geometries can coexist in a macroscopic system due to the small difference in free energy densities between them. Following Refs. [23-26], we consider a macroscopic volume V composed of different Wigner-Seitz cells of volume V_{WS}^N. Each cell is composed of unbound nucleons and electrons gases, which we assume to be of constant density over the entire volume to avoid discontinuities in the chemical potential between cells. Since the SNA is known to provide a good description of the average thermodynamic quantities of the system, the densities of the nucleon gas ρ_{pg}, ρ_{ng} are given by the solution of the coupled equations (5)-(8), $\rho_{q,g} = \rho_q^{II}$, and the electron density is $\rho_e = \rho_p$. The center of each cell is occupied by a cluster in the pasta phase, with proton and neutron densities ρ_p^N, ρ_n^N fluctuating from cell to cell, and we introduce a superscript N to all the variables which vary with the density fluctuations. We consider that for a same total density ρ_B, that is at a given depth inside the star, domains with pasta structures corresponding to different geometries ($d = 1, 2, 3$ for slabs, rods and droplets, respectively) may also coexist, due to the small free energy barriers.

In the presence of clusters with fluctuating densities and shapes, the global densities are given by

$$\rho_q = \sum_{N,d} n^{N,d} V^N \left(\rho_q^N - \rho_{qg}\right) + \rho_{qg}, \tag{10}$$

where $V^N = f^N V_{WS}^N$ is the volume of the cluster, and $n^{N,d} = \mathscr{N}^{N,d}/V$ is the number density of a cell containing a cluster of density $\rho^N = \rho_p^N + \rho_n^N$ and dimension d, normalized to $\sum_{N,d} n^{N,d} V_{WS}^N = 1$.

In principle, both the cluster volume V^N and the volume fraction f^N could fluctuate independently of ρ_p^N,ρ_n^N and d. However, in a variational theory the linear size of the cluster is determined by the equilibrium with the surrounding gas, whose density is considered constant throughout the system. We therefore consider that the minimization with respect to the linear size Eq.(8) holds in each cell, yielding:

$$R_d^N = \left(\frac{\sigma d}{4\pi e^2 (\rho_p^N - \rho_{pg})^2 \Phi_d(\beta^N)}\right)^{1/3}. \tag{11}$$

Nevertheless, we consider the cluster volume to be independent of its geometry. For a given fluctuation (ρ_p^N, ρ_n^N), the reference volume corresponds to the spherical one

$$V^N = 4\pi \left(R_3^N\right)^3/3, \tag{12}$$

and the Wigner-Seitz cell volume is $V_{WS}^N = V^N/f^N$. The number of protons in the cluster will therefore be given by:

$$Z^N = \left(\rho^N - \rho_{pg}\right) V^N, \tag{13}$$

independently of d. Moreover, we neglect possible long range Coulomb interactions between neighboring cells, by imposing charge neutrality in each cell, thus fixing the cluster volume fraction f^N:

$$\rho_e = f^N(\rho_p^N - \rho_{pg}) + \rho_{pg}. \tag{14}$$

Within these simplifications, we have only two independent variables that can fluctuate from cell to cell, that we take to be (ρ_p^N, ρ_n^N). The free energy density of the global system can be written as $\mathscr{F} = \mathscr{F}_{cl} + \mathscr{F}_g + \mathscr{F}_e$, with $\mathscr{F}_g = \mathscr{F}_b^{II}$, as obtained from the SNA calculation, and the cluster component corresponding to a linear-mixing multi-component plasma expression that reads:

$$\mathscr{F}_{cl} = \sum_{N,d} n^{N,d} V^N \left(\mathscr{F}_b^N - \mathscr{F}_g + \mathscr{F}_{sc,d}^N\right). \tag{15}$$

Because of the additivity of the free energy densities, the grand-partition function of the macroscopic system can be factorized in terms comprising the gases and the clusters [23]:

$$\mathcal{Z} = \mathcal{Z}_g^V \mathcal{Z}_e^V \mathcal{Z}_{cl} \tag{16}$$

with each term being given by

$$\mathcal{Z}_e = \exp\left[-\beta\left(\mathscr{F}_e - \mu_e \rho_e\right)\right], \tag{17}$$

$$\mathcal{Z}_g = \exp\left[-\beta\left(\mathscr{F}_g - \mu_n \rho_{ng} - \mu_p \rho_{pg}\right)\right], \tag{18}$$

$$\mathcal{Z}_{cl} = \sum_{\{n\}} \exp\left[-\beta V \sum_{N,d} n^{N,d} \tilde{\Omega}^{N,d}\right]. \tag{19}$$

Here, the chemical potentials are taken from Eq.(9), and the first sum in Eq.(19) is extended to all the possible values of $n^{N,d}$. $\tilde{\Omega}^{N,d}_{WS}$ is the single-cluster grand-canonical potential, given by [23]:

$$\tilde{\Omega}^{N,d} = V^N\left[\frac{\partial \mathscr{F}_{cl}}{\partial n^{N,d}} - \sum_q \mu_q\left(\rho_q^N - \rho_{qg}\right)\right]. \tag{20}$$

In calculating the variation $\partial \mathscr{F}_{cl}/\partial n^{N,d}$ we can see that a rearrangement term appears:

$$\frac{\partial \mathscr{F}_{cl}}{\partial n^{N,d}} = F^{N,d} + \sum_{M,d'} n^{M,d'} \frac{\partial F^{M,d'}}{\partial n^{N,d}}, \tag{21}$$

with $F^{N,d} = V^N\left[\mathscr{F}_b^N - \mathscr{F}_g + \mathscr{F}_{sc,d}^N\right]$ being the N-cluster free energy. Rearrangement terms systematically appear in thermodynamics when the appropriate thermodynamic potential (here: the Helmotz free energy density $\mathscr{F}_{cl}$) depends on (one of) the system densities. Indeed a variation of a specific cluster density $n^{N,d}$ according to Eq.(21) induces a variation of the global densities ρ_q, as it can be seen from Eq.(10), and consequently of the thermodynamic potential. In our model, $F^{N,d}$ does not specifically depend on ρ_n and ρ_p, but a dependence on ρ_p is enforced by the neutrality condition inside the cell Eq.(14), that can be viewed, for a given fluctuation (ρ_p^N, ρ_n^N), as a definition of the cell volume fraction as a function of the electron density, $f^N \equiv f^N(\rho_p)$.

Using Eqs. (10) and (14) we immediately get:

$$\begin{aligned}\frac{\partial \mathscr{F}_{cl}}{\partial n^{N,d}} &= F^{N,d} + \frac{\partial \rho_p}{\partial n^{N,d}} \sum_{M,d'} n^{M,d'} \frac{\partial F^{M,d'}}{\partial f^M} \frac{\partial f^M}{\partial \rho_p} \\ &= F^{N,d} + V^N\left(\rho_p^N - \rho_{pg}\right) \sum_{M,d'} n^{M,d'} \frac{\partial F^{M,d'}}{\partial f^M} \frac{V^M}{\rho_p^M - \rho_{pg}}.\end{aligned} \tag{22}$$

If we additionally assume that the different averaged quantities are not correlated, such that the average commutes with the product, we end up with the same expression proposed in Refs.[24–26] :

$$\frac{\partial \mathscr{F}_{cl}}{\partial n^{N,d}} = F^{N,d} + V^N\left(\rho_p^N - \rho_{pg}\right)\left\langle \frac{f^M}{\rho_p^M - \rho_{pg}} \frac{\partial \mathscr{F}_{sc,d}^M}{\partial f^M} \right\rangle, \tag{23}$$

where the notation $\langle X \rangle$ indicates an ensemble average, and can be identified with the value of the X variable taken in the SNA approximation with the optimal geometry d_0:

$$\begin{aligned}\left\langle \frac{f^M}{\rho_p^M - \rho_{pg}} \frac{\partial \mathscr{F}_{sc,d}^M}{\partial f^M} \right\rangle &= \frac{\mathscr{F}_{c,d_0}}{\Phi} \frac{d\Phi}{df} \\ &+ \frac{d_0 f}{R_{d_0}\rho_B} \frac{\left(\rho_p^I - \rho_{pg}\right) - Y_p\left(\rho^I - \rho_g\right)}{\rho_p^I - \rho_{pg}} \frac{\partial \sigma}{\partial Y_p}.\end{aligned} \tag{24}$$

Since the number of occurrences of the different configurations $\mathcal{N}^{N,d}$ in the thermodynamic limit can be any integer $m \geq 0$, the sum in Eq.(19) can be analytically computed as in Ref. [24]:

$$\mathscr{Z}_{cl} = \prod_{N,d} \sum_{m=0}^{\infty} \frac{\left(\exp\left[-\beta\tilde{\Omega}^{N,d}\right]\right)^m}{m!} = \prod_{N,d} \exp \omega^{N,d}, \tag{25}$$

with $\omega^{N,d} = \exp\left(-\beta\tilde{\Omega}^{N,d}\right)$.

We can remark that the cluster partition sum Eq.(25) has the same functional form as the ideal gas, with a reduced density $\rho_q^N - \rho_{qg}$ in order to fulfill particle number conservation. The equilibrium chemical potential of the clusters can be immediately deduced:

$$\mu^N = f^N V_{WS}^N\left(\mu_n(\rho_n^N - \rho_{ng}) + \mu_p(\rho_p^N - \rho_{pg})\right). \tag{26}$$

The equilibrium number density for a fluctuation (ρ_p^N, ρ_n^N) is then readily found from the cluster partition sum, and by summing up the different geometries:

$$n^N = \frac{1}{V}\frac{\partial \ln \mathcal{Z}_{cl}}{\partial \beta \mu^N} = \sum_{d=1}^{3} n^{N,d} = \sum_{d=1}^{3} \frac{\omega^{N,d}}{V} \tag{27}$$

Finally, the probability of a cluster with density (ρ_p^N, ρ_n^N) and geometry d is:

$$p^{N,d} = \frac{n^{N,d}}{\sum_{N,d} n^{N,d}} = \frac{\exp\left(-\beta\tilde{\Omega}^{N,d}\right)}{\sum_{N,d} \exp\left(-\beta\tilde{\Omega}^{N,d}\right)}. \tag{28}$$

Results:

To illustrate the proportion of different pasta structures at different thermodynamic conditions we show, in Fig. 1, the probability of each pasta structure for $Y_p = 0.1$ and 0.3, which are typical proton fractions encountered in the neutron star inner crust, and in supernova cores, respectively. We define the probability of a pasta structure by summing the probabilities of its occurence with different densities, $P^d = \sum_N p^{N,d}$. For increasing temperatures or isospin asymmetry, different pasta structures are more likely to coexist. However, shape coexistence cannot be neglected in a large range of densities even for the typical thermodynamic conditions of the inner crust at the crystallization point ($T \approx 1$ MeV, $Y_p \approx 0.1$ [10]), suggesting that important impurities may characterize even the catalyzed crust[8, 9].

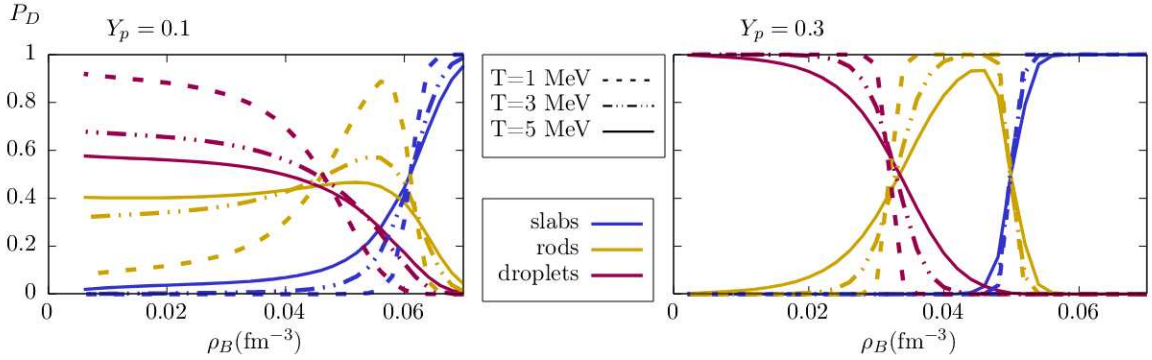

FIG. 1: Probability for the pasta structures at proton fractions $Y_p = 0.1$ (left) and 0.3 (right) and temperatures T=5, 3, 1 MeV plotted with solid, dash-double-dotted and dashed lines, respectively. Geometries are plotted with different colors: droplets are in magenta, rods in yellow and slabs in blue.

The linear dimension of the structures is measured by the average radius

$$\langle R^N \rangle = \sum_{N,d} p^{N,d} R_d^N, \tag{29}$$

illustrated for $T = 3$ MeV and $Y_p = 0.3$ and 0.5 in Fig. 2, where the dominant pasta structure occupies most of the system volume fraction away from the transition density between geometries. In such regions the average radius and the one obtained from the SNA solution – Eq. (8) – coincide, but differences are observed in the transition regions.

Finally, the disorder of the composition can be quantified by the variance of proton number:

$$\Delta Z = \sum_{N,d} p^{N,d} \left(Z^N - \langle Z^N \rangle \right)^2, \tag{30}$$

that is displayed in Fig.3 for T=1 MeV, as a solid line. As observed in previous works [25, 26], this variance is an increasing function of the baryonic density and temperature

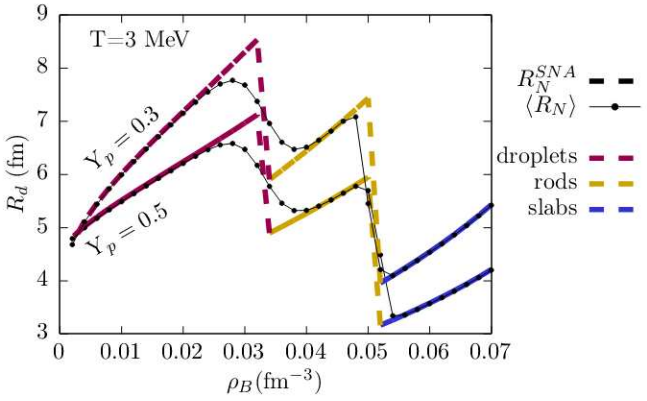

FIG. 2: Average linear radius (dashed-dotted) and equilibrium linear radius (colored dashed), as given by Eqs. (29) and (8), for proton fractions $Y_p = 0.1$, 0.3 and T=3 MeV. The values in the SNA are colorred according to the geometry, as described in Fig. 1.

(not shown). Notice that the variance is mostly independent of the presence of different geometries due to the normalization to the size of the spherical cell.

To quantify the impurities present due to the different pasta structures, we must consider that an incident probe is sensitive to their orientation [11]. A full calculation of the transport coefficients in the different thermodynamic conditions, and according to the possible pasta orientations is left for future work. However, we can appreciate the importance of the anisotropies due to the impurities, by computing the effective charge variance in the hypothesis of a common symmetry axis x for the different local domains characterized by a given geometry. To do so, we consider the free parameters $L_{d,WS}$ in the volume of slabs and rods:

$$V^N = \pi R_2^N L_{2,WS}, \quad \text{and} \quad V^N = R_1^N L_{1,WS}^2 \tag{31}$$

which can be determined by equating the above to the cluster volume defined in Eq. (12), in order to define the effective number of protons as seen by an incident probe

$$Z_{d,k}^{*N} = Z^N S_{d,k}^N / S_3^N, \tag{32}$$

where k=x, y, z is the axis of motion of the incident probe, $S_{d,k}$ is the surface area of the pasta geometry perceived by the probe, summarized in Tab. I and $S_3^N = 2\pi (R_3^N)^2$ is half of the droplet total surface. Thus we can calculate the variances for the different orientations using Eq.(30) by replacing $Z^N \to Z_{d,k}^{*N}$. The orientation-dependent variances are also shown in Fig. 3. Though the order of magnitude of this

Axis	$S_{2,k}$	$S_{1,k}$
x	$\pi (R_2^N)^2$	$R_1^N L_{1,WS}$
y	$\pi R_2^N L_{2,WS}$	$R_1^N L_{1,WS}$
z	$\pi R_2^N L_{2,WS}$	$L_{1,WS}^2$

TABLE I: Effective surface of the pasta structure in the axis of motion of an incident probe. The rods are considered to have length $L_{2,WS}$ in the x-axis, and the slabs have length $L_{1,WS}$ in the x and y directions.

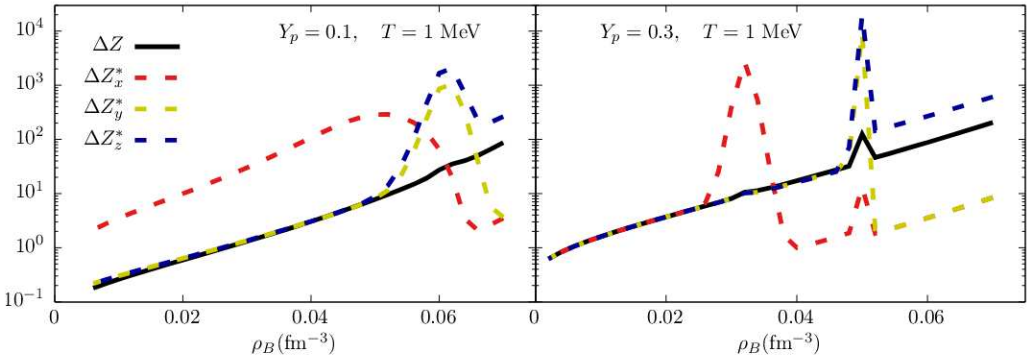

FIG. 3: Total (solid line) and orientation-dependent (dashed) proton number variances for T=1 MeV, $Y_p = 0.1$ (left) and 0.3 (right). The x, y and z axis denote the direction of motion of the probe, and are represented by the colors red, yellow and blue, respectively. We assume local domains of different geometries aligned along a common symmetry axis x.

effective impurity factor is consistent with previous estimations [5, 7], we can see that huge fluctuations are expected as a function of the orientation, at the densities corresponding to a change of dominant geometry.

Conclusions: Using a realistic microscopic energy functional (the IUFSU parametrization with Thomas-Fermi fitting for the surface energy), we calculated the probability of different pasta structures coexisting at thermodynamic conditions experienced in neutron star and supernovae matter, and made estimates of the proton number variance, considering the different orientations of the pasta structures. Quantitative calculation of the transport coefficients are in progress.

Acknowledgments This work is a part of the project INCT-FNA Proc. No. 464898/2014-5. D.P.M. is partially supported by Conselho Nacional de Desenvolvimento Científico e Tecnológico (CNPq/Brazil) under grant 301155.2017-8 and M.R.P. is supported with a doctorate scholarship by Coordenação de Aperfeiçoamento de Pessoal de Nível Superior (Capes/Brazil).

[1] D. G. Ravenhall, C. J. Pethick, and J. R. Wilson, Phys. Rev. Lett. **50**, 2066 (1983), URL https://link.aps.org/doi/10.1103/PhysRevLett.50.2066.

[2] A. Schmitt and P. Shternin, in The Physics and Astrophysics of Neutron Stars, edited by L. Rezzolla, P. Pizzochero, D. Jones, and I. Rea, N.and Vidana (Springer, Astrophysics and Space Science Library, 2018), vol. 457.

[3] C. J. Horowitz, M. A. Pérez-García, J. Carriere, D. K. Berry, and J. Piekarewicz, Phys. Rev. C **70**, 065806 (2004), URL https://link.aps.org/doi/10.1103/PhysRevC.70.065806.

[4] C. J. Horowitz, D. K. Berry, M. E. Caplan, T. Fischer, Z. Lin, W. G. Newton, E. O'Connor, and L. F. Roberts, arXiv e-prints arXiv:1611.10226 (2016), 1611.10226.

[5] J. Pons, D. Viganó, and N. Rea, Nature Physics pp. 431–434 (2013).

[6] M. Gearheart, W. G. Newton, J. Hooker, and B.-A. Li, Mon. Not. R. Astron. Soc. **418**, 2343 (2011).

[7] A. S. Schneider, D. K. Berry, M. E. Caplan, C. J. Horowitz, and Z. Lin, Phys. Rev. C **93**, 065806 (2016).

[8] A. S. Schneider, M. E. Caplan, D. K. Berry, and C. J. Horowitz, Phys. Rev. C **98**, 055801 (2018), URL https://link.aps.org/doi/10.1103/PhysRevC.98.055801.

[9] R. Nandi and S. Schramm, The Astrophysical Journal **852**, 135 (2018), URL https://doi.org/10.3847%2F1538-4357%2Faa9f12.

[10] T. Carreau, F. Gulminelli, N. Chamel, A. Fantina, and J. Pearson, Astron. Astrophys. **635**, A84 (2020), 1912.01265.

[11] D. G. Yakovlev, Monthly Notices of the Royal Astronomical Society **453**, 581 (2015), ISSN 0035-8711, https://academic.oup.com/mnras/article-pdf/453/1/581/4929833/stv1642.pdf, URL https://doi.org/10.1093/mnras/stv1642.

[12] S. S. Avancini, D. P. Menezes, M. D. Alloy, J. R. Marinelli, M. M. W. Moraes, and C. Providência, Phys. Rev. C **78**, 015802 (2008), URL https://link.aps.org/doi/10.1103/PhysRevC.78.015802.

[13] S. S. Avancini, L. Brito, J. R. Marinelli, D. P. Menezes, M. M. W. de Moraes, C. Providência, and A. M. Santos, Phys. Rev. C **79**, 035804 (2009), URL https://link.aps.org/doi/10.1103/PhysRevC.79.035804.

[14] F. J. Fattoyev, C. J. Horowitz, J. Piekarewicz, and G. Shen, Phys. Rev. C **82**, 055803 (2010), URL https://link.aps.org/doi/10.1103/PhysRevC.82.055803.

[15] J. Walecka, Annals of Physics **83**, 491 (1974), ISSN 0003-4916, URL https://www.sciencedirect.com/science/article/pii/0003491674902085.

[16] M. Dutra, O. Lourenço, S. S. Avancini, B. V. Carlson, A. Delfino, D. P. Menezes, C. Providência, S. Typel, and J. R. Stone, Phys. Rev. C **90**, 055203 (2014), URL https://link.aps.org/doi/10.1103/PhysRevC.90.055203.

[17] M. Dutra, O. Lourenço, and D. P. Menezes, Phys. Rev. C **93**, 025806 (2016), URL https://link.aps.org/doi/10.1103/PhysRevC.93.025806.

[18] O. Lourenço, M. Dutra, C. H. Lenzi, C. V. Flores, and D. P.

Menezes, Phys. Rev. C **99**, 045202 (2019), URL https://link.aps.org/doi/10.1103/PhysRevC.99.045202.

[19] T. Maruyama, T. Tatsumi, D. N. Voskresensky, T. Tanigawa, and S. Chiba, Phys. Rev. C **72**, 015802 (2005), URL https://link.aps.org/doi/10.1103/PhysRevC.72.015802.

[20] S. S. Avancini, C. C. Barros, L. Brito, S. Chiacchiera, D. P. Menezes, and C. Providência, Phys. Rev. C **85**, 035806 (2012), URL https://link.aps.org/doi/10.1103/PhysRevC.85.035806.

[21] H. Pais, F. Gulminelli, C. Providência, and G. Röpke, Nucl. Sci. Tech. **29**, 181 (2018).

[22] H. Pais, S. Chiacchiera, and C. Providência, Phys. Rev. C **91**, 055801 (2015), URL https://link.aps.org/doi/10.1103/PhysRevC.91.055801.

[23] F. Gulminelli and A. R. Raduta, Physical Review C **92** (2015), ISSN 1089-490X, URL http://dx.doi.org/10.1103/PhysRevC.92.055803.

[24] G. Grams, S. Giraud, A. F. Fantina, and F. Gulminelli, Phys. Rev. C **97**, 035807 (2018), URL https://link.aps.org/doi/10.1103/PhysRevC.97.035807.

[25] T. Carreau, A. Fantina, and F. Gulminelli, Astron. Astrophys. **640**, A77 (2020), 2005.02089.

[26] C. C. Barros, D. P. Menezes, and F. Gulminelli, Phys. Rev. C **101**, 035211 (2020), URL https://link.aps.org/doi/10.1103/PhysRevC.101.035211.

Exploring the effects of Delta Baryons in magnetars

K. D. Marquez,[1,*] M. R. Pelicer,[1] S. Ghosh,[2] J. Peterson,[3] D. Chatterjee,[2] V. Dexheimer,[3] and D. P. Menezes[1]

[1]*Depto de Física - CFM - Universidade Federal de Santa Catarina Florianópolis - SC - CP. 476 - CEP 88.040 - 900 - Brazil*
[2]*Inter-University Centre for Astronomy and Astrophysics, Post Bag 4, Ganeshkhind, Pune University Campus, Pune, 411007, India*
[3]*Department of Physics, Kent State University, Kent, OH 44243, USA*

Strong magnetic fields can modify the microscopic composition of matter with consequences on stellar macroscopic properties. Within this context, we study, for the first time, the possibility of the appearance of spin-3/2 Δ baryons in magnetars. We make use of two different relativistic models for the equation of state of dense matter under the influence of strong magnetic fields considering the effects of Landau levels and the anomalous magnetic moment (AMM) proportional to the spin of all baryons and leptons. In particular, we analyze the effects of the AMM of Δ baryons in dense matter for the first time. We also obtain global properties corresponding to the EoS models numerically and study the corresponding role of the Δ baryons. We find that they are favored over hyperons, which causes an increase in isopin asymmetry and a decrease in spin polarization. We also find that, contrary to what generally occurs when new degrees of freedom are introduced, the Δs do not make the EoS significantly softer and magnetars less massive. Finally, the magnetic field distribution inside a given star is not affected by the presence of Δs.

I. INTRODUCTION

Magnetars are a class of compact objects that possess the largest stable magnetic fields observed in nature, with surface magnitudes inferred for the poloidal component in the range of $10^{11}-10^{15}$ G at the surface [1] and values more than one order of magnitude larger in the interior [2, 3]. Although the strength of the magnetic field in the central region of these stars remains unknown, they could reach $\sim 10^{18}$ G according to the scalar virial theorem [4, 5], and simultaneous solutions of Einstein and Maxwells equations for poloidal [6, 7] and also toroidal configurations [8, 9]. Such extreme conditions certainly play a considerable role when determining the internal composition and structure of magnetars.

The starting point for determining the macroscopic structure of compact stars is the assumption of a specific microscopic model, which leads to the calculation of an equation of state (EoS) for dense matter. The EoS encodes the particle population of baryons and leptons and how they interact through the strong interactions, constrained by equilibrium conditions, such as β-stability and charge neutrality. The extremely high energies estimated in the core of neutron stars are more than sufficient to create heavier particle species, beyond the traditional proton-neutron-electron admixture. It has become common in the literature to consider the entire spin-1/2 baryon octet [e.g. 10–26] but, recently, the role of the spin-3/2 decuplet has been slowly gaining attention, not just for its influence on the microscopic aspects of dense matter but also for the astrophysical implications, since its presence may reduce the radius and tidal deformability in intermediate mass neutron stars [27–38]. The lightest spin-3/2 baryons (the Δs) are only $\sim 30\%$ heavier than the nucleons (protons and neutrons) and are even lighter than the heaviest spin-1/2 baryons of the octet (the Ξs). Thus, unless the Δs are subject to a very repulsive coupling, they are expected to appear at the same density range as the hyperons (around 2 or 3 times the nuclear saturation density). Not much is known about how Δ baryons couple in dense matter, but their potential for isospin-symmetric matter at saturation density is expected to be attractive and in a range of 2/3 to 1 times the potential of the nucleons, which is of order -80 MeV [39–41].

Additionally, it is of special interest to investigate how spin-3/2 baryons are affected by the presence of strong magnetic fields due to the possibility of them having large electric charge and additional spin and isospin projections. The effects of Landau levels in dense stellar matter containing Δ baryons was first discussed in the context of neutron-star matter by Thapa et al. [42] and later by Dexheimer et al. [37]. In this work we study for the first time the effects of strong magnetic fields in Δ-admixed hypernuclear stellar matter, accounting for effects due to their anomalous magnetic moments (AMMs).

For magnetic fields larger than $\sim 10^{16}$ G, the deformation of the stellar geometry away from spherical symmetry is above 2% [43]. Therefore, the usual relativistic hydrostatic equations usually employed when describing non-magnetised stars, i.e., the Tolman-Oppenheimer-Volkoff equations [44, 45], which assume spherical symmetry as part of their derivation from the general relativity equations, cease to be adequate. For this reason, we make use of anisotropic solutions from the Einstein and Maxwell equations to explore for the first time the macroscopic structure of magnetars with strong internal magnetic fields and containing Δ-admixed hypernuclear matter. Beyond accounting for the non-spherical configurations of stars and anisotropies introduced by magnetic fields, this approach allows us to obtain an *ab initio* magnetic field profile in the interior of a given star [46, 47].

*marquezkauan@gmail.com

This work is structured as follows. In Section II, the formalism employed in the microscopic description of magnetized neutron-star matter is presented, as well as the procedure of going from the EoS to the macroscopic description of a compact star through General Relativity. In Section III, the results for the matter composition and stellar structure are shown and discussed, and, in Section IV, the main conclusions are drawn.

II. FORMALISM

A. Anomalous magnetic moment

The AMM of a particle is a deviation from the magnetic moment of that particle, as predicted by the "classical" tree-level prediction. Historically, the term *anomalous* was used to describe the deviation from the Dirac equation prediction for a system of fermions under the influence of a magnetic field, the magnetic moment, and thus, refers to fundamental particles. *Dipole* moment, on the other hand, is used for composite particles, such as baryons, since their value depends on the configuration of quarks and gluons inside it, and thus, are not *anomalous* in the strict sense. As commonly used in the literature and for simplicity, in this work we use the term AMM in all cases.

The energy spectrum of baryons with an AMM can be empirically determined, but a theoretical derivation of their values from first principles is yet an unaccomplished task. The AMMs of nucleons are measured to a very high precision, with errors of the order of 10^{-9} [48, 49], but the same does not apply to heavier baryons. Measurements of the hyperon AMMs are precise to an order of 10^{-2} [50], while Δs are experimentally determined only for the positively charged Δ^{++} and Δ^{+}. For the Δ^{+}, there is a single measurement of $\mu_{\Delta^+}/\mu_N = 2.7^{+1.0}_{-1.3} \pm 1.5$ that comes from the $\gamma p \to p\pi\gamma'$ reaction [51], while for the Δ^{++} there are several measurements coming from the $\pi^+ p \to \pi^+ p\gamma$ bremsstrahlung cross section, with values in the range $\mu_{\Delta^{++}}/\mu_N = 3.7 - 7.5$ [50]. These measurements include systematic uncertainties, but additional theoretical uncertainties lead to errors $\sim \pm 3$. Complementary to experimental results, lattice quantum chromodynamics (LQCD) has been able to extract AMM values for Δ baryons. The values utilized in this paper are based on the predictions from LQCD provided in [52] that lie within the experimental uncertainties of the experimentally measured AMMs.

Different properties of baryons considered in this study are shown in Tab. I. The AMM strength coefficients κ_b are related to the magnetic moments μ_b through the relation

$$\kappa_b = \mu_b - q_b \mu_N \frac{M_p}{M_b} \ , \tag{1}$$

which depends on the baryon charge q_b, the nuclear magneton $\mu_N = e/2M_p$, with e being the electron charge,

TABLE I: Vacuum mass, electric charge, isospin 3$^{\rm rd}$ component, spin, normalized magnetic moment, and normalized anomalous magnetic moment of baryons considered in this work. Electric charge is shown in units of the electron charge and μ_N is the nuclear magneton.

	M_b (MeV)	$q_b(e)$	$I_{3\,b}$	S_b	μ_b/μ_N	κ_b/μ_N
p	939	$+1$	$+\frac{1}{2}$	1/2	2.79	1.79
n	939	0	$-\frac{1}{2}$	1/2	-1.91	-1.91
Λ	1116	0	0	1/2	-0.61	-0.61
Σ^+	1193	$+1$	$+1$	1/2	2.46	1.67
Σ^0	1193	0	0	1/2	1.61	1.61
Σ^-	1193	-1	-1	1/2	-1.16	-0.37
Ξ^0	1315	0	$+\frac{1}{2}$	1/2	-1.25	-1.25
Ξ^-	1315	-1	$-\frac{1}{2}$	1/2	-0.65	0.06
Δ^{++}	1232	$+2$	$+\frac{3}{2}$	3/2	4.99	3.47
Δ^+	1232	$+1$	$+\frac{1}{2}$	3/2	2.49	1.73
Δ^0	1232	0	$-\frac{1}{2}$	3/2	0.06	0.06
Δ^-	1232	-1	$-\frac{3}{2}$	3/2	-2.45	-1.69

and the ratio of the proton mass M_p to the baryon mass M_b. Although the expression (1) is derived for spin-1/2 fermions in the non-relativistic regime, it is still commonly employed to the description of the spin-3/2 particles [see 53, 54]. This subject is controversial, as the Rarita-Schwinger equation with minimal coupling predicts a gyromagnetic ratio of 2/3, while low energy/optical theorems predict a value of 2. For a more in-depth discussion we refer to Deser et al. [55], which studies a generic non-minimal electromagnetic coupling in the Rarita-Schwinger formalism. In this work, we also account for the leptons (electron and muon) AMMs, given by $\kappa_e/\mu_{B_e} = 1.15965 \times 10^{-3}$ and $\kappa_\mu/\mu_{B_\mu} = 1.16592 \times 10^{-3}$, respectively, with $\mu_{B_l} = e/2M_l$, for $l = \{e, \mu\}$.

B. Matter description

To describe baryon-dense matter subject to a strong magnetic field, we must start from a Lagrangian density describing how the particles interact with each other and with the external electromagnetic field. The photons are simply described by the massless Proca Lagrangian density, followed by a term containing the electromagnetic interaction for charged baryons and leptons, and a term describing the AMMs of baryons b and leptons l

$$\begin{aligned}\mathcal{L}_{EM} = & -\frac{1}{4}F^{\mu\nu}F_{\mu\nu} \\ & + \sum_{b,l} \bar{\psi}_{b,l}\left(-q_{b,l}A^\mu - \frac{1}{4}\kappa_b \sigma_{\mu\nu}F^{\mu\nu}\right)\psi_{b,l} \ , \end{aligned} \tag{2}$$

where $F_{\mu\nu} = \partial_\mu A_\nu - \partial_\nu A_\mu$, $\sigma^{\mu\nu} = \frac{i}{2}[\gamma^\mu, \gamma^\nu]$, and the vector potential $A_\mu = (0, 0, Bx, 0)$ is chosen such that the magnetic field is parallel to the z-axis. Leptons are described additionally by the (free with respect to the

strong force) Dirac Lagrangian density

$$\mathcal{L}_{\rm lepton} = \sum_l \bar{\psi}_l \left[i\gamma_\mu \partial^\mu - M_l \right] \psi_l \ . \tag{3}$$

We make use of two different relativistic models to describe the still widely unknown strong interaction between baryons. The first model is a non-linear version of the Walecka model, where the baryon interactions are mediated by the σ, ω, ρ and ϕ mesons, within the mean field approximation. We choose the recently proposed L3$\omega\rho$ parametrization [56], which includes an additional $\omega\rho$ interaction that allows the correct prediction of slope of the symmetry energy, neutron-star radii and tidal deformabilities. The ϕ meson (with hidden strangeness) couples only to the hyperons, allowing a higher maximum mass to be reproduced for neutron stars, thus circumventing the well-known hyperon puzzle [57], with an effect similar to the higher-order ω^4 self interaction, also included. In addition to satisfying standard astrophysical constraints from LIGO/VIRGO and NICER, the model satisfies nuclear ground-state properties of finite nuclei and bulk properties of infinite nuclear matter. It is also consistent with the PREX-2 results for the symmetry energy of $L = 106 \pm 37$ [58], though at the lower end of the error band.

The model Lagrangian density is written as $\mathcal{L} = \mathcal{L}_b + \mathcal{L}_{\rm m}$, where the first term is the (interacting) Dirac Lagrangian density for nucleons, hyperons, and Δs, and the second term accounts for the self interaction among scalar and vector mesons[1]

$$\mathcal{L}_b = \sum_b \bar{\psi}_b \left[i\gamma_\mu \partial^\mu - \gamma_0 \left(g_{\omega b}\omega + g_{\rho b} I_{3b} \rho + g_{\phi b}\phi \right) - M_b^* \right] \psi_b \ , \tag{5}$$

and

$$\begin{aligned} \mathcal{L}_{\rm m} = & -\frac{1}{2} m_\sigma^2 \sigma^2 - \frac{\lambda}{3}\sigma^3 - \frac{\kappa}{4}\sigma^4 + \frac{1}{2} m_\omega^2 \omega^2 + \frac{\xi}{4!} g_{\omega b}^4 \omega^4 \\ & + \frac{1}{2} m_\rho^2 \rho^2 + g_{\omega\rho}\, \omega^2 \rho^2 + \frac{1}{2} m_\phi^2 \phi^2 \ , \end{aligned} \tag{6}$$

where $I_{3\,b}$ is the baryon isospin 3rd component, given in Table I. The mass of the baryons is modified by the medium, giving rise to an effective mass $M_b^* = M_b - g_{\sigma b}\sigma$. The fittings of the self couplings λ and κ, and the couplings between the mesons $i = \{\sigma, \omega, \rho, \phi\}$ and baryons b, defined in terms of the ratios $x_{ib} = g_{ib}/g_{iN}$, are discussed in detail in Lopes [56].

Relevant for this work, the scalar meson couplings are fitted to reproduce the hyperon potential depth $U_\Lambda = -28$ MeV (for isospin-symmetric matter at saturation) and the remaining relative strength of the coupling constants are determined by SU(3) symmetry group arguments, as proposed by Lopes and Menezes [60], determining the complete hyperon-meson coupling scheme from a single free parameter, α_v. Despite the value of α_v, hyperons are always present in the neutron-star matter and the sequence of hyperon thresholds are always the same, with an inversely proportional relationship between α_v and the stiffness of the EoS. In this work, we choose to use $\alpha_v = 0.5$, which results in values for the additional potentials $U_\Sigma = +21.8$ MeV and $U_\Xi = +35.3$ MeV, and a stiffer EoS with respect to the values $\alpha_v = 0.75$ or 1.0 that are considered in Lopes and Menezes [60]. Though the potential for the Ξ^-mesons is repulsive in the parametrization used, recent observational constraints predict it to be attractive [61–63], but to reproduce such an attractive potential we would need an extra free parameter in the meson couplings [56].

The Δ couplings are treated more freely, as their behavior is not well known. The scarce information present in the literature, such as transport models [64] and quasi-elastic scattering of electrons off nuclei [65], allows us to infer that the nucleon-Δ potential is slightly more attractive than the nucleon-nucleon one, so that, $U_N - 30$ MeV $\lesssim U_\Delta \lesssim U_N$, which implies $x_{\sigma\Delta}$ is greater than 1. Also, the vector coupling is constrained by LQCD results as respecting the relation $0 \lesssim x_{\sigma\Delta} - x_{\omega\Delta} \lesssim 0.2$, and no constraint is put in the $x_{\rho\Delta}$ value [30, 41, 66]. Early investigations on the effect of these parameters were made in de Oliveira et al. [67, 68] and their role in the stellar particle composition and maximum-mass was studied considering $x_{\sigma\Delta} = 1.0$ and 1.1, within two classes of relativistic mean-field models in Dexheimer et al. [37]. Following the previous study, we analyse the scenarios with $x_{\sigma\Delta} = x_{\omega\Delta} = 1.0$ and $x_{\sigma\Delta} = x_{\omega\Delta} = 1.2$, keeping $x_{\rho\Delta} = 1.0$, that generates, respectively, potentials $U_\Delta = -66.25$ MeV (equal to the nucleon potential) and -79.50 MeV.

The second model we use in this work is the chiral mean-field (CMF) model, which is based on a nonlinear realization of the chiral sigma model. As in all chiral models, the masses of the baryons are generated (and not just modified) by the medium. In this way, at large temperatures and/or densities they decrease allowing chiral symmetry to be restored, in agreement with LQCD results [69]. In this work, we restrict ourselves to the hadronic version of the model (with leptons) developed by Dexheimer and Schramm [70], and disregard the possibility of phase transitions to quark matter. We add an additional $\omega\rho$ interaction to be in better agreement with data for the slope of the symmetry energy, neutron-star radii, and tidal deformabilities [71, 72]. We also add a higher-order ω^4 interaction to reproduce more massive

[1] Spin-3/2 baryons are in fact described by the Rarita-Schwinger Lagrangian density

$$\mathcal{L}_{RS} = -\sum_{b=\Delta} \frac{1}{2} \bar{\psi}_{\mu\, b} \left(\epsilon^{\mu\eta\lambda\nu} \gamma_5 \gamma_\eta \partial_\lambda - i m_b \sigma^{\mu\nu} \right) \psi_{\nu\, b} \ , \tag{4}$$

where $\epsilon^{\mu\eta\lambda\nu}$ is the Levi-Civita symbol, $\sigma^{\mu\nu} = \frac{i}{2}[\gamma^\mu, \gamma^\nu]$, and $\psi_{\mu\, b}$ is a vector-valued spinor with additional components (when compared to the four component spinor in the Dirac equation). Nonetheless, its equation of motion can be written compactly as $(i\gamma^\nu \partial_\nu - m)\,\psi_\mu = 0$, see de Paoli et al. [59].

neutron stars [73].

The mean-field model Lagrangian density has the terms

$$\mathcal{L}_b = \sum_b \bar{\psi}_b[i\gamma_\mu\partial^\mu - \gamma_0(g_{\omega b}\omega + g_{\rho b}I_{3_b}\rho + g_{\phi b}\phi) - M_b^*]\psi_i \ , \tag{7}$$

and

$$\begin{aligned}\mathcal{L}_{\rm m} = & \frac{1}{2}\left(m_\omega^2\omega^2 + m_\rho^2\rho^2 + m_\phi^2\phi^2\right) \\ & + g_4\left(\omega^4 + \frac{\phi^4}{4} + 3\omega^2\phi^2 + \frac{4\omega^3\phi}{\sqrt{2}} + \frac{2\omega\phi^3}{\sqrt{2}}\right) \\ & - k_0(\sigma^2+\zeta^2+\delta^2) - k_1(\sigma^2+\zeta^2+\delta^2)^2 \\ & - k_2\left(\frac{\sigma^4}{2} + \frac{\delta^4}{2} + 3\sigma^2\delta^2 + \zeta^4\right) - k_3(\sigma^2-\delta^2)\zeta \\ & - k_4\ \ln\frac{(\sigma^2-\delta^2)\zeta}{\sigma^2\zeta} - m_\pi^2 f_\pi\sigma \\ & - \left(\sqrt{2}m_k^2 f_k - \frac{1}{\sqrt{2}}m_\pi^2 f_\pi\right)\zeta \ , \end{aligned} \tag{8}$$

where the effective mass of baryons is $M_b^* = g_{\sigma b}\sigma + g_{\delta b}I_{3\,b}\delta + g_{\zeta b}\zeta + M_{0b}$, including additional corrections given by the scalar-isovector δ and scalar-isoscalar (with hidden strangeness) ζ mesons, and a small bare mass correction M_0. The couplings were fitted to reproduce hadronic vacuum masses, decay constants, nuclear saturation properties, and to reach more than 2.1 $M_\odot$ stars. See Roark and Dexheimer [74] for a complete list of coupling constants. We follow the SU(3) and SU(6) coupling schemes for the scalar and vector couplings of mesons and baryons. In this way, there are only two free parameters left: one fitted to reproduce for symmetric matter at saturation the potential $U_\Lambda = -27$ MeV and another one ($x_{\omega\Delta} = g_{\omega\Delta}/g_{\omega N} = 1.25$) fitted to reproduce under the same conditions $U_\Delta = -64$ MeV $\sim U_N$. They result additionally in $U_\Sigma = 6$ MeV and $U_\Xi = -17$ MeV. A much larger $x_{\omega\Delta}$ would suppress all Δs, while a much lower value would suppress all hyperons.

For both models, the equations of motion for the mesonic fields are obtained from the Lagrangian densities via the Euler-Lagrange equations. Under charge neutrality and β-equilibrium conditions, we can write the chemical potential of a baryon as a relation between the chemical potential of the neutron and the electron, μ_n and μ_e, respectively, and its electric charge, i.e.,

$$\mu_b = \mu_n - q_b\mu_e \ . \tag{9}$$

At low (effectively zero) temperature, the Fermi energy spectra of baryons is

$$E_{F\,b}^* = \mu_b - g_{\omega b}\omega - g_{\rho b}I_{3b}\rho - g_{\phi b}\phi \ , \tag{10}$$

while for leptons it is simply $E_{F\,l}^* = \mu_e$.

In the presence of a magnetic field, the Fermi momentum (squared) can be calculated from the difference between the Fermi energy (squared) and

1. the square of the effective mass modified by the AMM for particles that are not electrically charged ($q_b = 0$),

$$k_{F,b}^2(s) = {E_{F\,b}^*}^2 - \left(M_b^* - s\kappa_b B\right)^2 ; \tag{11}$$

2. the square of the effective mass modified by Landau quantization and AMM for particles that are electrically charged ($q_b \neq 0$),

$$k_{F,b}^2(\nu,s) = {E_{F\,b}^*}^2 - \left(\sqrt{M_b^{*2} + 2\nu|q_b|B} - s\kappa_b B\right)^2 . \tag{12}$$

For the momentum of leptons, M^* is simply M. In the latter case, the Fermi momentum refers to the local direction of the magnetic field, hereafter defined as the z-axis. In the transverse direction to the local magnetic field, the Fermi momentum is restricted to discrete values $2\nu|q_b|B$, where the Landau levels ν relate to the orbital angular momentum n via the relation

$$\nu = n + \frac{1}{2} - \frac{s}{2}\frac{q_b}{|q_b|} \ , \tag{13}$$

where $n = 0, 1, 2...$. For particles with spin 1/2, the first Landau level ($\nu = 0$) is occupied by a single spin projection: $s = +1$ for $q_b > 0$ and $s = -1$ for $q_b < 0$. The second level ($\nu = 1$) and above are occupied by both spin projections $s = \{\pm 1\}$. For the spin-3/2 positively charged Δs, the first level ($\nu = 0$) is occupied by the spin projections s= $\{+3, +1\}$, the second level ($\nu = 1$) by $s = \{+3, \pm 1\}$, and hereafter all spin states are occupied. For the negatively charged Δ^- spin projection, signs are reversed for the lowest levels.

At zero temperature, there is a maximum Landau level allowed, beyond which the momentum in Eq. (12) becomes imaginary given by

$$\nu_{{\rm max}b}(s) = \left\lfloor \frac{\left(E_{F\,b}^* + s\kappa_b B\right)^2 - M_b^{*2}}{2|q_b|B} \right\rfloor . \tag{14}$$

The number density for each baryon is also defined separately for electrically charged and uncharged particles, respectively,

$$n_b^{(q_b\neq 0)} = \frac{|q_b|B}{2\pi^2}\sum_{\nu,s} k_{F\,b}(\nu,s) \ ; \tag{15}$$

$$\begin{aligned} n_b^{(q_b=0)} = \bar{\psi}_b\psi_b = & \frac{1}{2\pi^2}\sum_s \left\{ \frac{k_{F\,b}^3(s)}{3} - \frac{s\kappa_b B}{2} \right. \\ & \left[\left(M_b^* - s\kappa_b B\right) k_{F\,b}(s) + \right. \\ & \left. \left. {E_{F\,b}^*}^2 \left(\arcsin\left(\frac{M_b^* - s\kappa_b B}{E_{F\,b}^*}\right) - \frac{\pi}{2}\right)\right]\right\} , \end{aligned} \tag{16}$$

as well as the scalar densities,

$$n_{s\,b}^{(q_b\neq 0)} = \bar{\psi}_b\gamma_0\psi_b = \frac{|q_b|BM_b^*}{2\pi^2}\sum_{s,\nu}\frac{\sqrt{M_b^{*2}+2\nu|q_b|B}-s\kappa_b B}{\sqrt{M_b^{*2}+2\nu|q_b|B}} \times \ln\left|\frac{k_{F\,b}(\nu,s)+E_{F\,b}^*}{\sqrt{M_b^{*2}+2\nu|q_b|B}-s\kappa_b B}\right| ; \quad (17)$$

$$n_{s\,b}^{(q_b=0)} = \frac{M_b^*}{4\pi^2}\sum_s\left[E_{F\,b}^* k_{F\,b}(s) - (M_b^*-s\kappa_b B)^2\ln\left|\frac{k_{F\,b}(s)+E_{F\,b}^*}{M_b^*-s\kappa_b B}\right|\right] . \quad (18)$$

The expressions for energy density and pressure are different for each model and can be obtained from the energy-momentum tensor for matter (discussed in the following).

C. Macroscopic structure

For spherically symmetric neutron stars, given an EoS $P(\varepsilon)$, the global structure can be obtained by solving the Tolman-Oppenheimer-Volkoff (TOV) equations of hydrostatic equilibrium

$$\frac{dM}{dr} = 4\pi r^2\varepsilon(r) , \quad (19)$$

$$\frac{d\nu}{dr} = \left(M(r)+4\pi r^3 P(r)\right)\frac{1}{r^2}\left(1-\frac{2M}{r}\right)^{-1} , \quad (20)$$

$$\frac{dP}{dr} = -\left(\varepsilon(r)+P(r)\right)\frac{d\nu}{dr} , \quad (21)$$

where $M(r)$ is the stellar mass contained within the radius r and $\nu(r)$ is a gravitational potential for the line element in spherical coordinates

$$ds^2 = -e^{2\nu(r)}dt^2+\left(1-\frac{2M}{r}\right)^{-1}dr^2+r^2(d\theta^2+\sin^2\theta d\phi^2) . \quad (22)$$

The TOV equations cannot be applied to describe the structure of the magnetars we study in this work because the spherical symmetries assumed in Eq. (22) will not hold. This is due to the strong magnetic fields we infer for such objects, which produce highly deformed stellar shapes. Instead, the stellar structure must be determined by solving equations in General Relativity describing the stationary configuration for the fluid, coupled with Einstein field equations. The energy-momentum tensor, which contains the information on the matter properties of stars, enters the stellar structure equations as the source of the Einstein equations. Neglecting the coupling to the electromagnetic field, one generally assumes a perfect fluid and the energy-momentum tensor takes the form

$$T_f^{\mu\nu} = (\varepsilon+P)\,u^\mu u^\nu + P\,g^{\mu\nu} , \quad (23)$$

where ε denotes the (matter) energy density, P the pressure, and u^μ the fluid four-velocity.

The EoS then relates pressure and energy density to the relevant thermodynamic quantities. In Chatterjee et al. [75], the general expression for the energy-momentum tensor in the presence of an electromagnetic field was derived, starting from a microscopic Lagrangian including interactions between matter and the electromagnetic field

$$T^{\mu\nu} = T_f^{\mu\nu}+\frac{1}{\mu_0}\left(-B^\mu B^\nu+(B\cdot B)u^\mu u^\nu+\frac{1}{2}g^{\mu\nu}(B\cdot B)\right) + \frac{x}{\mu_0}\left(B^\mu B^\nu-(B\cdot B)(u^\mu u^\nu+g^{\mu\nu})\right) , \quad (24)$$

where μ_0 is the vacuum permeability, $g^{\mu\nu}$ the metric tensor, and x is the magnetisation. The electromagnetic field tensor has been expressed as $F_{\mu\nu} = \epsilon_{\alpha\beta\mu\nu}u^\beta B^\alpha$, with $\epsilon_{\alpha\beta\mu\nu}$ being the four-dimensional Levi-Civita symbol [76]. Assuming an isotropic medium and a magnetisation parallel to the magnetic field, the magnetisation tensor $M_{\mu\nu}$ can be written as

$$M_{\mu\nu} = \epsilon_{\alpha\beta\mu\nu}u^\beta a^\alpha , \quad (25)$$

with the magnetization four-vector defined as $a_\mu = \frac{x}{\mu_0}B_\mu$. In the absence of magnetisation, i.e. for $x=0$, this expression reduces to the standard magnetohydrodynamics form for the energy-momentum tensor [c.f. 76].

Strong magnetic fields result in an anisotropy of the energy momentum tensor and break spherical symmetry, such that with increasing strength of the magnetic field, the shape of a magnetar departs more and more from a spherical shape. Interpreting the spatial elements of the fluid rest frame energy-momentum tensor as pressures, then there is a difference induced by the orientation of the magnetic field, commonly referred to as "parallel" and "perpendicular" pressures. Several earlier works tried to compute the mass-radius relations of strongly magnetised neutron stars through a first approach using isotropic TOV equations [77–82]. In these works, the components of the macroscopic energy-momentum tensor in the fluid rest frame are used to obtain the energy density ε, parallel ($P_\parallel$) and perpendicular ($P_\perp$) pressures. In Heaviside-Lorentz natural units, the pure electromagnetic contribution to the energy-momentum tensor, which is anisotropic, has values of $B^2/2$ and $-B^2/2$ in the perpendicular and parallel directions to the local magnetic field, respectively. However, this approach can drastically overestimate the mass of neutron stars [as shown in Fig. 3 of 83].

Several works obtained the global structure models of magnetars by solving coupled Einstein-Maxwell equations, taking into account the anisotropy of the stress-energy tensor [6, 7, 9, 42, 84–90]. In these studies either a perfect fluid, a polytropic EoS, or a realistic EoS was assumed, but do not take into account the magnetic field modifications due to its quantisation.

Ideally, to explore magnetic field effects such as Landau quantisation and AMM on the global properties of

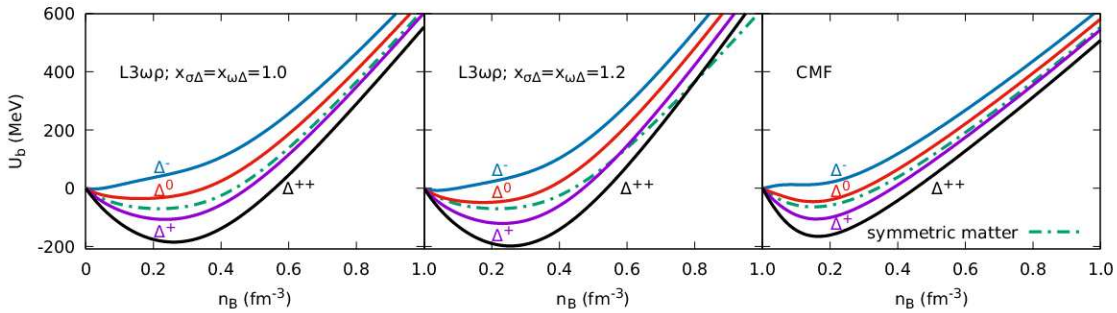

FIG. 1: Single-particle potentials of Δ baryons as a function of baryon number density in isospin-symmetric nuclear matter (dashed-dotted line) and pure neutron matter (solid lines) for the L3$\omega\rho$ model using two different Δ scalar interaction strengths (left and middle panels) and for the CMF model (right panel).

the star, one must solve the coupled Einstein-Maxwell equations, along with a magnetic field dependent EoS. In Chatterjee et al. [75] and Franzon et al. [91], global numerical models for magnetars were obtained by consistently solving Einstein-Maxwell equations with magnetic field dependent quark EoS. It was however explicitly demonstrated by Chatterjee et al. [75, 92] that the maximum mass of a neutron star is minimally modified due to the magnetic field dependence of the microscopic EoS, even for the highest magnetic fields. Therefore in this work, we assume a non-magnetic ($B = 0$) matter contribution to the EoS to compute global neutron-star models and the magnetic field enters structure calculations only through the dominant pure electromagnetic field contribution. Although it remains to be checked explicitly in future work, the effects of Landau quantisation and AMMs are not expected to sensibly affect the results of this study. Note however, that this is not the case for microscopic properties of matter, as discussed in the following.

III. RESULTS

A. Matter properties

We start our discussion with the single-particle interaction potential for the Δ baryons in dense nuclear matter, which is a measure of the energy cost of adding one particle b in a b-less matter with the given condition. For the L3$\omega\rho$ model, it can be written as

$$U_b = -g_{\sigma b}\sigma + g_{\omega b}\omega + g_{\rho b}I_{3b}\rho + g_{\phi b}\phi \ , \qquad (26)$$

and, for the CMF model,

$$U_b = g_{\sigma b}\sigma + g_{\delta b}I_{3_b}\delta + g_{\zeta b}\zeta - m_{b,vac} + g_{\omega b}\omega + g_{\rho b}I_{3b}\rho + g_{\phi b}\phi \ . \qquad (27)$$

In isospin-symmetric nuclear matter, all families of baryons experience the same potential, since the meson field ρ (and δ) are null in this situation. In neutron rich matter, particles with positive isospin projections (as the positively charged Δs) are more bound than their zero- and negative-isospin counterparts, with the largest difference occurring for pure neutron matter, that can be taken as an extrapolation of neutron-star matter in β-equilibrium. The first two panels of Fig. 1 show how the L3$\omega\rho$ model scalar and vector interactions affect the Δ potentials. In all cases, the particle potentials eventually become positive as the density increases, corresponding to unbound states, but they stay negative in the relevant interval of densities around nuclear saturation, where their depth determines how much they are bound.

For the L3$\omega\rho$ model, the larger the scalar coupling value (i.e., the parameter $x_{\sigma\Delta}$), the lower the potentials are in the low density regions. Complementary to that, the larger the vector coupling (i.e., the parameter $x_{\omega\Delta}$), the more repulsive the potentials for Δs are, which reflect in more positive curves in the high density region, where the repulsive channel dominates. Also, it can be seen that the potential depends less on the species of Δ in the CMF model. Magnetic-field effects are not included, but it was verified that fields up to $B = 3 \times 10^{18}$ G do not affect these results.

For $B = 0$, the matter EoS (namely, P vs. ε) shows a simple monotonically increasing behavior, however its derivatives show interesting features generated, e.g., by changes in particle composition. Next, we discuss the incompressibility modulus (usually referred to simply as compressibility), given by

$$K = 9\frac{\partial P}{\partial n_B} \ . \qquad (28)$$

At saturation density, compressibility values for isospin-symmetric matter can be compared with laboratory data. We find values of 256 MeV and 300 MeV for the L3$\omega\rho$ and CMF models, respectively. Laboratory values range between $220 < K < 260$ MeV [56, 93] and $250 < K < 315$ MeV [94].

The top panel of Fig. 2 shows the effect of the inclusion of different particle species in the compressibility for the L3$\omega\rho$ model, in the absence of an external magnetic field.

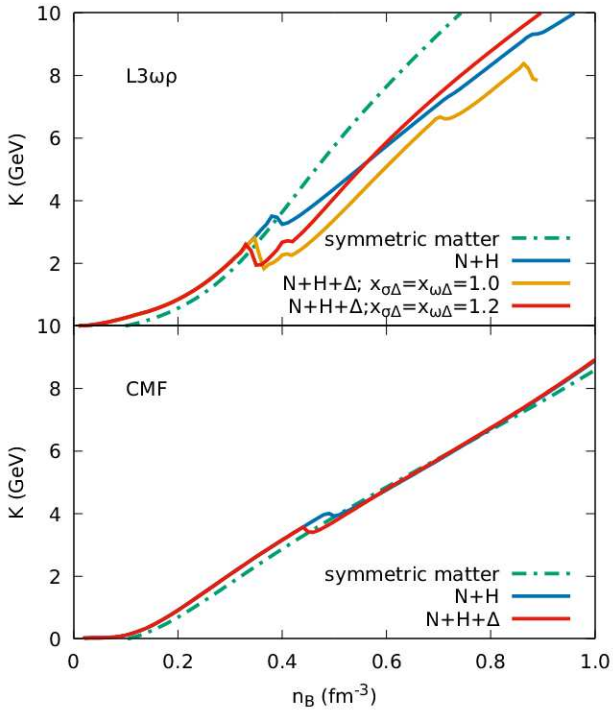

FIG. 2: Compressibility as a function of baryon number density in isospin-symmetric matter with only nucleons (dashed-dotted line) and neutron-star matter (full lines) shown for different compositions and interaction strengths for the L3$\omega\rho$ (top panel) and for the CMF model (bottom panel). $B = 0$.

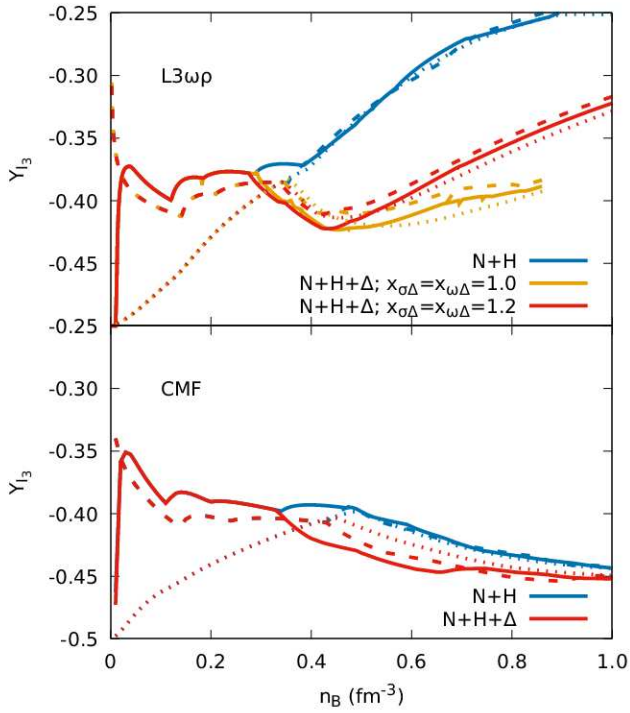

FIG. 3: Isospin fraction as a function of baryon number density for neutron-star matter with $B = 0$ (dotted lines) and with magnetic field $B = 3 \times 10^{18}$ G when considering (solid lines) or disregarding (dashed lines) the effects of the anomalous magnetic moments and shown for different compositions and interaction strengths. The top and bottom panels show results for the L3$\omega\rho$ and CMF models, respectively.

The kinks in the curves are consequence of the onset of new particle species, which are shifted to lower densities by the inclusion of both Δs and respective stronger scalar interactions. For $x_{\sigma\Delta} = 1$, the effective mass of nucleons becomes zero at $n_B \sim 0.85$ fm^{-3} and, for this reason we lack solutions at higher densities. The bottom panel of Fig. 2 shows that in the CMF model the kinks are much smaller than in the L3$\omega\rho$ model, with the only displacement of the curve occurring at the onset of the first non-nucleon baryon. As a consequence, the different CMF EoSs behave more similarly as the density increases.

The stiffer EoSs are formally the ones with larger values of the speed of sound v_s, but here we discuss stiffness with respect to K, related to v_s through $v_s^2 = K/(9\mu)$ ([95]). Isospin symmetric matter is softer at low densities, but becomes stiffer at large densities due to the Pauli exclusion principle because, as only nucleonic matter is considered, higher Fermi levels must be occupied (see Fig. 2). The behavior of neutron-star matter (charge neutral and in chemical equilibrium) depends on the composition, but it is always softer than the symmetric matter case after the hyperon or Δ onsets, as the presence of new Fermi levels turns the EoS softer. Matter with hyperons but no Δs is stiffer at intermediate densities (than matter with Δs), however it is softer at large densities, especially in the case of strong scalar interaction (for the L3$\omega\rho$ model). This trend was noticed previously by Dexheimer et al. [37], where we showed that the inclusion of Δs could turn the EoS stiffer (than the cases where they were absent), despite the fact that the new degrees of freedom soften the EoS. This is related to isospin asymmetry, which we discuss in the following.

We define the isospin fraction as the average 3$^{\rm rd}$ isospin component of a given matter composition, weighted by the relative densities, i.e.,

$$Y_{I_3} = \frac{\sum_b I_{3\,b} n_b}{\sum_b n_b} \ , \qquad (29)$$

as shown in Fig. 3. For nucleonic matter only, $Y_{I_3} = 0$ means matter with the same amount of protons and neutrons, while $Y_{I_3} = -0.5$ means pure neutron matter. The density at which the curves with and without Δs split marks the appearance of the Δ^-s, which increase the isospin asymmetry (turn the isospin fraction more negative). The effect is much larger for the L3$\omega\rho$ model (top panel) than the CMF model (bottom panel), which hints that the amount of Δs reproduced in each model is different. Both effects generated by the magnetic fields, i.e. Landau quantization and AMM, decrease the isospin

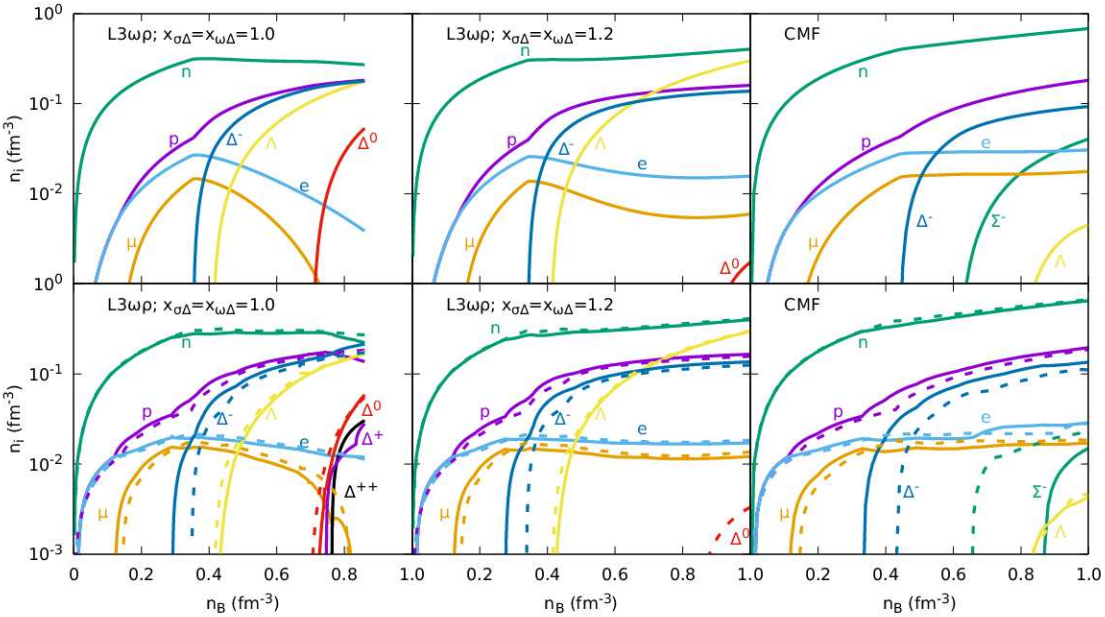

FIG. 4: Particle composition of neutron-star matter with Δs, with $B = 0$ (top panels) and magnetic field $B = 3 \times 10^{18}$ G (bottom panels), when considering (solid lines) or disregarding (dashed lines) the effects of the anomalous magnetic moment. The left and middle panels show results for the L3$\omega\rho$ model with different interactions, while the right panel shows results for the CMF model.

asymmetry (less negative Y_{I_3}) at low and intermediate densities.

A better understanding of the effects of the inclusion of Δ baryons, magnetic fields, and AMM in neutron-star matter subject to strong magnetic fields can be obtained from Fig. 4. Comparing the top row ($B = 0$) with the lower one ($B = 3 \times 10^{18}$ G), we can see that some of the charged particles are favored when magnetic field effects without AMMs are considered, an effect that is more pronounced for protons, whose onset density is pulled to very low densities for both models. As a consequence, their population becomes more similar to the neutron one in densities below ~ 0.05 fm^{-3}, turning Y_{I_3} less negative. The inclusion of AMM enhances this effect. This explains why the isospin asymmetry depends both on the magnetic field and on the AMM in the lower density region, as shown in Fig. 3. The Δ^- threshold (at densities around 0.3 fm^{-3}) coincides with the region at intermediate densities beyond which the N+H+Δ EoSs are softer than the respective N+H EoSs. The Λ (and the Σ in the CMF model) hyperons appear at larger densities than the Δ^-s. The remaining Δs appear at much larger densities and in amounts that depend on the interactions in the L3$\omega\rho$ model.

To discriminate AMM effects on the particle composition is not trivial, as they depend on the AMM coupling strength and sign, on the particle mass, charge, and density. Additionally, different spin projections are separately enhanced or suppressed, but this cannot be clearly seen in Fig. 4, as it follows the usual convention and shows the sum of all spin projections for each particle. For this reason, we make use of a quantity that reveals the degree of spin polarization, more suited to discuss spin projection asymmetry of fermions.

We define the total spin polarization of a given matter composition, weighted by the relative densities, in analogy to Eq. (29), i.e.,

$$Y_{\rm spin} = \frac{\sum_{b,s} s n_b(s)}{\sum_{b,s} n_b(s)} \ , \tag{30}$$

and shown the results in Fig. 5. For a fixed magnetic field strength, all charged particles are fully spin polarized at low densities: only spin projection 1/2 for protons and spin projection 3/2 for positive Δs, only spin projection -1/2 for leptons and negative Σs, and spin projection -3/2 for negative Δs. When AMMs are considered, neutral particles obey the same logic, presenting only positive (negative) spin projections according to their positive (negative) sign of κ_b. At intermediate densities, full polarization is broken for more massive particles, but not for leptons and Λs. But, regardless, the polarization never goes to zero, meaning that partial spin projection imbalance remains at high densities. Overall, spin polarization fraction is much stronger for the CMF model (bottom panel) than for the L3$\omega\rho$ model (top panel). Full polarization can be understood from Eqs. (11), (12), and (13), which explains why particles with different isospin projections present different momenta and why particles occupying the first Landau level ($\nu = 0$) are more abundant when only a few levels are occupied. This happens for strong magnetic fields and low particle densities, or

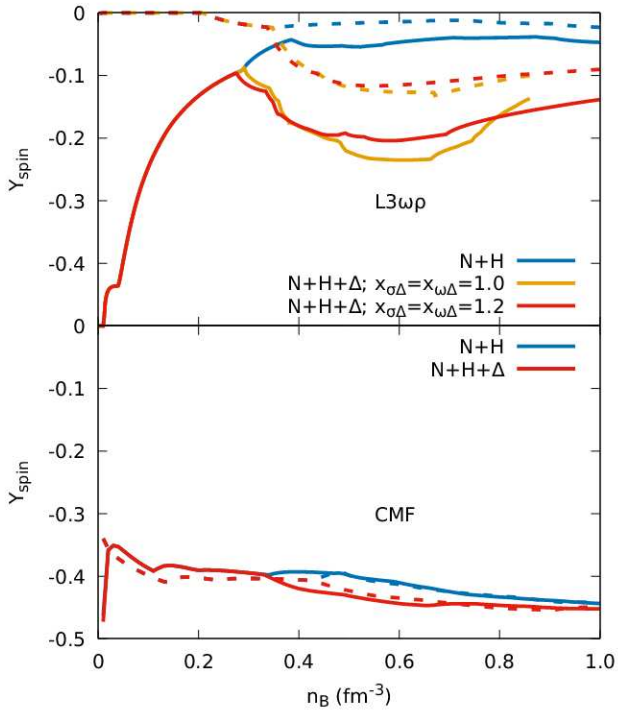

FIG. 5: Spin polarization fraction as a function of baryon number density for neutron-star matter with magnetic field $B = 3 \times 10^{18}$ G, when considering (solid lines) or disregarding (dashed lines) the effects of the anomalous magnetic moments and shown for different compositions and interaction strengths. The top and bottom panels show results for the L3$\omega\rho$ and CMF models, respectively.

simply less massive particles.

It is a well-established concept that the magnetic field is not constant within neutron stars, but increases towards their centers where the density is larger. But, before we discuss stellar configurations with macroscopic magnetic fields in detail, we study how one more relevant quantity changes as a function of magnetic field strength. The fraction of exotic particles can be defined as the following quantity

$$Y_i = \frac{\sum_{b\in i} n_b}{\sum_b n_b} \ , \tag{31}$$

for $i = H$ or Δ, shown in Fig. 6. On the left panel for the L3$\omega\rho$ model, the amount of Δs is slightly reduced at a given density but then increases tremendously at the larger density when the AMM is included, a behaviour quantitatively not reproduced with larger coupling constants, as seen on the middle panel. The amount of hyperons, on the other hand, is not significantly modified by the magnetic field, only slightly decreases in the presence of AMM and is affected by the small fluctuations related to the De Haas-Van Alphen oscillations [96]. The right panel shows the same qualitative behavior for the CMF model, which has a more clear substitution of hyperons in favor of deltas for higher values of B, independently of the density or accounting for the AMM.

B. Macroscopic structure

In a previous study, Dexheimer et al. [37] obtained results on the effects of the inclusion of Δs in neutron stars for both the $L3\omega\rho$ and CMF models without magnetic fields, using standard TOV equations. As expected from the discussion regarding the hyperon puzzle [57], pure nucleonic stars are always the most massive configuration, and the inclusion of hyperons decreases the maximum mass obtained. It was noticed that the inclusion of Δs, however, does not modify significantly (and in some cases increases) the maximum stellar mass in relation to the composition with only nucleons and hyperons, and this effect is more obvious for the cases where Δs are more abundant. It is argued that the addition of Δs decreases the fraction of nucleons (in fact, neutrons) and hyperons (mostly Λs) to create Δs and some protons, in a way that the overall increase in isospin asymmetry turns the EoS stiffer, even when more species are present.

As described here in section II C, to compute the effect of the strong magnetic fields on the structure of the magnetars, one must solve the coupled Einstein–Maxwell equations with the equations of state (described in section III A). For the chosen poloidal field geometry, we solve the Einstein–Maxwell equations within the numerical library LORENE[2] using a multi-domain spectral method. In Fig. 7, we show the mass radius relations for the $L3\omega\rho$ and the CMF models, with and without Δs, as a function of equatorial radius for sequences of constant stellar central magnetic field. Despite the fact that, for the choices discussed here for $x_{\sigma\Delta}$ and $x_{\omega\Delta}$ parameters in the $L3\omega\rho$ model, the masses of N+H+Δ stars never surpass the respective N+H configurations, we still observe that the the maximum mass (shown in Fig. 7) follows the same ordering of a large (and most relevant) portion of Fig. 3 for the compressibility.

In Fig. 7, any differences between the mass-radius curves for the $B = 0$ case (solid lines) arise from the differences in the (non-magnetic) EoS, while the differences with magnetic field come from the pure electromagnetic field contribution. We know that the Lorentz force originating from the pure electromagnetic field affects the low density part of the EoS. This is why the maximum mass of very massive stars does not change with increasing magnetic field strength, but the mass and radius of less massive stars increase significantly. For the $L3\omega\rho$ model, the inclusion of Δs decreases modestly the maximum stellar mass, especially for the larger coupling. However, for the CMF model, we do not see meaningful changes on the mass-radius diagram with the inclusion of Δs. From Ta-

[2] http://www.lorene.obspm.fr

h!

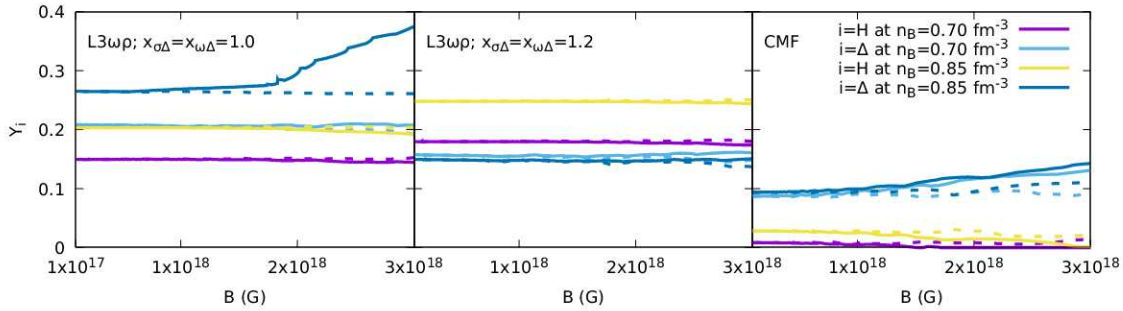

FIG. 6: Exotic particle (hyperon and Δ) fraction as a function of magnetic field strength when considering (solid lines) or disregarding (dashed lines) the effects of the anomalous magnetic moment, shown for two given densities. The left and right panels show results for the L3$\omega\rho$ with different interactions and CMF models, respectively.

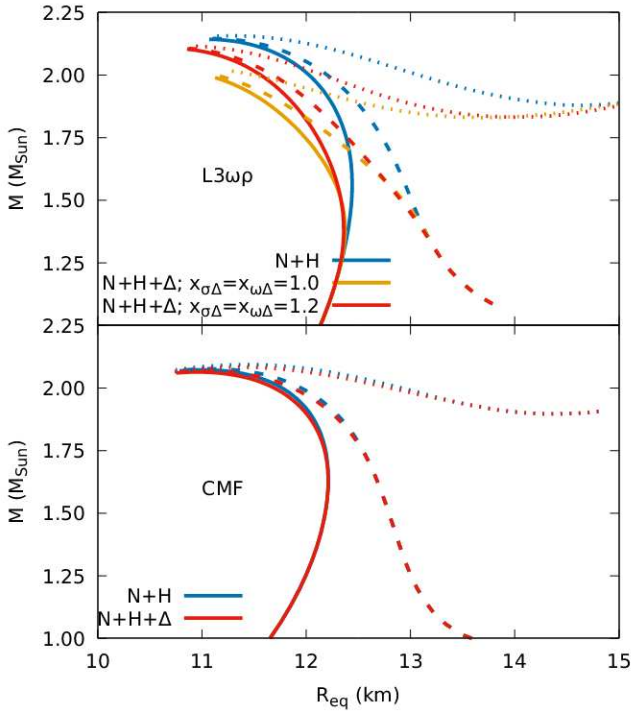

FIG. 7: Stellar mass as a function of equatorial radius for different compositions and interaction strengths, for central magnetic fields $B = 0$ (solid lines), $B = 5 \times 10^{17}$ G (dashed lines), and $B = 10^{18}$ G (dotted lines). The top and bottom panels show results for the L3$\omega\rho$ and CMF models, respectively.

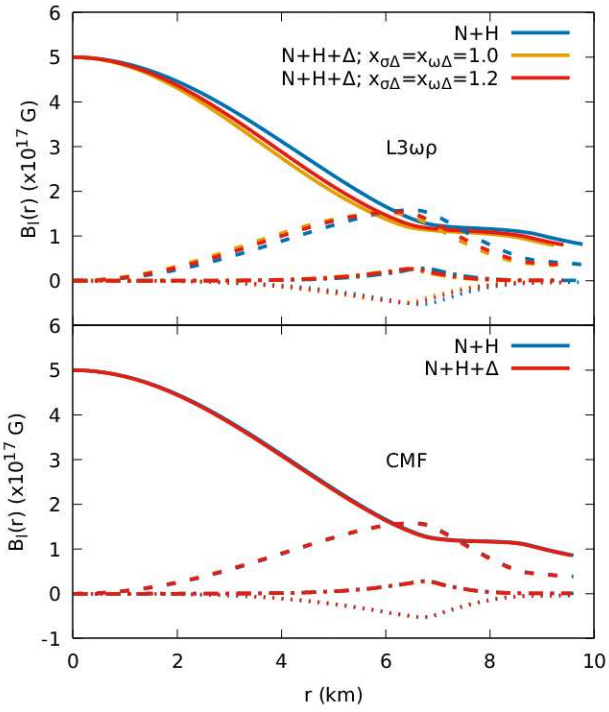

FIG. 8: Magnetic field distribution inside a neutron star of mass $1.8M_\odot$ and central magnetic field of $B = 5 \times 10^{17}$ G for different compositions and interaction strengths. Solid, dashed, dashed-dotted and dotted are, respectively, the first four even multipoles of the magnetic field norm ($l = 0, 2, 4, 6$), shown as functions of the coordinate radius. The top and bottom panels show results for the L3$\omega\rho$ and CMF models, respectively.

ble II we see that, keeping the radius of the neutron star fixed (going up vertically in Fig. 7), the increase in the strength of the central magnetic field increases both the central baryon and energy densities, as a larger matter pressure is necessary to balance the Lorentz force. The addition of Δs decreases both quantities, as these stars are naturally (at B=0) smaller.

At this point, we note that the maximum mass value of the stellar family described by the $L3\omega\rho$ model with Δs and $x_{\sigma\Delta} = 1.0$ (the yellow curve) has not been attained because, as explained earlier, the EoS numerical code stops converging at large densities due to reaching zero nucleon masses. Such behavior indicates that hadronic

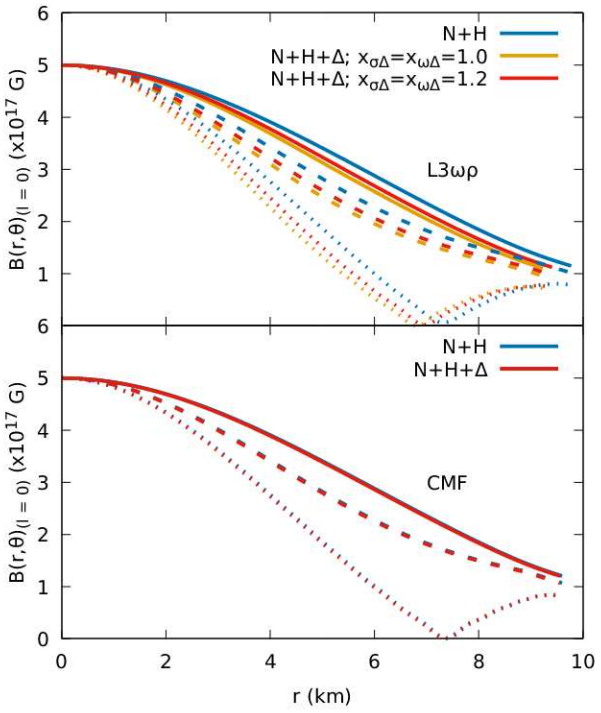

FIG. 9: Magnetic field distribution inside a neutron star of mass $1.8M_\odot$ and central magnetic field of $B = 5 \times 10^{17}$ G for different compositions and interaction strengths. Solid, dashed and dotted are the dominant monopolar ($l = 0$) term at the polar ($\theta = 0$), intermediate ($\theta = \pi/4$) and equatorial ($\theta = \pi/2$) orientations, respectively, shown as functions of the coordinate radius. The top and bottom panels show results for the L3$\omega\rho$ and CMF models, respectively.

matter is no longer stable at this point and deconfinement to quark matter must be considered. We leave such analysis to a future work. But, since the trend of the yellow curve is quite obvious, we can conclude that its maximum mass is lower when compared to the other coupling and composition.

Using the full numerical solution, we also study the effect of the EoS on the magnetic field configurations inside a given star. We decompose the magnetic field norm in terms of spherical harmonics

$$B(r,\theta) \approx \sum_{i=0}^{l_{max}} B_l(r) Y_l^0(\theta) \ , \tag{32}$$

and plot the first four even multipoles ($l = 0, 2, 4, 6$) as function of coordinate radius for both the EoS models and coupling strengths in Fig 8. We also plot the profile of the dominant monopolar, spherically symmetric, term ($l = 0$) inside the star in Fig 9. For $L3\omega\rho$ model, specially if we include Δs, the magnetic field norm decreases slightly inside the star but, for CMF model, we do not see any considerable changes.

TABLE II: Central baryon (n_c) and energy (ε_c) densities as a function of magnetic field strength for neutron stars of radius 12 km with L3$\omega\rho$ model for $x_{\sigma\Delta} = x_{\omega\Delta} = 1.0(1.2)$ in the top panel and CMF model in the bottom panel

B (G)	n_c (fm^{-3})		ε_c (MeV/fm^3)	
	N+H	N+H+Δ	N+H	N+H+Δ
0	0.672	0.618 (0.614)	742	658 (657)
5×10^{17}	0.701	0.659 (0.653)	783	712 (708)
1×10^{18}	0.747	0.714 (0.707)	850	786 (783)
0	0.629	0.625	678	672
5×10^{17}	0.680	0.677	747	741
1×10^{18}	0.749	0.746	843	837

IV. CONCLUSIONS

In the present work, we have used two different relativistic models, namely, one of the parametrizations of the Walecka model with non-linear terms called L3$\omega\rho$ and the chiral mean field (CMF) model, to investigate the effects of the presence of Δ baryons in dense matter. When the L3$\omega\rho$ is used, the unknown meson-hyperon coupling constants can be extracted from both phenomenology and symmetry group considerations, but the choice of meson-Δ couplings is still flexible. The CMF model, on the other hand, fixes the coupling constants with the help of phenomenological potentials uniquely. As a consequence, single particle Δ baryon potentials and the compressibility away from saturation are quantitatively different for both models, although they qualitatively present the same behavior. This is a consequence mainly of the different hyperon and Δ composition at intermediate and large densities. Those features are carried out when strong magnetic fields and anomalous magnetic moments (AMMs) are incorporated.

We carefully investigated particle composition and spin polarization when Δ baryons are included in neutron-star matter under the influence of strong magnetic fields with and without AMM corrections. Due to the effects of charge conservation and chemical equilibrium, there is no common behavior for all the particles (as predicted by their AMM signs and strengths). However, in general, while the population of charged particles increases with the inclusion of AMM, the population of neutral particles tends to decrease.

The macroscopic properties of magnetars for the above choice of EoS models were obtained by solving Einstein-Maxwell equations within the LORENE library. It was found that maximum masses as high as $2M_\odot$ can be attained even on inclusion of Δ particles. This is due to isospin readjustment at large densities, which turns the EoS stiffer. The Δs also respond more strongly to the AMM, which is expected due to the fact that they present additional electric charges and isospin projections. As a consequence, Δ-admixed hypernuclear stellar matter,

possesses larger spin polarization. The latter effect is more dramatic for the L3$\omega\rho$ model, which presents a larger number of exotic particles than the CMF model.

Considering strong magnetic fields, heavy stars tend to contain more Δs in their interiors. They are not necessarily more massive (than their B=0 counterparts), but are larger and, for a given radius, present larger central number density and energy density. While Δs modify the magnetic field distribution very little inside stars, they decrease their radii, improving the agreement with modern observational data of neutron-star radii and tidal deformability [97–101].

Our results do not show the significant increase of stiffness of neutron-star matter with Δs at large density, as initially observed by Dexheimer et al. [37]. In a more in depth analysis (to appear in a separate publication Marquez [102]), we will show that this effect can indeed occur and reproduce more massive magnetars, but is very sensitive to model parameters.

Acknowledgements

We thank Jorge Noronha for the very useful discussions. This work is a part of the project INCT-FNA Proc. No. 464898/2014-5. K.D.M. acknowledges a doctorate scholarship from Conselho Nacional de Desenvolvimento Científico e Tecnológico (CNPq/Brazil). M.R.P. acknowledges a doctorate scholarship from Coordenação de Aperfeiçoamento de Pessoal do Ensino Superior (Capes/Brazil). D.P.M. was partially supported by Conselho Nacional de Desenvolvimento Científico e Tecnológico (CNPq/Brazil) under grant 303490-2021-7. V. D. acknowledges support from the National Science Foundation under grants PHY1748621, MUSES OAC-2103680, and NP3M PHY-2116686, in addition to PHAROS (COST Action CA16214).

[1] P. Haensel, A. Potekhin, and D. Yakovlev, *Neutron Stars 1: Equation of State and Structure*, Astrophysics and Space Science Library (Springer New York, 2006), ISBN 9780387335438, URL https://books.google.fr/books?id=iIrj9nfHnesC.

[2] K. Makishima, T. Enoto, J. S. Hiraga, T. Nakano, K. Nakazawa, S. Sakurai, M. Sasano, and H. Murakami, Phys. Rev. Lett. **112**, 171102 (2014), URL https://link.aps.org/doi/10.1103/PhysRevLett.112.171102.

[3] S. Dall'Osso, L. Stella, and C. Palomba, Monthly Notices of the Royal Astronomical Society **480**, 1353 (2018), ISSN 0035-8711, https://academic.oup.com/mnras/article-pdf/480/1/1353/25405204/sty1706.pdf, URL https://doi.org/10.1093/mnras/sty1706.

[4] D. Lai and S. L. Shapiro, The Astrophysical Journal **383**, 745 (1991).

[5] S. Bonazzola, E. Gourgoulhon, M. Salgado, and J. A. Marck, Astron. Astrophys **278**, 421 (1993).

[6] M. Bocquet, S. Bonazzola, E. Gourgoulhon, and J. Novak, Astron. Astrophys **301**, 757 (1995), gr-qc/9503044.

[7] C. Y. Cardall, M. Prakash, and J. M. Lattimer, Astrophys. J. **554**, 322 (2001), astro-ph/0011148.

[8] A. G. Pili, N. Bucciantini, and L. Del Zanna, Monthly Notices of the Royal Astronomical Society **470**, 2469 (2017), ISSN 0035-8711, https://academic.oup.com/mnras/article-pdf/470/2/2469/18245433/stx1176.pdf, URL https://doi.org/10.1093/mnras/stx1176.

[9] A. Tsokaros, M. Ruiz, S. L. Shapiro, and K. Uryū, Phys. Rev. Lett. **128**, 061101 (2022), 2111.00013.

[10] N. Glendenning, Phys. Lett. B **114**, 392 (1982).

[11] M. Prakash, J. R. Cooke, and J. M. Lattimer, Phys. Rev. D **52**, 661 (1995).

[12] M. Baldo, G. F. Burgio, and H. J. Schulze, Phys. Rev. C **61**, 055801 (2000), nucl-th/9912066.

[13] G. Colucci and A. Sedrakian, J. Phys. Conf. Ser. **496**, 012003 (2014), 1401.1653.

[14] R. O. Gomes, V. Dexheimer, S. Schramm, and C. Vasconcellos, Astrophys. J. **808**, 8 (2015), 1411.4875.

[15] B. Bhowmick, M. Bhattacharya, A. Bhattacharyya, and G. Gangopadhyay, Phys. Rev. C **89**, 065806 (2014), 1403.0341.

[16] M. Oertel, C. Providência, F. Gulminelli, and A. R. Raduta, J. Phys. G **42**, 075202 (2015), 1412.4545.

[17] I. Vidaña, J. Phys. Conf. Ser. **668**, 012031 (2016), 1509.03587.

[18] D. Chatterjee and I. Vidaña, Eur. Phys. J. A **52**, 29 (2016), 1510.06306.

[19] K. D. Marquez and D. P. Menezes, Journal of Cosmology and Astroparticle Physics **2017**, 028 (2017).

[20] M. Isaka, Y. Yamamoto, and T. A. Rijken, Phys. Rev. C **95**, 044308 (2017), 1703.03117.

[21] J. Roark, X. Du, C. Constantinou, V. Dexheimer, A. W. Steiner, and J. Stone, Mon. Not. Roy. Astron. Soc. **486**, 5441 (2019), 1812.08157.

[22] J. R. Stone, V. Dexheimer, P. A. M. Guichon, A. W. Thomas, and S. Typel, Mon. Not. Roy. Astron. Soc. **502**, 3476 (2021), 1906.11100.

[23] A. Sedrakian, F. Weber, and J. J. Li, Phys. Rev. D **102**, 041301 (2020), 2007.09683.

[24] T. F. Motta and A. W. Thomas, Mod. Phys. Lett. A **37**, 2230001 (2022), 2201.11549.

[25] I. A. Rather, U. Rahaman, V. Dexheimer, A. A. Usmani, and S. K. Patra, Astrophys. J. **917**, 46 (2021), 2104.05950.

[26] K. Huang, J. Hu, Y. Zhang, and H. Shen, *The hyperonic star in relativistic mean-field model* (2022), 2203.12357.

[27] J. J. Li, A. Sedrakian, and F. Weber, Phys. Lett. B **783**, 234 (2018), 1803.03661.

[28] G.-S. Yang and H.-C. Kim, Phys. Lett. B **785**, 434 (2018), 1807.09090.

[29] T. Motta, A. Thomas, and P. A. Guichon, Phys. Lett. B **802**, 135266 (2020), 1906.05459.

[30] P. Ribes, A. Ramos, L. Tolos, C. Gonzalez-Boquera, and M. Centelles, The Astrophysical Journal **883**, 168 (2019), URL https://doi.org/10.3847/1538-4357/

ab3a93.
[31] G. Malfatti, M. G. Orsaria, I. F. Ranea-Sandoval, G. A. Contrera, and F. Weber, Phys. Rev. D **102**, 063008 (2020), 2008.06459.
[32] H. S. Sahoo, R. Mishra, and P. K. Panda, JPS Conf. Proc. **32**, 010054 (2020).
[33] J. J. Li, A. Sedrakian, and F. Weber, Phys. Lett. B **810**, 135812 (2020), 2010.02901.
[34] A. R. Raduta, M. Oertel, and A. Sedrakian, Mon. Not. Roy. Astron. Soc. **499**, 914 (2020), 2008.00213.
[35] B. C. Backes, K. D. Marquez, and D. P. Menezes, The European Physical Journal A **57**, 1 (2021).
[36] V. B. Thapa and M. Sinha, Phys. Rev. C **105**, 015802 (2022), 2112.12629.
[37] V. Dexheimer, K. D. Marquez, and D. P. Menezes, The European Physical Journal A **57** (2021), ISSN 1434-601X, URL http://dx.doi.org/10.1140/epja/s10050-021-00532-6.
[38] M. Marczenko, K. Redlich, and C. Sasaki, Phys. Rev. D **105**, 103009 (2022), 2203.00269.
[39] A. Drago, A. Lavagno, G. Pagliara, and D. Pigato, Phys. Rev. C **90**, 065809 (2014), 1407.2843.
[40] E. Kolomeitsev, K. Maslov, and D. Voskresensky, Nucl. Phys. A **961**, 106 (2017), 1610.09746.
[41] A. R. Raduta, Phys. Lett. B **814**, 136070 (2021), 2101.03718.
[42] V. B. Thapa, M. Sinha, J. J. Li, and A. Sedrakian, Particles **3**, 660 (2020), 2010.00981.
[43] R. O. Gomes, H. Pais, V. Dexheimer, C. Providência, and S. Schramm, Astron. Astrophys. **627**, A61 (2019), 1902.08146.
[44] R. C. Tolman, Phys. Rev. **55**, 364 (1939).
[45] J. R. Oppenheimer and G. M. Volkoff, Phys. Rev. **55**, 374 (1939).
[46] V. Dexheimer, B. Franzon, R. Gomes, R. Farias, S. Avancini, and S. Schramm, Phys. Lett. B **773**, 487 (2017), 1612.05795.
[47] D. Chatterjee, J. Novak, and M. Oertel, Phys. Rev. C **99**, 055811 (2019), 1808.01778.
[48] G. L. Greene, N. F. Ramsey, W. Mampe, J. M. Pendlebury, K. Smith, W. B. Dress, P. D. Miller, and P. Perrin, Phys. Rev. D **20**, 2139 (1979), URL https://link.aps.org/doi/10.1103/PhysRevD.20.2139.
[49] G. Schneider, A. Mooser, M. Bohman, N. Schön, J. Harrington, T. Higuchi, H. Nagahama, S. Sellner, C. Smorra, K. Blaum, et al., Science **358**, 1081 (2017), https://www.science.org/doi/pdf/10.1126/science.aan0207, URL https://www.science.org/doi/abs/10.1126/science.aan0207.
[50] P. A. Zyla et al. (Particle Data Group), PTEP **2020**, 083C01 (2020).
[51] M. Kotulla, J. Ahrens, J. R. M. Annand, R. Beck, G. Caselotti, L. S. Fog, D. Hornidge, S. Janssen, B. Krusche, J. C. McGeorge, et al., Phys. Rev. Lett. **89**, 272001 (2002), URL https://link.aps.org/doi/10.1103/PhysRevLett.89.272001.
[52] I. Cloet, D. Leinweber, and A. Thomas, Physics Letters B **563**, 157 (2003), ISSN 0370-2693, URL https://www.sciencedirect.com/science/article/pii/S0370269303004180.
[53] G. López Castro and A. Mariano, Nuclear Physics A **697**, 440 (2002), ISSN 0375-9474, URL https://www.sciencedirect.com/science/article/pii/S0375947401012465.
[54] G. López Castro and A. Mariano, Physics Letters B **517**, 339 (2001), ISSN 0370-2693, URL https://www.sciencedirect.com/science/article/pii/S0370269301009807.
[55] S. Deser, A. Waldron, and V. Pascalutsa, Phys. Rev. D **62**, 105031 (2000), URL https://link.aps.org/doi/10.1103/PhysRevD.62.105031.
[56] L. L. Lopes, Commun. Theor. Phys. **74**, 015302 (2022), 2107.02245.
[57] N. Chamel, P. Haensel, J. L. Zdunik, and A. F. Fantina, Int. J. Mod. Phys. E **22**, 1330018 (2013), 1307.3995.
[58] B. T. Reed, F. J. Fattoyev, C. J. Horowitz, and J. Piekarewicz, Phys. Rev. Lett. **126**, 172503 (2021), URL https://link.aps.org/doi/10.1103/PhysRevLett.126.172503.
[59] M. G. de Paoli, D. P. Menezes, L. B. Castro, and C. C. Barros, Jr, J. Phys. G **40**, 055007 (2013), 1207.4063.
[60] L. L. Lopes and D. P. Menezes, Physical Review C **89**, 25805 (2014).
[61] L. Fabbietti, V. M. Sarti, and O. V. Doce, Annual Review of Nuclear and Particle Science **71**, 377 (2021), https://doi.org/10.1146/annurev-nucl-102419-034438, URL https://doi.org/10.1146/annurev-nucl-102419-034438.
[62] S. Acharya, D. Adamová, S. P. Adhya, A. Adler, J. Adolfsson, M. M. Aggarwal, G. Aglieri Rinella, M. Agnello, N. Agrawal, Z. Ahammed, et al. (A Large Ion Collider Experiment Collaboration), Phys. Rev. Lett. **123**, 112002 (2019), URL https://link.aps.org/doi/10.1103/PhysRevLett.123.112002.
[63] E. Friedman and A. Gal, Phys. Lett. B **820**, 136555 (2021), 2104.00421.
[64] M. D. Cozma and M. B. Tsang, Eur. Phys. J. A **57**, 309 (2021), 2101.08679.
[65] A. Bodek and T. Cai, Eur. Phys. J. C **80**, 655 (2020), 2004.00087.
[66] K. Wehrberger, C. Bedau, and F. Beck, Nuclear Physics A **504**, 797 (1989), ISSN 0375-9474, URL https://www.sciencedirect.com/science/article/pii/0375947489900080.
[67] J. de Oliveira, M. Kyotoku, M. Chiapparini, H. Rodrigues, and S. Duarte, Modern Physics Letters A **15**, 1529 (2000).
[68] J. de Oliveira, S. Duarte, H. Rodrigues, M. Chiapparini, and M. Kyotoku, International Journal of Modern Physics D **16**, 175 (2007).
[69] G. Aarts, C. Allton, D. De Boni, S. Hands, B. Jäger, C. Praki, and J.-I. Skullerud, JHEP **06**, 034 (2017), 1703.09246.
[70] V. Dexheimer and S. Schramm, Astrophys. J. **683**, 943 (2008), 0802.1999.
[71] V. Dexheimer, R. Negreiros, and S. Schramm, Phys. Rev. C **92**, 012801 (2015), 1503.07785.
[72] V. Dexheimer, R. de Oliveira Gomes, S. Schramm, and H. Pais, J. Phys. G **46**, 034002 (2019), 1810.06109.
[73] V. Dexheimer, R. O. Gomes, T. Klähn, S. Han, and M. Salinas, Phys. Rev. C **103**, 025808 (2021), 2007.08493.
[74] J. Roark and V. Dexheimer, Phys. Rev. C **98**, 055805 (2018), 1803.02411.
[75] D. Chatterjee, T. Elghozi, J. Novak, and M. Oertel, Monthly Notices of the Royal Astronomical Society **447**, 3785–3796 (2015), ISSN 0035-8711, URL http://dx.doi.org/10.1093/mnras/stu2706.

[76] E. Gourgoulhon, *3+1 Formalism in General Relativity* (Springer Verlag, 2012), ISBN 978-3-642-24525-1.

[77] A. Rabhi, H. Pais, P. K. Panda, and C. Providência, Journal of Physics G: Nuclear and Particle Physics **36**, 115204 (2009), ISSN 1361-6471, URL http://dx.doi.org/10.1088/0954-3899/36/11/115204.

[78] E. J. Ferrer, V. de la Incera, J. P. Keith, I. Portillo, and P. L. Springsteen, Phys. Rev. C **82**, 065802 (2010), URL https://link.aps.org/doi/10.1103/PhysRevC.82.065802.

[79] M. Strickland, V. Dexheimer, and D. P. Menezes, Phys. Rev. D **86**, 125032 (2012), URL https://link.aps.org/doi/10.1103/PhysRevD.86.125032.

[80] L. L. Lopes and D. P. Menezes, Brazilian Journal of Physics **42**, 428–436 (2012), ISSN 1678-4448, URL http://dx.doi.org/10.1007/s13538-012-0093-y.

[81] V. Dexheimer, D. P. Menezes, and M. Strickland, Journal of Physics G: Nuclear and Particle Physics **41**, 015203 (2013), URL https://doi.org/10.1088/0954-3899/41/1/015203.

[82] R. H. Casali, L. B. Castro, and D. P. Menezes, Phys. Rev. C **89**, 015805 (2014), URL https://link.aps.org/doi/10.1103/PhysRevC.89.015805.

[83] R. O. Gomes, B. Franzon, V. Dexheimer, and S. Schramm, Astrophys. J. **850**, 20 (2017), 1709.01017.

[84] A. Oron, Phys. Rev. D **66**, 023006 (2002), URL https://link.aps.org/doi/10.1103/PhysRevD.66.023006.

[85] K. Ioka and M. Sasaki, The Astrophysical Journal **600**, 296–316 (2004), ISSN 1538-4357, URL http://dx.doi.org/10.1086/379650.

[86] K. Kiuchi and S. Yoshida, Phys. Rev. D **78**, 044045 (2008), URL https://link.aps.org/doi/10.1103/PhysRevD.78.044045.

[87] N. Yasutake, K. Kiuchi, and K. Kotake, Monthly Notices of the Royal Astronomical Society **401**, 2101 (2010).

[88] J. Frieben and L. Rezzolla, Mon. Not. Roy. Astron. Soc. **427**, 3406 (2012), 1207.4035.

[89] S. Yoshida, K. Kiuchi, and M. Shibata, Phys. Rev. D **86**, 044012 (2012), URL https://link.aps.org/doi/10.1103/PhysRevD.86.044012.

[90] A. Pili, N. Bucciantini, and L. Del Zanna, Monthly Notices of the Royal Astronomical Society **439**, 3541 (2014).

[91] B. Franzon, V. Dexheimer, and S. Schramm, Mon. Not. Roy. Astron. Soc. **456**, 2937 (2016), 1508.04431.

[92] D. Chatterjee, J. Novak, and M. Oertel, The European Physical Journal A **57** (2021), ISSN 1434-601X, URL http://dx.doi.org/10.1140/epja/s10050-021-00525-5.

[93] M. Dutra, O. Lourenço, S. Avancini, B. Carlson, A. Delfino, D. Menezes, C. Providência, S. Typel, and J. Stone, Physical Review C **90**, 055203 (2014).

[94] J. R. Stone, N. J. Stone, and S. A. Moszkowski, Phys. Rev. C **89**, 044316 (2014), 1404.0744.

[95] V. A. Dexheimer, C. A. Z. Vasconcellos, and B. E. J. Bodmann, Phys. Rev. C **77**, 065803 (2008), 0708.0131.

[96] W. J. De Haas and P. M. Van Alphen, Proc. Acad. Sci. Amst. **33**, 1106 (1930), URL https://www.dwc.knaw.nl/DL/publications/PU00015989.pdf.

[97] M. Miller et al., Astrophys. J. Lett. **887**, L24 (2019), 1912.05705.

[98] T. E. Riley et al., Astrophys. J. Lett. **887**, L21 (2019), 1912.05702.

[99] M. C. Miller et al., Astrophys. J. Lett. **918**, L28 (2021), 2105.06979.

[100] T. E. Riley et al., Astrophys. J. Lett. **918**, L27 (2021), 2105.06980.

[101] B. P. Abbott et al. (LIGO Scientific, Virgo), Phys. Rev. X **9**, 011001 (2019), 1805.11579.

[102] K. D. Marquez, *Delta baryons in neutron-star matter (private communication)* (2022), URL https://youtu.be/pbRzT9CpcYg.

Eur. Phys. J. A (2022) 58:177
https://doi.org/10.1140/epja/s10050-022-00829-0

THE EUROPEAN PHYSICAL JOURNAL A

Regular Article - Theoretical Physics

Phase transitions and latent heat in magnetized matter

Mateus R. Pelicer[a], **Débora P. Menezes**

Depto de Física - CFM , Universidade Federal de Santa Catarina Florianópolis, Florianópolis, SC CP. 476 - CEP 88.040 - 900, Brazil

Received: 11 July 2022 / Accepted: 5 September 2022 / Published online: 14 September 2022

Communicated by D. N. Voskresensky

Abstract Based on the assumption that the QCD phase diagram gives a realistic picture of hadronic and quark matter under different regimes, it is possible to claim that a quark core may be present inside compact objects commonly named hybrid neutron stars or even that a pure strange star may exist. In this work we explore how the phase transition is modified by the presence of strong magnetic fields and how it is impacted by parameters of the quark phase, for which we use the MIT-model with vector interactions. The phase transition is assumed to conserve flavor when hadrons turn into deconfined quarks. The hadronic equation of state is calculated with the NL3$\omega\rho^*$ parametrization of quantum hadrodynamics. We find that the magnetic field slightly reduces the pressure and chemical potential of the phase transition and the latent heat, the latter being very model dependent.

1 Introduction

Nuclear matter can be found in a variety of thermodynamic conditions, from low densities and high temperatures in heavy ions collision to high densities and low temperatures in compact stars [1–7]. The high temperatures achieved in heavy ion collisions provide the ideal environment for the formation of the quark-gluon plasma briefly after the collision, as the high energy enhances asymptotic freedom [8,9]. In compact stars, the high pressure environment may also favor a phase transition from hadronic to deconfined quark matter [10–12], so that the compact star can be either a hybrid hadron-quark or a pure quark star, if the Bodmer-Witten conjecture is satisfied [13–19]. The exact phase transition points at different temperatures remain unknown, since QCD is not exactly solvable from first principles and lattice QCD (LQCD) calculations have to deal with the sign problem and (so far) give accurate results only for the low chemical potential region [20–24]. Therefore effective models play an important role in the investigation of compact stars structure and composition. Analysis of QCD with Polyakov loops [25] predict the phase transition to occur at chemical potentials higher than $\sim$ 1050 MeV, models such as NJL, MIT and Quark-Meson coupling predict diverse values, depending on the hadronic model and on the choice of parameters of the quark phase [26–34]. It is also possible to constrain the most probable value of the phase transition, but analysis of this kind are model dependent [35,36].

In compact stars, the surface magnetic fields can vary from 10^{12} to 10^{15} G [37–40] and reach magnitudes of the order of 10^{18} G in the core, according to both the virial theorem [41,42] and solutions of coupled Einstein and Maxwell equations [43–46]. Since magnetic fields generate different pressures in the directions along and across the star [47,48], it is necessary to solve Einstein and Maxwell equations simultaneously, using a software such as LORENE, in order to determine the stellar structure of a magnetized star, instead of solving the axisymmetric TOV equations [49,50]. Nevertheless, it is possible to avoid such a complication and use an isotropic pressure for magnetized matter by using the chaotic field approximation, introduced in [51], which states that the magnetic field is disordered at small scales due to the short range magnetic interaction between moving charges, making the magnetic field approximately isotropic at very small scales while maintaining macroscopic order. Such a pressure is consistent with thermodynamics, and therefore it is also useful for analysing how the phase transition is modified in magnetized matter. Such an approximation has been applied to compact stars in Refs. [52–56].

The importance of the magnetic field on the strong interactions is long known, as it may alter the transition temperature, chemical potential and latent heat of the deconfinement phase transition, modify the vacuum structure, the dynamic

[a] e-mail: m.reinke.pelicer@posgrad.ufsc.br (corresponding author)

quark masses and the chiral transition [57–62]. The latent heat is an important ingredient as it quantifies the discontinuity in the energy density [63,64] and general upper bounds have been derived from nuclear physics alone [65], being applicable to effective models and to modified general relativity theories. Moreover, it also indicates the point where the transition changes from a first order to a crossover at finite temperatures, when its value is zero [62], a feature expected in the QCD phase diagram, where the critical end point is expected to exist [66].

In the present paper we study the effects of strong magnetic fields on the deconfinement phase transition at zero temperature using the non-linear Walecka model with a modified version of the NL3* [67] parametrization, proposed in [12], which we call NL3$\omega\rho^*$, for the hadron phase and the MIT-bag model with vector interactions for the quark phase. The hadronic parametrization is built to satisfy both up to date nuclear physics constraints and also a maximum stellar mass in the range 2.5−2.67 $M_\odot$, and can describe very massive compact objects, as the recently detected PSR J0952-0607, the fastest and heaviest known galactic neutron star [68] and even the one in the mass-gap region observed via the GW190814 [69], which is yet unidentified and can be either a very massive compact star or a black hole [70]. Reference [71] argues that GW190814 is likely to be a strange star, mainly due to the very stiff EoS required to produce such a high mass star and the small radius expected. However, depending on the choice of model parameters, it was shown in [12] that it can be a hadronic, a strange and even a hybrid star. The zero temperature approximation to phase transition calculations in compact stars is reasonable since, in the high density and low temperature regime, the point of the phase transition is not exceptionally changed by doing a small temperature calculation. Though thermal effects are less important microscopically it should be emphasized that heat and radiation released during the transition can be important in the cooling and spinning down of the star [72,73].

The MIT model with vector interactions has been discussed in [74–77], and a more through analysis of thermodynamic consistency, stability window, phase diagrams and astrophysical consequences can be found in [12,33,78]. To find the point of the phase transition we follow [79], where the authors argue that the phase transition does not occur with both phases in β-equilibrium, but rather with only the hadronic phase in β-equilibrium and the quark phase is determined such that the fractions of quark flavors are conserved during the transition, because the time scale over which the strong interaction acts is much shorter than the electroweak scale. After the phase transition occurs then β-equilibrium settles in. Hence, although matter in β-equilibrium is used in the construction of hybrid star EoS, flavour conservation may indeed be the favored situation during the phase transition. As far as the QCD phase diagram is concerned, the main difference between the transition with flavor conservation and β-equilibrium is that the later occurs at a much smaller pressure and chemical potential, as can be found in [12], where the non-magnetized phase transition with β-equilibrium is discussed.

In Sect. 2 we provide the main equations of quantum hadrodynamics and of the MIT model with a vector channel and concurrently discuss the parameters of each phase. In Sect. 4 we present the results, with a discussion on how the magnetic field and the quark parameters impact the point of the phase transition and the latent heat.

2 Formalism

2.1 Hadronic matter: Walecka-type model

For the hadronic phase we utilize the mean field approximation of the Walecka model with non linear terms considering the σ, ω, ρ and ϕ mesons, with lagrangian density written as [80–84]

$$\begin{aligned}\mathcal{L}_B = \sum_b \bar{\psi}_b\Big[i\gamma_\mu\left(\partial^\mu + ie_bA^\mu\right) - \gamma_0\left(g_{\omega b}\omega_0 + g_{\rho b}I_{3b}\rho_0\right.\\ \left.+g_{\phi b}\phi_0\right) - M_b^*\Big]\psi_b - \frac{1}{4}F_{\mu\nu}F^{\mu\nu} + \frac{1}{2}m_\phi^2\phi_0^2\\ - \frac{1}{2}m_\sigma^2\sigma_0^2 - \frac{\lambda}{3!}\sigma_0^3 - \frac{\kappa}{4!}\sigma_0^4 + \frac{1}{2}m_\omega^2\omega_0^2 + \frac{\xi}{4!}g_{\omega N}^4\omega_0^4\\ + \frac{1}{2}m_\rho^2\rho_0^2 + \Lambda_v g_{\omega N}^2 g_{\rho N}^2\omega_0^2\rho_0^2 \qquad (1)\end{aligned}$$

where ψ_b is the Dirac spinor for the baryon b, γ_μ are the Dirac matrices, $I_{3\,b}$ is the half of the Pauli isospin matrices τ, and $F_{\mu\nu} = \partial_\mu A_\nu - \partial_\nu A_\mu$ is the electromagnetic strength tensor. N refers to nucleon. The masses of baryons are modified by the medium, giving rise to an effective mass $M_b^* = M_b - g_{\sigma b}\sigma_0$, the ω-meson is responsible for the repulsive character of the strong force, the ρ-meson is responsible for properly adjusting the symmetry energy and its slope and the strange vector channel (ϕ) is essential to produce massive hyperonic stars [55,85]. The sum over b accounts for both nucleons and hyperons. The meson field equations are not altered by the magnetic field, and are given by

$$m_\sigma^2\sigma_0 + \frac{\kappa}{2}\sigma_0^2 + \frac{\lambda}{6}\sigma_0^3 = \sum_b g_{sb}n_{sb} \qquad (2)$$

$$m_\omega^2\omega_0 + \frac{1}{6}\xi g_\omega^4\omega_0^3 + 2\Lambda_v g_{\omega N}^2 g_{\rho N}^2\omega_0\rho_0^2 = \sum_b g_{\omega b}n_b \qquad (3)$$

$$m_\rho^2\rho_0 + 2\Lambda_v g_{\omega N}^2 g_{\rho N}^2\omega_0^2\rho_0 = \sum_b g_{\rho b}I_{3b}n_b \qquad (4)$$

$$m_\phi^2\phi_0 = \sum_b g_{\phi b}n_b. \qquad (5)$$

Neutral particles are not affected by the presence of the magnetic field, but the momentum of charged particles becomes quantized transversely to the magnetic field, occupying Landau levels quantified by the integer ν. The 3-dimensional integral over the momentum of particles at non-magnetized matter ($B = 0$) is thus replaced by a sum over the Landau levels [48,86,87]:

$$\int \frac{d^3\mathbf{k}}{(2\pi)^3} \to \frac{|e_b B|}{(2\pi)^2} \sum_{\nu,s(\nu)} \int_{-k_F}^{k_F} dk_z, \tag{6}$$

and the effective chemical potential is also modified, being given by

$$E^*_{Fb} = \begin{cases} \sqrt{k^2_{Fb} + 2\nu|e_b|B + M^{*2}_b} & e_b \neq 0 \\ \sqrt{k^2_{Fb} + M^{*2}_b}, & e_b = 0 \end{cases} \tag{7}$$

$$= \mu_b - g_\omega \omega_0 - g_\rho I_{3b} \rho_0 - g_\phi \phi_0, \tag{8}$$

where μ_b is the chemical potential of the baryon b, which is constrained by the β–equilibrium relation

$$\mu_b = \mu_B - e_b \mu_e, \tag{9}$$

and μ_B and μ_e are the baryonic and leptonic chemical potentials, respectively. It must be emphasized that the Fermi momentum k_F is the modulus of the 3-vector for uncharged particles and the z-component for charged ones, and in the later case it is a function of the Landau level, as it changes in order to keep the effective chemical potential fixed on the left hand side of Eq. (7). The spin degeneracy is also a function of the Landau level: the first level ($\nu = 0$) is occupied by a single spin state while higher levels are occupied by both, $\gamma(0) = 1$ and $\gamma_b(\nu > 0) = 2$. The sum over ν is limited from above by the point where the Fermi momentum becomes zero:

$$\nu_{max} \leq \left[\frac{{E^*_{Fb}}^2 - M^{*2}_b}{2|e_b|B} \right]. \tag{10}$$

The particle density is given by

$$n_b = \begin{cases} \frac{|e_b|B}{2\pi^2} \sum_\nu \gamma_b(\nu) k_{Fb} & e_b \neq 0 \\ \frac{\gamma_b k^3_{Fb}}{6\pi^2} & e_b = 0 \end{cases} \tag{11}$$

and the baryon scalar density is given by

$$n_{sb} = \begin{cases} \frac{|e_b|BM^*_b}{2\pi^2} \sum_\nu \gamma_b(\nu) \ln \left| \frac{k_{Fb} + E^*_{Fb}}{\sqrt{M^{*2}_b + 2\nu|e_b|B}} \right| & e_b \neq 0 \\ \frac{\gamma_b}{4\pi^2} \left[k_{Fb} E^*_{Fb} - M^{*2}_b \ln \left| \frac{k_{Fb} + E^*_{Fb}}{\sqrt{M^{*2}_b}} \right| \right] & e_b = 0 \end{cases} \tag{12}$$

Thermodynamic quantities can be calculated from the stress energy tensor. The energy density is calculated from the 00-component, and for charged particles it is given by

$$\varepsilon_b = \frac{|e_b|B}{4\pi^2} \sum_\nu \gamma_b(\nu) \left\{ k_{Fb} E^*_{Fb} + \left(M^{*2}_b + 2\nu|e_b|B \right) \ln \left| \frac{k_{Fb} + E^*_{Fb}}{\sqrt{M^{*2}_b + 2\nu|e_b|B}} \right| \right\} \quad e_b \neq 0 \tag{13}$$

while for for neutral ones it is

$$\varepsilon_b = \frac{\gamma_b}{16\pi^2} \left\{ k_{Fb} E^3_{Fb} + k^3_{Fb} E_{Fb} - M^{*4}_b \ln \left| \frac{k_{Fb}(\nu) + E^*_{Fb}}{\sqrt{M^{*2}_b}} \right| \right\} \quad e_b = 0 \tag{14}$$

The meson contribution is

$$\varepsilon_{\text{meson}} = \frac{m^2_\omega}{2}\omega^2_0 + \frac{\xi g^4_\omega}{8}\omega^4_0 + \frac{m^2_\phi}{2}\phi^2_0 + \frac{m^2_\sigma}{2}\sigma^2_0 + \frac{\kappa}{6}\sigma^3_0 + \frac{\lambda}{24}\sigma^4_0 + \frac{m^2_\rho}{2}\rho^2_0 + 3\Lambda_\nu g^2_{\omega N} g^2_{\rho N} \omega^2_0 \rho^2_0, \tag{15}$$

From these quantities we can calculate the total baryonic energy

$$\varepsilon_H = \sum_b \varepsilon_b + \varepsilon_{\text{meson}} \tag{16}$$

and the pressure, which can be written as

$$P_H = \sum_b \mu_b n_b - \varepsilon_H. \tag{17}$$

The lepton thermodynamics are given by the same equations for charged particles, with the change $E^*_{Fb} \to \mu_e$ and $M^*_b \to M_l$, such that

$$\varepsilon_{\text{tot}} = \varepsilon_H + \varepsilon_e + \varepsilon_\mu, \tag{18}$$

and

$$P_{\text{tot}} = P_H + P_e + P_\mu. \tag{19}$$

Formally, the contribution of the magnetic field must be added to the energy density ($+B^2/2$) and pressure ($+B^2/6$ in the chaotic field approximation), but since our goal is to study the phase transition this is not necessary, since this contribution is identical in both phases.

For the couplings and meson masses we use the parametrization proposed in [12], which we refer to as NL3$\omega\rho^*$, since it is a modification of the NL3* [67] force including an $\omega\rho$ interaction. This force has been parametrized to produce very massive stars ($2.5 \lesssim M_{\rm max}/M_\odot \lesssim 2.7$) even if the star has a quark core, for which the authors have used the same MIT-bag model with vector interactions that we use here. Constraints on the symmetry energy, slope, binding energy, effective mass, incompressibility and saturation density are based on the reviews [88,89]. The incompressibility is constrained mainly from giant monopole and dipole resonances. These are also sources of information for the symmetry energy, along with others, such as heavy-ion collisions, pygmy dipole resonances and neutron skin measurements. The symmetry energy slope is obtained from the derivative of the density dependent symmetry energy, and even though this parametrization satisfies constraints of L from the cited papers, it is not completely consistent with the recent PREX-2 inferred values: while one of the obtained values is $L = 106 \pm 37$ [90], another estimation that also takes astrophysical data into account predicts $L = 53^{+14}_{-15}$ MeV [91]. Nuclear constraints utilized in the parametrization can be found in Table I of [12]. Parameters are given in Table 1.

For the hyperon-meson couplings we use the SU(3) flavor symmetry [92–94], where couplings to vector mesons are calculated from a single parameter $0 \leq \alpha \leq 1$, while couplings to the scalar meson are fixed to reproduce the potentials $U_\Lambda = -28$ MeV, $U_\Sigma = +30$ MeV and $U_\Xi = -4$ MeV. The most well known potential is that of the Λ-hyperon [95,96], while the Σ and Ξ potentials are known to be repulsive and attractive, respectively, but their exact values are still uncertain [97–103]. Different choices of α impact the strangeness fraction of the star, with higher values favoring a larger hyperon fraction. In this work we choose to work with the intermediary value of $\alpha = 0.5$, which produces a maximum mass star of 2.57 $M_\odot$ with central density $n_c = 0.736$ fm^{-3}. Hyperon couplings are parametrized by the ratio $x_{Mb} = g_{Mb}/g_{Nb}$, where M is the meson and they are given by

$$x_{\sigma\Lambda} = 0.651 \quad x_{\sigma\Sigma} = 0.730 \quad x_{\sigma\Xi} = 0.428$$
$$x_{\omega\Lambda} = 0.714 \quad x_{\omega\Sigma} = 1.00 \quad x_{\omega\Xi} = 0.571$$
$$x_{\phi\Lambda} = -0.808 \quad x_{\phi\Sigma} = -0.404 \quad x_{\phi\Xi} = -1.01$$
$$x_{\rho\Lambda} = 0.00 \quad x_{\rho\Sigma} = 1.0 \quad x_{\rho\Xi} = 0.0.$$

3 Quarks: modified MIT bag model

The lagrangian density of the modified MIT model is given by

$$\mathcal{L}_Q = \sum_q \left\{ \bar{\psi}_q \left[i\gamma_\mu \partial^\mu - \gamma_0 g_{\omega q} \omega_0 - M_q \right] \psi_q - \mathcal{B} \right\} \Theta(\bar{\psi}_q \psi_q) + \frac{1}{2} m_\omega^2 \omega_0^2 + \frac{\xi}{4!} g_{\omega u}^4 \omega_0^4, \tag{20}$$

since both hadron (Eq. (1)) and quark lagrangian densities are of Dirac-type with different meson channels, the equations for quark densities n_q, energy density ε_q and pressure are the same as those for hadrons (Eqs. (11), (13), (14) and (17), with the substitutions $M_b^* \to M_q$ and $E_{Fb}^* \to E_{Fq}^* = \mu_q - g_{\omega q}\omega_0$. The quark degeneracy must be multiplied by 3 in order to include the colour degree of freedom, so now the first Landau level has degeneracy $\gamma(0) = 3$ and levels above have $\gamma(\nu > 0) = 6$. The bag parameter $\mathcal{B}$ can be interpreted as the pressure exerted inwards the hadron, balancing the outward pressure due to quarks on the hadronic surface [104].

The total quark energy density is

$$\varepsilon_Q = \sum_q \varepsilon_q + \frac{m_\omega^2}{2}\omega_0^2 + \frac{\xi g_{\omega u}^4}{8}\omega_0^4 + \mathcal{B}, \tag{21}$$

the baryon density is

$$n_B = \frac{1}{3}\sum_q n_q \tag{22}$$

and the pressure is given by

$$P_Q = \sum_q \mu_q n_q - \varepsilon_Q. \tag{23}$$

Table 1 Parameters for the NL3$\omega\rho^*$ model on the left and nuclear properties at saturation density on the right. The meson masses are $M_\sigma = 502.574$ MeV, $M_\omega = 782.600$ MeV, $M_\phi = 1020.00$ MeV and $M_\rho = 763.000$ MeV

$g_{\sigma N}$	10.0944	n_0 (fm^{-3})	0.150
$g_{\omega N}$	12.8065	M^*/M_N	0.594
$g_{\rho N}$	14.4410	B/A (MeV)	16.31
κ	21.6186 (fm^{-1})	K (MeV)	258
λ	180.8916	J (MeV)	30.7
Λ_v	0.045	L (MeV)	42

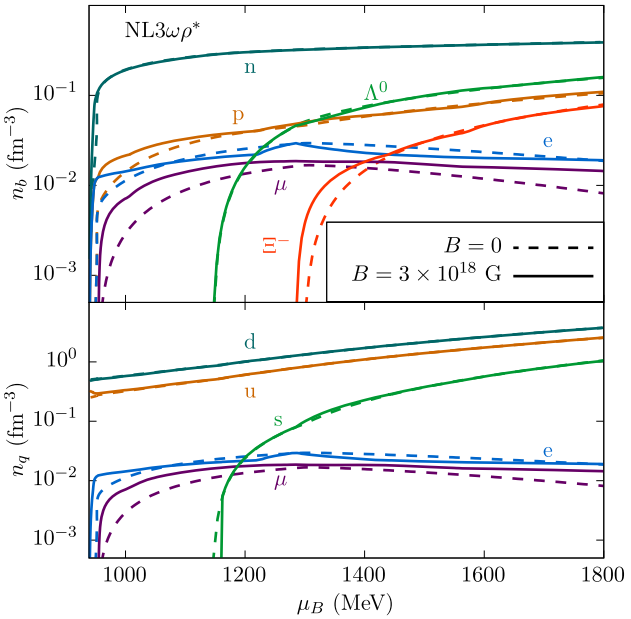

Fig. 1 Density of baryons (top) and quarks (bottom) as a function of the chemical potential. Full lines are densities with $B = 0$ and dashed lines are densities calculated with $B = 3 \times 10^{18}$ G

We define the chemical potential in the quark phase, at $T = 0$, as [79]

$$\mu_Q = \frac{\varepsilon_Q + P_Q}{n_Q} \tag{24}$$

In order to study the parameter dependence we define the variables

$$G_V = \left(\frac{g_{\omega u}}{m_\omega}\right)^2, \quad X_V = \frac{g_{\omega s}}{g_{\omega u}}, \tag{25}$$

In Ref. [78] it was shown that the stability window ranges between $148 \leq \mathcal{B}^{1/4} \leq 159$ MeV when the vector channel is not included and $m_s = 95$ MeV and it diminishes to $138 \lesssim \mathcal{B}^{1/4} \lesssim 145$ MeV when $G_V = 0.3$ fm^2, as shown in Fig. 4 of the mentioned paper. Figure 7 of the same paper shows how ξ modifies the stability window, but it must be remarked that their parameter b_4 differs from ξ in this paper by a factor of 6. Their analysis of the stability window is done in β-equilibrium, and since in the current work quark properties are calculated with flavor conservation we no longer consider the stability window. We fix a universal quark coupling to the vector meson, therefore $g_{\omega u} = g_{\omega d} = g_{\omega s}$, or $X_V = 1.0$.

4 Phase transition

To analyse how the magnetic field alters the phase transition, we consider it to be a first order transition with flavor

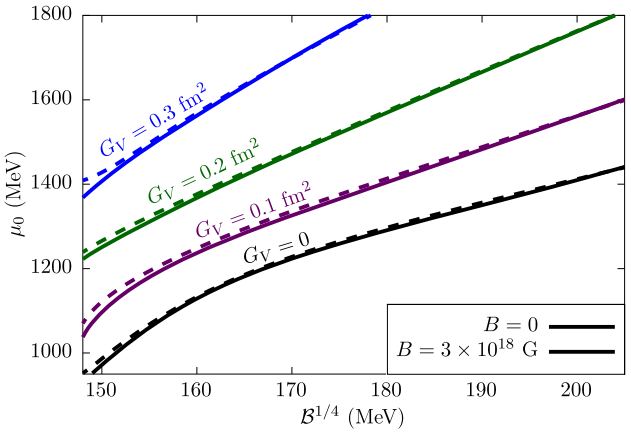

Fig. 2 Chemical potential of the phase transition as a function of the bag parameter with $G_V = 0$, 0.1, 0.2 and 0.3 fm^2 (black, purple, red and blue curves, respectively) and $X_V = 1.0$. Dashed lines are curves with $B = 0$ and solid ones with $B = 3 \times 10^{18}$ G

conservation. To do so we utilize the Maxwell construction

$$\mu_B = \mu_Q = \mu_0 \quad P_B = P_Q = P_0 \quad T_H = T_Q = 0, \tag{26}$$

and assume that only hadrons are in β-equilibrium, but not quarks, as proposed in [79], with the physical justification that the time scale of the strong interaction, responsible for deconfinement, is much shorter than the time scale of the electroweak interaction, responsible for β-equilibrium, meaning that the deconfinement transition will take place first, preserving the quark flavor fraction

$$Y_q = \sum_b \frac{1}{3} N_{qb} Y_b, \tag{27}$$

where N_{qb} is the number of quarks of flavor q on the hadron b and $Y_b = n_b/n_B$. Afterwards, the electroweak interaction will take place and β-equilibrium will be established in the quark phase. We assume the leptonic density is fixed during the transition, such that its energy density and pressure are also unchanged. The assumption of a first order phase transition is the one always found within RMF calculations and can be justified at low temperatures only. According to LQCD results, at low chemical potentials and high temperatures, a cross over is expected and it can be obtained if quantum fluctuations are taken into account [105,106]. As we are only investigating the zero temperature situation, quantum fluctuations can be disregarded.

The densities of hadrons and quarks are shown as a function of the chemical potential in Fig. 1 for $B = 0$ and 3×10^{18} G. The magnetic field favors the appearance of negatively charged particles at lower chemical potentials. In order to find the point of the phase transition, the flavor fraction is fixed at equal chemical potentials. Another possibility would be to fix the quark fractions at equal pressures, which would

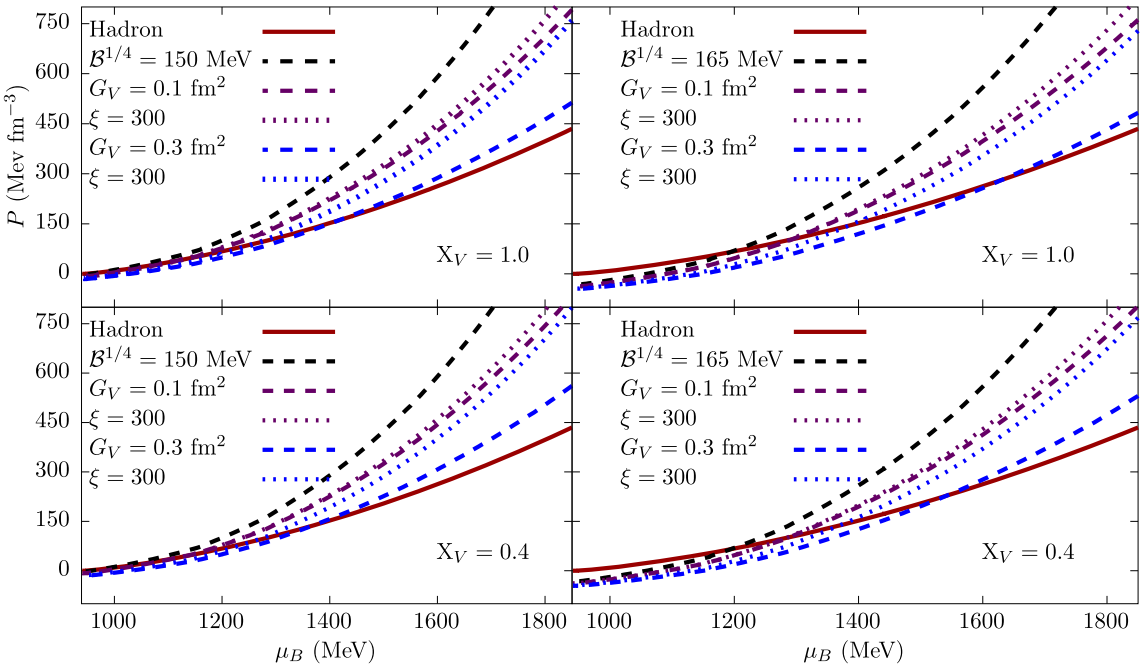

Fig. 3 Pressure of magnetized matter as a function of chemical potential with $\mathcal{B}^{1/4} = 150$ and 165 MeV (left and right, respectively) with $G_V = 0$, 0.1 and 0.3 fm^2 and $\xi = 0$ and 300. We show the pressure for $X_V = 1.0$ on the upper panels and $X_V = 0.4$ on the lower ones

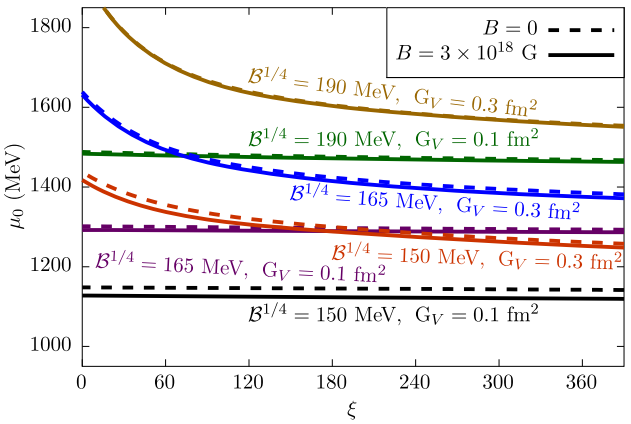

Fig. 4 Chemical potential of the phase transition as a function of fourth order coupling parameter ξ, with varying values for the $\mathcal{B}^{1/4}$ and $G_V =$ and $X_V = 1.0$. Dashed lines are curves with $B = 0$ and solid ones with $B = 3 \times 10^{18}$ G

lead to the same transition point, but to different quark densities and thermodynamic properties out of the transition point. Numerically it is simpler to fix the flavor fraction in the chemical potential, since the pressure of the quark phase can be negative but not the hadronic one, so one might exclude a large portion of chemical potential by fixing the flavor fraction at equal pressures and make it difficult to find the phase transition at very low chemical potentials.

Firstly we examine how the chemical potentials of the transition are altered with the magnetic field for values of $\mathcal{B}^{1/4}$ ranging between 148 and 205 MeV, with $G_V = 0$, 0.1, 0.2 and 0.3 fm^2. As shown in Fig. 2, increasing values of the bag parameter and of the ω-coupling G_V increase the chemical potential, and thus also the pressure of the phase transition. For values of G_V larger than 0.3 the phase transition occurs at chemical potentials larger than 1800 MeV, which are beyond those expected in neutron stars [12]. The difference in the phase transition in magnetized and demagnetized matter is larger for lower values of the bag parameter, with the magnetic field favoring a slightly smaller chemical potential. As the bag parameter is increased, the effect of the magnetic field becomes less noticeable because the bag term dominates the pressure.

The addition of a fourth order self interaction for the ω-meson stiffens the EoS and reduces the chemical potential of the phase transition, with its importance being more pronounced at large chemical potentials and for higher values of the ω-coupling G_V, as shown in Fig. 3, where one can see in the upper panels that for $G_V = 0.1$ fm^2, a $\xi = 300$ stiffens the EoS only slightly, while for $G_V = 0.3$ fm^2 the stiffening is much more pronounced. The parameter X_V, which is kept fixed at 1.0 in all other figures, affects the coupling of the ω-meson to the strange quark and thus it will not affect the qualitative behavior of our results. On the bottom panel we show the pressure when the ω-coupling to the strange meson is determined from symmetry to be $X_V = 0.4$ [78], stiffening the equation of state since the hyperonic contribution is suppressed and their effect is to soften the equation of state. Thus, a smaller X_V also lowers the chemical potential of the phase transition.

Table 2 Values of μ_0 (in MeV) and P_0 (in MeV/fm^3) for the phase transition at T= 0 considering three–flavored matter. Results are shown for sets of parameters $\mathcal{B}^{1/4}$, G_V, X_V, ξ within and outside of the stability window of SQM, for both magnetised and demagnetized matter

$\mathcal{B}^{1/4}$ (MeV)	G_V (fm^2)	X_V	ξ	B = 0	B = 3×10^{18} G
150	0.0	–	0	$P_0 = 4.99601$	$P_0 = 3.31123$
				$\mu_0 = 983.957$	$\mu_0 = 969.932$
				$L\big\vert_\varepsilon = 0.0102476$	$L\big\vert_\varepsilon = 0.0082077$
165	0.0	–	0	$P_0 = 65.4288$	$P_0 = 64.9179$
				$\mu_0 = 1198.74$	$\mu_0 = 1193.33$
				$L\big\vert_\varepsilon = 0.069284$	$L\big\vert_\varepsilon = 0.0688982$
190	0.0	–	0	$P_0 = 129.98$	$P_0 = 128.162$
				$\mu_0 = 1356.8$	$\mu_0 = 1349.32$
				$L\big\vert_\varepsilon = 0.142094$	$L\big\vert_\varepsilon = 0.140982$
150	0.1	1.0	0	$P_0 = 48.3109$	$P_0 = 43.2135$
				$\mu_0 = 1148.14$	$\mu_0 = 1127.69$
				$L\big\vert_\varepsilon = 0.0252144$	$L\big\vert_\varepsilon = 0.0214088$
150	0.1	1.0	300	$P_0 = 46.7929$	$P_0 = 41.173$
				$\mu_0 = 1143.39$	$\mu_0 = 1121.07$
				$L\big\vert_\varepsilon = 0.025398$	$L\big\vert_\varepsilon = 0.0211815$
150	0.3	1.0	0	$P_0 = 169.208$	$P_0 = 160.899$
				$\mu_0 = 1437.43$	$\mu_0 = 1417.6$
				$L\big\vert_\varepsilon = 0.0249172$	$L\big\vert_\varepsilon = 0.0212103$
150	0.3	1.0	300	$P_0 = 92.873$	$P_0 = 90.7844$
				$\mu_0 = 1270.92$	$\mu_0 = 1262.1$
				$L\big\vert_\varepsilon = 0.0387617$	$L\big\vert_\varepsilon = 0.0345084$
165	0.1	1.0	0	$P_0 = 105.568$	$P_0 = 103.109$
				$\mu_0 = 1301.59$	$\mu_0 = 1292.22$
				$L\big\vert_\varepsilon = 0.0738039$	$L\big\vert_\varepsilon = 0.0720843$
165	0.1	1.0	300	$P_0 = 102.619$	$P_0 = 101.187$
				$\mu_0 = 1294.59$	$\mu_0 = 1287.62$
				$L\big\vert_\varepsilon = 0.0755038$	$L\big\vert_\varepsilon = 0.0741826$
165	0.3	1.0	0	$P_0 = 284.83$	$P_0 = 282.095$
				$\mu_0 = 1638.55$	$\mu_0 = 1631.37$
				$L\big\vert_\varepsilon = 0.0758115$	$L\big\vert_\varepsilon = 0.0745062$
165	0.3	1.0	300	$P_0 = 147.724$	$P_0 = 144.561$
				$\mu_0 = 1394.34$	$\mu_0 = 1384.29$
				$L\big\vert_\varepsilon = 0.0917639$	$L\big\vert_\varepsilon = 0.0891916$
150	0.1	0.4	0	$P_0 = 48.2897$	$P_0 = 43.2128$
				$\mu_0 = 1148.08$	$\mu_0 = 1127.68$
				$L\big\vert_\varepsilon = 0.0252111$	$L\big\vert_\varepsilon = 0.0214087$
150	0.1	0.4	300	$P_0 = 46.7934$	$P_0 = 41.1729$
				$\mu_0 = 1143.39$	$\mu_0 = 1121.07$
				$L\big\vert_\varepsilon = 0.0253982$	$L\big\vert_\varepsilon = 0.0211814$
150	0.3	0.4	0	$P_0 = 144.805$	$P_0 = 136.405$
				$\mu_0 = 1388.3$	$\mu_0 = 1367.1$
				$L\big\vert_\varepsilon = 0.0245113$	$L\big\vert_\varepsilon = 0.0198264$
150	0.3	0.4	300	$P_0 = 89.5491$	$P_0 = 87.461$
				$\mu_0 = 1262.64$	$\mu_0 = 1253.72$
				$L\big\vert_\varepsilon = 0.0377602$	$L\big\vert_\varepsilon = 0.0338778$

Table 2 continued

$\mathcal{B}^{1/4}$ (MeV)	G_V (fm^2)	X_V	ξ	B = 0	B = 3 × 10^{18} G
165	0.1	0.4	0	$P_0 = 103.382$	$P_0 = 101.707$
				$\mu_0 = 1296.41$	$\mu_0 = 1288.87$
				$L\big\vert_\varepsilon = 0.0737347$	$L\big\vert_\varepsilon = 0.0724917$
165	0.1	0.4	300	$P_0 = 100.603$	$P_0 = 99.9313$
				$\mu_0 = 1289.77$	$\mu_0 = 1284.58$
				$L\big\vert_\varepsilon = 0.0751441$	$L\big\vert_\varepsilon = 0.0742676$
165	0.3	0.4	0	$P_0 = 229.087$	$P_0 = 227.519$
				$\mu_0 = 1546.98$	$\mu_0 = 1541.16$
				$L\big\vert_\varepsilon = 0.0742462$	$L\big\vert_\varepsilon = 0.0741287$
165	0.3	0.4	300	$P_0 = 141.044$	$P_0 = 137.474$
				$\mu_0 = 1380.43$	$\mu_0 = 1369.38$
				$L\big\vert_\varepsilon = 0.0899391$	$L\big\vert_\varepsilon = 0.0859813$

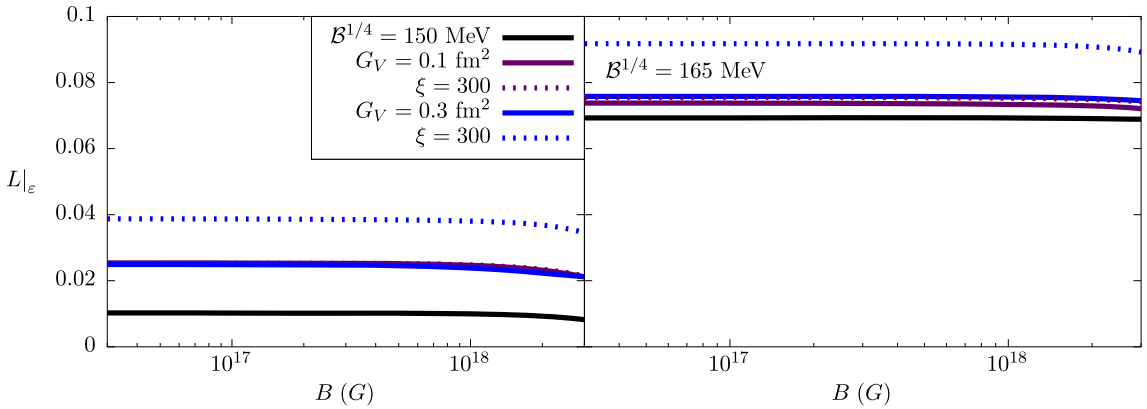

Fig. 5 Latent heat as a function of the magnetic field for bag values of 150 and 165 (left and right, respectively), with $G_V = 0$, 0.1 and 0.3 fm^2 and $\xi = 0$ and 300

In Fig. 4 we show how the chemical potential of the phase transition is changed as a function of ξ, for both magnetized and demagnetized matter. As we turn on the fourth order interaction the chemical potential decreases rapidly, and as ξ grows larger the chemical potential varies less. This is more attenuated for larger G_V, since the fourth order interactions is weighted by G_V^2.

The magnetic field slightly reduces the transition chemical potential, with the effect pronounced at lower chemical potential. To quantify how the phase transition is affected by the magnetic field and by the choice of parameters we show in Table 2 the chemical potential and pressure of the transition for different $\mathcal{B}^{1/4} = 0$, 150 and 165 MeV, $G_V = 0.1$ and 0.3 fm^2, $\xi = 0$ and 300 and $X_V = 1.0$ and 0.4. We also show the relativistic latent heat, given by

$$L\big\vert_\varepsilon = P_H \frac{\varepsilon_Q - \varepsilon_H}{\varepsilon_Q \varepsilon_H}, \tag{28}$$

as proposed in [65], which quantifies the intensity of the phase transition, i.e., the discontinuity in the energy density between phases. The latent heat diminishes in magnetized matter, more prominently for smaller bag values. The magnetic field becomes important on the latent heat for magnetic fields of the order of 10^{18} G only, as shown in Fig. 5, where the latent heat is shown as a function of the magnetic field.

5 Conclusion

In the present paper we analysed how the deconfinement phase transition is affected by strong magnetic fields (3×10^{18} G), possibly present in the interior of neutron stars. For the hadron phase we have utilized the NL3$\omega\rho^*$ parametrization of the Walecka model and for the quark phase, the MIT bag model with a repulsive vector channel. We find the phase transition with the assumptions of flavor conservation, so the hadron phase is in β-equilibrium and the quark phase is not, as the electroweak interaction has no time to act during the

occurrence of the transition, and of a chaotic magnetic field, such that it can be approximated as isotropic on microscopic scales.

We have obtained the phase transition point over a large range of parameters of the quark phase at zero temperature. We find that the magnetic field slightly diminishes the chemical potential and pressure point of the phase transition .The effect of the magnetic field is more pronounced for smaller bag values ($\mathcal{B}$) and hadron–meson coupling (G_V), which corresponds to transitions at lower chemical potentials. The fourth order self-interaction of the ω-meson stiffens the quark equation of state, reducing the chemical potential of the phase transition, and the effect of the magnetic field is uniform for different strengths of the self-coupling. The latent heat is extremely dependent on the parametrization of the quark phase, changing by a factor of two to three for different bag values. We expect it to be also dependent on the hadron model or parametrization, but this is left for future inspection.

As already mentioned, the approximation of zero temperature (T=0) is standard in phase transition calculations in compact stars and it is a reasonable approximation due to the high density environment, and thus very high Fermi energy, which makes thermal effects less important microscopically. However, we do think that a calculation at finite temperature has to be performed and we will investigate the effects of the magnetic fields on the whole QCD phase transition diagram and search for the zero latent heat, which may indicate the CEP, in a future work.

Acknowledgements This work is a part of the project INCT-FNA Proc. No. 464898/2014-5. D.P.M. is partially supported by Conselho Nacional de Desenvolvimento Científico e Tecnológico (CNPq/Brazil) respectively under grant 301155.2017-8 and M.R.P. is supported by Coordenação de Aperfeiçoamento de Pessoal de Nível Superior (CAPES). M.R.P. thanks fruitful discussions with Carline Biesdorf.

Data Availability Statement This manuscript has no associated data or the data will not be deposited. [Authors' comment: All results obtained in this work are either numerical or analytical, hence, there is no associated data.]

References

1. Garima, P.K. Deshwal, M.K. Yadav, AIP Conference Proceedings **2352**, 030004 (2021). https://aip.scitation.org/doi/pdf/10.1063/5.0052529
2. E. Shuryak, Rev. Mod. Phys. **89**, 035001 (2017)
3. R. Pasechnik, M. Šumbera, Universe **3**, 7 (2017). arXiv:1611.01533
4. F. Weber, Pulsars as Astrophysical Laboratories for Nuclear and Particle Physics, Series in High Energy Physics, Cosmology and Gravitation (CRC Press, 2017), ISBN 9781351420945. https://books.google.com.br/books?id=SSw2DwAAQBAJ
5. N. Glendenning, Compact Stars: Nuclear Physics, Particle Physics and General Relativity, Astronomy and Astrophysics Library (Springer New York, 2012), ISBN 9781468404913. https://books.google.com.br/books?id=cCDlBwAAQBAJ
6. I. Vidaña, Eur. Phys. J. Plus **133**, 445 (2018). arXiv:1805.00837
7. D.P. Menezes, Universe **7**, 267 (2021). arXiv:2106.09515
8. R. Bellwied, Nuclear. Phys. A **752**, 398 (2005). (**proceedings of the 22nd International Nuclear Physics Conference (Part 2)**)
9. K. Adcox, S. Adler, S. Afanasiev, C. Aidala, N. Ajitanand, Y. Akiba, A. Al-Jamel, J. Alexander, R. Amirikas, K. Aoki et al., Nuclear Phys. A **757**, 184 (2005). (**first Three Years of Operation of RHIC**)
10. E. Annala, C. Ecker, C. Hoyos, N. Jokela, D. Rodríguez Fernández, A. Vuorinen, JHEP **12**, 078 (2018). arXiv:1711.06244
11. E. Annala, T. Gorda, A. Kurkela, J. Nättilä, A. Vuorinen, Nature Phys. **16**, 907 (2020). arXiv:1903.09121
12. L.L. Lopes, D.P. Menezes, Astrophys. J. **936**, 41 (2022). https://doi.org/10.3847/1538-4357/ac81c4
13. D.D. Ivanenko, D.F. Kurdgelaidze, Astrophysics **1**, 251 (1965)
14. A.R. Bodmer, Phys. Rev. D **4**, 1601 (1971)
15. E. Witten, Phys. Rev. D **30**, 272 (1984)
16. E. Østgaard, Phys. Rep. **242**, 313 (1994)
17. S. Schramm, R. Negreiros, J. Steinheimer, T. Schurhoff, V. Dexheimer, Acta Phys. Polon. B **43**, 749 (2012). arXiv:1112.1853
18. G. Mitra, H.S. Sahoo, R. Mishra, P.K. Panda, Phys. Rev. C **105**, 045802 (2022)
19. M. Hanauske, L.R. Weih, H. Stöcker, L. Rezzolla, Eur. Phys. J. Special Topics **230**, 543 (2021)
20. A. Borici, Prog. Theor. Phys. Suppl. **153**, 335 (2004)
21. A. Alexandru, M. Faber, I. Horvath, K.F. Liu, Phys. Rev. D **72**, 114513 (2005). arXiv:hep-lat/0507020
22. T. Mendes, Braz. J. Phys. **37**, 597 (2007). arXiv:hep-lat/0609035
23. T. Bhattacharya et al., Phys. Rev. Lett. **113**, 082001 (2014). arXiv:1402.5175
24. V.A. Goy, V. Bornyakov, D. Boyda, A. Molochkov, A. Nakamura, A. Nikolaev, V. Zakharov, PTEP **2017**, 031D01 (2017). arXiv:1611.08093
25. K. Fukushima, T. Hatsuda, Rept. Prog. Phys. **74**, 014001 (2011). arXiv:1005.4814
26. S. Kagiyama, S. Hirooka, H. Kikukawa, J. Kikukawa, Progress Theoret. Phys. **69**, 579 (1983)
27. G. Alaverdyan, Symmetry **13** (2021)
28. C.A. Graeff, M.D. Alloy, K.D. Marquez, C. Providência, D.P. Menezes, JCAP **01**, 024 (2019). arXiv:1806.04170
29. L.A.H. Mamani, C.V. Flores, V.T. Zanchin, Phys. Rev. D **102**, 066006 (2020). arXiv:2006.09401
30. M. Buballa, Phys. Rept. **407**, 205 (2005). arXiv:hep-ph/0402234
31. M. Buballa, Phys. Rep. **407**, 205 (2005)
32. S.B. Rüster, V. Werth, M. Buballa, I.A. Shovkovy, D.H. Rischke, Phys. Rev. D **72**, 034004 (2005)
33. L.L. Lopes, C. Biesdorf, K.D. Marquez, D.P. Menezes, Phys. Scripta **96**, 065302 (2021). arXiv:2009.13552
34. M. Ju, X. Wu, F. Ji, J. Hu, H. Shen, Phys. Rev. C **103**, 025809 (2021). arXiv:2102.12276
35. Z. Bai, Y.x. Liu, AIP Conf. Proc. **2127**, 020030 (2019). arXiv:1904.01978
36. Z. Miao, A. Li, Z. Zhu, S. Han, Astrophys. J. **904**, 103 (2020)
37. U. Geppert, M. Rheinhardt, J. Gil, Astron. Astrophys. **412**, L33 (2003). arXiv:astro-ph/0311121
38. F. Haberl, A.D. Schwope, V. Hambaryan, G. Hasinger, C. Motch, A&A **403**, L19 (2003)
39. Q.H. Peng, H. Tong, Mon. Notices R. Astron. Soc. **378**, 159 (2007)
40. M. Revnivtsev, S. Mereghetti, Space Sci. Rev. **191**, 293 (2015). arXiv:1411.5843
41. D. Lai, S.L. Shapiro, Astrophys. J. **383**, 745 (1991)
42. S. Bonazzola, E. Gourgoulhon, M. Salgado, J.A. Marck, Astron. Astrophys. **278**, 421 (1993)
43. M. Bocquet, S. Bonazzola, E. Gourgoulhon, J. Novak, Astron. Astrophys. **301**, 757 (1995). arXiv:gr-qc/9503044

44. C.Y. Cardall, M. Prakash, J.M. Lattimer, Astrophys. J. **554**, 322 (2001). arXiv:astro-ph/0011148
45. A.G. Pili, N. Bucciantini, L. Del Zanna, Mon. Notices R. Astron. Soc. **470**, 2469 (2017)
46. A. Tsokaros, M. Ruiz, S.L. Shapiro, K. Uryū, Phys. Rev. Lett. **128**, 061101 (2022). arXiv:2111.00013
47. E.J. Ferrer, V. de la Incera, J.P. Keith, I. Portillo, P.L. Springsteen, Phys. Rev. C **82**, 065802 (2010)
48. M. Strickland, V. Dexheimer, D.P. Menezes, Phys. Rev. D **86**, 125032 (2012)
49. J.R. Oppenheimer, G.M. Volkoff, Phys. Rev. **55**, 374 (1939)
50. R.C. Tolman, Phys. Rev. **55**, 364 (1939)
51. Y. Zel'dovich, I. Novikov, Stars and Relativity, Dover Books on Physics (Dover Publications, 2014), ISBN 9780486171326. arXiv:https://books.google.com.br/books?id=69YIBAAAQBAJ
52. L.L. Lopes, D. Menezes, JCAP **08**, 002 (2015). arXiv:1411.7209
53. D.P. Menezes, L.L. Lopes, Eur. Phys. J. A **52**, 17 (2016). arXiv:1505.06714
54. F. Wu, C. Wu, Z. Ren, Chin. Phys. C **41**, 045102 (2017). arXiv:1612.04553
55. L.L. Lopes, D.P. Menezes, Eur. Phys. J. A **56**, 122 (2020)
56. B.C.T. Backes, K.D. Marquez, D.P. Menezes, Eur. Phys. J. A **57**, 229 (2021). arXiv:2103.14733
57. R. Gatto, M. Ruggieri, Lect. Notes Phys. **871**, 87 (2013). arXiv:1207.3190
58. G.S. Bali, F. Bruckmann, G. Endrődi, Z. Fodor, S.D. Katz, A. Schäfer, Phys. Rev. D **86**, 071502 (2012)
59. V. Dexheimer, R. Negreiros, S. Schramm, Eur. Phys. J. A **48**, 189 (2012). arXiv:1108.4479
60. V. Dexheimer, R. Negreiros, S. Schramm, M. Hempel, AIP Conf. Proc. **1520**, 264 (2013). arXiv:1208.1320
61. E.S. Fraga, Lect. Notes Phys. **871**, 121 (2013). arXiv:1208.0917
62. N.O. Agasian, S.M. Fedorov, Phys. Lett. B **663**, 445 (2008). arXiv:0803.3156
63. A. Carbone, A. Polls, A. Rios, I. Vidaña, Phys. Rev. C **83**, 024308 (2011)
64. I. Bombaci, D. Logoteta, P. Panda, C. Providência, I. Vidaña, Phys. Lett. B **680**, 448 (2009)
65. E. Lope-Oter, F.J. Llanes–Estrada, Phys. Rev. C **105**, L052801 (2022). arXiv:2103.10799
66. P. Costa, M. Ferreira, D.P. Menezes, J.A. Moreira, C.M.C. Providência, Phys. Rev. D **92**, 036012 (2015)
67. G.A. Lalazissis, S. Karatzikos, R. Fossion, D. Pena Arteaga, A.V. Afanasjev, P. Ring, Phys. Lett. B **671**, 36 (2009). arXiv:0909.1432
68. R.W. Romani, D. Kandel, A.V. Filippenko, T.G. Brink, W. Zheng, Astrophys. J. Lett. **934**, L18 (2022). arXiv:2207.05124
69. R. Abbott, T.D. Abbott, S. Abraham, F. Acernese, K. Ackley, C. Adams, R.X. Adhikari, V.B. Adya, C. Affeldt, M. Agathos et al., Astrophys. J. Lett. **896**, L44 (2020). arXiv:2006.12611
70. A. Tsokaros, M. Ruiz, S.L. Shapiro, Astrophys. J. **905**, 48 (2020)
71. I. Bombaci, A. Drago, D. Logoteta, G. Pagliara, I. Vidaña, Phys. Rev. Lett. **126**, 162702 (2021)
72. N.N. Pan, X.P. Zheng, J.R. Li, Mon. Not. Roy. Astron. Soc. **371**, 1359 (2006). arXiv:astro-ph/0607051
73. M. Stejner, F. Weber, J. Madsen, Astrophys. J. **694**, 1019 (2009). arXiv:0801.0358
74. T. Klahn, T. Fischer, Astrophys. J. **810**, 134 (2015). arXiv:1503.07442
75. B. Franzon, R.O. Gomes, S. Schramm, Mon. Notices R. Astron. Soc. **463**, 571 (2016). arXiv:1608.02845
76. R.O. Gomes, P. Char, S. Schramm, Astrophys. J. **877**, 139 (2019). arXiv:1806.04763
77. M.B. Albino, R. Fariello, F.S. Navarra, Phys. Rev. D **104**, 083011 (2021). arXiv:2106.12956
78. L.L. Lopes, C. Biesdorf, D.P. Menezes, Phys. Scripta **96**, 065303 (2021). arXiv:2005.13136
79. I. Bombaci, D. Logoteta, Int. J. Modern Phys. D **26**, 1730004 (2017)
80. J. Walecka, Ann. Phys. **83**, 491 (1974)
81. J. Boguta, A. Bodmer, Nucl. Phys. A **292**, 413 (1977)
82. H. Mueller, B.D. Serot, Nucl. Phys. A **606**, 508 (1996). arXiv:nucl-th/9603037
83. F.J. Fattoyev, C.J. Horowitz, J. Piekarewicz, G. Shen, Phys. Rev. C **82**, 055803 (2010)
84. L.L. Lopes, Communications in Theoretical Physics (2021)
85. S. Weissenborn, D. Chatterjee, J. Schaffner-Bielich, Nuclear Phys. A **881**, 62 (2012). (**progress in Strangeness Nuclear Physics**)
86. A. Broderick, M. Prakash, J.M. Lattimer, Astrophys. J. **537**, 351 (2000)
87. G.J. Mao, A. Iwamoto, Z.X. Li, Chin. J. Astron. Astrophys. **3**, 359 (2003)
88. M. Dutra, O. Lourenço, S.S. Avancini, B.V. Carlson, A. Delfino, D.P. Menezes, C. Providência, S. Typel, J.R. Stone, Phys. Rev. C **90**, 055203 (2014)
89. M. Oertel, M. Hempel, T. Klähn, S. Typel, Rev. Mod. Phys. **89**, 015007 (2017)
90. B.T. Reed, F.J. Fattoyev, C.J. Horowitz, J. Piekarewicz, Phys. Rev. Lett. **126**, 172503 (2021)
91. R. Essick, I. Tews, P. Landry, A. Schwenk, Phys. Rev. Lett. **127**, 192701 (2021)
92. L.L. Lopes, D.P. Menezes, Phys. Rev. C **89**, 025805 (2014)
93. L.L. Lopes, D.P. Menezes, Nucl. Phys. A **1009**, 122171 (2021)
94. T. Miyatsu, M.K. Cheoun, K. Saito, Phys. Rev. C **88**, 015802 (2013)
95. D.J. Millener, C.B. Dover, A. Gal, Phys. Rev. C **38**, 2700 (1988)
96. J. Schaffner, C. Greiner, H. Stöcker, Phys. Rev. C **46**, 322 (1992)
97. J. Mareš, E. Friedman, A. Gal, B. Jenning, Nucl. Phys. A **594**, 311 (1995)
98. P. Khaustov, D.E. Alburger, P.D. Barnes, B. Bassalleck, A.R. Berdoz, A. Biglan, T. Bürger, D.S. Carman, R.E. Chrien, C.A. Davis, The AGS E885 Collaboration et al., Phys. Rev. C **61**, 054603 (2000)
99. J. Schaffner-Bielich, A. Gal, Phys. Rev. C **62**, 034311 (2000)
100. E. Friedman, A. Gal, Phys. Rep. **452**, 89 (2007)
101. L. Fabbietti, V.M. Sarti, O.V. Doce, Ann. Rev. Nucl. Part. Sci. **71**, 377 (2021). arXiv:https://doi.org/10.1146/annurev-nucl-102419-034438
102. S. Acharya, D. Adamová, S.P. Adhya, A. Adler, J. Adolfsson, M.M. Aggarwal, G. Aglieri Rinella, M. Agnello, N. Agrawal, Z. Ahammed et al. (A Large Ion Collider Experiment Collaboration), Phys. Rev. Lett. **123**, 112002 (2019)
103. E. Friedman, A. Gal, Phys. Lett. B **820**, 136555 (2021). arXiv:2104.00421
104. R. Bhaduri, R. Bhaduri, Models of the Nucleon: From Quarks to Soliton, Advanced book program (Addison-Wesley, Advanced Book Program, 1988), ISBN 9780201156737. arXiv:https://books.google.com.br/books?id=7smBAAAAIAAJ
105. Y. Aoki, G. Endrodi, Z. Fodor, S.D. Katz, K.K. Szabo, Nature **443**, 675 (2006). arXiv:hep-lat/0611014
106. S. Borsanyi, Z. Fodor, J.N. Guenther, R. Kara, S.D. Katz, P. Parotto, A. Pasztor, C. Ratti, K.K. Szabo, Phys. Rev. Lett. **125**, 052001 (2020). arXiv:2002.02821

Do short range correlations inhibit the appearance of the nuclear pasta?

M. R. Pelicer[1], D. P. Menezes[1], M. Dutra[2], and O. Lourenço[2]
[1] *Depto de Física - CFM - Universidade Federal de Santa Catarina Florianópolis - SC - CP. 476 - CEP 88.040 - 900 - Brazil*
[2] *Departamento de Física, Instituto Tecnológico de Aeronáutica, DCTA, 12228-900, São José dos Campos, SP, Brazil*

It is well known that strongly correlated neutron-proton pairs, the short-range correlations (SRC), can modify many of the nuclear properties. In this work we have introduced, for the first time, short range correlations in the calculation of the nuclear pasta phase at zero temperature and checked how they affect its size and internal structure. We have used two different parameterizations of relativistic models in a mean field approximation and the coexistence phase approximation as a first estimation of the effects. We have seen that for very asymmetric neutron-proton-electon matter, the pasta phase shrinks considerably as compared with the results without SRC and all internal structures vanish, except the simple spherically symmetric one, the droplets. Our results indicate a possible disappearance of these complicated structures as the temperature increases.

Introduction.—Nonspherical complex structures that appear due to a frustration in sub-saturation nuclear densities are believed to be present in the inner crust of neutron stars and in core-collapse supernova cores [1, 2]. Although possibly present only in a small range of densities and temperatures, different studies suggest that these exotic structures may have considerable impact on different astrophysical phenomena and on the magnetic evolution of neutron stars [3]. Some of the consequences of the existence of the pasta phase are expected to leave signatures in quasiperiodic oscillations observed in soft-gamma ray repeaters [4] and magnetar giant flares [5]. More recently, the detection of late-time neutrinos from a Milky Way core-collapse supernova seems to be approaching reality [6] and it was claimed that neutrino diffusion seems to be affected by the pasta phase in protoneutron stars in such a way that its signal can be greatly enhanced after core collapse [7].

From the theoretical point of view, there are some models and simulations that predict that the pasta structures can be very complex indeed. Calculations departed from the more traditional 3D, 2D and 1D geometries in a single unit cell to density fluctuations [8, 9] as well as to structures resembling waffle, parking garage and TPMS [10–12]. Different calculations also show that the pasta phase size decreases as temperature increases and may even occupy just a small portion in between two homogeneous phases at certain temperatures [13–15].

Most of the pasta phase calculations depend on equations of state (EOS) parameterized to satisfy nuclear matter bulk properties. One missing ingredient in all pasta calculations is the inclusion of short-range correlations (SRC). Strongly correlated neutron-proton pairs can modify the internal structure of the nucleus and generate a series of non trivial consequences [16–30]. In a seminal paper on cold dense matter obtained with the inclusion of SRC [31], the authors claimed that the difference between the types of pairs (proton-proton, neutron-neutron and proton-neutron) *is due to the nature of the strong force and has implications for understanding cold dense nuclear systems such as neutron stars.* Hence, the introduction of SRC in the pasta phase structure is long due.

So...what if the complicated pasta structures are simply not there when SRC are taken into account? As a first study, we investigate the effects of the SRC on the pasta phase and its structure with a simple prescription, the coexistence phase approximation (CPA) [13] within relativistic mean field models at zero temperature.

SRC (homogeneous phase).— We start by studying the effects of the SRC on the homogeneous phase with two different parametrizations, namely IUFSU [32] and FSU2R [33]. When SRC are included, the momentum (k) distribution present in the kinetic terms of the energy density, pressure and scalar density is modified by the inclusion of a "high momentum tail" proportional to k^{-4} and, as a consequence, the model has to be reparameterized in order to reproduce nuclear bulk properties. The Lagrangian density used in the present work, the new expressions for the quantities necessary to compute the EOS and the new parameters for the FSU2R model are given in [27–30]. For the IUFSU, the constants for the model with and without SRC are given in Table I.

TABLE I: Coupling constants of the IUFSU parametrization with and without SRC included. $M_{\rm nuc} = 939$ MeV is the nucleon rest mass. In both cases, the last constant is fixed in $C = 5.000 \times 10^{-3}$.

coupling	IUFSU	IUFSU-SRC
g_σ	9.971	10.132
g_ω	13.032	11.867
g_ρ	13.590	15.551
$A/M_{\rm nuc}$	1.785	2.956
B	0.488	−29.880
α_3' ($\times 10^{-2}$)	9.200	1.094

As the results obtained with the two models are qualitatively similar, we display the graphs for the IUFSU parameterization only. We have chosen to show re-

sults for symmetric matter (proton fraction $Y_p = 0.5$), $Y_p = 0.35$, usually considered in core-collapse supernova and $Y_p = 0.1$, a quantity that relates to the amount of protons in neutron star matter.

In Fig. 1, we compare the proton and neutron chemical potentials with and without SRC for different proton fractions. It is notorious that very asymmetric matter is more susceptible to changes than symmetric nuclear matter.

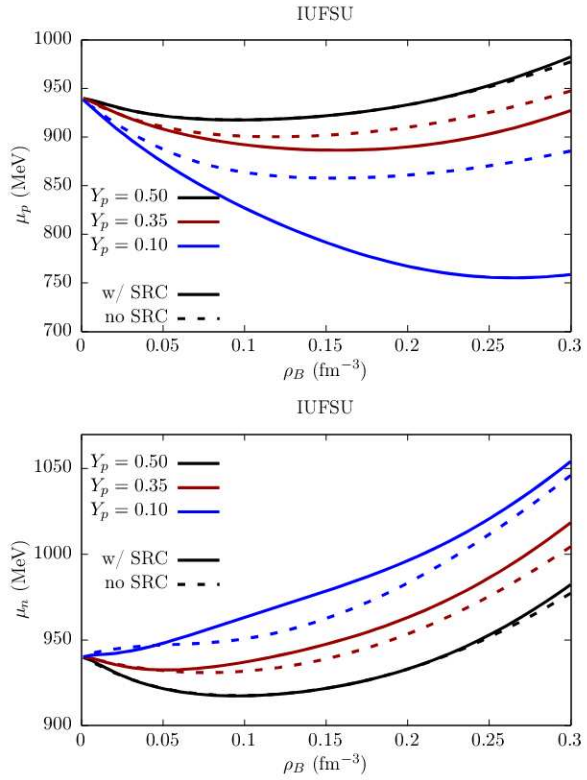

FIG. 1: Chemical potential of protons (top) and neutrons (bottom) for homogeneous matter with the IUFSU parametrization for different proton fractions, both without (dashed curves) and with (full curves) short range correlations.

As the main objective of this work is to investigate the influence of SRC on the pasta phase and the pressure is an important quantity in its construction, in Fig. 2 we also show how the pressure behaves as a function of the density. The differences at very low densities, the region important in the present study, are shown in the inset, corroborating the statement that very asymmetric matter feels the effect of SRC more strongly.

SRC (pasta phase).— Once we have understood how the homogeneous matter is affected, we can obtain the pasta phase and check its structure. In these calculations, as generally done when homogeneous matter is compared with the pasta phase, neutron-proton-electron (npe) matter is considered, i.e., not only nucleons, but also electrons that are responsible for a charge neutral

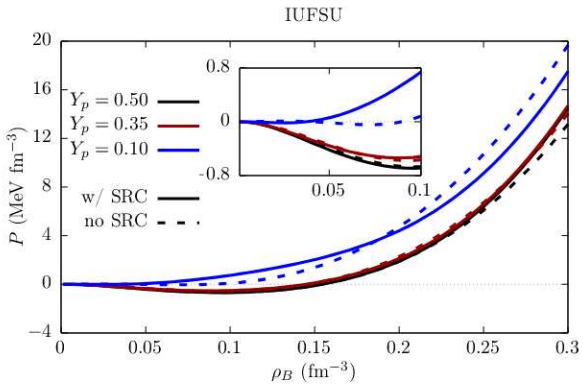

FIG. 2: Pressure of homogeneous baryon matter for different proton fractions with IUFSU without (dashed curves) and with (full curves) short range correlations for different proton fractions.

matter, are taken into account.

As already mentioned, we use the simplest possible prescription, in which Gibbs conditions are enforced and the electron gas remains in the background. The two phases are generally referred as liquid (the denser one) and gas phase. As the proton fraction decreases, a gas richer in neutrons starts to be contaminated with protons as well.

The Gibbs conditions that have to be satisfied by the CPA method are given in [13]. The surface tension coefficient is a crucial quantity in this formalism and we have used a fitting to the Thomas-Fermi calculation as a function of the proton fraction calculated in [15]. For the FSU2R functional, we used a fixed surface tension $\sigma_0 = 1.2$ MeV fm^{-2}. The geometries considered are droplets and bubbles (3D), rods and tubes (2D) and slabs (1D). In this work, fluctuations are not taken into account as done in [8, 9], but an extension to take them into account is planned for a future work. Hence, to obtain the preferential ground state and its corresponding geometry at each density, the homogeneous phase is compared with the pasta phase for each internal structure. The lower one in free energy is the preferential matter.

In Fig. 3, our results are shown for the IUFSU model without (left) and with (right) SRC. As a consequence of the already observed differences in homogeneous matter, the larger the asymmetry, the stronger the effects of the SRC. For symmetric matter, the results are very similar, both as far as the size of the pasta phase as well as its internal structure. For $Y_p = 0.35$, the similarities disappear: not only the pasta phase shrinks when SRC are included, but one of its internal structure, the tubes, vanishes. When we analyse $Y_p = 0.1$, the most important result for the neutron star inner crust, the pasta phase diminishes even more and only droplets survive.

For the sake of completeness, we also show the free energy density for different proton fractions without and

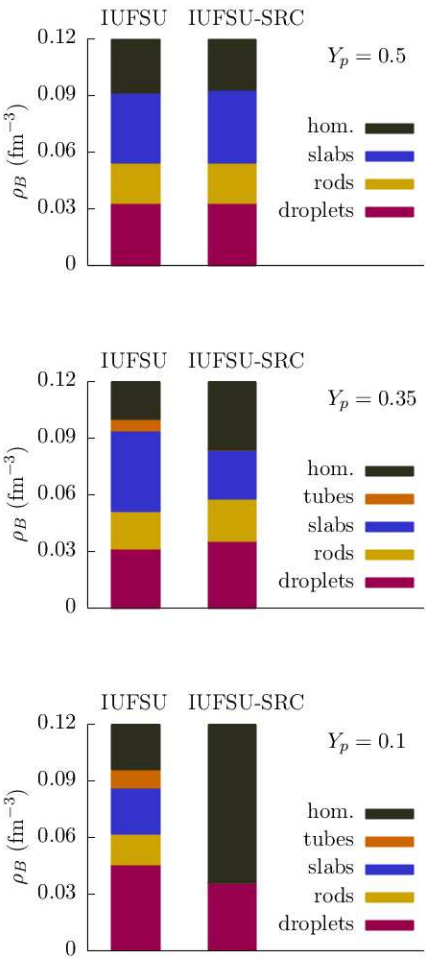

FIG. 3: Baryon densities where each pasta geometry is dominant for the IUFSU (left) and IUFSU-SRC (right) for proton fractions Y_p =0.5, 0.35 and 0.1 (left, center and right, respectively).

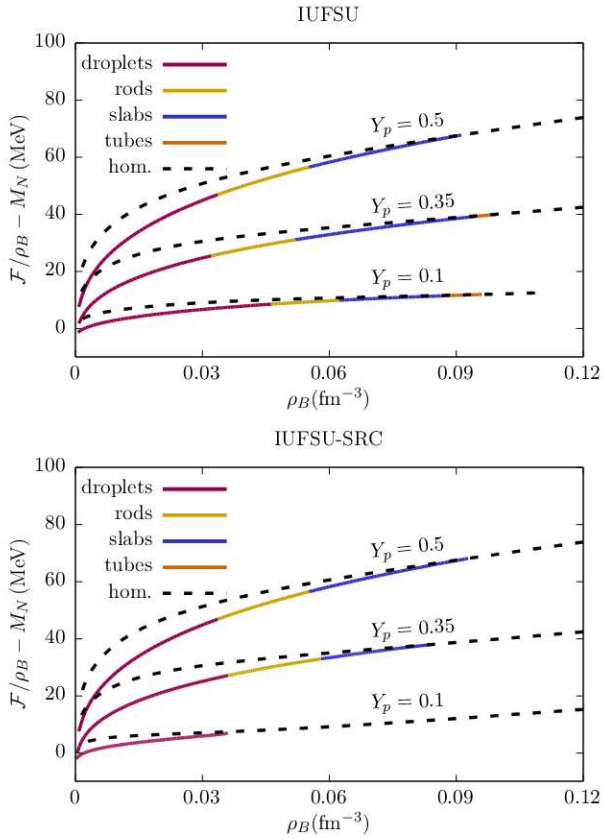

FIG. 4: Free energy density per baryon of homogeneous npe matter (dashed curves) and pasta (full curves) with (top) and without (bottom) short range correlations.

with SRC in Fig. 4, from where the densities related to each pasta structure are obtained.

At this point, a word of caution is necessary: more robust calculations in which the surface tension can be self-consistently calculated, as explained in [14, 15], must be carried out when the SRC are included. The modifications with respect to the fitting obtained without SRC are certainly minor, but the quantitative results can be slightly modified.

Analysing the present results in face of the knowledge we have accumulated from previous works, we can guess two important outcomes, at least for the inner crust of neutron stars: 1) as the temperature increases just to a few keV, probably no pasta phase will survive if SRC are considered and if so 2) the calculation of transport properties [34, 35] can be greatly simplified, as the breaking of the clusters spherical symmetry that could lead to anisotropies in the collision frequencies would be greatly inhibited. These features will be analysed in future works.

Acknowledgements.— This work is a part of the project INCT-FNA Proc. No. 464898/2014-5. D.P.M. is partially supported by Conselho Nacional de Desenvolvimento Científico e Tecnológico (CNPq/Brazil) under grant 301155.2017-8 and M.R.P. is supported with a doctorate scholarship by Coordenação de Aperfeiçoamento de Pessoal de Nível Superior (Capes/Brazil). The work is also supported by CNPq under Grants No. 312410/2020-4 (O.L.) and No. 308528/2021-2 (M.D.). O.L. and M.D. also acknowledge Fundação de Amparo à Pesquisa do Estado de São Paulo (FAPESP/Brazil) under Thematic Project 2017/05660-0 and Grant No. 2020/05238-9.

[1] D. G. Ravenhall, C. J. Pethick, and J. R. Wilson, Phys. Rev. Lett. **50**, 2066 (1983), URL https://link.aps.org/doi/10.1103/PhysRevLett.50.2066.

[2] C. J. Horowitz, M. A. Pérez-García, J. Carriere, D. K. Berry, and J. Piekarewicz, Phys. Rev. C **70**, 065806 (2004), URL https://link.aps.org/doi/10.

1103/PhysRevC.70.065806.
[3] J. Pons, D. Viganó, and N. Rea, Nature Physics pp. 431–434 (2013).
[4] H. Sotani, Monthly Notices of the Royal Astronomical Society: Letters **417**, L70 (2011), ISSN 1745-3925.
[5] C. J. Horowitz, Phys. Rev. D **81**, 103001 (2010), URL https://link.aps.org/doi/10.1103/PhysRevD.81.103001.
[6] S. W. Li, L. F. Roberts, and J. F. Beacom, Phys. Rev. D **103**, 023016 (2021), URL https://link.aps.org/doi/10.1103/PhysRevD.103.023016.
[7] C. J. Horowitz, D. K. Berry, M. E. Caplan, T. Fischer, Z. Lin, W. G. Newton, E. O'Connor, and L. F. Roberts, Nuclear pasta and supernova neutrinos at late times (2016), URL https://arxiv.org/abs/1611.10226.
[8] C. C. Barros, D. P. Menezes, and F. Gulminelli, Phys. Rev. C **101**, 035211 (2020), URL https://link.aps.org/doi/10.1103/PhysRevC.101.035211.
[9] M. R. Pelicer, D. P. Menezes, C. C. Barros, and F. Gulminelli, Phys. Rev. C **104**, L022801 (2021), URL https://link.aps.org/doi/10.1103/PhysRevC.104.L022801.
[10] F. J. Fattoyev, C. J. Horowitz, and B. Schuetrumpf, Phys. Rev. C **95**, 055804 (2017), URL https://link.aps.org/doi/10.1103/PhysRevC.95.055804.
[11] A. S. Schneider, M. E. Caplan, D. K. Berry, and C. J. Horowitz, Phys. Rev. C **98**, 055801 (2018), URL https://link.aps.org/doi/10.1103/PhysRevC.98.055801.
[12] B. Schuetrumpf, G. Martínez-Pinedo, M. Afibuzzaman, and H. M. Aktulga, Phys. Rev. C **100**, 045806 (2019), URL https://link.aps.org/doi/10.1103/PhysRevC.100.045806.
[13] S. S. Avancini, D. P. Menezes, M. D. Alloy, J. R. Marinelli, M. M. W. Moraes, and C. Providência, Phys. Rev. C **78**, 015802 (2008), URL https://link.aps.org/doi/10.1103/PhysRevC.78.015802.
[14] S. S. Avancini, S. Chiacchiera, D. P. Menezes, , and C. Providência, Phys. Rev. C **82**, 055807 (2010), URL https://link.aps.org/doi/10.1103/PhysRevC.82.055807.
[15] S. S. Avancini, C. C. Barros, L. Brito, S. Chiacchiera, D. P. Menezes, and C. Providência, Phys. Rev. C **85**, 035806 (2012), URL https://link.aps.org/doi/10.1103/PhysRevC.85.035806.
[16] O. Hen et al., Science **346**, 614 (2014), URL https://www.science.org/doi/abs/10.1126/science.1256785.
[17] CLAS Collaboration, Nature **560**, 617 (2018).
[18] CLAS Collaboration, Nature **566**, 354 (2019).
[19] A. Schmidt et al., Nature **578**, 540 (2020).
[20] O. Hen, G. A. Miller, E. Piasetzky, and L. B. Weinstein, Rev. Mod. Phys. **89**, 045002 (2017), URL https://link.aps.org/doi/10.1103/RevModPhys.89.045002.
[21] M. Duer et al., Physics Letters B **797**, 134792 (2019).
[22] B.-A. Li, L.-W. Chen, and C. M. Ko, Physics Reports **464**, 113 (2008), ISSN 0370-1573, URL https://www.sciencedirect.com/science/article/pii/S0370157308001269.
[23] B.-J. Cai and B.-A. Li, Phys. Rev. C **93**, 014619 (2016), URL https://link.aps.org/doi/10.1103/PhysRevC.93.014619.
[24] W.-M. Guo, B.-A. Li, and G.-C. Yong, Phys. Rev. C **104**, 034603 (2021), URL https://link.aps.org/doi/10.1103/PhysRevC.104.034603.
[25] B.-J. Cai and B.-A. Li, Phys. Rev. C **105**, 064607 (2022), URL https://link.aps.org/doi/10.1103/PhysRevC.105.064607.
[26] B.-J. Cai and B.-A. Li, Annals of Physics **444**, 169062 (2022), ISSN 0003-4916, URL https://www.sciencedirect.com/science/article/pii/S000349162200183X.
[27] L. A. Souza, M. Dutra, C. H. Lenzi, and O. Lourenço, Phys. Rev. C **101**, 065202 (2020), URL https://link.aps.org/doi/10.1103/PhysRevC.101.065202.
[28] O. Lourenço, T. Frederico, and M. Dutra, Phys. Rev. D **105**, 023008 (2022), URL https://link.aps.org/doi/10.1103/PhysRevD.105.023008.
[29] O. Lourenço, C. H. Lenzi, T. Frederico, and M. Dutra, Phys. Rev. D **106**, 043010 (2022), URL https://link.aps.org/doi/10.1103/PhysRevD.106.043010.
[30] M. Dutra, C. H. Lenzi, and O. Lourenço, Monthly Notices of the Royal Astronomical Society **517**, 4265 (2022), ISSN 0035-8711, URL https://doi.org/10.1093/mnras/stac2986.
[31] R. Subedi et al., Science **320**, 1476 (2008), URL https://www.science.org/doi/abs/10.1126/science.1156675.
[32] F. J. Fattoyev, C. J. Horowitz, J. Piekarewicz, and G. Shen, Phys. Rev. C **82**, 055803 (2010), URL https://link.aps.org/doi/10.1103/PhysRevC.82.055803.
[33] L. Tolos, M. Centelles, and A. Ramos, Publications of the Astronomical Society of Australia **34**, e065 (2017), URL https://doi.org/10.1017/pasa.2017.60.
[34] D. G. Yakovlev, Monthly Notices of the Royal Astronomical Society **453**, 581 (2015), ISSN 0035-8711, https://academic.oup.com/mnras/article-pdf/453/1/581/4929833/stv1642.pdf, URL https://doi.org/10.1093/mnras/stv1642.
[35] M. R. Pelicer, M. Antonelli, D. P. Menezes, and F. Gulminelli, in preparation.

MNRAS 000, 1–15 (2022) Preprint 20 February 2023 Compiled using MNRAS LATEX style file v3.0

Anisotropic electron transport in the nuclear pasta phase

M. R. Pelicer[1] ⋆, M. Antonelli[2] †, D. P. Menezes[1] ‡, F. Gulminelli[2] §

[1] *Depto de Física - CFM - Universidade Federal de Santa Catarina Florianópolis - SC - CP. 476 - CEP 88.040 - 900 - Brazil*
[2] *CNRS and ENSICAEN, Laboratoire de Physique Corpusculaire, 14050 Caen, France*

20 February 2023

ABSTRACT

The presence of nuclear pasta is expected to modify the transport properties in the mantle of neutron stars. The non-spherical geometry of the pasta nuclear clusters leads to anisotropies in the collision frequencies, impacting the thermal and electrical conductivity. We derive analytical expressions for the anisotropic collision frequencies using the Boltzmann equation in the relaxation time approximation. The average parallel, perpendicular and Hall electrical conductivities are computed in the high-temperature regime above crustal melting, considering incoherent elastic electron-pasta scattering and randomly oriented pasta structures. Numerical values are obtained at different densities and temperatures by using the IUFSU parametrization of the non-linear Walecka model to determine the crustal structure. We find that the anisotropy of the collision frequencies grows with the length of the pasta structures and, independently of the magnetic field, the presence of rod and slab phases decreases the conductivity by more than one order of magnitude. Our numerical results indicate that, even if the pasta structures might survive above the crustal melting point, no strong anisotropies are to be expected in the conduction properties in this temperature regime, even in the presence of a very high magnetic field.

Key words: dense matter – conduction – stars: neutron

1 INTRODUCTION

Observations related to the thermal, magnetic and spin evolution of neutron stars can provide us with indirect information on the transport properties of ultra-dense matter, e.g. Horowitz et al. (2015); Montoli et al. (2020); Potekhin & Chabrier (2021). In principle, the observations must be compared with simulations by properly modelling the coupled magneto-thermal evolution. Hence, models are necessary for the microscopic processes that give rise to the thermal and electric conductivities and viscosity throughout the star (Page & Reddy 2012; Chamel & Haensel 2008; Schmitt & Shternin 2018), which are then used as inputs to the macroscopic simulations, see Bransgrove et al. (2018); Pons & Viganò (2019); Camelio et al. (2022).

In the crust, transport properties are determined by the scattering of electrons by other electrons, ionic impurities and phonons in the crystal lattice. Electron-ion scattering dominates at the lowest densities and has been extensively studied (Flowers & Itoh 1976; Yakovlev & Urpin 1980; Nandkumar & Pethick 1984; Baiko et al. 1998; Potekhin et al. 1999; Chugunov & Yakovlev 2005; Aguilera et al. 2009). In the inner crust at temperatures $T < 10^7$ K, thermal conductivity due to degenerate electron-electron Coulomb scattering dominates over the contribution due to electron-phonon scattering (Shternin & Yakovlev 2006) and becomes competitive with the electron conductivity due to the scattering of electrons by impurity ions (Chamel & Haensel 2008).

The situation gets more complicated in the innermost part of the crust, where it might be energetically favourable for the ions composing the crystal lattice to deform in complex structures known as "pasta" (Ravenhall et al. 1983; Hashimoto et al. 1984; Oyamatsu 1993). Classical molecular dynamics simulations suggest that this matter is disordered and amorphous and that different shapes might coexist at a given depth of the star, due to the small energy barriers between them (Schneider et al. 2014; Horowitz et al. 2015; Caplan et al. 2021; Newton et al. 2022). This shape coexistence has been validated by relativistic mean field (RMF) calculations (Pelicer et al. 2021). In the case of a disordered and amorphous inner crust with randomly distributed nuclear clusters of different sizes (Carreau et al. 2020; Potekhin & Chabrier 2021) and geometries (Pelicer et al. 2021), the main mechanism of charge and heat transport is given by uncorrelated scattering processes between the electrons and the clusters, which play a role similar to one of the lattice impurities in a crystallized phase.

Regarding the possible astrophysical consequences, a high impurity parameter in the inner crust raises the electrical resistivity of the star, decreasing steeply the magnetic field after a certain age and thus the spin-down. This may ex-

⋆ E-mail: m.reinke.pelicer@posgrad.ufsc.br
† E-mail: antonelli@lpccaen.in2p3.fr
‡ E-mail: debora.p.m.26@gmail.com
§ E-mail: gulminelli@lpccaen.in2p3.fr

plain the very small number of isolated X-ray pulsars with spin periods larger than 12s (Pons et al. 2013; Newton 2013; Hambaryan et al. 2017; Tan et al. 2018). The high impurity also lowers the thermal conductivity, leading to a better fit of the late-time cooling of the binary MXB 1659-29 (Horowitz et al. 2015; Deibel et al. 2017). Furthermore, the presence of the pasta layers modifies the so-called mutual friction force between the nuclear clusters and the neutron superfluid, with consequences on the pulsar glitch phenomenon (Antonelli & Haskell 2020). Gravitational waves (Horowitz 2010), quasi-periodic oscillations (Sotani 2012), quasi-persistent sources of SXRTs and giant flares due to the relaxation of the crust after heat deposition and neutrino emissivity (Alloy & Menezes 2011; Horowitz et al. 2004; Lin et al. 2020) are also influenced by the presence of an amorphous layer in the inner crust.

In the presence of a strong B field, electron transport is anisotropic, as the field bends the electron trajectories in the orthogonal plane and suppresses electron transport across the direction of $\boldsymbol{B}$, e.g. (Chamel & Haensel 2008). This argument considers that the only source of anisotropy is given by the $\boldsymbol{B}$ direction. However, the spherical symmetry of nuclear clusters is spontaneously broken in the pasta layers, leading to additional anisotropies already at the level of the microscopic scattering process: in particular, Yakovlev (2015) has shown that, even in the case of random orientation of the pasta structures, anisotropic scattering can modify the transport properties.

In the analysis of Yakovlev (2015), the scattering rates along and across the pasta symmetry axis were taken as free parameters. While molecular dynamics has been able to provide estimates of the transport properties in the inner crust, by taking the angular average of the effective structure factor of the charge distribution (Horowitz & Berry 2008; Horowitz et al. 2015; Nandi & Schramm 2018), to our knowledge no estimation of the different collision frequencies that arise due to the pasta anisotropic shapes has been performed to date.

The existing microscopic simulations of the finite temperature pasta (Schneider et al. 2014; Horowitz et al. 2015; Caplan et al. 2021; Newton et al. 2022; Nandi & Schramm 2018) are typically done at fixed proton fraction and high temperatures $T \geq 10^{10}$ K, thermodynamic conditions that are especially aimed at the description of proto-neutron stars formed in supernova events. In these conditions, it appears from those calculations that the distribution of baryonic matter is strongly disordered, and one might expect that anisotropies should not have a strong effect on the transport properties. On the other hand, in the case of neutron star binaries and soft X-ray transients, the inner crust is close to β-equilibrium and temperatures are one or two orders of magnitude lower, which might preserve both the peculiar pasta geometrical shapes and the lattice quasi-long range order, potentially leading to a strong anisotropy of the scattering rates, as assumed by Yakovlev (2015).

In this paper, we show how the anisotropic collision frequencies can be calculated from the Boltzmann equation in the relaxation time approximation, in the case of elastic scattering of ultra-relativistic degenerate electrons off pasta structures. We limit ourselves to the hypothesis of incoherent scattering sources following the Matthiessen rule (Schmitt & Shternin 2018; Heiselberg & Pethick 1993; Shternin & Yakovlev 2006). Based on the behaviour of the static structure factor, we argue that this hypothesis should be valid in the high-temperature regime above crustal melting.

The paper is organized as follows. In Sec. 2 we calculate the general anisotropic collision frequencies. The collision integral and the transition matrix elements are first expanded in the spherical harmonics basis in Sec. 2.1. Then, to extract the physical real collision frequencies, in Sec. 2.2 we consider the lowest order (dipole) deviation from equilibrium and take advantage of the axial symmetry of the pasta phase. The contribution of the collision integral to the conductivity is given in terms of axial and perpendicular collision frequencies, in agreement with the analysis of Yakovlev (2015). Analytical expressions for the conductivity matrix are given in Sec. 3 for the case of a liquid, disordered, pasta phase. In Sec. 3.1, the transition matrix is numerically evaluated in the temperature domain of validity of our approximations. The conductivity tensor with and without magnetic field is finally obtained in Sec. 3.2. To illustrate the formalism and give quantitative estimations of the transport coefficients, in Sec. 4 we present numerical calculations for the collision frequencies and conductivity for different densities and B values in the high-temperature regime. Conclusions are presented in Sec. 5.

All the numerical estimates reported in this paper are obtained using the IUFSU parametrization of the RMF approach for the crustal composition, see Fattoyev et al. 2010; Avancini et al. 2012, but our expressions can be employed with any nuclear physics model that gives the static structure of the crust. In particular, while our quantitative numerical results might be model dependent, the qualitative conclusions remain valid for any other realistic equation of state model.

We use natural units $\hbar = c = k_B = 1$ all over the paper.

2 RELAXATION TIME APPROXIMATION FOR ANISOTROPIC ELASTIC COLLISIONS

The thermal and electrical electron conductivities due to electron-ion scattering have been calculated in a wide range of temperatures T and electron densities n_e, see e.g. Potekhin (1999): for homogeneous media, and in the absence of a magnetic field, they are expressed in terms of the effective collision frequencies $\nu_{\sigma,\kappa}$ as

$$\sigma = \frac{e^2 n_e}{m_e^* \nu_\sigma} \qquad \kappa = \frac{\pi^2 T n_e}{3 m_e^* \nu_\kappa}\,, \tag{1}$$

where m_e^* is the effective electron mass, and in the liquid regime $\nu_\sigma = \nu_\kappa \equiv \nu$, with the collision frequency ν defined as the inverse of the relaxation time, $\nu = 1/\tau$. Because of the isotropy assumption, the collision frequencies only depend on the modulus of the momentum transfer according to the general expression (Flowers & Itoh 1976; Yakovlev & Urpin 1980; Nandkumar & Pethick 1984):

$$\nu = \frac{4\pi n_i e^4 Z^2}{v_F p_F^2} \int_0^{2p_F} \frac{dq}{q} \left(1 - \frac{q^2}{4\epsilon_F^2}\right) \frac{F^2(q)}{\varepsilon^2(q)} S(q)\,, \tag{2}$$

where $F(q)$ is the ion form factor, $\epsilon(q)$ is the dielectric function, $S(q)$ is the effective structure factor that accounts for ion correlations, and v_F, p_F, and ϵ_F are the Fermi velocity, momentum and energy respectively. Unfortunately, eqs (1) and (2) cannot be straightforwardly generalized to the case of anisotropic scatterings. To derive the anisotropic collision

frequencies, we consider a multipole expansion of the Boltzmann equation in the relaxation time approximation, as we detail below.

2.1 Anisotropic case: expansion in spherical harmonics

We consider a strongly degenerate relativistic electron gas with position-dependent temperature and chemical potential fields $T(\boldsymbol{r})$ and $\mu(\boldsymbol{r})$ in a constant external magnetic field $\boldsymbol{B}$ and a weak electric field $\boldsymbol{E}$. Assuming that the gas is only slightly out of equilibrium, we can write its distribution function as $f(\boldsymbol{r},\boldsymbol{p},t) = f_0(\boldsymbol{r},\epsilon_p) + \delta f(\epsilon_p)$, where $\boldsymbol{r}$, $\boldsymbol{v}$ and $\boldsymbol{p}$ are the electron position, velocity and momentum, respectively, with the latter given by $\boldsymbol{p} = \epsilon_p \boldsymbol{v}$. The Fermi-Dirac function f_0 is given by

$$f_0(\boldsymbol{r},\epsilon_p) = \left[1 + \exp\left(\frac{\epsilon_p - \mu(\boldsymbol{r})}{T(\boldsymbol{r})}\right)\right]^{-1}. \tag{3}$$

The deviation from equilibrium can be found by solving the linearized Boltzmann equation (Heiselberg & Pethick 1993; Shternin & Yakovlev 2006)

$$\left(-\frac{\partial f_0}{\partial \epsilon_p}\right)\boldsymbol{v}\cdot\left[\nabla\mu + e\boldsymbol{E} + \frac{\epsilon_p-\mu}{T}\nabla T\right] - e(\boldsymbol{v}\times\boldsymbol{B})\cdot\frac{\partial\delta f}{\partial \boldsymbol{p}} = I[f]\,, \tag{4}$$

where $I[f]$ is the collision integral that can be written as

$$I[f] = \int \frac{d^3\boldsymbol{p}'}{(2\pi)^3}\left[\Gamma_{p'\to p} f(\boldsymbol{p}')\left(1-f(\boldsymbol{p})\right) - \Gamma_{p\to p'} f(\boldsymbol{p})\left(1-f(\boldsymbol{p}')\right)\right]. \tag{5}$$

Here, $\Gamma_{p\to p'}$ is the transition rate from an initial momentum $\boldsymbol{p}$ to a final momentum $\boldsymbol{p}'$, introduced to account for electron scattering with any generic potential, and we have omitted the position dependencies as they do not affect the calculation. We restrict ourselves to elastic scatterings with a localized source for the potential, such that the following simplification applies:

$$\Gamma_{p\to p'} = \Gamma_{p'\to p} = 2\pi\delta(\epsilon_p - \epsilon_{p'})W_{pp'}, \tag{6}$$

where $W_{pp'}$ is the transition matrix element, which we will write explicitly for the case of electron-pasta scattering in the next section. Taking into account that deviations from equilibrium are small, we can rewrite the collision integral, eq. (5), as

$$I[f] = -2\pi\int \frac{d^3\boldsymbol{p}'}{(2\pi)^3}\delta(\epsilon_p-\epsilon_{p'})W_{pp'}\left[\delta f(\boldsymbol{p}) - \delta f(\boldsymbol{p}')\right], \tag{7}$$

where the Fermi-Dirac terms coming from the different momenta have cancelled out due to the elasticity assumption in eq. (6).

In isotropic scatterings, $W_{pp'}$ is a function of $q = |\boldsymbol{p}-\boldsymbol{p}'|$ and of the electron energy only. Since in this work we are dealing with general anisotropic scatterings, we will assume the matrix elements to be functions of the solid angles of both incoming and outgoing electron momenta ($\boldsymbol{p}$ and $\boldsymbol{p}'$), as well as the energy ϵ_p, so there is no assumption of symmetry for the source of potential. The transition matrix can be expanded in the basis of spherical harmonics as

$$W_{p\,p'}(\Omega_p,\Omega_{p'},\epsilon_p) = \sum_{lm\,l'm'}\mathcal{W}_{lm\,l'm'}(\epsilon_p)Y_l^m(\Omega_p)Y_{l'}^{m'}(\Omega_{p'}), \tag{8}$$

whereas the assumption of elasticity implies that Ω_p and $\Omega_{p'}$ are interchangeable, such that

$$W_{pp'} = W_{p'p} \implies \mathcal{W}_{lm\,l'm'} = \mathcal{W}_{l'm'\,lm}. \tag{9}$$

This is a generalization of the Legendre expansion used for scattering with isotropic targets – see Sec. 3 in Pines & Nozières (2018). In App. A we show how the isotropic limit can be recovered from our calculation.

The deviation from equilibrium of the electron distribution is expanded as:

$$\delta f(\boldsymbol{p}) = \sum_{lm}\delta f_{lm}(\epsilon_p)Y_l^m(\Omega_p). \tag{10}$$

Substitution of eqs (8) and (10) into eq. (7) allows us to use the orthogonality of spherical harmonics and the contraction rule

$$Y_l^m(\Omega)Y_{l'}^{m'}(\Omega) = \sum_{L\,M}(-1)^M\sqrt{\frac{(2L+1)(2l+1)(2l'+1)}{4\pi}} \times \begin{pmatrix} l & l' & L\\ 0 & 0 & 0\end{pmatrix}\begin{pmatrix} l & l' & L\\ m & m' & -M\end{pmatrix}Y_L^M(\Omega) \tag{11}$$

to rewrite the collision integral as

$$I[f] = -\frac{p^2}{4\pi^2 v}\sum_{lm,l'm'}\delta f_{lm}\left[\mathcal{W}_{l'm'\,00}\sum_{LM}(-1)^M\sqrt{(2l+1)(2l'+1)(2L+1)} \times \begin{pmatrix} l & l' & L\\ 0 & 0 & 0\end{pmatrix}\begin{pmatrix} l & l' & L\\ m & m' & -M\end{pmatrix}Y_L^M(\Omega_p) - (-1)^m\mathcal{W}_{l'm'\,l-m}Y_{l'}^{m'}(\Omega_p)\right]. \tag{12}$$

The 3-j Wigner symbols $\begin{pmatrix} l_1 & l_2 & l_3\\ m_1 & m_2 & m_3\end{pmatrix}$ are invariant under even permutations of the columns and non-zero only if $m_1+m_2+m_3 = 0$, $|l_1-l_2| < l_3 < l_1+l_2$ and $l_1+l_2+l_3$ is an integer (Brink & Satchler 1968; Edmonds 2016).

We define the anisotropic collision frequencies by expand-

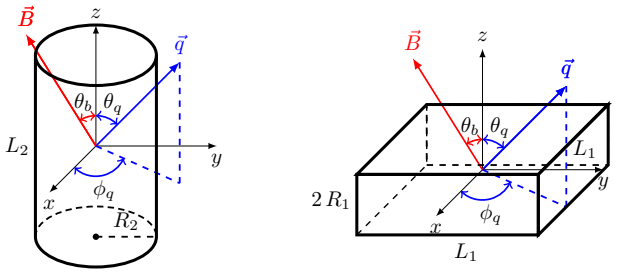

Figure 1. Cylindrical (rod and tube) and planar (slab) geometries of the nuclear pasta with z as the symmetry axis. The transferred momentum vector $\boldsymbol{q}$ is drawn arbitrarily and the magnetic field B lies in the xz–plane.

ing the collision integral linearly in δf,

$$I[f] = -\sum_{lm,l'm'} \delta f_{lm}\left(\epsilon_p\right)\left[\nu\left(\epsilon_p\right)\right]_{lm}^{l'm'} Y_{l'}^{m'}(\Omega_p), \tag{13}$$

Integration of eqs (12) and (13) in Ω_p yields

$$[\nu]_{lm}^{l'm'} = \frac{p^2}{4\pi^2 v}\left[(-1)^{m'}\sqrt{(2l+1)(2l'+1)}\sum_{LM}\mathcal{W}_{LM\,00}\sqrt{2L+1}\begin{pmatrix} l & l' & L \\ 0 & 0 & 0\end{pmatrix}\begin{pmatrix} L & l & l' \\ M & m & -m'\end{pmatrix} - (-1)^m\,\mathcal{W}_{l'm'\,l-m}\right]. \tag{14}$$

We can obtain a more compact form of this expression by using the Wigner–Eckart theorem and the spherical harmonics representation of irreducible tensor operators of rank l (Racah 1942a,b),

$$C_m^l = \sqrt{\frac{4\pi}{2l+1}}Y_{lm}(\Omega)\,, \tag{15}$$

such that eq. (14) becomes

$$[\nu]_{lm}^{l'm'} = \frac{p^2}{4\pi^2 v}\left[\sum_{LM}\mathcal{W}_{LM\,00}\sqrt{2L+1}\langle l'm'|C_M^L|lm\rangle - (-1)^m\,\mathcal{W}_{l'm'\,l-m}\right]. \tag{16}$$

2.2 Derivation of the collision frequencies

To evaluate the collision frequencies in the pasta phase, we consider idealized rod and slab-like geometries, as expected in the basic liquid-drop modelling of the inner crust (Ravenhall et al. 1983; Hashimoto et al. 1984). These geometries and the definitions entering the calculations are sketched in Fig. 1.

Equation (16) is not yet a multipole expansion of the collision rates because the different expansion coefficients of the collision integral $[\nu]_{lm}^{l'm'}$ are complex numbers. This is due to the fact that both the electron distribution function and the collision integral are written on the basis of complex spherical harmonics. To relate eq. (16) to the physical quantities, we must rewrite eqs (10) and (13) in terms of real coefficients.

To do so, we notice that the coefficients $\mathcal{W}_{l'm'\,lm}$ in eq. (8) are constrained by the symmetries of rods and slabs. Both geometries are invariant under inversion of the z-axis ($z \to -z$), implying that the only non-zero $\mathcal{W}_{l'm'\,lm}$ are the ones having the sum $l+l'$ that is even. The sum $m+m'$ is constrained by the xy–plane symmetries: cylinders are invariant under arbitrary rotations: the non-zero $\mathcal{W}_{l'm'\,lm}$ are only those with $m+m'=0$; slabs are invariant over $\pi/2$ rotations, so the sum $m+m'$ must be a multiple of 4. To summarize, the $\mathcal{W}_{lm\,l'm'}$ are not zero if and only if:

$$\text{Rods}\ \begin{cases} l+l'=2k \\ m+m'=0\end{cases} \qquad \text{Slabs}\ \begin{cases} l+l'=2k \\ m+m'=4k'\end{cases} \tag{17}$$

with $k, k' \in \mathbb{Z}$. To further progress, we restrict ourselves to the case of electric and thermal conductivities. Accounting for spin degeneracy, the electric current and heat flow are given by

$$\boldsymbol{j} = -2e\int\frac{d^3\boldsymbol{p}}{(2\pi)^3}\boldsymbol{v}\delta f \qquad \boldsymbol{q} = 2\int\frac{d^3\boldsymbol{p}}{(2\pi)^3}\boldsymbol{v}(\epsilon-\mu)\delta f\,, \tag{18}$$

so that only the odd l terms in the expansion (10) contribute to the integrals in eq. (18). Moreover, in the relaxation time approximation, the collision integral, eq. (7), is linear in δf. The left-hand side of eq. (4) is linear in $\boldsymbol{p}$, implying that only the coefficient $l'=1$ in the expansion of the collision integral, eq. (13) contributes to the currents[1]. This is also discussed in depth in the case of isotropic scattering in Sykes & Brooker (1970), and mentioned in the case of pasta in Schmitt & Shternin (2018).

In the isotropic case, there is no mixing between the different terms of $I[f]$ in eq. (13) and those of δf in eq. (10). However, in the anisotropic case, the collision frequencies can mix the $l'=1$ contributions in eq. (13) with the $l=2,3...$ components of δf_{lm} in eq. (13). For simplicity, we neglect such mixing and restrict ourselves to the most important

[1] The multiplicity l of the spherical harmonics coincides with the power of $\boldsymbol{p}$ in an equivalent expansion in homogeneous harmonic polynomials since they are isomorphic (Gallier 2013; Freire 2022).

contribution (see also Schmitt & Shternin 2018) by writing $\nu_{lm}^{l'm'} = \nu_{1m}^{1m'}\delta_{l1}\delta_{l'1}$ in eq. (13). This approximate approach is probably good in the case of pasta, due to the symmetry rules in (17).

We will show that the axial symmetry of the problem limits the number of physical collision frequencies to two: an axial frequency ν_a, and a perpendicular one ν_p. To do so, we need to rewrite the expansions eqs (10) and (13) in terms of real coefficients. We introduce the real spherical harmonics:

$$\mathcal{Y}_{lm} = \begin{cases} \frac{i}{\sqrt{2}}\left(Y_l^m - (-1)^m Y_l^{-m}\right) & m < 0 \\ Y_l^0 & m = 0 \\ \frac{1}{\sqrt{2}}\left(Y_l^{-m} + (-1)^m Y_l^m\right) & m > 0 \end{cases} \tag{19}$$

and rewrite the $l = 1$ term of eq. (10), δf_{1m}, as:

$$\delta f(\boldsymbol{p})\Big|_{l=1} = \mathcal{Y}_{11}\delta f_x + \mathcal{Y}_{1-1}\delta f_y + \mathcal{Y}_{10}\delta f_z \tag{20}$$

where the coefficients are given by

$$\delta f_x = \frac{\delta f_{1-1} - \delta f_{11}}{\sqrt{2}}, \quad \delta f_y = \frac{\delta f_{1-1} + \delta f_{11}}{\sqrt{2}i}, \quad \delta f_z = \delta f_{10}. \tag{21}$$

Since the electron distribution function is real, so are the coefficients defined above. Substituting eq. (19) and eq. (21) in the collision integral eq. (13), we get

$$I[f] = \begin{pmatrix}\mathcal{Y}_{11} & \mathcal{Y}_{1-1} & \mathcal{Y}_{10}\end{pmatrix}\begin{pmatrix}\nu_{xx} & \nu_{xy} & \nu_{xz} \\ \nu_{yx} & \nu_{yy} & \nu_{yz} \\ \nu_{zx} & \nu_{zy} & \nu_{zz}\end{pmatrix}\begin{pmatrix}\delta f_x \\ \delta f_y \\ \delta f_z\end{pmatrix} \tag{22}$$

with the physical collision frequencies given by:

$$\hat{\nu} = \begin{pmatrix} \frac{1}{2}\left(\nu_{11}^{11} + \nu_{1-1}^{1-1} - \nu_{11}^{1-1} - \nu_{1-1}^{11}\right) & \frac{i}{2}\left(\nu_{11}^{11} - \nu_{1-1}^{1-1} + \nu_{11}^{1-1} - \nu_{1-1}^{11}\right) & \frac{1}{\sqrt{2}}\left(\nu_{1-1}^{10} - \nu_{11}^{10}\right) \\ \frac{i}{2}\left(-\nu_{11}^{11} + \nu_{1-1}^{1-1} + \nu_{11}^{1-1} + \nu_{1-1}^{11}\right) & \frac{i}{2}\left(\nu_{11}^{11} + \nu_{1-1}^{1-1} + \nu_{11}^{1-1} + \nu_{1-1}^{11}\right) & \frac{i}{\sqrt{2}}\left(\nu_{1-1}^{10} + \nu_{11}^{10}\right) \\ \frac{1}{\sqrt{2}}\left(\nu_{10}^{1-1} - \nu_{10}^{11}\right) & \frac{-i}{\sqrt{2}}\left(\nu_{10}^{11} + \nu_{10}^{1-1}\right) & \nu_{10}^{10} \end{pmatrix} \tag{23}$$

The constraint of elasticity eq. (9) implies that the collision frequency matrix is symmetric, $\nu_{ij} = \nu_{ji}$. Moreover, we can see from the pasta symmetries in eq. (17) that the off-diagonal terms vanish and that the xx and yy terms are equal. This is valid for slabs because $L_{1x} = L_{1y} = L_1$. Thus,

$$\hat{\nu} = \begin{pmatrix}\nu_{xx} & \nu_{xy} & \nu_{xz} \\ \nu_{yx} & \nu_{yy} & \nu_{yz} \\ \nu_{zx} & \nu_{zy} & \nu_{zz}\end{pmatrix} = \begin{pmatrix}\nu_p & 0 & 0 \\ 0 & \nu_p & 0 \\ 0 & 0 & \nu_a\end{pmatrix} \tag{24}$$

where $\nu_p = \nu_{11}^{11}$ and $\nu_a = \nu_{10}^{10}$. Writing, without any loss of generality, $\delta f_{1m} = \sqrt{4\pi/3}\Phi_{1m}(\epsilon_p)|\boldsymbol{v}|$, the collision integral expansion, eq. (13), can be simply rewritten as

$$I[f] = -v_z\Phi_z\nu_a - \boldsymbol{v}_p \cdot \boldsymbol{\Phi}_p\nu_p, \tag{25}$$

where $\boldsymbol{\Phi}$ is a vector that can depend on ϵ_p, and the collision frequencies ν_a and ν_p are defined parallel and perpendicular to the pasta symmetry axis. This result exactly coincides with the generalization of the relaxation time approximation proposed by Yakovlev (2015) on symmetry arguments to include the effect of the anisotropic medium.

The axial and perpendicular collision frequencies can be calculated from eq. (14):

$$\nu_a(\epsilon_p) = \frac{p^2}{4\pi^2 v}\left[\mathcal{W}_{00,00} - \mathcal{W}_{10,10} + \frac{1}{\sqrt{5}}\left(W_{20,00} + \mathcal{W}_{00,20}\right)\right] \tag{26}$$

$$\nu_p(\epsilon_p) = \frac{p^2}{4\pi^2 v}\left[\mathcal{W}_{00,00} - \frac{1}{2\sqrt{5}}\left(\mathcal{W}_{20,00} + \mathcal{W}_{00,20}\right) + \frac{1}{2}\left(\mathcal{W}_{11,1-1} + \mathcal{W}_{1-1,11}\right)\right]. \tag{27}$$

To rewrite ν_a and ν_p in terms of the transition matrix $W_{pp'}$, we invert eq. (8) using the orthogonality of spherical harmonics:

$$\mathcal{W}_{lm\,l'm'} = \int d\Omega_p d\Omega_{p'} W_{pp'} Y_l^{m*}(\Omega_p) Y_{l'}^{m'*}(\Omega_{p'}). \tag{28}$$

This leads to the final expression of the collision rates, for an arbitrary interaction preserving axial symmetry, and assuming a dipole-like deviation from the equilibrium of the electron distribution function:

$$\nu_a(\epsilon_p) = \frac{3}{32\pi^3 v}\int d\Omega_p d\Omega_{p'} W_{pp'}\, q^2\, \cos^2\theta_q \tag{29}$$

$$\nu_p(\epsilon_p) = \frac{3}{32\pi^3 v}\int d\Omega_p d\Omega_{p'}\, W_{pp'}\, q^2 \frac{1}{2}\sin^2\theta_q. \tag{30}$$

To get the generalization of eqs (1) and (2) to the physical problem of electron-pasta scattering, we now turn to evaluate the transition matrix $W_{pp'}$.

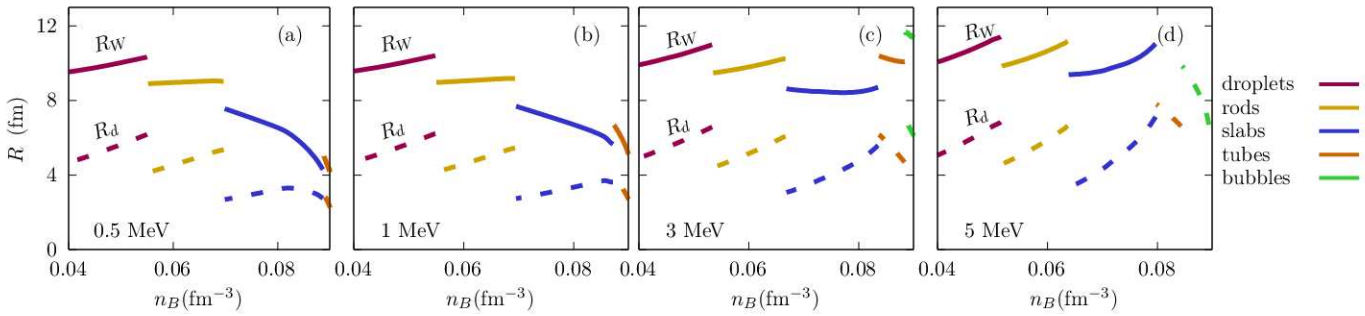

Figure 2. Linear and Wigner-Seitz radius of the pasta as a function of density in dashed and full curves for $T = 0.5, 1, 3$ and 5 MeV (panels a, b c and d, respectively). The different pasta geometries are indicated with different colours. The results for $T = 0$ and $T = 0.5$ MeV are indistinguishable.

3 CONDUCTIVITY TENSOR FOR RODS AND SLABS

3.1 Elastic scattering matrix in the incoherent scattering limit

In the case of isotropic scattering, the transition matrix (8) depends solely on the absolute value of the transferred momentum $\boldsymbol{q} = \boldsymbol{p} - \boldsymbol{p}'$. This is equivalent to a dependence on the angle between the incoming and outgoing electron momentum because one can write $q^2 = 2p^2(1 - \hat{p} \cdot \hat{p}')$. In the case of anisotropic scattering, the transition matrix can depend separately on the angles of both incoming and outgoing momenta. However, because of the axial symmetry of the pasta structures, it can only depend on the projections of the transferred momentum in the axis perpendicular and parallel to the symmetry axis of the pasta. We can assume without loss of generality that the pasta symmetry axis coincides with the z axis, such that the transition matrix becomes a function of the vector $\boldsymbol{q}$ itself, see Fig.1.

The transition matrix $W_{pp'}$ for the elastic scattering in the Born approximation is given by (see, e.g., equation 81.5 of Berestetskii et al. 1971)

$$W_{pp'}(\boldsymbol{q}, \epsilon_p) = \frac{1}{2} \sum_{s,s'} \left| \frac{e}{2\epsilon_p} \bar{u}_{p',s'} \gamma^0 u_{p,s} \int d^3\boldsymbol{x} A_0(\boldsymbol{x}) e^{-i\boldsymbol{q}\cdot\boldsymbol{x}} \right|^2 = e^2 \left(1 - \frac{q^2}{4\epsilon_p^2}\right) |U(\boldsymbol{q})|^2 S(\boldsymbol{q}) \quad (31)$$

where in the first line $u_{p,s}$ is the electron spinor, $A_0(\boldsymbol{x})$ is the electric potential generated by nuclei and γ^0 is the Dirac matrix. In the second line, the Fourier transform of the potential $U(\boldsymbol{q})$ is introduced, and the static structure factor is defined as (Flowers & Itoh 1976):

$$S(\boldsymbol{q}) = \langle n_p(\boldsymbol{q}) n_p(-\boldsymbol{q}) \rangle_T = \frac{1}{V} \int d^3\boldsymbol{r} d^3\boldsymbol{r'} e^{i\boldsymbol{q}\cdot(\boldsymbol{r}-\boldsymbol{r'})} \langle n_p(\boldsymbol{r}) n_p(\boldsymbol{r'}) \rangle_T, \quad (32)$$

where $n_p(\boldsymbol{q})$ is the charge density of the scatterer in momentum space, $\langle ... \rangle_T$ is the thermal average that accounts for correlations between protons, and the integral covers the entire thermodynamic system of volume V. The structure factor carries the whole information regarding the anisotropy of the system both through the anisotropic shape of the pasta and through the lattice arrangement. In principle, $S(\boldsymbol{q})$ also carries information about thermal excitations. The contribution of single-nucleon thermal excitations to $S(\boldsymbol{q})$ has been calculated by Schuetrumpf et al. (2020), within the framework of density functional theory. Since this is not a main source of anisotropy, we do not consider it here. On the other hand, larger-scale collective thermal vibrations of pasta structures and deviations from lattice periodicity are likely important to the anisotropic behaviour of transport coefficients. To the best of our knowledge, these have not been calculated yet and will be addressed in future work.

Still, variational theory in Wigner-Seitz (WS) cells of different geometries with energy densities obtained from the RMF approach, is routinely used by nuclear physicists to obtain a microscopically funded estimation of the optimal average charge distribution $\langle n_p(\boldsymbol{r}) \rangle_T$, see e.g. Avancini et al. (2009, 2008, 2012) and Haensel et al. (2007); Chamel & Haensel (2008) for reviews. In the simplest liquid-drop modelling of Fig. 1, the pasta structures are characterized by constant density profiles. We can write for rods ($d = 2$) and slabs ($d = 1$), respectively:

$$\langle n_p(\boldsymbol{r}) \rangle_T^{d=2} = n_p \sum_m \Theta(R_2 - r - mR_{W2}) \qquad \langle n_p(\boldsymbol{r}) \rangle_T^{d=1} = n_p \sum_m \Theta(R_1 - z - mR_{W1}) \quad (33)$$

where the average linear size of the cluster R_d, its internal proton (neutron) density n_p (n_n) and average WS cell radius R_{Wd} are variationally obtained for any given temperature T and baryon density n_B, as well as the (uniform) electron density, and the density of the dripped neutrons[2]. The sum in (33) runs over the parallel structures in the lattice. For this application, we use the relativistic mean-field approach of Avancini et al. (2012). The mean field Lagrangian is given by the non-linear Walecka model, parametrized by the IUFSU force (Fattoyev et al. 2010) with a surface tension fitted to reproduce a Thomas-Fermi simulation, see Avancini et al. (2012) for details. In Fig. 2 we show the linear and WS cell radii as a function of the density, for some representative temperatures that will be considered below. We can see that non-spherical geometries are expected in the innermost part of the inner crust, and are found to persist even at high temperatures well above crustal melting, that occurs around $T_m \approx 1$ MeV in this density region (Carreau et al. 2020). The different colours correspond to the geometries that are associated, for a given baryon density, with the minimal free energy

[2] This last quantity does not play any role in the calculations concerned by the present paper.

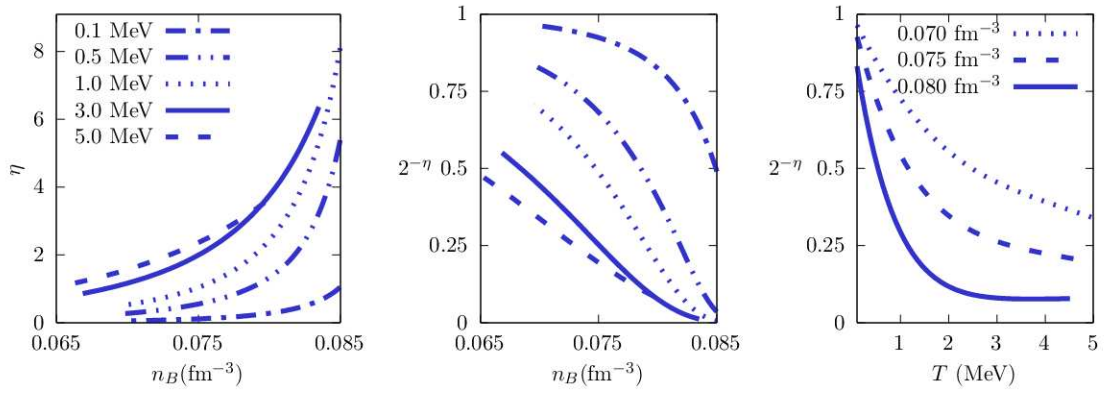

Figure 3. Left panel: correlation function decay parameter η for slabs. Middle (right) panel: estimation of the correlation between neighbouring slab structures as a function of density (temperature), see text for details. Curves for T =0.1, 0.5, 1, 3, and 5 MeV are shown on the left and center, and for n_B = 0.07, 0.075 and 0.08 fm^{-3} on the right.

density. It is known that the pasta properties are model dependent (Dinh Thi et al. 2021), mainly the densities at which the different geometries appear, but the qualitative behaviour shown in Fig.2 is obtained in all realistic nuclear models found in the literature (Dinh Thi et al. 2021; Parmar et al. 2022).

In the case of a perfect lattice, electron band structures suppress the scattering rates and charge transport occurs only through electron-phonon interactions. However, thermal fluctuations disturb the lattice periodicity and destroy the long-range order. In particular, in the disordered limit expected to dominate with increasing temperature, the correlation function drops to zero on a length scale of the linear size of the cluster, and the different pasta structures are fully uncorrelated and act as incoherent impurity scatterers. These fluctuations have been calculated for the pasta by Pethick & Potekhin (1998) within the classical approach of the Landau-de Gennes model of liquid crystals (de Gennes & Prost 1993; Chandrasekhar 1992). For slabs, the thermal displacement presents a logarithmic divergence with the linear dimension of the sample, reflecting the well-known Landau-Peierls instability (Landau & Lifshitz 1969). Concerning the rod phase, the thermal displacement is finite and the long-range order in the transverse plane is in principle preserved. A critical temperature for the long (or quasi-long) range order was estimated by Watanabe et al. (2000) as the temperature at which the thermal displacement becomes comparable to the cell radius. Such a temperature was shown to strongly decrease with increasing baryonic density and, for fiducial values of the elastic constants, to be of the order of a few MeV both for slabs and for rods (Watanabe et al. 2000). Above such temperatures, it is reasonable to expect that the conventional pasta phase is fully destroyed by thermal fluctuations, even if complex deformed disordered cluster structures may still be present, as suggested by molecular dynamics simulations (Horowitz et al. 2015; Schneider et al. 2014; Newton et al. 2022; Nandi & Schramm 2018). Below the critical temperature, the consequence of the reduced dimensionality of the pasta phase is that the long-range order (or quasi-long in the case of slabs) is only preserved in the directions corresponding to the lattice periodicity (that is along $\boldsymbol{u}_z$ for the slab phase, and $\boldsymbol{u}_\perp$ for the rod one), potentially leading to strong anisotropies in the collision frequencies.

Interestingly, limiting behaviours can be obtained for the density correlation of slabs (Poniewierski et al. 1998; de Gennes & Prost 1993) $\langle n_p(\boldsymbol{r}) n_p(\boldsymbol{r'})\rangle_T \equiv \langle \delta n^2(\boldsymbol{r}-\boldsymbol{r'})\rangle_T$ showing the power law behaviour characteristic of the quasi-long range order of the smectic (slab) phase:

$$\langle \delta n^2(\boldsymbol{r})\rangle_T \propto |z|^{-\eta} \quad |z| \to \infty \tag{34}$$

$$\propto r_\perp^{-2\eta} \quad r_\perp \to \infty, \tag{35}$$

where

$$\eta = \frac{q_0^2 T}{8\pi\lambda C_0}, \tag{36}$$

with $q_0 = \pi/R_{W1}$, $\lambda^2 = R_{W1}^2(1+2f-2f^2)/45$ where $f = R_1/R_{W1}$ is the average volume fraction of the cluster,and $C_0 = 6E_C$, where E_C is the average Coulomb energy density in the cell Pethick & Potekhin (1998). More recently, the calculations of elastic constants were improved by Pethick et al. (2020), but for our estimates we stick to the simpler prescription of Pethick & Potekhin (1998). The numerical values of the η parameter as a function of the density, as numerically obtained from the average pasta configuration predicted by the RMF model, are displayed in the left part of Fig. 3 for different temperatures. As expected, the correlation decreases with temperature and density.

In the absence of a complete calculation of the correlation function, we limit ourselves in this paper to temperatures high enough for the hypothesis of uncorrelated scatterers to be realistic. To this aim, we plot in the center and right parts of Fig. 3 the quantity $2^{-\eta}$ as an estimation of the ratio between the correlation function at $z = 2R_{W1}$, corresponding to a distance containing two different slabs, and the same quantity at $z = R_{W1}$, such that a single slab is accounted for,

$$2^{-\eta} \approx \frac{\delta n^2(2R_{W1})}{\delta n^2(R_{W1})}. \tag{37}$$

Even if these distances might be small to justify the use of the asymptotic behaviour given by eq. (34), the quantity $2^{-\eta}$ can be taken as an estimation of the correlation reduction due to thermal effects. From Fig.3 we can see that only at very high temperatures above 1 MeV the hypothesis of incoherent scattering appears justified. For the following numerical applications, we will focus on T = 3 MeV as a representative temperature value.

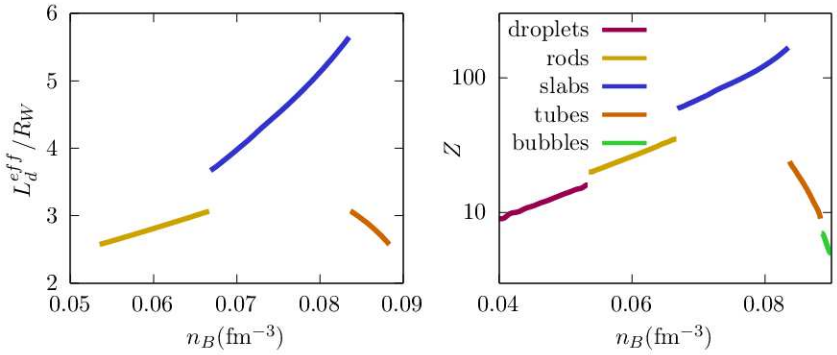

Figure 4. Left: Effective length of the pasta transverse to the symmetry axis, normalized to the Wigner-Seitz radius (see text). Right: Proton number of the pasta as a function of density. The different pasta geometries are indicated with different colours. The temperature is fixed to $T = 3$ MeV.

Since the correlation asymptotically follows the same power law in the transverse as in the longitudinal plane see eq. (35), we define the effective length of the slab L_1 from the same order-of-magnitude consideration:

$$\frac{\delta n^2(L_1^{eff})}{\delta n^2(L_{W1})} \approx 2^{-\eta} \tag{38}$$

where L_{W1} is defined by normalizing the slab WS volume to the droplet volume at identical thermodynamic conditions. Comparing eqs (37) and (38), we consider that the effective length of the slabs is

$$L_1^{eff} = \sqrt{2} L_{1W}. \tag{39}$$

For the rods, in the absence of an exact calculation of $S(\boldsymbol{q})$, we assume the length of interest to be equal to the slabs one if they were dominant at the same density, $L_2^{eff} = L_1^{eff}$. The resulting numerical values of the pasta length and proton number at $T = 3$ MeV are shown in Fig. 4.

Within the hypothesis of incoherent scatterings, the structure factor integral is limited to a single cell. Charge fluctuations within the cell being negligible we can write $\langle n_p(\boldsymbol{r}) n_p(\boldsymbol{r'})\rangle_T = \langle n_p(\boldsymbol{r})\rangle_T \langle n_p(\boldsymbol{r'})\rangle_T$, leading to:

$$S(\boldsymbol{q}) \approx Z^2 n_i |F(q)|^2, \tag{40}$$

with the form factor $F(\boldsymbol{q})$ defined as the Fourier transform of the charge density normalized by the number of protons composing the cluster (Z):

$$F(\boldsymbol{q}) = \frac{1}{Z} \int_{\mathrm{WS}} d^3\boldsymbol{r} e^{i\boldsymbol{q}\cdot\boldsymbol{r}} n_p(\boldsymbol{r}), \tag{41}$$

and the number density of targets within the medium as $n_i = 1/V$.

Analytic expressions can be found for the form factor by direct integration of eq. (41) for spherical, cylindrical, and planar geometries (labelled $d = 3, 2, 1$, respectively):

$$F_d(\boldsymbol{q}) = \begin{cases} \dfrac{3}{(qR_3)^3}\left[\sin(qR_3) - qR_3\cos(qR_3)\right], & \text{d=3} \\ \dfrac{2}{q_z L_2}\sin\left(\dfrac{q_z L_2}{2}\right)\dfrac{2}{q_\perp R_2} J_1\left(q_\perp R_2\right), & \text{d=2} \\ \dfrac{2}{L_1 q_x}\sin\left(\dfrac{L_1 q_x}{2}\right)\dfrac{2}{L_1 q_y}\sin\left(\dfrac{L_1 q_y}{2}\right)\dfrac{1}{R_1 q_z}\sin\left(R_1 q_z\right), & \text{d=1} \end{cases} \tag{42}$$

Here, $q_x = q\sin\theta_q\cos\phi_q$, $q_y = q\sin\theta_q\sin\phi_q$, $q_z = q\cos\theta_q$, $q_\perp = \sqrt{q_x^2 + q_y^2}$, and J_1 is the cylindrical Bessel function,

$$J_1(x) = \frac{1}{i\pi}\int_0^\pi d\phi e^{ix\cos(\phi)}\cos(\phi). \tag{43}$$

Finally, using the Fourier transform of the electric potential

$$U(\boldsymbol{q}) = \frac{4\pi e}{q^2\varepsilon(\boldsymbol{q})}, \tag{44}$$

the transition matrix element is written as:

$$W_{pp'}(\boldsymbol{q}, \epsilon_p) = n_i e^2 \left(1 - \frac{q^2}{4\epsilon_p^2}\right)\left|\frac{4\pi e Z F_d(\boldsymbol{q})}{q^2\varepsilon(q)}\right|^2, \tag{45}$$

where the dielectric function $\varepsilon(q)$ is introduced, regularizing the divergence at $q = 0$, to account for electron screening. A complete calculation within relativistic quantum mechanics, in the random phase approximation, gives (Jancovici 1962; Haensel et al. 2007):

$$\begin{aligned}\epsilon(q) = 1 + \frac{k_{TF}^2}{q^2}\Bigg\{ &\frac{2}{3} - \frac{2}{3}\frac{y^2 x_r}{\gamma_r}\ln(x_r + \gamma_r) \\ &+ \frac{x_r^2 + 1 - 3x_r^2 y^2}{6yx_r^2}\ln\left|\frac{1+y}{1-y}\right| \\ &+ \frac{2y^2x_r^2 - 1}{6yx_r^2}\frac{\sqrt{1+x_r^2y^2}}{\gamma_r}\ln\left|\frac{y\gamma_r + \sqrt{1+x_r^2y^2}}{y\gamma_r - \sqrt{1+x_r^2y^2}}\right|\Bigg\},\end{aligned} \tag{46}$$

where $y = q/2p_F$, $x_r = p_F/m_e$, $\gamma_r = \sqrt{1+x_r^2}$, k_{TF} is the

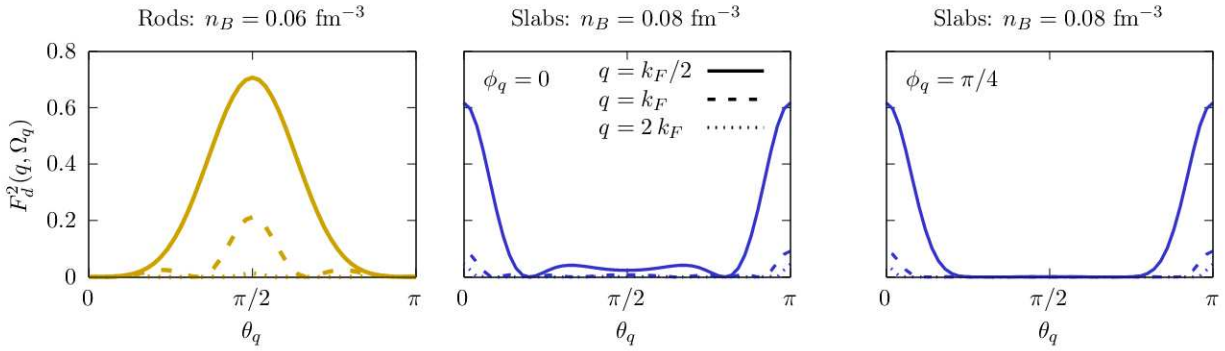

Figure 5. Form factor squared of rods at the representative density $n_B = 0.06$ fm^{-3} (left, yellow) and slabs at $n_B = 0.08$ fm^{-3} (middle and right, blue) as a function of the azimuthal angle, for different transferred momenta $q = k_F/2, k_F$ and $2k_F$ shown as continuous, dashed and dotted curves, respectively. For slabs we fix $\phi_q = 0$ (middle) and $\pi/4$ (right). The effective lengths L are taken from Figure 4. The temperature is fixed to $T = 3$ MeV.

Thomas-Fermi momentum, defined as:

$$k_{TF} = \sqrt{4\pi e^2 \partial n_e/\partial \mu_e} = 2\sqrt{\alpha_{em}\gamma_r/(\pi x_r)}k_F, \tag{47}$$

and the second equality supposes a strongly degenerate electron gas (Haensel et al. 2007). Though in this work we assume that the screening is isotropic, it is important to observe that strong magnetic fields lead to anisotropic behaviour and can produce Friedel oscillations (Horing 1969; Sharma & Reddy 2011). We leave the consideration of this source of further anisotropies to a future study.

3.2 Collision frequencies and conductivities

The expression of the transition matrix in eq. (45) allows us to get the final result for the collision rates. We substitute this expression into eqs (29) and (30) and make the change of variables

$$\int d\Omega_p d\Omega'_p = \frac{2\pi}{p^2}\int \frac{d^3\boldsymbol{q}}{q}\,, \tag{48}$$

to get the collision frequencies

$$\nu_a(\epsilon_p) = \frac{12\pi n_i e^4 Z^2}{vp^2}\int_0^{2p} dq \frac{1}{q\varepsilon^2(q)}\left(1 - \frac{q^2}{4\epsilon_p^2}\right)\int \frac{d\Omega_q}{4\pi}|F_d(\boldsymbol{q})|^2\cos^2\theta_q \tag{49}$$

$$\nu_p(\epsilon_p) = \frac{12\pi n_i e^4 Z^2}{vp^2}\int_0^{2p} dq \frac{1}{q\varepsilon^2(q)}\left(1 - \frac{q^2}{4\epsilon_p^2}\right)\int \frac{d\Omega_q}{4\pi}|F_d(\boldsymbol{q})|^2\frac{1}{2}\sin^2\theta_q\,. \tag{50}$$

Eqs (49) and (50) are the main results of the paper. Under the assumption of incoherent scatterings among the different pasta structures, and using the analytical expressions eq. (42) for the form factors, they allow calculating the thermal and electric conductivity of the pasta phase (see eq. (55) below) at any arbitrary temperature, density, proton fraction and magnetic field value from a given nuclear physics model providing the composition of the matter, namely the values of L, R and Z for the dominant pasta geometry. Some representative results will be given in the next section.

To compute the transport coefficients, the collision frequencies eqs (49) and (50) must be calculated at the Fermi energy $\epsilon_p = \epsilon_F$, since in the strongly degenerate electron gas transport occurs close to the Fermi surface. They can be written compactly as

$$\nu_K = \frac{12\pi n_i e^4 Z^2}{v_F p_F^2}\Lambda_K, \tag{51}$$

where p_F (v_F) is the Fermi momentum (velocity). We have also defined the axial ($K = a$) and perpendicular ($K = p$) Coulomb logarithms as

$$\Lambda_K = \int_0^{2p_F}\frac{dq}{q}\frac{1}{\varepsilon^2(q)}\left(1 - \frac{q^2}{4\epsilon_F^2}\right)\langle F^2\rangle_K\,, \tag{52}$$

and the averages $\langle F^2\rangle_K$ as

$$\langle F^2\rangle_a = \int \frac{d\Omega_q}{4\pi}|F_d(\boldsymbol{q})|^2\cos^2\theta_q\,, \tag{53}$$

and

$$\langle F^2\rangle_p = \int \frac{d\Omega_q}{4\pi}|F_d(\boldsymbol{q})|^2\frac{1}{2}\sin^2\theta_q\,. \tag{54}$$

The calculation of the conductivities with the anisotropic collision frequencies has been worked out in Yakovlev (2015), so here we only report the main equations. The magnetic field is assumed, without loss of generality, to lie in the xz–plane. By defining the unit vector $\boldsymbol{b} = \boldsymbol{B}/B = b_x\hat{x} + b_z\hat{z}$ and the cyclotron frequency for electrons $\omega = eB/\epsilon_F$, the electric conductivity tensor can be written as

$$\hat{\sigma} = \frac{e^2 n_e}{m_e^* \Delta}\begin{pmatrix} \nu_a\nu_p + \omega^2 b_x^2 & -\omega b_z \nu_a & \omega^2 b_x b_z \\ \omega b_z \nu_a & \nu_a\nu_p & -\omega b_x \nu_p \\ \omega^2 b_x b_z & \omega b_x \nu_p & \nu_p^2 + \omega^2 b_z^2 \end{pmatrix}, \tag{55}$$

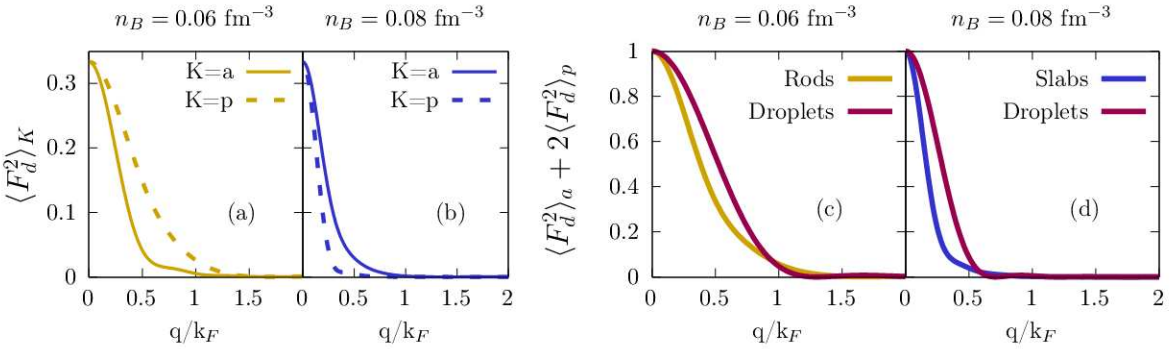

Figure 6. Left panels (a,b): axial (full) and perpendicular (dashed) square form factor of rods (yellow) and slabs (blue) at $n_B = 0.06$ (a) and 0.08 (b) fm^{-3}. Right panels (c,d): average square form factors of rods (yellow, c panel) and slabs (blue, d panel) are compared to the ones of droplets (magenta) at the same density. The representative temperature T=3 MeV is chosen.

where $\Delta = \nu_p^2\nu_a + \omega^2 b_x^2\nu_p + \omega^2 b_z^2\nu_a$. The thermal conductivity can be obtained by the Wiedemann-Franz law $\kappa_{ij} = \sigma_{ij}(\pi^2 T/3e^2)$ which is valid for strongly degenerate electrons (Ziman 2001). We do not consider neutron superfluidity, which results in corrections to the thermal conductivity, but not to the electrical (Aguilera et al. 2009). For $B = 0$, the conductivity becomes

$$\hat{\sigma}_0 = \frac{e^2 n_e}{m_e^*}\begin{pmatrix} \nu_p^{-1} & 0 & 0 \\ 0 & \nu_p^{-1} & 0 \\ 0 & 0 & \nu_a^{-1} \end{pmatrix}. \tag{56}$$

4 NUMERICAL RESULTS

The source of anisotropy entering the collision frequencies eq. (3) lies in the angular dependence of the form factors $F_d(\boldsymbol{q})$. The latter is displayed for rods and slabs in Fig. 5, as a function of the azimuthal angle θ_q (see Fig.1) for different values of $q = k_F/2, k_F, 2k_F$. In these figures, the temperature is fixed to $T = 3$ MeV and the two representative densities n_B =0.06, 0.08 fm^{-3} are chosen, where rods (slabs) are expected to be dominant according to the results presented in Fig. 2. We can see from Fig. 5 that for the rods, the form factor is strongly peaked at $\theta_q = \pi/2$, while for slabs it is peaked at $\theta_q = 0$ and π. Such behaviour is expected from their geometries, as the form factors are peaked in the elongated direction.

However, this dependence is smoothed out by the angular average implied by eqs (53) and (54). This is shown in Fig. 6, that displays the averaged form factors $\langle F^2\rangle_{a,p}$ defined in eqs (53),(54). The average value, given by $2\langle F^2\rangle_p + \langle F^2\rangle_a$, is also plotted, in the same thermodynamic conditions as in Fig. 5. As we can expect from Fig.1 and eq. (42), the form factor is maximum (minimum) in the symmetry axis direction in the case of slabs (rods). This difference is pronounced at momentum transfers smaller than $q = k_F$, as afterwards, both axial and perpendicular components tend to zero. When comparing the form factors to the one of the equivalent spherical droplet (right side of Fig.6), we can see that the difference is essentially seen at low momentum as well, where the form factor is systematically smaller within a deformed shape than for the equivalent spherical geometry.

In the previous figures, we have estimated the effective pasta length L_d based on the asymptotic behaviour of the thermal density correlation function of the smectic phase in the perpendicular plane (see Figure 3 and associated discussion). Though qualitatively the physical origin of the electron-pasta scattering is certainly the breaking of the long-range order due to thermal fluctuations, our estimations are very rough and would deserve to be confronted with microscopic molecular dynamics simulations (Horowitz et al. 2015; Caplan et al. 2021; Newton et al. 2022; Pelicer et al. 2021; Nandi & Schramm 2018). To evaluate the effect of the uncertainty on the estimation of L_d, in Fig. 7 we show the axial and perpendicular Coulomb logarithms eq.(52) and the ratio of perpendicular to axial collision frequency eq.(51) as a function of the ratio of the pasta length L_d to the WS-radius R_{Wd} for rods and slabs.

For both geometries, the Coulomb logarithm decreases with the increasing length of the pasta, and its value tends to zero as L_d becomes sufficiently large. This is consistent with the expectation that the lattice order should suppress the electron-ion scattering and increase the conductivity of matter.

For rods (slabs), the perpendicular component is larger (smaller) than the axial one, and the difference between them increases with the growing length of the pasta, varying up to 100 (0.01) when $L_d \approx 150R_W$. We can see that a precise estimation of the length of the structures is important for the quantitative determination of the collision frequencies, as it affects in a considerable way the difference between the two scattering directions. In particular, the deviation from an isotropic scattering is small only for small values of L_d/R_W, corresponding to the high-temperature regime. At smaller temperatures, as correlations become more important, a larger transverse length will contribute to the scattering, so the difference in the anisotropic frequencies will be more pronounced, likely reaching those expected in Yakovlev (2015).

In Fig. 8 the Coulomb logarithms eqs(52) are shown as a function of the density for T=1 and 3 MeV. In both cases, we can see that the abrupt change of favoured geometry leads to slight discontinuities in the Coulomb logarithms, and both overall decrease with density. This can be understood from the increase in length, shown in Fig. 4, and from Fig. 7.

The ratio of perpendicular to axial collision frequency eqs (51) and the average conductivity are shown in Fig. 9 for the same temperatures. The slight increase in the ratio with density is due to the increasing length. It is important to note

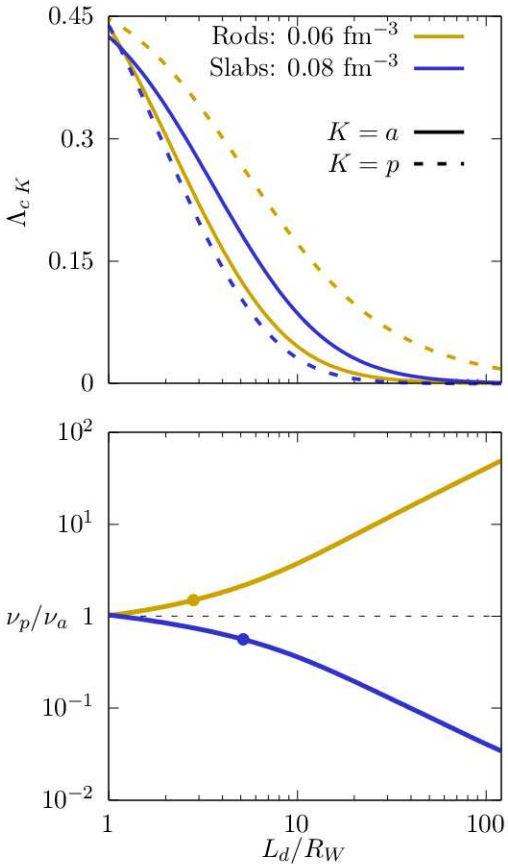

Figure 7. The Coulomb logarithms (upper part) and the ratio of perpendicular to axial collision frequency (lower part) are shown as a function of the pasta length normalized to the Wigner-Seitz radius, L_d/R_W. Quantities for rods (slabs) are calculated at $n_B = 0.06$ fm^{-3} ($n_B = 0.08$ fm^{-3}) and plotted in yellow (blue). In the upper panel, the perpendicular (axial) component are displayed as dashed (continuous) lines. The points in the lower plot indicate the estimated effective length $L_1^{eff} = \sqrt{2}\, L_{1W}$ (see text).The representative temperature $T = 3$ is chosen.

that, at the temperatures and lengths we are considering, the different collision frequencies differ by a factor smaller than two, so there is only a small deviation from isotropic scattering at high temperatures. In the average conductivity on the other hand, there is a larger discontinuity when the abrupt change of geometry happens. This difference is mainly due to the associated discontinuity in proton number, which can be seen on the right side of Fig. 4. All in all, the anomalously high resistivity of the pasta layer reported in the literature (Caplan et al. 2018) is nicely reproduced by our calculations, and it is seen to be essentially due to the high Z value of the clusters close to the crust-core transition, more than to the specific geometry of the pasta phases.

We now turn to the effect of the magnetic field on the conductivities. When including the magnetic field, we show all components of the conductivity in units of the dominant conductivity at zero magnetic field, i.e. the perpendicular (axial) conductivity for rods (slabs). In Figs. 10 (11) we show the conductivity components when the magnetic field forms an angle $\theta_b = 0, 45^o$, and 90^o with the symmetry axis of the pasta. Different off-diagonal components appear depending on the angle of the magnetic field: if it lies in the symmetry axis of the pasta, only the perpendicular xy component is not zero, the zz component depends only on ν_a, and the perpendicular xx and yy components are determined by both ν_p and $\boldsymbol{B}$. If it lies perpendicularly to the symmetry axis, only zy is not zero, the zz component is determined by ν_a and $\boldsymbol{B}$ and $xx = yy$ only by ν_p. At magnetic fields $B < 10^{18}$ G, the zz component is not drastically modified, transverse components increase (decrease) for rods (slabs), and the off-diagonal terms increase steadily. At $\sim 10^{18}$ G, the diagonal components parallel to the magnetic field are unaffected, but the perpendicular and off-diagonal components start to decrease. A magnetic field of this order is not far from the one expected at the very bottom of the inner crust of magnetars, which is about 20% of the field in the core (Chatterjee et al. 2019; Fujisawa & Kisaka 2014).

For the average conductivity, we follow Yakovlev (2015) once more, and assume the pasta takes random orientations with respect to the magnetic field since up to date there is no information regarding its orientation or prevalence of domains. To calculate the average parallel, perpendicular, and Hall terms we define a plane orthogonal to the magnetic field with the vectors $\boldsymbol{e}_1$, $\boldsymbol{e}_2 = \boldsymbol{e}_1 \times \boldsymbol{b}$ and make the projections: $\sigma_\perp = \boldsymbol{b}\cdot\hat{\sigma}\cdot\boldsymbol{b}$, $\sigma_\parallel = \boldsymbol{e}_1\cdot\hat{\sigma}\cdot\boldsymbol{e}_1$ and $\sigma_H = \boldsymbol{e}_1\cdot\hat{\sigma}\cdot\boldsymbol{e}_2$, such that averaging the coefficients over all directions leads to:

$$\begin{pmatrix}\langle\sigma_\perp\rangle\\ \langle\sigma_\parallel\rangle\\ \langle\sigma_H\rangle\end{pmatrix} = \frac{e^2 n_e}{m_e^*\omega^2}\begin{pmatrix}(\omega^2+\nu_p\nu_a)(\nu_p^2+\omega^2)H-\nu_p\\ \frac{1}{2}[\nu_a\nu_p(\omega^2-\nu_p^2)H+\nu_p]\\ \omega(1-\nu_a\nu_p H)\end{pmatrix} \text{ with } H = \begin{cases}(sr)^{-1}\arctan(s/r) & \nu_a > \nu_p\\ (sr)^{-1}\operatorname{arctanh}(s/r) & \nu_a < \nu_p\\ (\nu_a^3+\omega^2\nu_a)^{-1} & \nu_a = \nu_p\end{cases} \quad (57)$$

$s = \omega\sqrt{|\nu_a-\nu_p|}$ and $r = \sqrt{\nu_p(\omega^2+\nu_a\nu_p)}$. For $B \to 0$ we get

$$\langle\sigma_\perp\rangle = \langle\sigma_\parallel\rangle = \frac{e^2 n_e}{m_e^*}\langle\nu^{-1}\rangle, \quad \langle\nu^{-1}\rangle = \frac{1}{3}\left(\frac{2}{\nu_p}+\frac{1}{\nu_a}\right) \quad (58)$$

and the Hall parameters is zero $\langle\sigma_H\rangle \to 0$. One must notice that the average conductivity is proportional to the average of the inverse of $\langle\nu\rangle$, and not $\langle\nu\rangle$ itself, therefore its calculation does not amount to averaging the matrix element over Ω_q.

In Fig. 12 we show the average conductivities for rods and slabs, respectively, in units of the average conductivity with $B = 0$. This figure can be compared with Fig.3 of Yakovlev (2015), though the parallel component in our calculation is not so different from the perpendicular one due to the small difference we found between the anisotropic frequencies, unlike the assumption of Yakovlev (2015). To conclude this discussion, it is important to note that for all the calculations re-

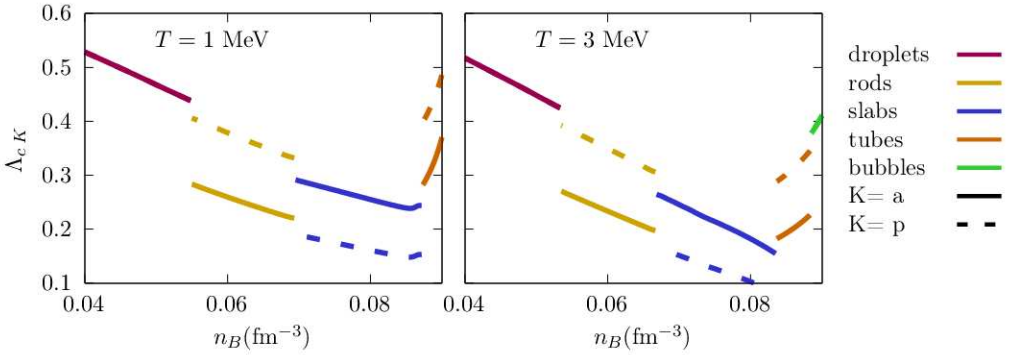

Figure 8. Axial (continuous) and perpendicular (dashed) Coulomb logarithms as a function of baryon density, for $T = 1$ MeV (left panel) and $T = 3$ MeV (right panel). The different pasta geometries are indicated with different colours.

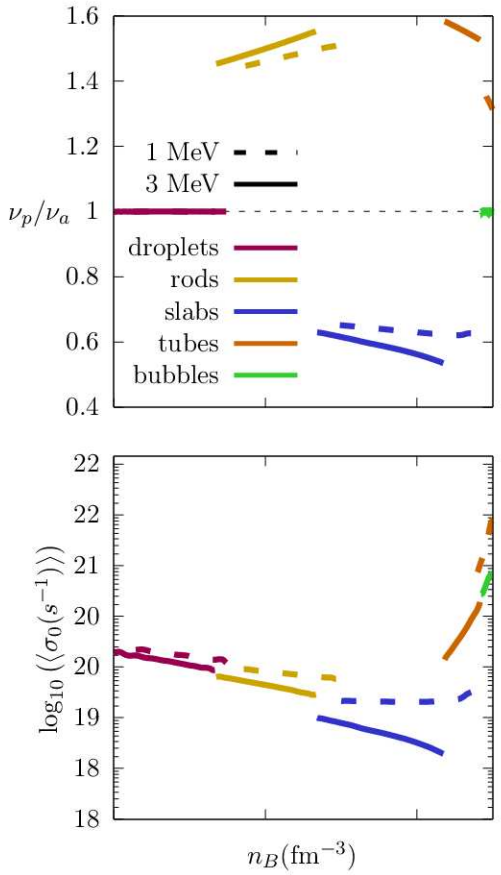

Figure 9. Top: ratio of perpendicular to axial relaxation time. Bottom: Average electric conductivity. Curves are shown as a function of density for the representative temperatures of $T = 1$ (dashed) and 3 (continuous) MeV. The different pasta geometries are indicated with different colours.

ported in this paper, the inner crust structure was computed without accounting for the magnetic field. Numerous studies exist in the literature addressing this point, using CLD or Thomas-Fermi techniques with different nuclear models, see e.g. Nandi et al. (2011); de Lima et al. (2013); Bao et al. (2021); Wang et al. (2022). The general result of these works is that only extreme magnetic fields of the order of $B = 10^{18}$ G affect the density profiles of the Wigner-Seitz cells, with an increased average proton fraction, particularly in the outer part of the inner crust dominated by spherical nuclei, and an increase of the charge of the pasta structures, that however does not exceed $\approx 10 - 20\%$. These modifications would not affect the results presented in Figs. 11 and 12, and would lead to an extra decrease of the conductivity in Fig. 9, since $\sigma \propto Z^{-2}$, see eq.(51).

5 CONCLUSIONS

In this paper, we studied the collision frequencies for elastic scattering between electrons and two different pasta phase structures. To do so, we performed an expansion of the collision integral in spherical harmonics, which allowed us to treat also the scattering with non-spherical targets. We applied this framework to calculate the electrical conductivity tensor.

The form factor of the pasta structures was evaluated by direct integration, although we neglected contributions from the structure factor, which is equivalent to assuming that electron scatterings with different pasta targets are completely incoherent. This is a reasonable first approximation at high temperatures of the order of the MeV or above. More work is needed to evaluate the anisotropy of the transport coefficients at lower temperatures where the lattice long-range order along the pasta symmetry axis is likely to be preserved.

We find that anisotropic collision frequencies are highly dependent on the length of the pasta structures. In the high-temperature regime, where the effective length that participates in the scattering is comparable to the WS length, the anisotropy is small and affects mainly the components of the conductivity perpendicular to the pasta symmetry axis. It should be emphasized that neutron star properties are expected to be significantly impacted by the presence of different and mixed pasta geometries (Caplan et al. 2021; Schneider et al. 2016; Newton et al. 2022), and their (possibly disordered) mesoscopic arrangement. Unfortunately, information is still lacking on how pasta domains, defects, and impurities appear at larger scales, but the presence of this kind of disorder is considered to be a likely feature of the pasta layers (Caplan et al. 2021; Schneider et al. 2016; Newton et al. 2022; Pelicer et al. 2021). Our treatment, at the moment, does not include precise corrections coming from scattering with domain boundaries and mixed geometries. Future inves-

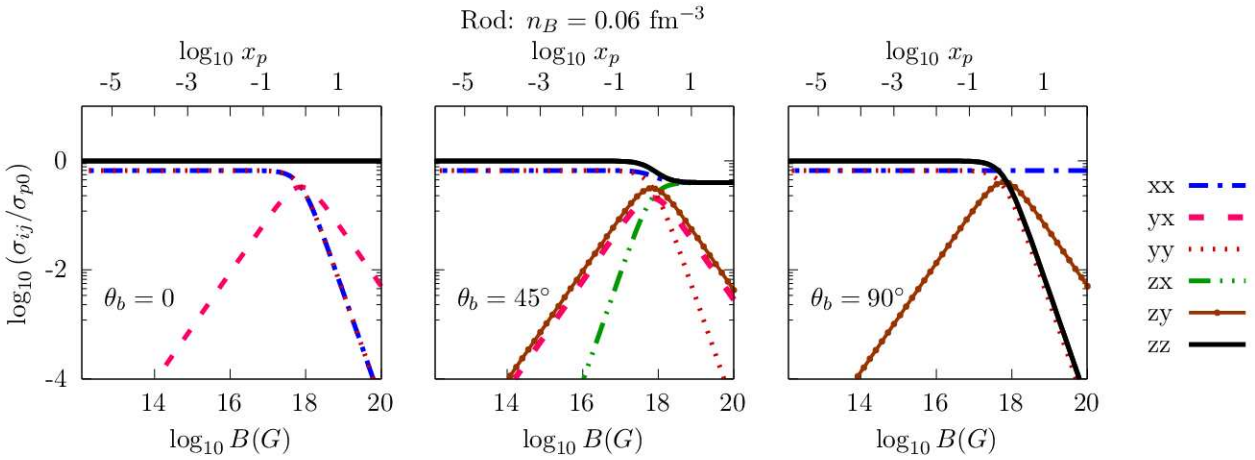

Figure 10. Components of the electric conductivity in units of the perpendicular conductivity at $B = 0$, as a function of the magnetic field for rods at $n_B = 0.06$ fm^{-3}. The angle between the pasta symmetry axis and the magnetic field is fixed at 0 (left), 45º (center) and 90º (right). In the top axis, we show the variable $x_p = eB/(\epsilon_F \nu_p)$.

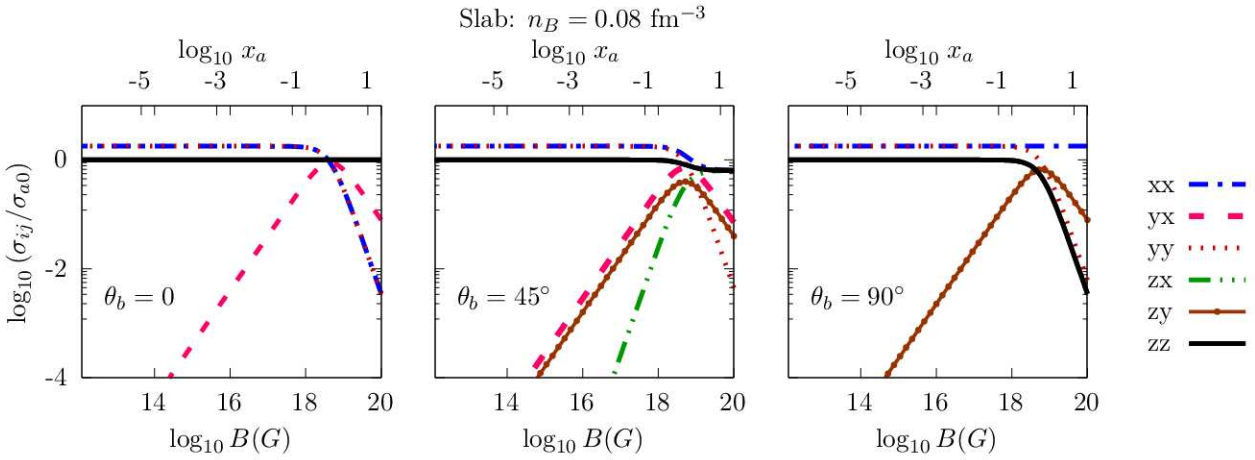

Figure 11. Components of the electron conductivity in units of the axial conductivity at $B = 0$, as a function of the magnetic field for slabs at $n_B = 0.08$ fm^{-3}. The angle between the pasta symmetry axis and the magnetic field is fixed at 0 (left), 45º (center) and 90º (right). In the top axis, we show the variable $x_a = \omega/\nu_a$.

tigations of these matters must be incorporated within the present framework to improve it.

Our numerical results are based on the IUFSU force, a simplified modelling of the pasta phase using a one-component liquid drop approach, and an estimation of the pasta sizes based on the values of the correlation between neighbouring WS cells. However, the analytical results are general and can be used to calculate the transport properties of the inner crust, with and without a magnetic field, by using any microscopic estimation of the pasta linear dimensions and proton number from microscopic mean-field or molecular dynamics simulations.

ACKNOWLEDGEMENTS

This work is a part of the project INCT-FNA Proc. No. 464898/2014-5, and of the Master project In2p3 NewMAC. D.P.M. is partially supported by Conselho Nacional de Desenvolvimento Científico e Tecnológico (CNPq/Brazil) under grant 303490/2021-7 and M.R.P. is supported by Conselho Nacional de Desenvolvimento Científico e Tecnológico - Brasil (CNPq) and with a doctorate scholarship by Coordenação de Aperfeiçoamento de Pessoal de Nível Superior (Capes/Brazil). M. R. P. also acknowledges partial support from LPC Caen. MA acknowledges partial support from PHAROS, COST Action CA16214.

6 DATA AVAILABILITY

No new data were generated or analysed in support of this research.

REFERENCES

Aguilera D. N., Cirigliano V., Pons J. A., Reddy S., Sharma R., 2009, Phys. Rev. Lett., 102, 091101

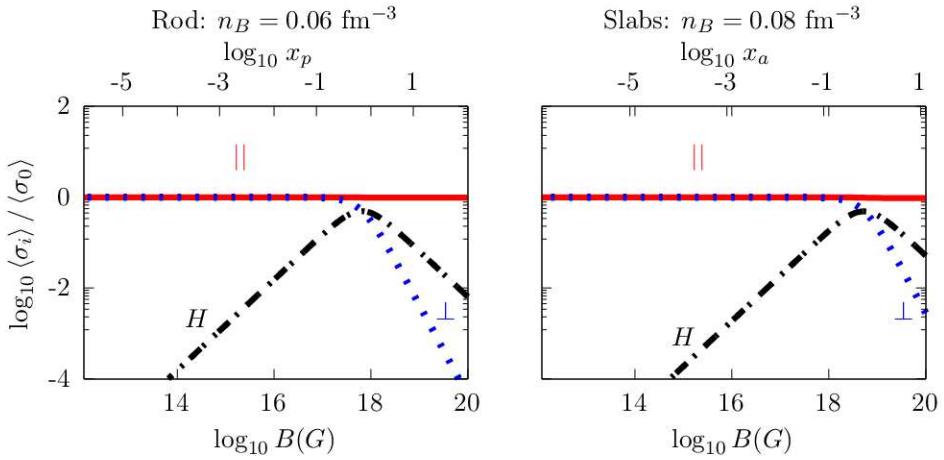

Figure 12. Average parallel, perpendicular and Hall conductivities for randomly oriented rods (left) and slabs (right) at $n_B = 0.06$ fm^{-3} and $n_B = 0.08$ fm^{-3}, respectively. In the top axis, we show the variable $x_i = \omega/\nu_i$, with $i = p$ (a) on the left (right).

Alloy M. D., Menezes D. P., 2011, Phys. Rev. C, 83, 035803
Antonelli M., Haskell B., 2020, MNRAS, 499, 3690
Avancini S. S., Menezes D. P., Alloy M. D., Marinelli J. R., Moraes M. M. W., Providência C., 2008, Phys. Rev. C, 78, 015802
Avancini S. S., Brito L., Marinelli J. R., Menezes D. P., de Moraes M. M. W., Providencia C., Santos A. M., 2009, Phys. Rev. C, 79, 035804
Avancini S. S., Barros C. C., Brito L., Chiacchiera S., Menezes D. P., Providência C., 2012, Phys. Rev. C, 85, 035806
Baiko D. A., Kaminker A. D., Potekhin A. Y., Yakovlev D. G., 1998, Phys. Rev. Lett., 81, 5556
Bao S. S., Hu J. N., Shen H., 2021, Phys. Rev. C, 103, 015804
Berestetskii V., Lifshitz E., Pitaevskii V., 1971, Course of theoretical physics-Pergamon International Library of Science
Bransgrove A., Levin Y., Beloborodov A., 2018, MNRAS, 473, 2771
Brink D., Satchler G., 1968, Theory of Angular Momentum
Camelio G., Gavassino L., Antonelli M., Bernuzzi S., Haskell B., 2022, arXiv e-prints, p. arXiv:2204.11809
Caplan M. E., Schneider A. S., Horowitz C. J., 2018, Phys. Rev. Lett., 121, 132701
Caplan M. E., Forsman C. R., Schneider A. S., 2021, Phys. Rev. C, 103, 055810
Carreau T., Fantina A. F., Gulminelli F., 2020, A&A, 640, A77
Chamel N., Haensel P., 2008, Living Reviews in Relativity, 11, 10
Chandrasekhar S., 1992, Liquid crystals. Cambridge University Press
Chatterjee D., Novak J., Oertel M., 2019, Phys. Rev. C, 99, 055811
Chugunov A. I., Yakovlev D. G., 2005, Astron. Rep., 49, 724
Deibel A., Cumming A., Brown E. F., Reddy S., 2017, ApJ, 839, 95
Dinh Thi H., Fantina A. F., Gulminelli F., 2021, Eur. Phys. J. A, 57, 296
Edmonds A. R., 2016, Angular momentum in quantum mechanics. Princeton university press
Fattoyev F. J., Horowitz C. J., Piekarewicz J., Shen G., 2010, Phys. Rev. C, 82, 055803
Flowers E., Itoh N., 1976, ApJ, 206, 218
Freire A., 2022, Partial differential equations. University of Tennessee
Fujisawa K., Kisaka S., 2014, Monthly Notices of the Royal Astronomical Society, 445, 2777
Gallier J., 2013, Notes on Spherical Harmonics and Linear Representations of Lie Groups. University of Pennsylvania
Haensel P., Potekhin A. Y., Yakovlev D. G., 2007, Neutron Stars 1 : Equation of State and Structure. Astrophysics and Space Science Library Vol. 326, Springer Science & Business Media
Hambaryan V., Suleimanov V., Haberl F., Schwope A. D., Neuhäuser R., Hohle M., Werner K., 2017, A&A, 601, A108
Hashimoto M.-a., Seki H., Yamada M., 1984, Progress of Theoretical Physics, 71, 320
Heiselberg H., Pethick C. J., 1993, Phys. Rev. D, 48, 2916
Horing N. J., 1969, Phys. Rev., 186, 434
Horowitz C. J., 2010, Phys. Rev. D, 81, 103001
Horowitz C. J., Berry D. K., 2008, Phys. Rev. C, 78, 035806
Horowitz C. J., Pérez-García M. A., Carriere J., Berry D. K., Piekarewicz J., 2004, Phys. Rev. C, 70, 065806
Horowitz C. J., Berry D. K., Briggs C. M., Caplan M. E., Cumming A., Schneider A. S., 2015, Phys. Rev. Lett., 114, 031102
Jancovici B., 1962, Il Nuovo Cimento (1955-1965), 25, 428
Landau L. D., Lifshitz E. M., 1969, Statistical Physics. Pergamon Press, Oxford
Lin Z., Caplan M. E., Horowitz C. J., Lunardini C., 2020, Phys. Rev. C, 102, 045801
Montoli A., Antonelli M., Magistrelli F., Pizzochero P. M., 2020, A&A, 642, A223
Nandi R., Schramm S., 2018, The Astrophysical Journal, 852, 135
Nandi R., Bandyopadhyay D., Mishustin I. N., Greiner W., 2011, The Astrophysical Journal, 736, 156
Nandkumar R., Pethick C. J., 1984, Monthly Notices of the Royal Astronomical Society, 209, 511
Newton W. G., 2013, Nature Physics, 9, 396
Newton W. G., Cantu S., Wang S., Stinson A., Kaltenborn M. A., Stone J. R., 2022, Phys. Rev. C, 105, 025806
Oyamatsu K., 1993, Nucl. Phys. A, 561, 431
Page D., Reddy S., 2012, arXiv e-prints, p. arXiv:1201.5602
Parmar V., Das H. C., Kumar A., Kumar A., Sharma M. K., Arumugam P., Patra S. K., 2022, Phys. Rev. D, 106, 023031
Pelicer M. R., Menezes D. P., Barros C. C., Gulminelli F., 2021, Phys. Rev. C, 104, L022801
Pethick C., Potekhin A., 1998, Physics Letters B, 427, 7
Pethick C. J., Zhang Z., Kobyakov D. N., 2020, Phys. Rev. C, 101, 055802
Pines D., Nozières P., 2018, Theory of Quantum Liquids: Normal Fermi Liquids. CRC Press
Poniewierski A., Holyst R., Price A., Sorensen L., Kevan S., Toner J., 1998, Phys. Rev. E, 58, 2027
Pons J. A., Viganò D., 2019, Living Reviews in Computational Astrophysics, 5
Pons J., Viganó D., Rea N., 2013, Nature Physics, pp 431–434
Potekhin A. Y., 1999, A&A, 351, 787

Potekhin A. Y., Chabrier G., 2021, Astron. Astrophys., 645, A102
Potekhin A. Y., Baiko D. A., Haensel P., Yakovlev D. G., 1999, Astron. Astrophys., 346, 345
Racah G., 1942a, Phys. Rev., 61, 186
Racah G., 1942b, Phys. Rev., 62, 438
Ravenhall D. G., Pethick C. J., Wilson J. R., 1983, Phys. Rev. Lett., 50, 2066
Schmitt A., Shternin P., 2018, in Rezzolla L., Pizzochero P., Jones D., Rea N.and Vidana I., eds, , Vol. 457, The Physics and Astrophysics of Neutron Stars. Springer, Astrophysics and Space Science Library
Schneider A. S., Berry D. K., Briggs C. M., Caplan M. E., Horowitz C. J., 2014, Phys. Rev. C, 90, 055805
Schneider A. S., Berry D. K., Caplan M. E., Horowitz C. J., Lin Z., 2016, Phys. Rev. C, 93, 065806
Schuetrumpf B., Martínez-Pinedo G., Reinhard P.-G., 2020, Phys. Rev. C, 101, 055804
Sharma R., Reddy S., 2011, Phys. Rev. C, 83, 025803
Shternin P. S., Yakovlev D. G., 2006, Phys. Rev. D, 74, 043004
Sotani H., 2012, in 21st Workshop on General Relativity and Gravitation in Japan. pp 100–103
Sykes J., Brooker G., 1970, Annals of Physics, 56, 1
Tan C. M., et al., 2018, ApJ, 866, 54
Wang X., Li J., Fang J., Pais H., Providência C. m. c., 2022, Phys. Rev. D, 105, 063004
Watanabe G., Iida K., Sato K., 2000, Nuclear Physics A, 676, 455
Yakovlev D. G., 2015, Monthly Notices of the Royal Astronomical Society, 453, 581
Yakovlev D. G., Urpin V. A., 1980, Soviet Astronomy, 24, 303
Ziman J. M., 2001, Electrons and phonons: the theory of transport phenomena in solids. Oxford university press
de Gennes P. G., Prost J., 1993, The physics of liquid crystals. Clarendon, Oxford
de Lima R. C. R., Avancini S. S., Providência C., 2013, Phys. Rev. C, 88, 035804

APPENDIX A: ISOTROPIC LIMIT

In this appendix, we show that the isotropic limit is obtained from eq. (14) when $W_{pp'}$ is a function only of $|\boldsymbol{q}|$ The equation obtained is equivalent to to eq. (3.135) of Pines & Nozières (2018). In the isotropic case, there is no change in the l index of spherical harmonics during the collision, and the sum of m and m' indexes are zero since $W_{pp'}$ is a function of the relative angle between $\boldsymbol{p}$ and $\boldsymbol{p'}$, therefore:

$$\mathcal{W}_{lm\,l'm'} = \mathcal{W}_{lm}\delta_{ll'}\delta_{m\,-m'}. \tag{A1}$$

This can be understood from the expansion in eq. (8), where in the isotropic case the pair of spherical harmonics must be replaced by the Legendre polynomial. Eq. (14) can be rewritten as

$$[\nu]_{lm}^{l'm'} = \frac{p^2}{4\pi^2 v}\Bigg[(-1)^{m'}\sqrt{(2l+1)(2l'+1)}\mathcal{W}_{00\,00}\begin{pmatrix} l & l' & 0 \\ 0 & 0 & 0\end{pmatrix} \times \begin{pmatrix} 0 & l & l' \\ 0 & m & -m'\end{pmatrix} - (-1)^{m}\,\mathcal{W}_{lm\,l-m}\delta_{ll'}\delta_{mm'}\Bigg]. \tag{A2}$$

We simplify this expression by utilizing the following property of the 3j-Wigner symbols:

$$\begin{pmatrix} l & l' & 0 \\ 0 & 0 & 0\end{pmatrix}\begin{pmatrix} 0 & l & l' \\ 0 & m & -m'\end{pmatrix} = \frac{(-1)^{-2l+m}}{2l+1}\delta_{ll'}\delta_{mm'} \tag{A3}$$

and defining $\mathcal{W}_{lm} = \mathcal{W}_{lm\,l-m}$, such that:

$$[\nu]_{lm}^{l'm'} = \frac{p^2}{4\pi^2 v}\delta_{ll'}\delta_{mm'}\Big[\mathcal{W}_{00} - (-1)^m\mathcal{W}_{lm}\Big]. \tag{A4}$$

To recover the usual integral equation with the transition matrix element we use eq. (28), with the aid of eq. (48)

$$\mathcal{W}_{lm} = \frac{2\pi}{p^2}\int\frac{d^3\boldsymbol{q}}{q}W_{pp'}(-1)^m Y_l^{m*}(\Omega_p)Y_l^{m*}(\Omega_{p'}) \tag{A5}$$

into eq. (A4) and average over the m index:

$$\nu_l = \frac{p^2}{4\pi^2 v(2l+1)}\int\frac{d^3\boldsymbol{q}}{q}W_{pp'}\sum_m\Bigg[\frac{1}{4\pi} - Y_l^{m*}(\Omega_p)Y_l^{m*}(\Omega_{p'})\Bigg]. \tag{A6}$$

Using the property of spherical harmonics

$$\sum_m Y_l^{m*}(\Omega_p)Y_l^{m*}(\Omega_{p'}) = P_l(cos\xi) \tag{A7}$$

where $\cos\xi = \boldsymbol{p}\cdot\boldsymbol{p'}/(|\boldsymbol{p}||\boldsymbol{p'}|)$ and changing variables as $2qdq = -p^2 d(\cos\xi)$, we obtain

$$\nu_l = \frac{p^2}{4\pi v}\int_{-1}^{1} d(\cos\xi)W_{pp'}\Big[1 - P_l(\cos\xi)\Big], \tag{A8}$$

which is equivalent to eq. (3.135) of Pines & Nozières (2018) for electron scattering with isotropic targets. We use $q^2 = p_F^2(1-\cos\xi)$ to change variables and write, for $l = 1$:

$$\nu_1(\epsilon_p) = \frac{1}{4\pi p^2 v}\int_0^{2p} q^3\,dqW_{pp'}, \tag{A9}$$

Using eq. (31), we recover eq. (2). Likewise, the viscosity can be obtained with the $l = 2$ – see eqs (2) and (3) of Chugunov & Yakovlev (2005):

$$\nu_2(\epsilon_p) = \frac{3}{4\pi p^2 v}\int_0^{2p} q^3\,dq\Big(1 - \frac{q^2}{4p^2}\Big)W_{pp'}. \tag{A10}$$